Magnetic quantum dots in II-VI semiconductor nanowires

Pamela Rueda-Fonseca

UNIVERSITÉ DE GRENOBLE

THÈSE

Pour obtenir le grade de

DOCTEUR DE L'UNIVERSITÉ DE GRENOBLE

Spécialité : **Physique/Nanophysique**

Arrêté ministériel : 7 août 2006

Présentée par

Pamela Carolina Rueda-Fonseca

Thèse dirigée par **Serge Tatarenko**
et codirigée par **Joël Cibert et Edith Bellet-Amalric**

préparée au sein de **l'équipe mixte CNRS-CEA Nanophysique et Semiconducteurs à l'Institut Néel et à l'INAC.**
et à **l'École Doctorale de Physique de Grenoble**

Magnetic quantum dots in II-VI semiconductor nanowires

Thèse soutenue publiquement le **16/02/2015**,
devant le jury composé de :

Etienne Gheeraert
Professeur, Université Joseph Fourier, Institut Néel, Grenoble, Président
Jean-Christophe Harmand
Directeur de recherche CNRS, LPN, Marcoussis, Rapporteur
Isabelle Berbezier
Directrice de recherche CNRS, IM2NP, Marseille, Rapporteur
Anna Fontcuberta i Morral
Professeure, École polytechnique fédérale de Lausanne, Examinatrice
Evelyne Gil
Professeure, Université Blaise Pascal, Institut Pascal, Clermont-Ferrand, Examinatrice
Serge Tatarenko
Directeur de recherche CNRS, Institut Néel, Grenoble, Directeur de thèse
Joël Cibert
Directeur de recherche CNRS, Institut Néel, Grenoble, Co-Directeur de thèse
Edith Bellet-Amalric
Ingénieur CEA, INAC, Grenoble, Co-Encadrant de thèse

"La persistencia me ha enseñado que aquello que se logra con trabajo y dedicación es de mayor riqueza; que aquella batalla librada contra la corriente y de la cual se sale victorioso es la que a la postre termina construyendo futuro."

Goyenechus

Acknowledgements

Finding the right words to thank all of the people that help me in this project is very challenging. I learn so many things, at so many different levels, from so many people, that this few words surely cannot show how grateful I really am for this experience. In the quest for accuracy, I will continue by addressing each person in the language we normally communicate.

Je voudrais commencer par remercier mes trois directeurs de thèse pour leur disponibilité sans faille, leur aide tout au long de ce projet et leur soutien pendant les moments critiques (parmi beaucoup d'autres choses !). Un grand merci à Joël Cibert pour m'avoir appris sa façon ingénieuse d'analyser les résultats et de les observer avec une perspective différente; à Edith Bellet-Amalric pour sa façon positive d'aborder les difficultés et à Serge Tatarenko pour son encouragement et accompagnement optimiste. Travailler avec eux a été un véritable privilège.

Un grand merci également aux personnes avec lesquelles j'ai collaboré pendant ma thèse et qui ont assisté à mes réunions hebdomadaires pendant 3 ans ! L'échange dynamique entre les domaines de la croissance, de l'optique et de la microscopie a été très enrichissant pour moi. Merci à Régis André pour son grand sens de l'humour, son aide lors de la préparation des présentations (particulièrement à Levi !) et pour m'avoir fortement encouragé à obtenir la nationalité française. Merci à Martien den Hertog pour m'avoir transmis la patience requise pour faire de la microscopie électronique à haute résolution des nanofils ayant moins de 10 nm de diamètre, qui vibrent sans arrêt! Merci à Yann de m'avoir appris les secrets de la MBE et pour son patience à toute épreuve à chaque fois que j'ai bloqué la canne ou que j'ai fait tombé un molybloc. Merci à David Ferrant, Alberto Artioli et Petr Stepanov pour leur excellent travail lors de la caractérisation optique. Merci à Eric Robin pour tout le temps que nous avons passé

à comprendre et analyser les mesures EDX sur des nanofils des fois un peu biscornus! Merci à Henri Mariette pour ses remarques pointues et son enthousiasme. Travailler avec eux a été un grand plaisir.

Je remercie chaleureusement toutes les autres personnes du laboratoire qui se sont intéressé à mon travail et avec lesquelles j'ai pu avoir des discussions intéressantes. Merci à Catherine Bougerol, Didier Boilot, Yoann Cure, Thibault Cremel, Kuntheak Kheng, Gilles Nogues, Dang Le-Si, Bruno Daudin, Joël Eymery, Hervé Boukari, Fabrice Donatini, Joël Bleuse, Marta Orru, Bruno Gayral, Myriam Elouneg-Jamroz, et à tous les autres membres de l'équipe mixte NPSC. Merci également à l'ensemble de mon jury de thèse pour le temps consacré à lire en détail mon manuscrit de thèse et pour leurs questions qui ont continué de faire progresser ce travail lors de ma soutenance.

Merci à mes amis chers pour tous les bons moments et leur soutien pendant ma thèse. Merci à Diane et Gabriel pour tous ces bons conseils, corrections et aide à J-1 de ma soutenance. Merci à Lionel, Aurélie, Emanuel, Damien, Karine, Thomas pour une superbe ambiance au labo! Un grand merci à (e)Steph, Emilie, Hélène, Virginie, Guillaume, Erwan et Nelly pour les moments en montagne qui m'ont permis de souffler lors des étapes compliquées. Merci à Alex pour tout (il y a trop de choses!). Gracias a Elvira, Soan y Sirona por su apoyo y alegría. Gracias a Juliana que vivió conmigo el día a día aun estando lejos. Gracias a Daniel por su ejemplo e inspiración. Gracias a toda mi familia por su amor.

Especialmente le doy las gracias a mi mamá que me ha apoyado incondicionalmente en todos mis proyectos. Su ejemplo, su fuerza, su integridad y su amor fueron esenciales para mi.

Finalement, je remercie Nicolas pour partager et construire sa vie avec moi, pour me rendre heureuse chaque jour et pour son grand soutien qui a été indispensable pour la rédaction de ce travail.

CONTENTS

Résumé en français **1**

Introduction **9**

1 II-VI SC properties, MBE & characterization techniques **15**
1.1 Properties of II-VI semiconductors 16
1.1.1 Crystal structure and polarity 16
1.1.2 Electronic properties 18
1.1.3 Diluted magnetic semiconductors 19
1.2 Molecular Beam Epitaxy (MBE) 20
1.3 Characterization techniques 24
1.3.1 Reflection High Energy Electron Diffraction (RHEED) 24
1.3.2 Electron microscopy (SEM & (S)TEM) 26
1.3.3 Energy-dispersive X-ray spectrometry (EDX) 29

2 Dewetting of Au catalytic droplets on ZnTe(111)B layers **31**
2.1 State of the art & purpose of this study 32
2.2 ZnTe(111)B layers: Growth, diffusion & surface reconstructions 35
2.2.1 Substrate preparation 35
2.2.2 Growth of ZnTe layers 36
2.2.3 Strain relaxation 38
2.2.4 Twins 39
2.2.5 High temperature smoothening 41
2.2.6 Conclusions 45
2.3 Properties of the dewetting of thin films of Au over ZnTe layers 46
2.3.1 Experimental details 46

2.3.2 Thermodynamic phase of the Au catalyst . . . 48
2.3.3 Calibration of the quantity of Au deposited . . . 49
2.3.4 Shape of the Au droplets . . . 51
2.3.5 Volume of the Au catalyst droplets . . . 54
2.3.6 Quantity of Au incorporated in the droplets . . . 60
2.4 Control of the Au-dewetting process . . . 65
2.4.1 Control of the Au-catalyst diameter . . . 65
2.4.2 Control of the Au-catalyst density . . . 68
2.4.3 Influence of the quality of the ZnTe(111)B buffer layer . . . 71
2.5 Conclusions . . . 73

3 Growth and properties of ZnTe nanowires 75
3.1 State of the art & purpose of this study . . . 76
3.2 Sample preparation . . . 80
3.3 Influence of different stoichiometric conditions on the nanowire growth 82
3.4 Cone-shaped and cylinder-shaped ZnTe NWs . . . 86
3.4.1 Lateral *versus* axial growth . . . 86
3.4.2 Crystal structure of the nanowires . . . 91
3.4.3 NW polarity . . . 93
3.4.4 Discussion . . . 95
3.5 Early stages of the nanowire growth . . . 97
3.5.1 Surface densities . . . 99
3.5.2 Morphological characteristics of the NWs . . . 101
3.6 Influence of the temperature on the NW growth . . . 109
3.7 Diffusion-driven nanowire growth model . . . 114
3.8 Conclusions . . . 127

4 Axial and radial NW-based heterostructures 131
4.1 State of the art & purpose of this study . . . 132
4.2 Sample growth . . . 135
4.2.1 Growth of a ZnMgTe shell over ZnTe NWs . . . 135
4.2.2 Growth of a Cd(Mn)Te QD in a ZnTe(/ZnMgTe) NW . . . 137
4.3 EDX analysis and modeling . . . 144
4.4 Results . . . 152
4.4.1 EDX of sample A: ZnTe NWs with a ZnMgTe shell . . . 152
4.4.2 EDX of sample B: ZnTe NWs with a CdTe QD insertion . . . 154
4.4.3 EDX of sample C: ZnTe NWs with a CdMnTe QD insertion and a ZnMgTe shell . . . 165
4.4.4 Spectroscopy results . . . 175
4.5 Discussion . . . 182

4.5.1 Quantum dot insertion 182
4.5.2 Core-multi shell NW structures 185
4.6 Conclusion 192

General conclusions **195**

Appendix **200**

Bibliography **205**

Résumé en français

Introduction

L'étude des **nanofils à base de semiconducteurs** a connu une croissance importante ces derniers années: avant 2004, seulement une petite centaine d'articles avaient été publiés alors que leur nombre total aujourd'hui dépasse les cent mille. Ce domaine de recherche vaste et diversifié inclut plusieurs techniques de croissance et de nombreux matériaux semiconducteurs (semiconducteurs du groupe IV et des alliages des groupes III-V et II-VI).

La géométrie unidimensionnelle des nanofils offre la possibilité de dépasser diverses limitations rencontrées dans le domaine de l'épitaxie des semiconducteurs. La croissance des hétérostructures semiconductrices avec un grand désaccord de maille et ayant une excellent qualité cristalline, ou la croissance des alliages semiconducteurs III-V et II-VI sur des substrats de silicium, en sont des exemples. De plus, cette géométrie offre la possibilité de manipuler les propriétés électroniques à travers le dopage ou l'ingénierie de la contrainte. La synthèse des nanofils avec un degré de complexité structurale élevée pourrait donner lieu à de nouvelles propriétés électriques et optiques. Des dispositifs à base de nanofils ont déjà montré des résultats encourageants dans le cas des capteurs ou des cellules solaires de troisième génération. Un bon contrôle de la modulation de la composition et du dopage dans ces nanostructures est indispensable pour explorer de nouvelles propriétés fondamentales et pour leur intégration dans de futurs dispositifs.

Des **hétérostructures axiales**, composées d'une ou plusieurs insertions nanométriques d'un semiconducteur ayant une bande interdite inférieure à l'intérieur d'un matériau semiconducteur ayant une bande interdite supérieure, forment des boîtes quantiques. La croissance d'une boîte quantique dans un nanofil offre au moins sept avantages:

1. La taille de la boîte quantique peut être contrôlée selon la direction radiale (déterminée par la surface de contact entre le nanofil et la goutte d'or qui catalyse sa croissance) et dans la direction axiale (en fonction du temps de croissance et du flux atomique ou moléculaire incident). Un fort confinement des porteurs peut être obtenu dans des boîtes quantiques ayant un petit diamètre.

2. La relaxation de la contrainte selon les parois du nanofil permet la croissance des boîtes quantiques ayant une forme allongée sans la formation de dislocations d'interface: l'épaisseur critique nécessaire pour la relaxation plastique devient infinie pour des nanofils avec un rayon inférieur à une valeur critique.

3. La position de la boîte quantique dans le plan parallèle au substrat est determinée par la position du nanofil. C'est-à-dire qu'en utilisant des substrats à motifs, la densité et la position des nanofils peuvent être contrôlées. En outre, la position de la boîte quantique selon l'axe du nanofil peut être choisie, ainsi que la croissance de plusieurs boîtes quantiques à l'intérieur du même nanofil.

4. Grâce à un processus de formation de la boîte quantique qui n'est pas induit par la contrainte (c'est-à-dire qui n'est pas dû à la différence de paramètre de maille entre les matériaux semiconducteurs), il est possible de combiner une grande variété de matériaux semiconducteurs dans la même nanostructure. La grande flexibilité dans le choix des matériaux offre l'opportunité de tester la croissance d'hétérostructures qui seraient très difficiles à obtenir lors de la croissance sous forme massive. Cette possibilité ouvre la voie à lÕexploration de nouvelles propriétés physiques.

5. L'absence d'une couche de mouillage permet l'obtention d'excellentes propriétés spectroscopiques par rapport aux boîtes quantiques obtenues par la méthode Stranski Krastanov, où la couche de mouillage permet la fuite de porteurs confinés dans la boîte.

6. Les excitons confinés dans une boîte quantique insérée dans un nanofil sont protégés des effets de surface. Cette configuration augmente l'efficacité de luminescence, permet d'obtenir des largeurs de raie plus fines et des longueurs de cohérence plus importantes.

7. Le couplage des mécanismes optiques et de transport dans le même objet quantique est possible et peut étre utilisé pour des applications d'émission ou de détection de la lumière.

Les **hétérostructures radiales** sont formées par la croissance de couches (coquilles) d'un matériau semiconducteur autour d'un cœur d'un autre matériau semiconducteur.

Si le cœur est en forme de nanofil on obtient donc des nanofils de structures dites cœur-coquille. Parmi les avantages de ces structures, nous pouvons mentionner l'effet de la passivation de la surface pour améliorer leurs propriétés optiques et de transport, ainsi que l'utilisation d'une coquille ayant une bande interdite plus grande que celle du cœur pour optimiser le confinement des porteurs dans le nanofil.

Grâce à la grande quantité d'articles publiés sur les nanofils, ce domaine de recherche a atteint une maturité qui permet l'exploration de deux sujets complexes qui n'ont pas été abordés auparavant: l'ingénierie de la contrainte dans des nanofils cœur-coquille et les hétérostructures magnétiques à base de nanofils.

La contrainte dans des nanofils cœur-coquille peut avoir un effet important sur les propriétés du couplage photonique, électronique et magnétique des porteurs à l'intérieur du matériau semiconducteur (en particulier sur les trous). Il est bien connu que la modulation de la contrainte permet de modifier les propriétés électroniques, par exemple elle permet d'obtenir une bande interdite directe dans des nanofils Si-Ge ou d'introduire un effet piézo-électrique pour accélérer la séparation des paires électron-trou dans des applications photovoltaïques. En outre, la configuration de la contrainte accumulée peut diminuer la dégénérescence de la bande de valence et permettre de choisir de façon convenable le type de porteurs pour des applications spintroniques. Cela implique de sélectionner: i) la partie orbitale du trou (responsable du couplage avec la lumière), les régles de sélection et les propriétés de polarisation lors de la recombinaison de la paire électron-trou, et ii) la partie du spin du trou, responsable des propriétés magnétiques. Par exemple le choix des trous avec un spin plus grand peut augmenter le couplage spin-porteur dans des semiconducteurs magnétique dilués.

Les nanofils magnétiques à base de semiconducteurs II-VI constituent une plateforme idéale pour tester et développer des mécanismes et des dispositifs spintroniques. La possibilité d'étudier les effets magnéto-optiques dans des objets nanométriques sur lesquels nous pouvons aussi injecter des porteurs et avoir un haut niveau de contrôle optique, les rendent des systèmes idéaux. L'incorporation d'ions magnétiques dans des nanofils de ZnTe/ZnMgTe et une manifestation de leur comportement magnétique sous champ magnétique ont été récemment démontrées.

Le couplage des porteurs confinés avec des ions magnétiques localisés donne lieu à la formation du polaron magnétique. Il s'agit d'un ordre ferromagnétique local du spin des atomes magnétiques induits par leur couplage avec un porteur ou un exciton. Des **polarons magnétiques anisotropes et stables** peuvent être formés si le porteur est confiné dans les 3 dimensions, créant ainsi des nano-objets ferromagnétiques ultimes qui offrent la possibilité de lire et de manipuler des états magnétiques. Réussir la

croissance d'un polaron magnétique anisotrope et stable dans un nano-objet unique, ainsi que leur étude et la compréhension de ses propriétés fondamentales est un défi majeur de la recherche en spintronique. L'étude de ces objets en utilisant des boîtes quantiques magnétiques à base de semiconducteurs II-VI à l'intérieur des nanofils cœur-coquille offre plusieurs avantages:

- L'incorporation d'ions manganèse dans la maille des semiconducteurs II-VI est optimale puisque le Mn a deux électrons de valence (identique aux éléments du groupe IIB comme le zinc et le cadmium). De ce fait, les ions manganèse n'agissent pas comme des dopants électriques dans les semiconducteurs II-VI.

- La densité et la distribution des atomes de manganèse sont déterminées par les conditions de croissance. Ainsi l'insertion des atomes magnétiques peut varier du spin unique aux grandes concentrations.

- Le ZnTe est un matériau avec une bande interdite directe qui peut être facilement dopé, ainsi une majorité de trous permet un couplage plus fort avec les impuretés magnétiques.

- Les boîtes quantiques de (Cd,Mn)Te peuvent être insérées à l'intérieur des nanofils de ZnTe. L'incorporation des ions de manganèse est seulement possible à basse température, ce qui est compatible avec les températures de croissance des nanofils de ZnTe. D'autres systèmes tels que les nanofils de GaAs ou Ge doivent être épitaxiés à haute température, alors que l'incorporation des impuretés magnétiques doit être réalisée à basse température.

- La formation d'un polaron magnétique stable peut être possible grâce au confinement dans les trois dimensions dans la boîte quantique. De plus, la maîtrise de la géométrie et de la contrainte de la boîte quantique permet de contrôler la forme du potentiel de confinement et l'anisotropie de spin des trous.

Objectifs et plan du manuscrit

L'objectif de ce travail est de développer un nouveau type de structures magnétiques en profitant des propriétés avantageuses des nanofils semiconducteurs. Dans ce contexte, nous avons étudié les mécanismes de croissance et les propriétés fondamentales des hétérostructures complexes à base de nanofils de type cœur-coquille: des boîtes quantiques de Cd(Mn)Te dans des nanofils de ZnTe, entourées d'une coquille de ZnMgTe.

Le premier chapitre fournit un aperçu général des propriétés structurales et électroniques des matériaux semiconducteurs II-VI et des méthodes expérimentales les plus courantes. Nous abordons la croissance par épitaxie par jets moléculaires et les techniques de caractérisation utilisées dans ce travail, en particulier la diffraction d'électrons de haute énergie en incidence rasante (RHEED), l'analyse dispersive en énergie (EDX) et la microscopie électronique en transmission (TEM). Le but du premier chapitre est d'introduire les concepts essentiels nécessaires pour comprendre les résultats présentés dans les chapitres suivants, sans être exhaustif.

Le deuxième chapitre est consacré à l'étude des propriétés de démouillage des gouttes d'or sur des couches de ZnTe(111)B. En premier lieu, la croissance des couches de ZnTe(111)B très faiblement rugueuses sur des substrats de GaAs(111)B est explorée. La relaxation de la contrainte, la formation de mâcles et la composition du diagramme de reconstruction de surface sont discutées. En deuxième lieu, le processus de démouillage de l'or est étudié dans un régime où la quantité d'or déposée sur la surface de ZnTe est inférieure à la monocouche. Ceci inclut, d'un côté, la détermination de la phase thermodynamique, la forme, le volume et l'angle de contact des particules d'or; et de l'autre côté, l'effet des paramètres clé tels que la quantité d'or disponible en surface pour la formation des particules, la température et le temps de démouillage, sur le diamètre moyen des gouttes d'or et la densité de surface. L'objectif de cette partie est de maitriser la formation des particules d'or pour obtenir un bon contrôle des surfaces permettant de mettre au point les propriétés des boîtes quantiques et des nanofils comme leur diamètre, leur densité, la nature et le profil des interfaces, etc.

Le troisième chapitre introduit la croissance catalysée par l'or des nanofils de ZnTe. Nous abordons l'influence des différentes conditions de croissance, comme le ratio des flux II/VI et la température, sur la croissance simultanée de deux types de nanofils (avec une forme conique ou cylindrique). Ces nanofils sont étudiés par TEM et EDX pour déterminer la structure cristalline (wurtzite/zinc-blende), la polarité (Te ou Zn en surface) et la présence/absence de croissance latérale. Les premières étapes de croissance et l'évolution avec le temps de la morphologie de ces nanofils sont aussi examinées. Finalement, nous discutons quelques résultats obtenus avec un modèle de croissance des nanofils basé sur la diffusion de surface. Des valeurs quantitatives de la longueur de diffusion sur le substrat et le long des parois du nanofil sont déduites.

Le quatrième chapitre est séparé en deux parties. La première se concentre sur la croissance des hétérostructures magnétiques à base de nanofils. Nous avons commencé par le cas le plus simple: la croissance des fils ZnTe avec une coquille de ZnMgTe. Ensuite, un deuxième échantillon est proposé avec une boîte quantique de CdTe insérée dans un fil pur de ZnTe et pour finir, le cas le plus complexe: une boîte quantique

de $Cd_{1-x}Mn_xTe$ insérée dans un nanofil cÏur-coquille de ZnTe/ZnMgTe. La deuxième partie consiste en la caractérisation structurale et optique sur un même nanofil. Nous proposons une nouvelle méthode pour obtenir une info quantitative et locale sur la concentration, la dimension, la forme et la position des différentes couches dans les nanofils de type cœur-coquille en faisant une analyse quantitative des mesures EDX. De plus, des résultats magnéto-optiques qui complètent cette étude sont résumés pour donner une description intégrale de ces hétérostructures.

Résultats principaux et conclusion de ce travail de recherche

Deux questions principales ont été abordées:

1. Comment maîtriser la croissance de ces nanostructures pour sélectionner les propriétés structurales, électroniques et magnéto-optiques visées?

2. Comment interpréter la caractérisation chimique, basée sur des mesures par microscopie électronique, de ces objets complexes et non homogènes pour acquérir une connaissance quantitative et locale de leur composition?

La première question a été abordée en trois étapes: i) le contrôle de la formation des particules d'or pour catalyser la croissance des nanofils, ii) l'analyse des mécanismes et paramètres qui gouvernent la croissance des nanofils de ZnTe, et iii) l'étude de l'insertion d'une boîte quantique de CdTe contenant des ions de manganèse à l'intérieur des nanofils cœur-coquille à base de tellurures.

i) **Le démouillage de l'or** pour former des particules sur un pseudo-substrat de ZnTe a été examiné. Les conditions optimales pour la croissance d'une couche de ZnTe(111)B sur un substrat GaAs(111)B ayant une rugosité minimale ont été établies. Les résultats principaux sont:

- Une reconstruction de surface $3\sqrt{3}\times3\sqrt{3}$ R30° est formée sur la couche ZnTe(111)B. Celle-ci consomme seulement 7% d'une monocouche d'or. Nous avons proposé un modèle basé sur la structure d'une reconstruction de surface d'or observée sur GaAs(111)B.

- Les particules d'or formées ont un volume correspondant à 40% du volume total d'une sphère complète et sont dans un état solide.

- La température de démouillage contrôle le diamètre de la particule d'or.

- La quantité d'or déposée sur la surface influence seulement la densité des particules, ceci est valable après la formation complète de la reconstruction de surface et une fois que la taille des particules a été fixée (avec la température de démouillage).

En conclusion, nous avons réussi à préparer des surfaces de ZnTe recouvertes de particules d'or de très basse densité (below 10 particules/μm^2) ayant un diamètre homogène de 10-20 nm, qui sont optimales pour démarrer la croissance de nanofils.

ii) La croissance des **nanofils de ZnTe** a été réalisée avec la méthode d'épitaxie par jet moléculaire à basse température (350°C). La coexistence de nanofils avec la structure zinc-blende et des nanofils avec la structure wurtzite, distribués de façon homogène sur tout le substrat, est observée lors de la croissance pour des conditions de flux stoechiométrique. Toutes les nanostructures ont la même polarité que le substrat: Te en surface.

Les nanofils avec la **structure wurtzite** adoptent une **forme cylindrique**, probablement résultant d'une longueur de diffusion selon l'axe du nanofil plus grande que la hauteur du nanofil. La formation d'une pyramide autour de la base de chaque nanofil est observée. Elle émerge grâce à la présence d'un flux latéral sur les parois du nanofil. Les nanofils de ce type montrent une distribution de hauteurs limitée par des mécanismes de nucléation à l'interface entre le nanofil et la particule d'or.

Les nanofils avec la **structure zincblende** adoptent une **forme conique** due à une longueur de diffusion sur les parois du nanofil inférieure au cas précédent. Cela donne lieu à une croissance latérale, à une réduction de la croissance axiale et favorise la présence d'un cratère à la base de chaque nanofil. La morphologie des nanofils coniques a été expliquée en considèrant un modèle de croissance basé sur des phénomènes de diffusion uniquement. En comparant ce modèle aux données expérimentales, les longueurs de diffusion sur le substrat et sur les parois du nanofil ont été estimées à 60 nm et 180 nm respectivement.

La croissance des nanofils de ZnTe a aussi été explorée sous des conditions de croissance riches en tellure. Dans ce cas, les nanofils cylindriques sont supprimés à basse température (350°C), mais leur proportion est augmentée à haute température ($375 - 400$°C). Dans le cas opposé, sous des conditions de croissance riches en zinc la croissance des nanofils est complètement absente.

iii) Nous avons réussi la croissance de **boîtes quantiques allongées composées de CdTe pur** à l'intérieur des nanofils coniques de ZnTe. Le diamètre de la boîte quantique est déterminé par la section de contact entre le nanofil et la particule catalytique d'or

(6-8 nm de diamètre). La hauteur de l'insertion est contrôlée par le ratio des flux et par l'angle d'incidence du flux latéral. L'interface entre la boîte quantique de CdTe et le nanofil de ZnTe n'est pas abrupte à l'échelle atomique: elle est caractérisée par une diminution exponentielle de la concentration de cadmium. Une incorporation de $\sim 10\%$ de Mn à l'intérieur de la sous-maille de CdTe a été réalisée avec succès grâce à une température de croissance basse pour les nanofils. Le pourcentage de Mn dans la boîte quantique correspond au ratio de flux choisi entre le manganèse et le cadmium.

Finalement, la croissance d'une couche de ZnMgTe sur les nanofils coniques de ZnTe a démontré une passivation efficace de la surface. Ce résultat permet d'envisager un futur contr^le de la contrainte sur ces hétérostructures.

La deuxième question a été abordée en développant une méthode pour interpréter les mesures EDX sur des nanofils uniques avec une composition inhomogéne. Deux nanofils ont été analysés en détail: un nanofil de ZnTe avec une insertion de CdTe et un autre avec une insertion de CdMnTe recouverte d'une coquille de ZnMgTe. Un modèle géométrique est proposé pour simuler les mesures EDX. En comparant ce modèle aux mesures expérimentales, nous avons extrait la forme, la taille et la composition locale de la boîte quantique et des multi-couches de l'hétérostructure. À notre connaissance, c'est la première fois qu'une **étude EDX permet l'obtention d'une composition chimique quantitative et locale sur des nanofils semiconducteurs complexes de type cœur-coquille**. Cette méthode peut être adaptée à l'étude d'autres types d'hétérostructures à base de nanofils.

Cette étude quantitative en EDX a été couplée aux autres mesures de caractérisation complémentaires **sur le même nanofil**, telle que la cathodo- et la photo-luminescence, ainsi que la spectroscopie magnéto-optique.

En conclusion, nous avons développé des hétérostructures à base de nanofils de semiconducteurs II-VI, ainsi qu'une méthode puissante de caractérisation pour mesurer leur composition chimique. Cette étude ouvre des nouvelles possibilités pour analyser les propriétés magnétiques des hétérostructures semiconductrices.

Introduction

Semiconductor nanowires (SC NWs) have been increasingly studied for the last years, both for fundamental research and for potential device applications. It is a fast advancing research field: only a few hundred of articles were published until 2004 whereas the total number of published articles today (2014) is over one hundred thousands. This large and highly diversified field includes many techniques of growth and many SC materials (group IV, III-V and II-VI compounds).

The nanowire geometry offers the possibility to overcome several limitations in the field of semiconductor (SC) epitaxy [1], for instance: the growth of large lattice mismatch SC heterostructures with high crystal quality, the growth of III-V and II-VI SC compounds on Si substrates, and the capability of tailoring electronic properties by doping or strain engineering. Unusual electrical and optical properties can be potentially obtained by the synthesis of nanowires with a high degree of structural complexity. NW-based devices have already demonstrated encouraging results for instance in the domain of sensors or third generation photovoltaic cells. A high control of the modulation of composition and doping is a key requirement to test novel fundamental properties and for the implementation of NW-based structures into future devices.

Axial heterostructures consisting in the insertion of a small section of a lower band gap material inside a higher band gap material result in the formation of a quantum dot (QD). The growth of a QD in NWs present at least seven advantages.

1. The size of the QD can be controlled radially (it is determined by the contact surface between the Au catalyst particle and the NW) and axially (it depends on the growth time and on the atomic or molecular fluxes). Strong confinement of the carriers in QD with small diameter can be achieved.

2. Elastic relaxation of strain in the NW's sidewalls allows one to grow elongated QDs without interfacial dislocations: the critical thickness for the plastic relaxation becomes infinite below a critical NW radius [2].

3. The QD position in the plane parallel to the substrate is determined by the position of the NW. Hence, by using patterned substrates the density and position

of the NWs can be controlled. Also, the position of the QD along the NW can be chosen and several QDs can be grown in the same NW.

4. Since the formation of the QD is not induced by strain (due to the mismatch between lattice parameters of the SC components), it is possible to combine a larger range of SC materials in the same nanostructure. The high flexibility in the choice of materials offers an opportunity to test heterostructures difficult to grow in bulk and opens the field to new physical properties.

5. The absence of a wetting layer allows to obtain excellent spectroscopy properties in comparison with SK quantum dots, where the wetting layer acts as an efficient thermal escape route for the confined carriers.

6. Excitons confined in QD embedded in NWs are protected from surface effects and traps. This configuration enhances the luminescence efficiency, allows to obtain sharper linewidths and longer coherence times.

7. Coupling optical and transport mechanism on the same quantum object is possible and can be used for light emission or detection applications.

Radial heterostructures involve the growth of layers (shells) around an inner core material, forming core-shell or core-multishell NW. Some advantages of these structures are: the passivation of surfaces to enhance optical and transport properties and the use of a shell of higher band gap material than the core, to improve carrier and photon confinement in the NW.

Thanks to the large amount of work published on nanowires, this research field has reached sufficient maturity to investigate two complex topics that have been rarely addressed before: strain engineering in core-shell nanowires and magnetic nanowire-based heterostructures.

Strain engineering in core-shell NWs can have an important effect on the photonic, electronic and magnetic coupling properties of semiconductor charge carriers (specially the holes). It is well known that modulation of the strain allows one to modify the electronic properties, for example it is possible to obtain direct band gap configuration for Si-Ge NWs or to induce a piezoelectric effect to generate a faster separation of electron-hole pairs in photovoltaic applications. Furthermore, the configuration of the built-in strain can lower the degeneracy of the valence band and conveniently select the type of holes for spintronic applications. This means selecting: i) the orbital part of the hole, which is responsible for the coupling to light, the selection rules and the

polarization properties upon electron-hole recombination, and ii) the spin part of the hole, which is responsible for the magnetic properties. For example, choosing holes with larger spin, can raise the spin-carrier coupling in diluted magnetic SC [3, 4].

Magnetic II-VI NW-based heterostructures constitute a promising platform to test and develop spintronics mechanisms and devices. The possibility to study magneto-optical effects in nanoscale objects where carriers injection and a high level of optical control can be attained, makes them ideal systems. The incorporation of Mn ions into ZnTe/ZnMgTe NWs along with a manifestation of their magnetic behavior under field has been recently demonstrated [4].

Coupling of confined carriers with a localized magnetic ion results in the formation of a magnetic polaron. It is a local ferromagnetic order of the spins of magnetic atoms, induced by the coupling to a charge carrier or an exciton. **Stable anisotropic magnetic polarons** may be formed if the carrier is confined to 0D, creating ultimate ferromagnetic nano-objects offering the possibility to read and to manipulate magnetic states. The successful growth of stable anisotropic magnetic polarons in single nano-objects, as well as the investigation and understanding of their fundamental properties is a major challenge for spintronic research. The study of those objects using II-VI magnetic quantum dots in core-shell nanowires offers several advantages:

- The incorporation of Mn ions into the II-VI SC lattice is optimal since Mn has two valence electrons (like group IIB elements such as Zn and Cd). As a result, Mn is not an electrical dopant in II-VI SC systems.
- The density and distribution of the Mn atoms is determined by the growth conditions. The insertion of magnetic atoms can vary from the single spin limit up to large concentrations.
- ZnTe is a direct band SC material that can be easily doped p-type. Hence, a majority of hole carriers allows a stronger coupling with magnetic impurities.
- (Cd, Mn)Te magnetic QD can be inserted in ZnTe NWs. The incorporation of Mn is only possible at low growth temperature compatible with the growth of telluride NWs. Other SC systems such as GaAs or Ge NWs require a high temperature for the growth of NWs and a low temperature for the incorporation of Mn impurities.
- Formation of a stable magnetic polaron may be possible due to the 0D confinement in the QD. Additionally, control of the QD geometry and tailoring of strain in the QD allows to control the shape of the confinement potential enabling also to control the spin anisotropy of the holes.

The goal of this PhD work is to investigate the growth and the properties of novel magnetic nanowire structures such as ZnTe/ZnMgTe core-shell NWs containing a CdMnTe magnetic QD insertion. For that purpose, we not only optimized the NW growth, but also, we searched to control the relevant parameters influencing the magneto-optical properties, such as the QD confinement, the Mn concentration, and the strain anisotropy.

In this work, the NWs are grown on ZnTe pseudo-substrates by Molecular Beam Epitaxy (MBE) using gold particles as catalyst. We have investigated the dewetting process of Au catalyst particles on ZnTe layers, and the growth and properties of: i) pure ZnTe NWs, ii) ZnTe NWs with a ZnMgTe shell, iii) ZnTe NWs with a CdTe QD insertion and finally, iv) ZnTe NWs with a ZnMgTe shell and a CdMnTe QD insertion. In the last case, the structural and optical characterization of the same NW is achieved.

Outline of the manuscript

The first chapter presents a general overview of the basic structural and electrical properties of II-VI SC materials and of the experimental methods used in this work. We focus on the growth by Molecular Beam Epitaxy (MBE) and on the main characterization techniques exploited in this document, in particular Reflection High Energy Electron Diffraction (RHEED), Energy-dispersive X-ray spectrometry (EDX) and (Scanning) Transmission Electron Microscopy (S)TEM. The goal of this first chapter is to introduce the essential concepts needed to understand the results presented in the following chapters without being exhaustive.

The second chapter is devoted to the study of the dewetting properties of Au droplets over ZnTe(111)B layers. First, the growth of highly smoothed ZnTe(111)B layers over GaAs(111)B substrates is explored. The relaxation of strain, the formation of twin boundaries and the composition of the surface reconstructions diagram are discussed. In second place, the properties of the Au dewetting process on ZnTe layers are investigated in detail at the sub-monolayer regime. This includes, on one hand, the determination of the thermodynamic phase, the shape, the volume and the contact angle of the Au droplets. And on the other hand, the effect of key parameters such as the quantity of Au available to form the droplets, the dewetting temperature and dewetting time, on the Au-droplet diameter and on the surface density. The purpose of this research is to master the Au-droplets formation to obtain highly controlled surface allowing us to tune the QD/NWs properties, such as: diameter, density, nature and abruptness of the interfaces, etc.

The third chapter introduces the growth of Au-catalyzed ZnTe NWs. The influence of different II/VI flux ratio conditions and of the growth temperature on the simultaneous growth of two types of ZnTe NWs (cone-shaped NWs and cylinder-shaped NWs) is presented. These NWs are studied by TEM and EDX measurements to determine the crystal structure (wurtzite/zinc-blende), the polarity (Te or Zn at the surface) and the presence -or not- of lateral growth. The first stages of the growth and the evolution with time of the morphology of these NWs is also presented. Finally, we discuss some of our results with a diffusion-driven NW-growth model. Values of the diffusion length on the substrate and along the NWs can be deduced.

The fourth chapter is divided into two main parts. The fist one, is focussed on the growth of magnetic NW-based heterostructures. We start with the simplest case: the growth of ZnTe NWs with a ZnMgTe shell, followed by a second sample with CdTe QD insertion on bare ZnTe NWs, to finish with the more complex case of $Cd_{1-x}Mn_xTe$ QDs in core-shell ZnTe/ZnMgTe NWs. The second one, involves the structural and optical characterization of *the same nanowire*. We propose a new method to obtain *quantitative and local* information on the concentrations, sizes, shapes and positions of the different layers of complex core-shell NW heterostructures, by performing a quantitative analysis of EDX measurements. Complementary magneto-spectroscopy results are summarized to give a complete description of those heterostructures.

CHAPTER 1

II-VI SC properties, MBE & characterization techniques

Contents

1.1 Properties of II-VI semiconductors 16
1.1.1 Crystal structure and polarity 16
1.1.2 Electronic properties 18
1.1.3 Diluted magnetic semiconductors 19
1.2 Molecular Beam Epitaxy (MBE) 20
1.3 Characterization techniques 24
1.3.1 Reflection High Energy Electron Diffraction (RHEED) 24
1.3.2 Electron microscopy (SEM & (S)TEM) 26
1.3.3 Energy-dispersive X-ray spectrometry (EDX) 29

The goal of this first chapter is to give an overview of the properties of II-VI SC materials and of the experimental tools employed in this work. Its aim is not to be exhaustive but to introduce the essential concepts needed for the comprehension of the results presented in this document. The first part is devoted to a brief summary of the basic structural and electrical properties of II-VI semiconductors. In the second part, we focus on the growth by molecular beam epitaxy. In the last part, a description of the main characterization techniques is presented.

1.1 Properties of II-VI semiconductors

II-VI semiconductors are alloys composed from one or several elements from the II column of the periodic table (Zn, Cd, Mg...) and one element from the VI column (Te, Se, S, O...). Group II elements have two valence electrons on their external s-shell and group VI elements have six valence electrons, two on a s-shell and four on a p-shell. II and VI elements fill their valence shells by forming a covalent bond. In this work we develop the growth of telluride nanowires, therefore, this chapter is mainly focused on the properties of telluride semiconductors.

1.1.1 Crystal structure and polarity

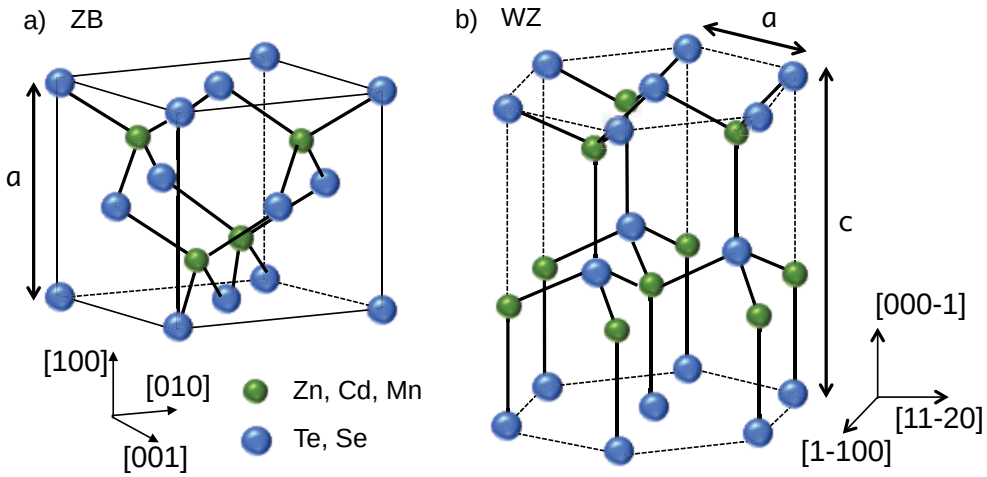

Figure 1.1 – Zinc-blende (ZB) and Wurtzite (WZ) crystal structure of II-VI semiconductors.

The crystalline structure of bulk ZnTe, CdTe and other alloys such as CdZnTe, CdMnTe and ZnMgTe is the zinc-blende (ZB) crystal structure. This structure consists of two face centered cubic lattices, one composed of element II atoms and the other of element VI, that are shifted from each other by 1/4 of the distance along the $< 111 >$ direction. However, in this work we show that in the form of NWs, the hexagonal wurtzite (WZ) structure is also found in Telluride NWs. Note that the hexagonal WZ phase can be preferential in other II-VI SC, such as in bulk CdSe. The ZB and WZ structures are shown in Figure 1.1. Remark that the co-existence of these phases (polytypism) is frequently observed in NWs. Understanding and controlling the origin of polytypism in NW is a topic of interest in the NW community since the electronic band structure of the materials depends on their crystal phase.

In figure 1.2 we show the stacking sequences of the ZB [111] direction and the WZ [0001] direction. The difference between them is only 60° rotation in its tetrahedrons. The ZB atomic layers sequence is: ABCABCABC (where the C plane is rotated of 60° compared to A) while the wurtzite atomic sequence is constituted of stacks ABABAB.

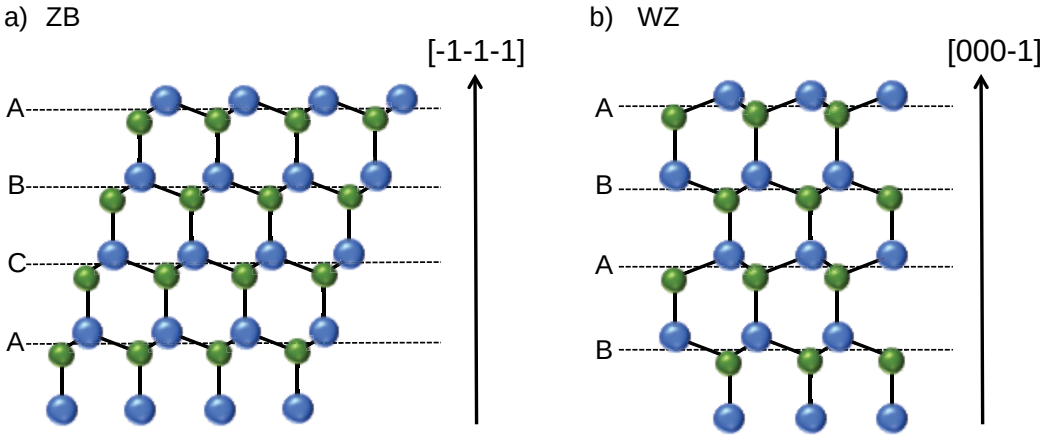

Figure 1.2 – Zinc-blende (ZB) and Wurtzite (WZ) stack sequences along the [111] and the [0001] direction.

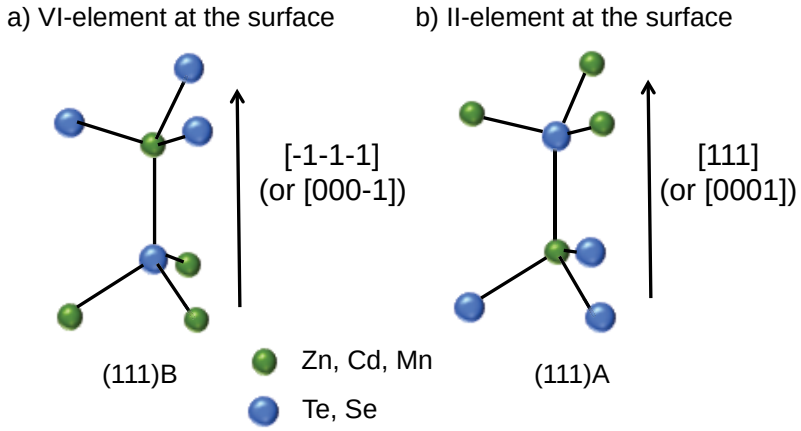

Figure 1.3 – Orientation of the II-VI dumbbell along: a) the $[-1-1-1]$ direction: element VI is at the surface and the surface is called (111)B; and b) the [111] direction: element II is at the surface and the surface is called (111)A.

The II-VI dumbbell is not symmetric in the ZB structure along the [111] and $[-1-1-1]$ directions neither in the WZ structure along the [0001] and $[000-1]$ directions. In figure 1.3 the two different polar directions are illustrated. By convention the surface with the II-element on top of the surface is named (111)A and with the VI-element (111)B.

1.1.2 Electronic properties

The lattice parameter and band gap values of some binary telluride SC are shown in table 1.1.

	ZnTe	CdTe	MgTe	MnTe
a (Å)	6.104	6.481	6.42	6.337
E_G (meV)	2391	1606	3600	3198

Table 1.1 – Lattice parameters and band gap energies (at T= 2K) of some Te-based semiconductor materials in the zinc-blende structure.

For ternary alloys of the type $A_{1-x}B_xC$, the lattice parameter a can be calculated by the Vegard's law [5], which states that there is a linear dependence between the composition of the alloy x and it lattice constant:

$$a(A_{1-x}B_xC) = (1-x)a(AC) + xa(BC) \tag{1.1}$$

The band gap of a ternary alloy presents a nonlinear behavior with the composition x and can be described by a quadratic expression:

$$E_G^{ABC}(x) = (1-x)E_G^{AC} + x\,E_G^{BC} - b_{ABC}\,x(1-x) \tag{1.2}$$

where b is the bowing parameter measured experimentally. $E_g(x)$ is usually an upward concave parabola. The expressions describing the band gap variation for some Te-based SC are:

$$\begin{aligned} E_G^{Cd_{1-x}Zn_xTe}(x) &= 1606 + 525x + 260x^2 \\ E_G^{Zn_{1-x}Mg_xTe}(x) &= 2391 + 959x + 250x^2 \\ E_G^{Cd_{1-x}Mn_xTe}(x) &= 1606 + 1592x \end{aligned}$$

In figure 1.4, the variation of the band gap with the lattice parameter for different SC materials is plotted.

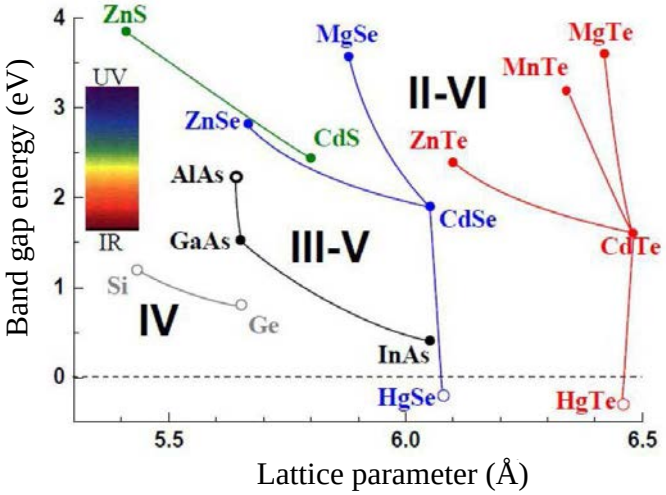

Figure 1.4 – Band gap energy at T=4 K as a function of the lattice parameter for different SC materials. Filled and empty symbols correspond respectively to SC with direct and indirect band gap. Image taken from [6].

1.1.3 Diluted magnetic semiconductors

Diluted magnetic semiconductors (DMS) are semiconductors compounds doped with a few percent of magnetic elements (usually Mn). The incorporation of a fraction of magnetic atoms into the SC material, introduces magnetic properties without losing its usual SC properties. The strong coupling between the carriers (electrons in the conduction band or holes in the valence band) with the localized magnetic moments of these magnetic impurities is named the $sp-d$ interaction. This interaction is at the origin of the Giant Zeeman splitting, where the splitting of the conduction and valence band is proportional to the magnetization of magnetic impurities, which is a key feature of DMS.

The most studied diluted magnetic semiconductors are (Ga,Mn)As and (Cd, Mn)Te, where Mn is substituted to Ga or Cd. The advantage of II-VI DMS with respect to III-V DMS compound is that the Mn ions do not dope the material (Mn has two valence electrons like Cd) allowing to control separately the carriers and the Mn concentrations. Additionally, the synthesis of low-dimensional structures by MBE is eased by the lower growth temperatures of II-VI SC which allow the Mn incorporation. Note that carrier-controlled ferromagnetism in Mn-doped SC has been observed in III-V SC (in GaMnAs with a critical temperature of 200K [7]) and in II-VI SC (in ZnMnTe with a critical temperature of 3K [8]).

A local orientation of the Mn spins induced around a single localized carrier or exciton (electron-hole pair) results in the formation of the "magnetic polaron" (illustrated in figure 1.5). The optical properties of the magnetic polaron have been studied in 3D, 2D and single QD DMS [6]. In DMS QDs the formation of a magnetic polaron is enhanced due to the stronger confinement of the carriers [9].

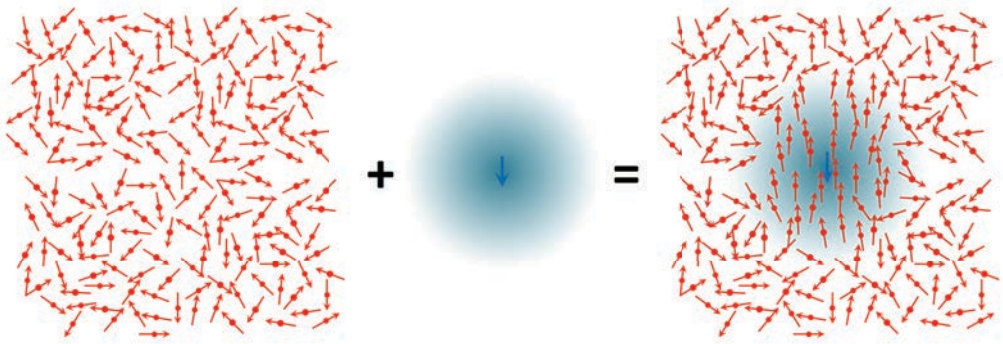

Figure 1.5 – Illustration of the magnetic polaron formation.

1.2 Molecular Beam Epitaxy (MBE)

Epitaxial growth refers to the formation of a monocrystalline material on a monocrystalline substrate. If the material grown (traditionally in the form of a thin layer) is the same as the substrate, we refer to homoepitaxy and when it is different to heteroepitaxy. Normally, the epilayer grown has the crystalline structure of the substrate and a lattice parameter which differs from the one of the substrate by no more than $\sim 10\%$. Among the advantages of the epitaxial growth, we can mention the possibility to grow a higher quality material (lower defect density than the substrate), the possibility to grow a material where a substrate cannot be obtained and the synthesis of an interface of two materials with particular properties (heterostructure).

Molecular beam epitaxy is a technique in which the epitaxial growth of materials takes place when atomic or molecular beams are sent on a heated crystalline substrate under ultra high vacuum (UHV) conditions. The atomic or molecular beams are sent by evaporation or sublimation of materials contained in ultra-pure crucibles (Knudsen effusion cells). The growth of binary semiconductor compounds (here we take the case of II-VI semiconductors) is a kinetic-driven process (illustrated in figure 1.6). First, the atoms or molecules projected onto the surface are absorbed via Van der Waals forces (week interaction that does not involve the electronic structure). Then the absorbed

atoms or molecules (called adatoms) can either diffuse on the surface or desorb from it. When interaction between adatoms of the group II and group VI diffusing on the surface takes place, near a vacant lattice site, they are incorporated into the substrate surface: they form chemical bonds with the substrate species changing the chemical nature of the interface. Adatoms can be incorporated either in a surface vacancy or in a ledge vacancy site. In the first case, the incorporation can lead to the formation of an aggregate (nucleation) and in the second case to a step-propagation growth mode.

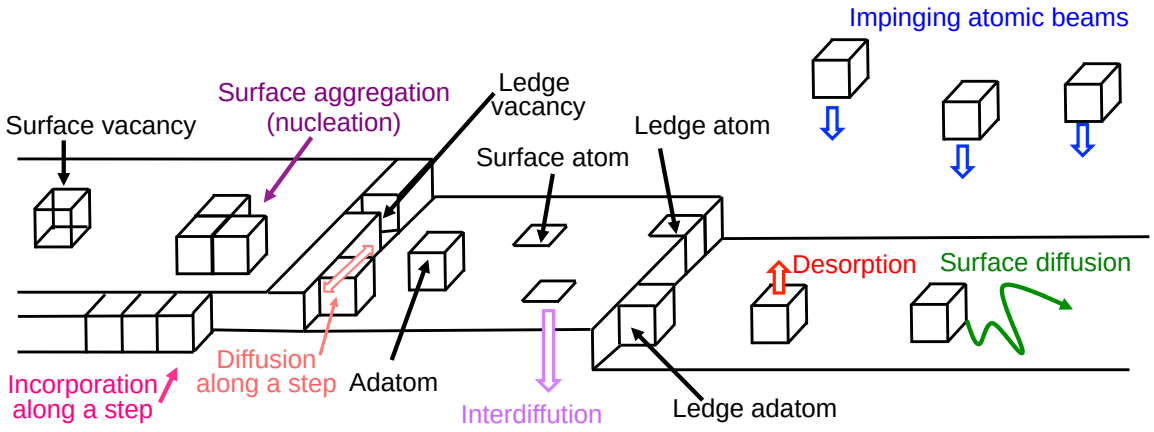

Figure 1.6 – Scheme of the kinetic processes involved on a 2D surface during MBE growth.

The optimal growth temperature is a key factor since it is necessary for the efficient migration of adatoms on the surface. It depends on the material grown and on the substrate used. The UHV conditions are also necessary since they allow the growth of materials with low impurities from the environment. At UHV conditions, the growth takes place in a molecular regime where the mean free path between collision of atoms is larger than the distance between the cells and the substrate. In that case, the atoms in the beam do not interact during their path between the cells and the substrate and a directional beam of atoms can be switched on and off abruptly with a mechanical shutter. This characteristic allows to grow abrupt interfaces of materials. To finish, it is important to mention that a major advantage of the MBE growth, in comparison to other epitaxy techniques, is the low deposition rate which is typically between one and several hundreds of nm per hour (usually less than 1 ML/s), that allows to precisely control the thickness of the deposited material at a sub-monolayer scale.

The MBE machine used to grow the samples studied in this work consists of an ensemble comprising a RIBER 32P II-VI chamber connected under UHV to a MECA2000 III-V chamber (see Figure 1.7).

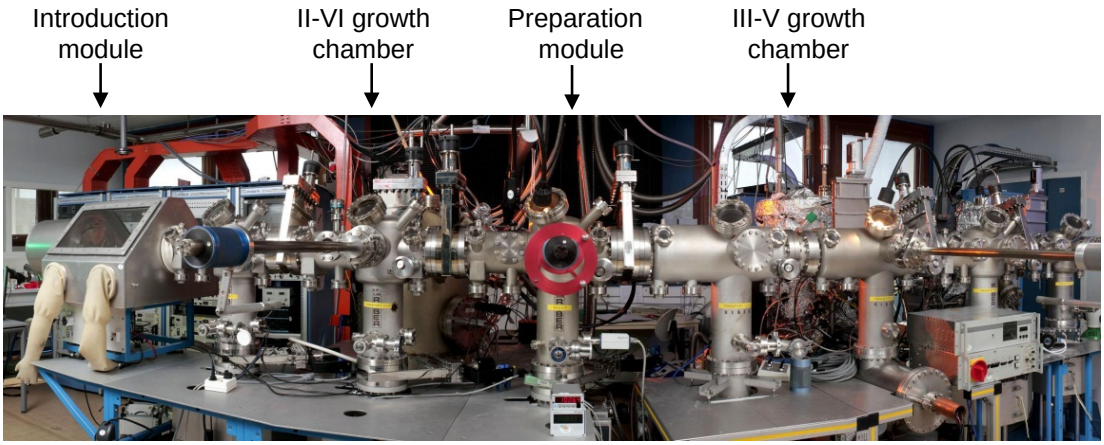

Figure 1.7 – Photo of the II-VI and III-V MBE chambers, connected under ultra high vacuum, used for the epitaxial growth of the samples presented in this document.

The II-VI MBE chamber is dedicated to the growth of tellurides and selenides, a schema is presented in figure 1.8. The III-V chamber is dedicated to the deoxidation process of GaAs substrates and it contains an Au effusion cell that is used for the deposition of a thin layer of Au (to form the catalyst particles). Both MBE chambers are equipped with a Reflection High Energy Electron Diffraction (RHEED)monitoring system. The RHEED diffraction pattern is observed through a fluorescent screen and it is captured by a CCD camera. The composition of the background vacuum (pressure in 10^{-11} Torr range) is controlled using a mass spectrometer. The sample temperatures are measured by a thermocouple in direct contact with a molybdenum sample-holder. The molecular beam fluxes are measured as equivalent beam pressures (BEP) using an ion gauge that can be positioned at the same position as the substrate.

Notice that the effusion cells are tilted with respect to the sample normal. This can have an effect on the nanowire growth, even if the sample is rotated, since the impinging flux arriving on the substrate and on the NW's facets is different depending on the tilt of the effusion cells. Also, shadowing of the flux beams on tilted NW is possible. In table 1.2, the incident angle (α) from the cells in our II-VI MBE chamber with respect to the samples normal are given. The tangent of this angles is also given since it is proportional to the ratio of fluxes arriving to the substrate (J_s) and to the facets (J_f) of a vertical NWs ($\tan \alpha = \pi J_f / J_s$).

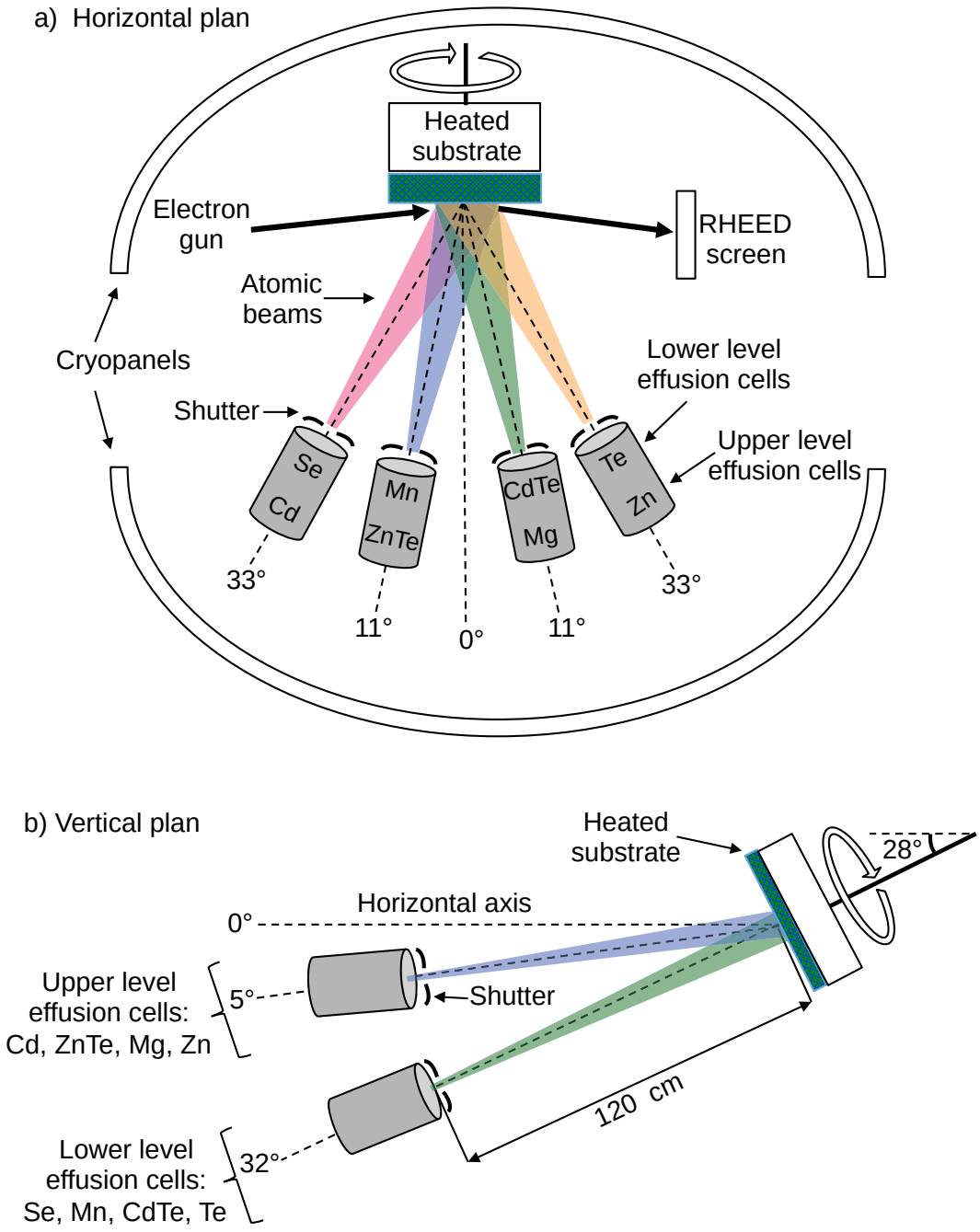

Figure 1.8 – Scheme of the II-VI MBE chamber used for in this work. The angles of the effusion cells with respect to the sample normal are indicated.

MBE cells	α (°)	tan α
ZnTe, Mg	25.5	0.48
CdTe, Mn	11.7	0.21
Cd, Zn	40.2	0.85
Te, Se	33	0.65

Table 1.2 – Incident angle (α) from the cells in our the II-VI MBE chamber with respect to the samples normal.

1.3 Characterization techniques

1.3.1 Reflection High Energy Electron Diffraction (RHEED)

In situ characterization of the samples surface is possible during the MBE growth thanks to a Reflection High-Energy Electron Diffraction (RHEED) gun positioned inside the chamber. Electrons are accelerated at 30 keV, then the collimated beam (over several millimeters) is sent towards the sample at grazing incidence (typically of the order of 2-3°). The scattered beam is observed on a CCD camera connected to a fluorescent screen. The diffracted pattern originates from the scattering of electrons with the first atomic monolayers on the sample surface (low penetration of electron beam due to the small incident angle). The electron beam images the reciprocal lattice of the substrate surface. Real-time analysis of the diffraction patterns is an essential tool allowing to control the surface during growth. A home-made RHEED program[1] allows us to analyze numerically the diffraction pattern to gain information on the sample.

Different surface morphology corresponds to a different diffraction pattern. A smooth perfect crystalline surface will show a streaky diffraction pattern with the lines perpendicular to the surface. For a rough surface or a substrate with some 3D object lying on the surface (for example islands, vertical nanowires, etc) the RHEED diffraction pattern will be spotty. For a polycrystalline surface, the RHEED pattern will give a series of circles since the random orientation of atoms will show diffraction in all directions. In Figure 1.9, we present a schema of the typical RHEED patterns observed depending on the surface.

[1] AnaRheed software developed by Y. Curé at the NPSC lab.

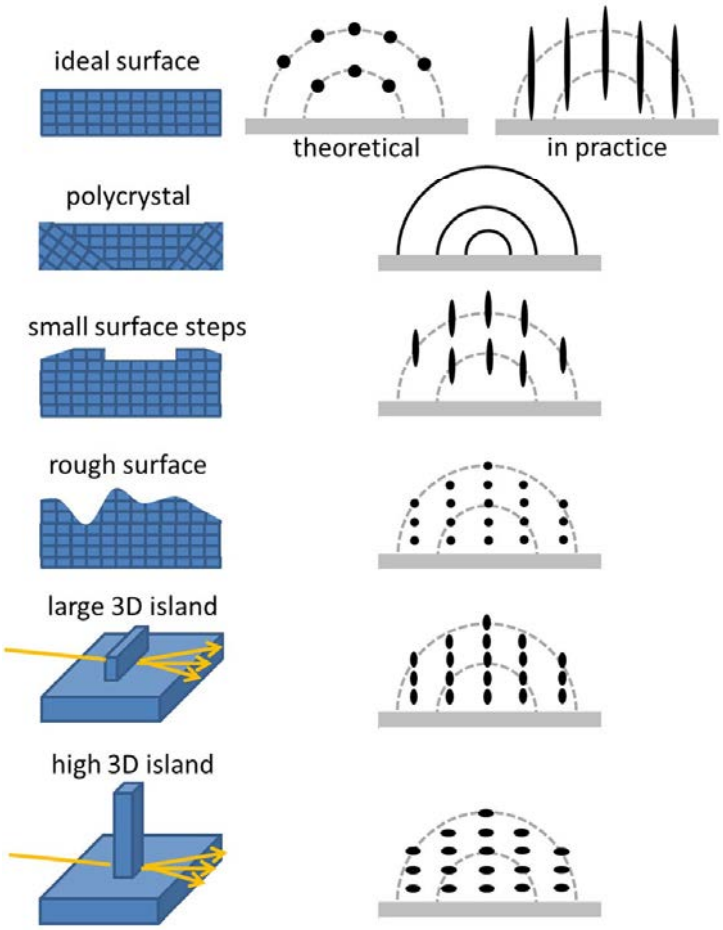

Figure 1.9 – Schema of the typical RHEED pattern observed for different surface morphology. Image taken from the PhD thesis of K. Hestroffer [10].

Real-time information on the in-plane lattice parameter and on the speed of growth can be obtained by following the RHEED pattern. The horizontal distance between the streaks or the raws of spots Δx is inversely proportional to the in-plane distance d: $\Delta x \sim \frac{\lambda D}{d}$ where D is the distance between the sample and the screen and λ is the electron wavelength. Moreover, the intensity of the specular RHEED spot (reflected spot) depends on the layer coverage at instant t during the growth. For instance, if the last atomic layer is completed the intensity is high and if it is only half covered the intensity is lower. Hence, during growth the intensity of this specular spot oscillates in time and the period of time of 1 single oscillation corresponds to the growth of one complete monolayer. RHEED oscillation provide a measurement of the growth rate (monolayers per unit of time). This principle is illustrated in figure 1.10.

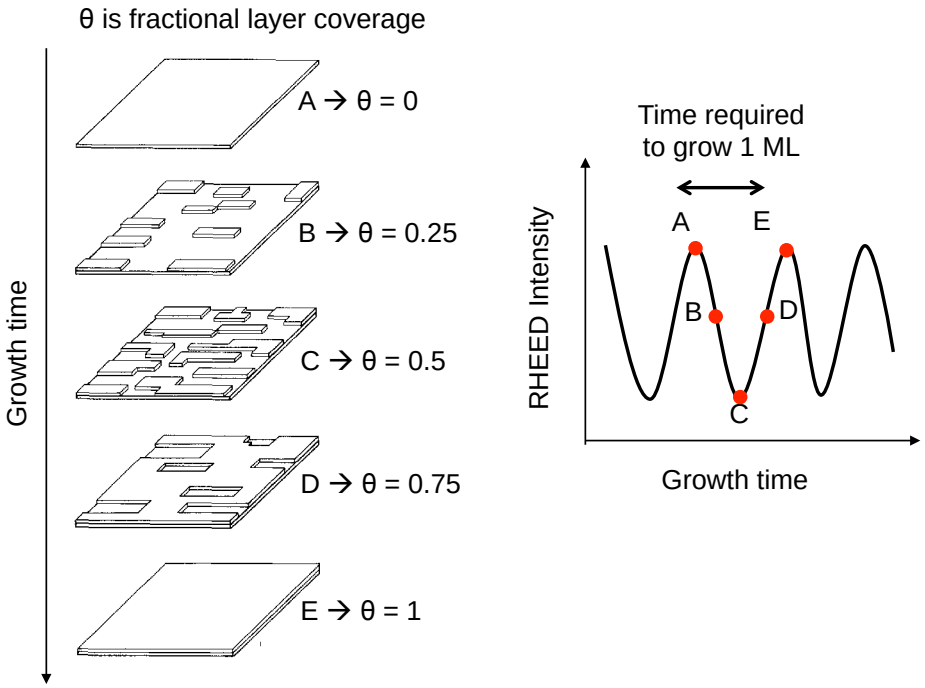

Figure 1.10 – Schema illustrating the principle of RHEED oscillations.

The observation of RHEED oscillation over (111)B oriented surface is not simple. In this work, we have never observed RHEED oscillations for the growth of ZnTe(111)B over GaAs(111)B, probably due to the high lattice mismatch entraining a fast strain relaxation (see 2.2 for more details). In some cases we observed RHEED oscillations when the growth of ZnTe(111)B was stopped and then initialized subsequently, but the oscillations were rapidly dumped. In fact, to obtain a high number of oscillations the growth should be kept in a 2D layer-by-layer mode. If the growth takes place in a step-flow mode, or if there is roughening of the surface or island nucleation, the oscillations are dumped and disappear rapidly. We used RHEED oscillations as a technique to precisely calibrate atomic fluxes on ZnTe and CdTe(100) where we systematically observed more than 10 oscillation periods.

1.3.2 Electron microscopy (SEM & (S)TEM)

Electron microscopy is an essential tool to characterize the samples presented in this work. In this technique it is possible to observe nano scale sized objects by accelerating electrons at voltages between 1 kV and 300 kV (corresponding to low wavelengths of the order of 0.4 Å and 0.01 Å). Interaction between the incident electrons and the

atoms of the sample changes the path of the electron (elastic interaction with the atoms nucleus) or the energy (inelastic interaction with the electrons of the atoms). As a consequence, emission on other particles is possible such as secondary electrons, photons X or UV/visible. These different signals provide different information on the sample and can be collected depending on the position of the detector. Figure 1.11 shows some of the signals that can be studied.

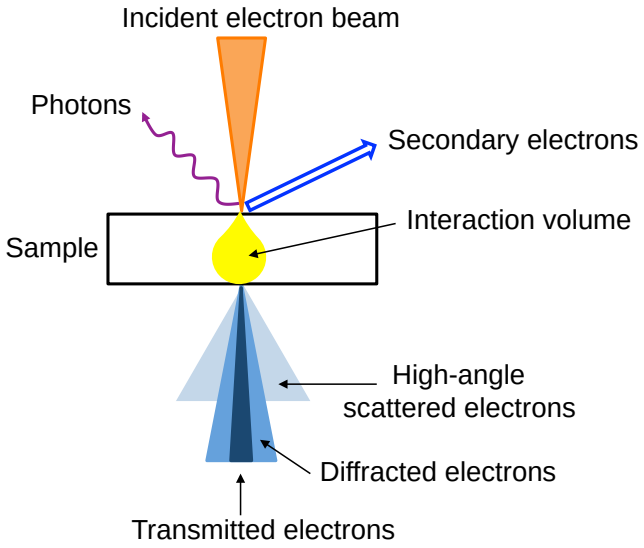

Figure 1.11 – Simplified schema of the interactions between an incident electron beam and a solid sample.

Scanning electron microscopy (SEM)

In scanning electron microscopy a focalized electron beam scans the sample. The electrons are accelerated at tensions between 1 and 30 kV hence only the sample's surface is probed (no need to have thin samples as in TEM). The images are built from the secondary electrons emitted at each scanned position. Depending on the magnification used, this technique gives access to a large view of the surface of the sample (useful to gain information on the distribution and density of the NW or Au particles) and to more detailed informations on the size and the morphology of individual objects (for example the Au particle or NW diameter). Additionally, the contrast of the image generated with secondary electrons is not only linked to the topography of the surface, but it is also linked to large changes in the chemical composition. For example, large changes in atomic number Z can produced a chemical contrast between the ZnTe NWs and the Au catalyst in top of them ($Z_{Zn} = 30$, $Z_{Te} = 52$ and $Z_{Au} = 79$).

An advantage of this technique is that there is no need to prepare the sample to characterize the NWs. In this work we systematically observed as-grown samples using a SEM Zeiss U55 operated at 10kV and at a working distance of 4 mm. The spacial resolution of this microscope is of the order on 1 nm. The SEM images were taken from the top or from the side of the sample (sample tilted at 65° and 90°).

Scanning/Transmission electron microscopy (S/TEM)

Transmission Electron Microscopy (TEM) is an essential characterization technique to study the structural properties of NW. It allows us to determine: the NW's crystal structure, their crystallographic growth direction, the epitaxial relationship between the NWs and the substrate, the NW's dimensions with nanometric precision, the NW's chemical composition and the presence -or absence- of defects or twin boundaries. All of these are possible since electrons accelerated at a higher voltage can penetrate a thicker thickness of material. In TEM the voltage is high enough (and the sample thickness is low enough), so that electrons can completely cross the sample. The parallel electron beam interacts with the sample and diffraction takes place when the atomic planes satisfy Bragg's conditions. To form an image, the diffracted beam is focalized and then amplified. Therefore, under optimal conditions, this technique allows to acquire high resolution images were the atomic columns can be observed (HR(S)TEM). Note that the diffraction pattern of the sample can also be observed.

In TEM the sample is illuminated with a parallel electron beam and an image of the illuminated zone is obtained whereas in STEM a small focalized probe is scanned over the sample and the intensity on the detector at each point is recorded to form the image. Different detection modes are possible: a) Bright-field (BF) detection consists in collecting transmitted electrons that have not been scattered nor diffracted (detector placed in the same axe as the microscope); b) in the Dark-Field (DF) detection mode the diffracted electrons are used (detector place around the central detector); and c) in High-Angle Annular Dark-Field (HAADF) electrons scattered at high angles are detected by an annular detector placed at a larger angle from the microscope axis (see figure 1.11). Note that HAADF images show a chemical contrast since scattering at high angles is roughly proportional to the square of the atomic number of the element Z. Hence, heavier atoms have a signal more intense than lighter atoms (for example: Te atoms will be brighter than Zn atoms).

(S)TEM samples were prepared either using the cleaving technique [11, 12] or by conventional mechanical polishing followed by Ar ion milling using a Gatan PIPS. Note one of the drawbacks of this technique is that sample preparation can be delicate and

time consuming. Additionally, the high energy of the electrons generates a strong interaction with matter that can cause a large beam damage of the sample. This damage is particularly important on thin NWs (diameter < 10 nm) which complicated imaging of those NWs. Therefore, the number of NWs imaged by (S)TEM is very low in comparison to the NW's imaged by SEM.

The High Resolution TEM (HRTEM) images presented in this work were performed on a Philips CM300 TEM equipped with a CCD camera, and the STEM images on a probe corrected FEI Titan, both operated at 300 kV.

1.3.3 Energy-dispersive X-ray spectrometry (EDX)

The Energy-Dispersive X-ray spectrometry (EDX) is a technique that uses the X-ray spectrum that is emitted by the scattering of a focus beam of electrons on a solid. The principle is simple: when an incident electron impacts an atom it can eject an electron from the inner-shells of the atom creating an electron vacancie. The excited atom emits a photon when an electron from a higher-outer shell fills the hole to return to its fundamental level. The emitted photon has an energy corresponding to the difference between the higher-energy and lower-energy shells. The spectrum obtained is composed of the characteristic lines of the elements detected therefore it allows to retrieve the composition of the sample. A first chemical analysis consists of identifying the lines observed on a raw spectrum of the sample (see figure 4.8), which can tell us straight away whether an element is present or not in the sample (in this work this was performed using the Quantax software from Bruker). As a result, EDX measurements are very useful to detect the presence and the location of the quantum dots inserted in NWs and the presence of a particular element on a layer of a core-shell NW.

Obtaining quantitative information needs further analysis. To retrieve the concentration of the element in the sample, the background needs to be subtracted and the intensity of each element line in the spectrum needs to be calibrated to the intensity of a standard sample (sample with well known thickness and concentration). Keep in mind that light elements (low Z) have a weaker integrated intensity. Additionally, the sample thickness should be taken into account since the emitted photons can be absorbed by neighboring atoms. This phenomena is important mainly in thick samples. The effect of absorption was calculated for the NWs measured in this work and was shown to be negligible. Non homogeneous samples need special quantification methods: a geometrical model was developed to seize local and quantitative information from the EDX measurements presented in this work (see section 4.3).

We use EDX spectroscopy coupled to a SEM to obtain a first representation of the chemical distribution of elements on the NW. EDX imaging of Te, Zn, Cd, Au, Mg and O was performed at 30 kV in a Zeiss U55 SEM, using an XF5030 Silicon Drift Detector (127 eV at the Mn Kα line). The automatic drift correction tool was systematically used. The sample preparation consists in mechanically removing the NWs from the as-grown samples and then depositing them on a holey carbon-coated copper grid.

For particularly complex NW structures we used EDX spectroscopy coupled to a (S)TEM. We used a FEI Tecnai Osiris S/TEM equipped with four Silicon Drift Detectors and operated at 200 kV. When coupled to a TEM, EDX measurements have a superior resolution and a higher signal/background ratio particularly useful to detect elements present only in small volumes of the NW (for example Cd inside the QD) or in very small concentrations (few Mn %). This technique allowed us to observe multicore-shell structures and to determine the shape, concentration and position of the Cd(Mn)Te QDs. The quantitative results obtained using this technique will be discussed in Chapter 4.

CHAPTER 2

Dewetting of Au catalytic droplets on ZnTe(111)B layers

Contents

2.1 State of the art & purpose of this study 32
2.2 ZnTe(111)B layers: Growth, diffusion & surface reconstructions . . 35
2.2.1 Substrate preparation 35
2.2.2 Growth of ZnTe layers 36
2.2.3 Strain relaxation 38
2.2.4 Twins 39
2.2.5 High temperature smoothening 41
2.2.6 Conclusions 45
2.3 Properties of the dewetting of thin films of Au over ZnTe layers . . 46
2.3.1 Experimental details 46
2.3.2 Thermodynamic phase of the Au catalyst 48
2.3.3 Calibration of the quantity of Au deposited 49
2.3.4 Shape of the Au droplets 51
2.3.5 Volume of the Au catalyst droplets 54
2.3.6 Quantity of Au incorporated in the droplets 60
2.4 Control of the Au-dewetting process 65
2.4.1 Control of the Au-catalyst diameter 65
2.4.2 Control of the Au-catalyst density 68
2.4.3 Influence of the quality of the ZnTe(111)B buffer layer 71
2.5 Conclusions 73

2.1 State of the art & purpose of this study

Among the key factors that control the growth of NWs, the state of the initial surface (from which the NW will grow) plays an essential role on the final morphology of the NWs and determines the reproducibility of the sample. In this chapter, a description of the formation of Au nano-droplets and a detailed study of the parameters governing this process is presented. The objective of this study is to master the dewetting of extremely thin layers of Au over ZnTe(111)B layers to produce a surface covered with catalyst droplets of specific shape, size and density in order to catalyze the growth of NWs from a well-controlled surface.

Optical properties of QDs embedded in NWs are of topmost interest in the scientific community. A necessary condition to develop such structures is that the NW diameter, determined by the Au-catalyst diameter, should be small enough to ensure quantum confinement of carriers along that direction. To accomplish the growth of these NW-based structures, we target a surface covered with Au catalytic droplets with diameters at most in the $[20 - 25$ nm$]$ range. This range of values is chosen to match the Bohr radius in ZnTe: $a_0 = 6.2$ nm and in CdTe: $a_0 = 7.3$ nm. This values correspond to a diameter of 12.4 nm in ZnTe and of 14.6 nm in CdTe.

Beside this, as complex structures are considered, understanding the growth mechanism involved in the catalyzed-growth of NWs is a central objective of this work. To achieve this goal, independent growth of NW is needed. A very low NW density (few NWs/μm^2) is required in order to avoid competition between NWs or shadowing effects and to simplify the characterization of single NWs. Considering this and supposing that each Au particle will catalyze a NW, we aim to grow samples with a Au-droplet surface density of a few particles per μm^2.

The amount of Au needed to form small-diameter droplets $[20 - 30$ nm$]$ with ultra low density (< 10 droplets $/\mu$m^2), when assuming the catalyst droplets are half-spheres, should be less than one third of a single Au monolayer (ML)[1]. This is important because the amount of Au deposited over the surface changes the manner in which the Au particles will be formed when annealing the sample. If several MLs are deposited: the surface will be completely covered by Au atoms, and at the annealing temperature, dewetting of Au will take place by formation of holes in the Au layer and coalescence of these holes. This generally produces big size droplets. If the Au deposition is $<<$ 1ML:

[1] This is one ML of metal Au with the face center cubic structure and lattice parameter of 0.408 nm. In this work, Au is deposited over (111)-oriented substrates, hence 1 Au ML corresponds to a deposited thickness of 0.235 nm, i. e. the distance between two Au(111) planes in bulk. We assume that the gold monolayer density is identical to that of the Au(111) planes: 1.39×10^{15} atoms/cm^2.

adatoms and small clusters will be created and stabilized during Au deposition (at low temperature). There are many numerical studies developed to explain MBE growth (for example [13, 14]), that show the existence of a critical nuclei which is dependent of the sample deposition temperature. When annealing the sample, the mobility of the Au adatoms and of the subcritical nuclei increases, inducing the formation of the Au droplets. Note that the possibility of Ostwald ripening may increase the size of these Au droplets.

In the literature, it is often found that NWs are grown with diameters and surface densities well above our targets. In these cases, the amount of metal used to form the catalytic droplets is definitely larger than a single metal ML. As a matter of fact, the growth of NWs has hardly been explored in the submonolayer regime. Among the few authors that have tackled this issue, we mention the work published by Li and Wang in 2008 [15]. They study the growth of GaN NWs by depositing thin films of Ni (less than 1 nm thick). Although they manage to grow ultrathin NWs using Ni layers with a thickness of 0.8 Å ($\sim$ 0.5 ML), their conditions lead to high NW densities. Nevertheless, they established that submonolayer metal catalyst improve the vertical alignment and size uniformity of GaN NWs grown on sapphire.

A precise control of the NWs density needs an extensive knowledge of the metal dewetting over semiconductor (SC) surfaces. The behavior of Au wetting a SC surface has been studied extensively in the literature, both in the sub-monolayer [16, 17, 18] regime and above it [17, 19, 20, 21]. Two mechanisms to obtain metal particles have been observed, one is direct nucleation of Au (2D island or nanocrystals) and the other is dewetting of Au adatoms by thermal activation. In addition, the system Au/Si(100), Au/Si (111) and Au/GaAs(100) showed the existence of several Au-induced surface reconstructions (SR). The nature of the SR depends on the substrate temperature and the metal coverage on the surface [22, 16]. A complex surface reconstruction diagram of Au/Si(111) was proposed by Plass in 1997 [18].

Although those systems have quite different surface properties compared to II-VI surfaces, the knowledge gained on those systems is a strong base to develop an understanding of metal dewetting on II-VI surfaces. The literature published of the dewetting of Au over II-VI substrates is very limited. The work of Chan [23] and Bellet-Amalric [24, 25] can be mentioned for the Au/ZnSe(100) system. For Au over ZnTe surfaces, we have not found any references in the literature. Other groups working on the growth of Au-catalysed ZnTe NWs deposit Au directly over GaAs surfaces. In this chapter, we will present results showing a Au-induced SR over ZnTe(111)B buffers that complements the knowledge of Au dewetting over II-VI SC surfaces.

In this chapter, the optimized growth of 2D ZnTe (111)B layers, and the dewetting of Au droplets over them is explored in detail at the sub-monolayer regime. The chapter is structured in three main parts:

- In the first part of the chapter (section 2.2) we describe the optimal conditions for the growth of ZnTe(111)B layers and their properties. In particular, we studied the relaxation of strain, we showed the manifestation of twin boundaries on the ZnTe layers and we determined the surface reconstructions diagram of the ZnTe(111)B surface at different temperatures and Te-exposures. Altogether, the goal of this study was to grow highly smoothed ZnTe(111)B buffer layers over GaAs(111)B substrates.

- In the second part (section 2.3), the properties of the Au dewetting process on ZnTe layers will be described and discussed in detail. First, a description of the experimental details of the Au deposition and dewetting will be given (subsection 2.3.1). Next, we will calibrate the quantity of Au sent to the surface and determine the thermodynamic phase, shape, volume and contact angle of the Au droplets (subsections 2.3.2 to 2.3.5). Additionally, we will show the existence of a Au-induced surface reconstruction. Finally, we will discuss the effect of the dewetting temperature and dewetting time on the quantity of Au incorporated in the droplets (subsection 2.3.6).

- The third part of the chapter will be devoted to mastering the Au dewetting process in order to obtain highly controlled Au droplets (section 2.4). We will study the effect of: a) the quantity of Au available to form the droplets and b) the temperature and time of the annealing process, on the Au-droplets formation. The impact of these parameters on the Au-droplet diameter (subsections 2.4.1) and on the surface density (subsection 2.4.2) will be presented. In fact, tuning of both the diameter and the density of catalytic Au particles is achieved. Finally, the influence of the quality of the ZnTe layer on the Au dewetting process is also commented (subsection 2.4.3).

This chapter will end with a brief list of the main results discussed (sections 2.5).

Keep in mind that the purpose of this study remains to quantify the influence of critical parameters on the droplet formation process to produce a highly controlled initial surface favorable for NW growth. It is beyond the scope of this study to unravel the complexities underneath this phenomenon.

2.2 ZnTe(111)B layers: Growth, diffusion & surface reconstructions

The MBE growth of ZnTe(111) layers is not common and it has not been previously reported in the literature. In this section we present the optimized growth conditions of ZnTe(111)B layers over GaAs(111)B substrates. The properties of these layers such as the strain relaxation, the surface diffusion and the twin formation will be presented. The influence of these properties on the growth of ZnTe NWs will be discussed. The growth of these layers is an important step towards the growth of ZnTe NWs for several reasons. First, it allows to avoid a possible incorporation of impurities inside the NWs, notably contamination coming from the substrate like Ga [4] or As atoms. Second, the absence of lattice mismatch at the base of the NWs should avoid or reduce the formation of stacking faults or microtwins in the bottom part of the NWs (observed on the NW grown directly GaAs [26]). Third, the formation of Au catalyst can be well controlled. In particular, the range of Au-droplets diameters and surface density is large. At last, growing high quality ZnTe buffer layers over GaAs substrates is a low cost-high quality solution compared to the direct growth over a 111-oriented II-VI substrate. Henceforth, this allows to grow bigger samples than on II-VI substrates (surface ~ 1.5 cm^2). One advantage is that the sample can then be clived into various parts, allowing to perform different structural and optical characterization techniques on the same sample.

2.2.1 Substrate preparation

The complete growth process of these ZnTe layers takes place under ultra high vacuum (UHV) in an ensemble comprising a RIBER 32P II-VI chamber connected to a III-V chamber. The growth starts from a (111)B GaAs substrate[2] that is first deoxidized at 650°C under a strong As flux (1×10^{-5} torr) in the III-V chamber. This annealing is monitored by reflection high-energy electron diffraction (RHEED). This technique allows us to see when the substrate is well deoxidized. When the substrate is initially observed at room temperature, the diffraction pattern is not seen due to the oxide layer covering the substrate surface. The sample temperature is increased first up to 400°C, then the strong As flux is send on to the surface, and subsequently up to 650°C. After several minutes at this temperature, the RHEED diffraction becomes clear and bright. We are able to observe the characteristic surface reconstructions (SR) of a GaAs(111)B substrate (2×2 and $\sqrt{19} \times \sqrt{19}$) [27]. This process results in a smooth surface, with a root mean square (RMS) roughness as low as 0.3 nm over a 5 μm^2 area, measured by atomic force microscopy and shown in Figure 2.1. We observe lines

[2]The B-surface is an anion terminated surface. Accordingly, GaAs(111)B is an As terminated surface.

on the surface probably from a polishing process performed at the factory. Remark that we have grown an intermediate buffer of GaAs(111)B but the surface roughness was not improved. For that reason, we have decided to omit this step of the preparation.

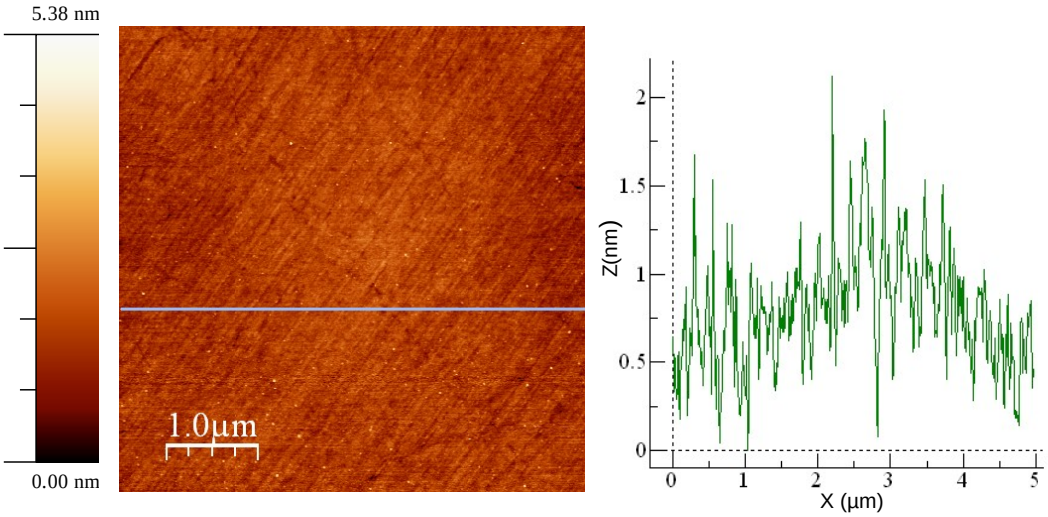

Figure 2.1 – AFM image of a deoxidized GaAs(111)B substrate. The scale is shown at the left of the image. At the right, we present the height profile along the line scan shown on the AFM image. The root mean square (RMS) roughness over the whole image is 0.3 nm and the average roughness is 0.23 nm.

2.2.2 Growth of ZnTe layers

After deoxidization of the GaAs substrate, the sample is cooled down and transferred to the II-VI chamber. Then, a thick ZnTe layer is grown for 60 min. The best growth conditions were found at $T_{growth} = 260°C$ using a stoichiometric flux[3]. We used a flux in the $2.5 - 5{\times}10^{-7}$ Torr range from the ZnTe effusion cell which corresponds to a buffer of thickness around $250 - 500$ nm. This conditions were found by comparing the RHEED diffraction pattern between different conditions (under Zn or Te-rich growth and at different growth temperatures from 230°C to 350°C). At the optimal conditions we systematically obtained a bright thin streaky 2D pattern after only 5 min of growth. Note that during the first minute of growth, the RHEED pattern drastically changes, it gets dull and the distance between the streaks increases due to the lattice mismatch relaxation (there is a high lattice mismatch between GaAs and ZnTe). This process will be discussed in the next section.

[3]Such low growth temperature, more than 150°C lower than ZnTe layers grown on a 001-surface, were also observed for CdTe(111) layers [28]

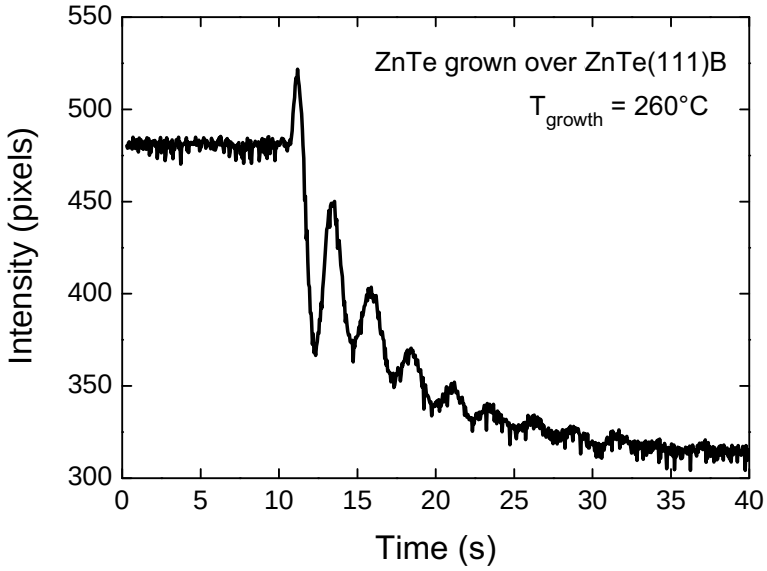

Figure 2.2 – RHEED oscillations of ZnTe grown over a ZnTe(111)B layer. The diffraction intensity of the specular spot is plotted against the growth time. The speed measured from these oscillations is 0.4 ML/s ($1ML^{111}_{ZnTe} = 0.35$ nm). The growth temperature is 260°C.

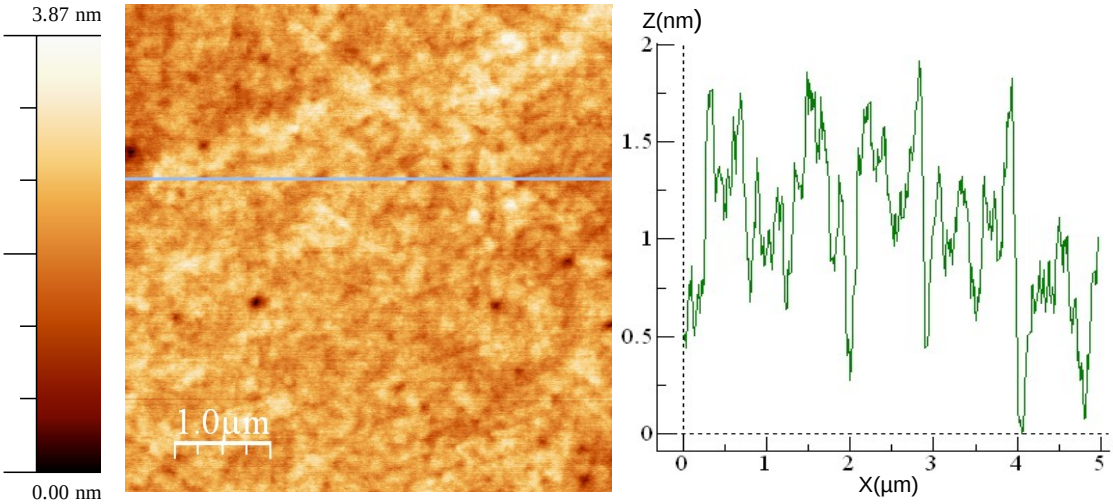

Figure 2.3 – AFM image of a ZnTe(111)B layer grown over a deoxidized GaAs(111)B substrate. The scale is shown at the left of the image. At the right, the height profile along the line scan shown on the AFM image is presented. The root mean square (RMS) roughness over the whole image is 0.36 nm and the average roughness is 0.28 nm.

After some minutes of growth, if the ZnTe flux is stopped and started again, we are able to record RHEED oscillations. These oscillations of the intensity of the specular spot correspond to a layer-by-layer growth and allow to extract the growth speed (see section 1.3.1). An example of these oscillations is shown in Figure 2.2. We found a growth speed of ZnTe over a ZnTe(111)B layer under stoichiometric conditions, when the flux from the ZnTe cell is 5×10^{-7} Torr and T_{growth} = 260°C, of 0.4 ML/s. The fact that we are able to observe these oscillations reflects the growth of a flat high quality surface. For example, we do not observe this kind of oscillations when the growth starts directly from the GaAs substrate since the surface needs to relax the strain due to the lattice mismatch. This means that far away from the GaAs/ZnTe interface we are able to grow a flat surface. This is proven by AFM measurements performed after 1h of growth of the ZnTe layer (Figure 2.3). The roughness of the ZnTe layer grown is almost equal to the roughness of the GaAs layer after deoxydation: RMS roughness = 0.36 nm (0.3 nm for the GaAs substrate).

2.2.3 Strain relaxation

Due to the high lattice mismatch between GaAs and ZnTe (7.7%), plastic relaxation is expected to take place at a very early stage: for ZnTe(001) layers grown on GaAs(001), it starts at 5 ML [29]. Here, for the ZnTe/GaAs(111)B system, we found that it occurs even earlier.

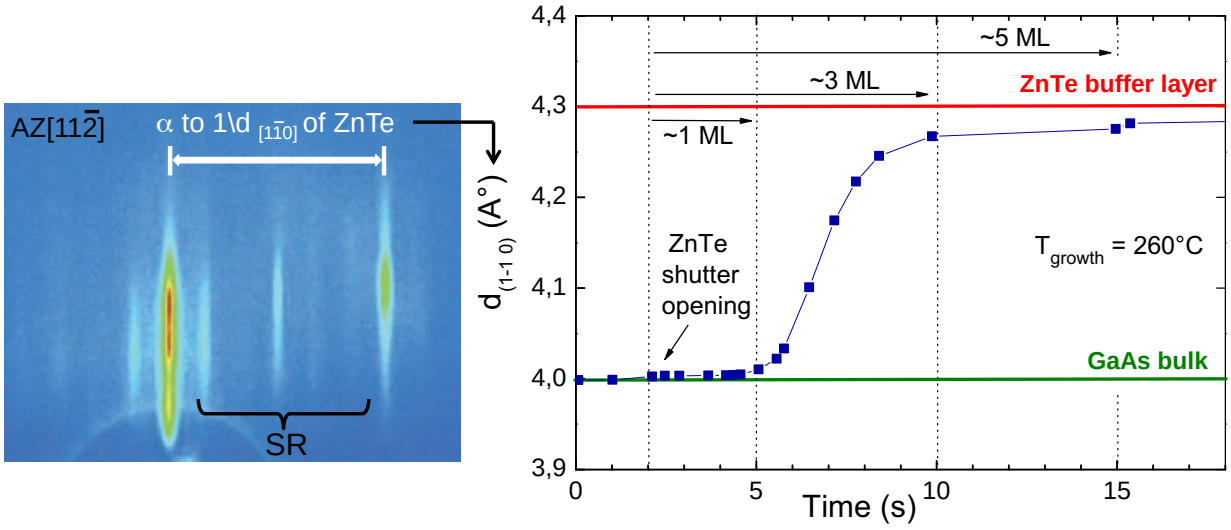

Figure 2.4 – Strain relaxation of a ZnTe(111)B layer over a GaAs(111)B substrate. The distance between the planes [1-10] (d_{1-10}) versus the growth time. These data are obtained from the RHEED diffraction pattern during growth.

In figure 2.4 we plot the distance between the planes [1-10] (d_{1-10}) versus the growth time. The distance between the diffraction lines observed in the RHEED pattern is inversely proportional to d_{1-10}. We calibrate the initial distance between the diffraction lines corresponding to the inter-plane distance of bulk GaAs(111) ($d_{1-10}^{GaAs} = 0.39$ nm) and when the growth of the ZnTe layer starts (time = 2 s), we observe the evolution of this distance with time. We see that the ZnTe layer is strained for only ∼1 ML (∼3 s of growth) and immediately after starts to relax being almost completely relaxed after the deposition of ∼3 ML (∼10 s of growth). After only ∼5 ML (∼15 s of growth) the measured inter-plane distance is 0.428 nm, a value already very close to the value for bulk ZnTe ($d_{1-10}^{ZnTe} = 0.43$ nm).

2.2.4 Twins

The fast relaxation of ZnTe over GaAs(111)B is probably due to the formation of twin defects at the interface. Crystal twinning occurs when two crystals share the same crystal lattice in a symmetrical manner. Twin boundaries are formed when two crystals grow in such a way that only one misorientation exists between them. In that case, the interface is highly symmetrical and often the crystals have lattice structures that are mirror images of each other in the plane of the boundary. In Figure 2.5 a twin boundary is illustrated.

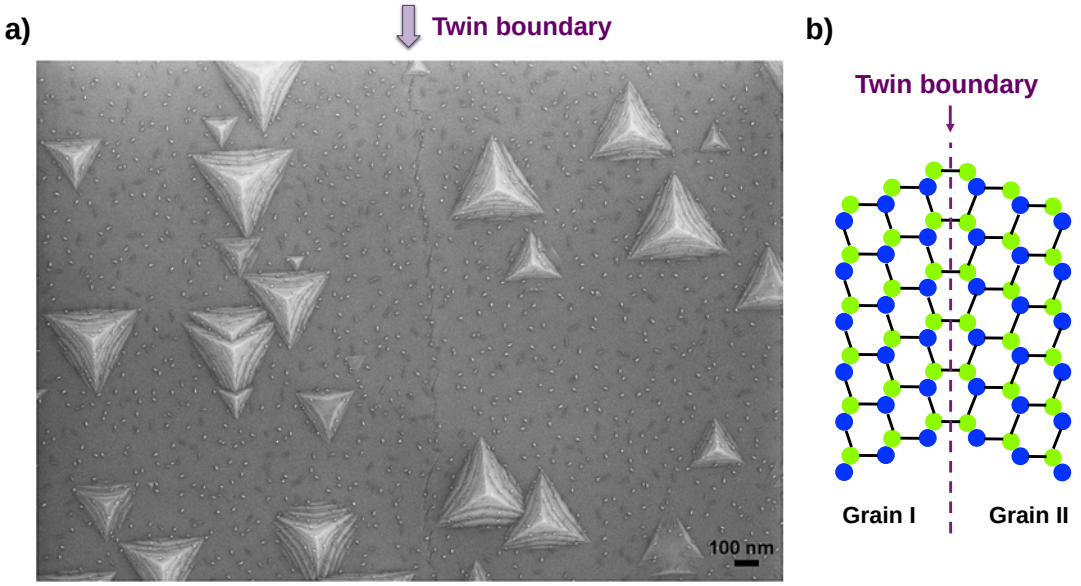

Figure 2.5 – a) A twin boundary is observed in a ZnTe layer annealed at 500°C for only few seconds. We observe the formation of triangular pyramids on the surface, that are oriented in opposite directions (180° rotation) in each side of the twin boundary. b) Schema of a twin boundary.

Actually, twin formation is very common for the epitaxial growth along the [111] direction, both in 2D layers and in NWs [11], due to the low formation energy of a twin along the [111]-orientation. For example, during the growth of [111]-oriented semiconductors, the most frequently found type of twins can be described as a stacking fault of the crystal lattice. For instance, if the atomic sequence is:

AaBbCcAaBbCcAaBb...

where A, B, C = Zn or Cd and a, b , c =Te, a twin boundary (indicated by | in the sequence) corresponds to a staking fault like:

AaBbCc|BbAaCcBbAa...

In that case, the staking fault can be interpreted as if one part of the crystal has been rotated of 180° around the [111] axis with respect to the other.

In addition, twining is particularly frequent in II-VI with respect to III-V semiconductors, since the energy cost of making a staking fault is weaker. For example the staking fault energy for ZnTe [30] is 16 ± 4 mJ/m^2 and for CdTe is 10.1 ± 1.4 mJ/m^2, whereas for GaAs is 55 ± 5 mJ/m^2 and for InSb is 38 ± 4 mJ/m^2. Henceforth, the formation of twins is a well known problem of the growth of CdTe(111), where it was found that it can be avoided by using slightly misoriented substrates [31, 32].

For ZnTe(111)B layer, we have observed the presence of twins that are revealed by high temperature annealing. In Figure 2.5a we observe the surface of a ZnTe(111)B layer that was annealed at 500°C for only few seconds. We observe the formation of triangular pyramids on the surface. These pyramids are oriented along 2 opposite directions (180° rotation). We observe a line on the surface (indicated with two purple arrows) that separates the two regions. We believe this is a twin boundary. Note that over the surface and over the pyramids there are small particles. These are frequently observed. Even if we ignore their origin or composition, we know that they are not Au particles because they are also observed on samples where no Au deposition was done. One possible hypothesis is that they are linked to the oxidation process of the ZnTe surface.

2.2.5 High temperature smoothening

The quality of the surface of the ZnTe(111)B layer can be improved (flattened) by annealing the sample at high temperature under Te- flux conditions. This is confirmed by the appearance of surface reconstructions (SR) similar to those observed on CdTe(111)B [33,34]. In contrast, any exposure to a Zn flux deteriorates the ZnTe(111)B surface: we observed that the RHEED pattern becomes spotty (3D). This suggests that the diffusion on the ZnTe(111)B surface is low under Zn excess and large under Te excess[4].

We have performed two types of annealing process to flatten the ZnTe surface. Once the growth of the ZnTe layer is finished (sample at 260°C), we annealed the sample at 420°C under a very strong Te flux (1×10^{-6}). The sample stays at this temperature for only a few seconds and then the temperature is decreased at a)380°C or b) 300°C (depending on the process) where the Te flux is stopped and the sample temperature is decreased to room temperature under vacuum. SR appear as soon as the Te flux is open at 260°C. For the first process (Te flux stopped at 380°C), the SR disappears as soon as the Te flux is stopped. For the second process (Te flux stopped at 300°C), the SR remains visible without the Te flux and when the temperature is decreased. The fact that the SR remains indicate that the ZnTe surface is smoother (less rough) by using the second process. This is confirmed by SEM images of the surface that show a nicer surface when the second smoothing process is performed. This step is important because it influences the dewetting of Au particles. This point will be discussed in detail in section 2.4.3.

The surface reconstructions observed in the ZnTe(111)B surface are mainly the c(8x4) and the $2\sqrt{3} \times 2\sqrt{3}$ R30° (RHEED diffraction pattern shown in Figures 2.6 and 2.8). The c(8x4) SR is characterized by a 8-fold and a 2-fold surface reconstruction in the [11-2] and [1-10] azimuths. This means that the SR cell is 8 times bigger than the ZnTe unit cell along the [11-2] azimuth and 4 times bigger along the [1-10] azimuth. The 'c' indicates that it has an atom placed at the center of the cell. This cell is indicated with a discontinuous black line in Figure 2.7. The cell of the $2\sqrt{3} \times 2\sqrt{3}$ R30° SR is smaller than the cell of the c(8x4) SR and it is characterized by a 6-fold surface reconstruction in the [11-2] azimuth(instead of 8-fold) and a 2-fold surface reconstruction in the [1-10] azimuth (like the c(8x4) SR). Hence, it is 6 times bigger than the ZnTe unit cell along the [11-2] azimuth and 4 times bigger along the [1-10] azimuth. The cell of this surface reconstruction is rotated by 30° with respect to the ZnTe unit cell and it is shown with a discontinuous black line in Figure 2.9.

[4] as already known for CdTe(111)B [33].

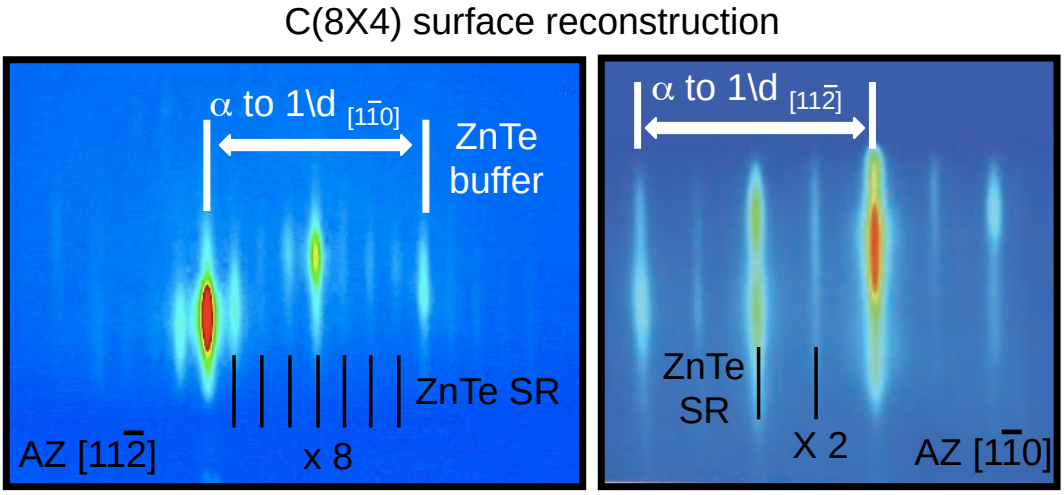

Figure 2.6 – RHEED diffraction pattern of the c(8x4) SR on the ZnTe(111)B surface along the [11-2] and [1-10] azimuths. The 2D diffraction of the ZnTe layer is indicated in white and the streaks corresponding to the SR in black.

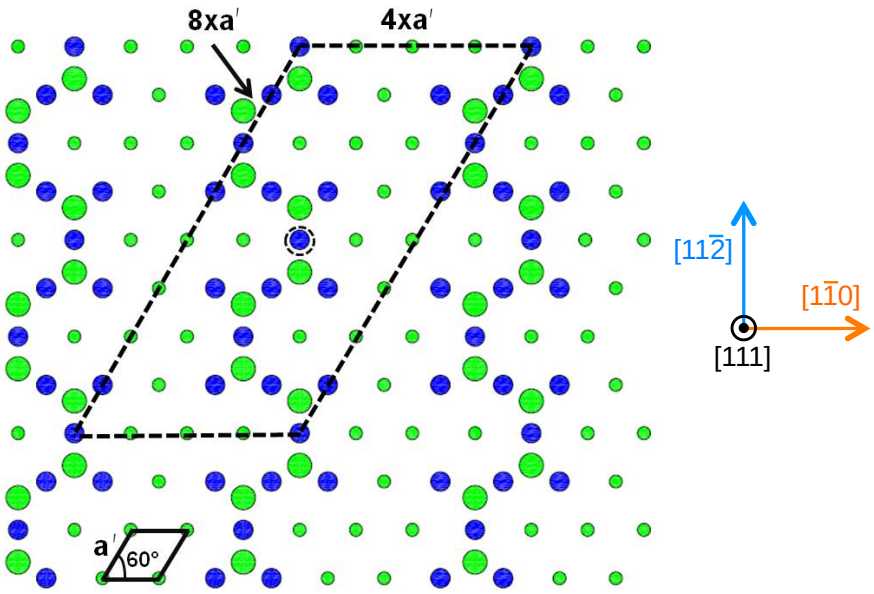

Figure 2.7 – The c(8x4) surface reconstruction (SR) is illustrated (based on the motif of the CdTe SR [33,34]). The SR cell is indicated with the dashed line in black and the ZnTe unit cell with a black continuous line ($a' = \frac{a}{\sqrt{2}}$ and a is the lattice parameter of ZnTe). Zn atoms are represented in blue and Te atoms in green. The big circles are the first Te layer (exterior layer) and the small circles are the second Te layer.

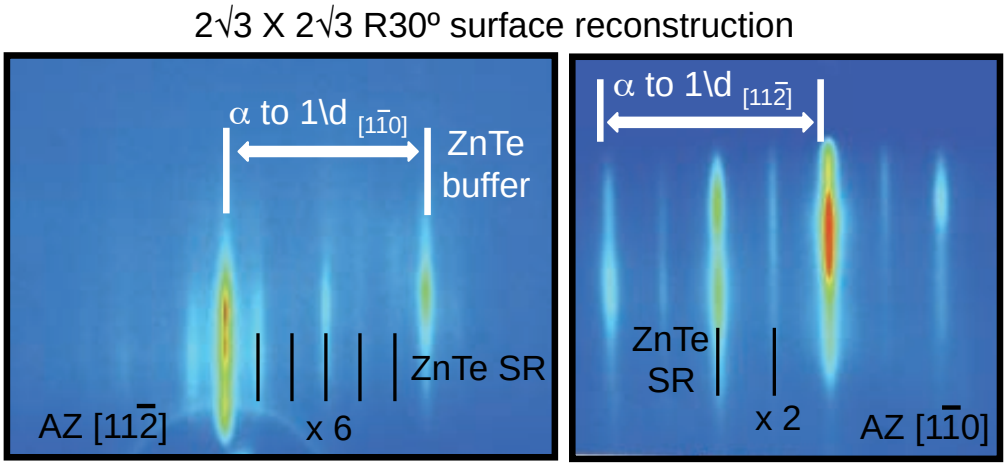

Figure 2.8 – RHEED diffraction pattern of the $2\sqrt{3} \times 2\sqrt{3}$ R30° SR on the ZnTe(111)B surface along the [11-2] and [1-10] azimuths. The 2D diffraction of the ZnTe layer is indicated in white and the streaks corresponding to the SR in black.

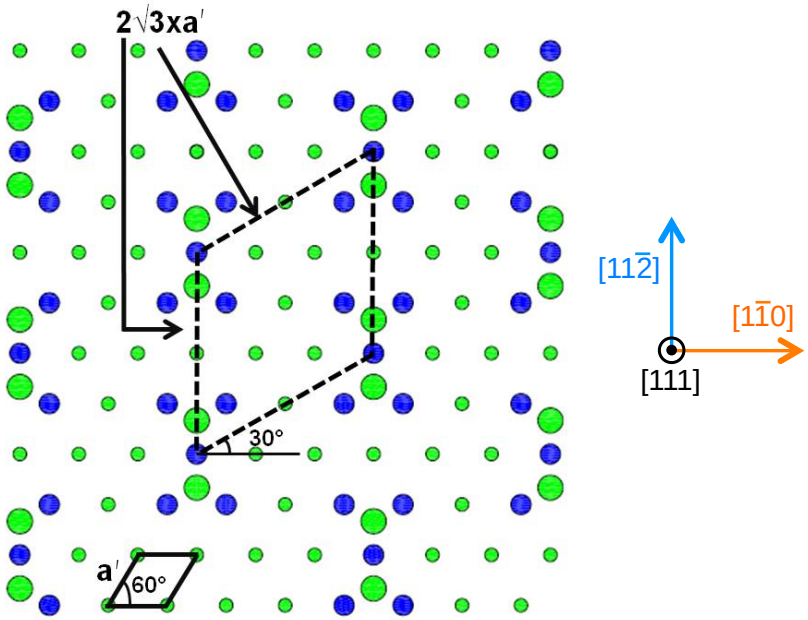

Figure 2.9 – The $2\sqrt{3} \times 2\sqrt{3}$R30° surface reconstruction (SR) is illustrated (based on the motif of the CdTe SR [33,34]). The SR cell is indicated with the dash line in black and the ZnTe unit cell with a black continuos line ($a' = \frac{a}{\sqrt{2}}$ and a is the lattice parameter of ZnTe). Zn atoms are represented in blue and Te atoms in green. The big circles are the first Te layer and the small circles are the second Te layer.

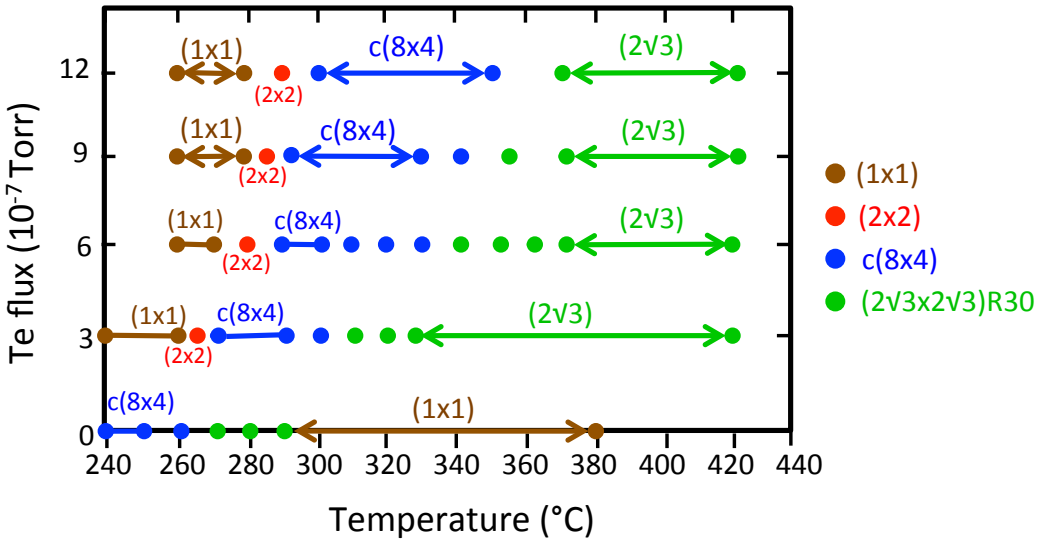

Figure 2.10 – ZnTe(111)B surface reconstruction diagram. We represent in this diagram the SR observed by RHEED after the ZnTe(111)B layer has been grown and exposed to Te-rich atmospheres at different sample temperatures. We clearly observed the c(8x4) SR (arrows in blue) and the $2\sqrt{3} \times 2\sqrt{3}$R30° (arrows in green). There are regions where we simultaneously observed 2 different SRs, these are indicated with points. The color of the points indicate which of the two SR is brighter and shows the transition between single-SR regions. The 2×2 SR is barely seen (points in red).

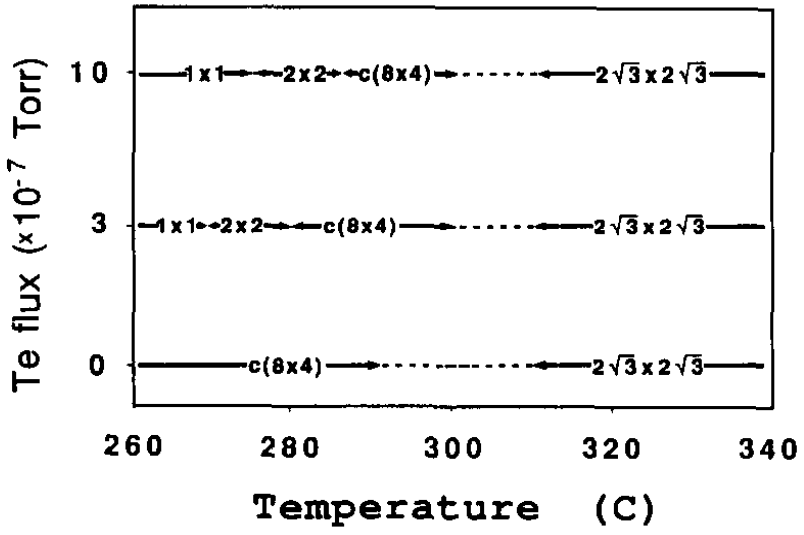

Figure 2.11 – CdTe(111)B surface reconstruction diagram publish by R. Duszak et al. in 1991 [33]

These two SR have the same cell (same diffraction pattern) as the ones observed in the CdTe(111)B surface. This resemblance between CdTe and ZnTe, justifies the hypothesis that the motif may be the same. To illustrate the possible motif of the two main SR in ZnTe(111)B, we replace the Cd atoms by Zn atoms in the motif found for CdTe(111)B[5], these are illustrated in Fig.2.7 for the c(8x4) and in Fig. 2.9 for $2\sqrt{3} \times 2\sqrt{3}$R30° surface reconstructions.

The most significant difference between the SR of ZnTe(111)B and CdTe(111)B, is that the first appear shifted to higher sample temperatures. In figure 2.10 we present the surface reconstruction diagram that we found for ZnTe(111)B surface. The SR observed at different values of Te flux and sample temperature are shown. The equivalent SR diagram was published for CdTe(111)B by R. Duszak et al. in 1991 [33] and is shown in Fig. 2.11. Apart from a shift in temperature where the c(8x4) and the $2\sqrt{3} \times 2\sqrt{3}$R30° appear, the two SR diagrams are very similar. In both cases, there are large regions where we can observe transitions from one SR to the next, hence where we observed simultaneously the presence of two SR. In the case of ZnTe, the (2x2) SR is observed with very weak intensity.

2.2.6 Conclusions

We have found the optimal conditions to grow a high quality low roughness ZnTe(111)B layer over GaAs(111)B substrates. The surface reconstruction diagram is explored and established for these layers. We found mainly two surface reconstructions: c(8x4) and $2\sqrt{3} \times 2\sqrt{3}$R30°. We also found large regions of the diagram where there is a mixed of SR. Under those conditions both SR can be stabilized, hence we may have regions on the surface with a c(8x4) SR and others with a $2\sqrt{3} \times 2\sqrt{3}$R30° SR. Finally, we have shown the existence of twins on the surface.

[5]The motif was proposed by Duszak et al. [33] and was then confirmed by Etgan et al. [34] using scanning tunneling microscopy for the c(8x4) SR of the CdTe(111)B system.

2.3 Properties of the dewetting of thin films of Au over ZnTe layers

2.3.1 Experimental details

To form the Au nano-droplets a fraction of a ML of gold is deposited in the III-V chamber, at room temperature (RT) and under ultra high vacuum (UHV), over a ZnTe(111)B buffer layer (see Chapter 2.2 for details on the growth and surface reconstructions of this pseudo-substrate). To be sure that the Au deposition is done under excellent UHV conditions, the III-V chamber is left one day without As pressure before the Au is deposited. Annealing of the surface induces dewetting of the Au adatoms to form droplets. Figure 2.12 illustrates this process.

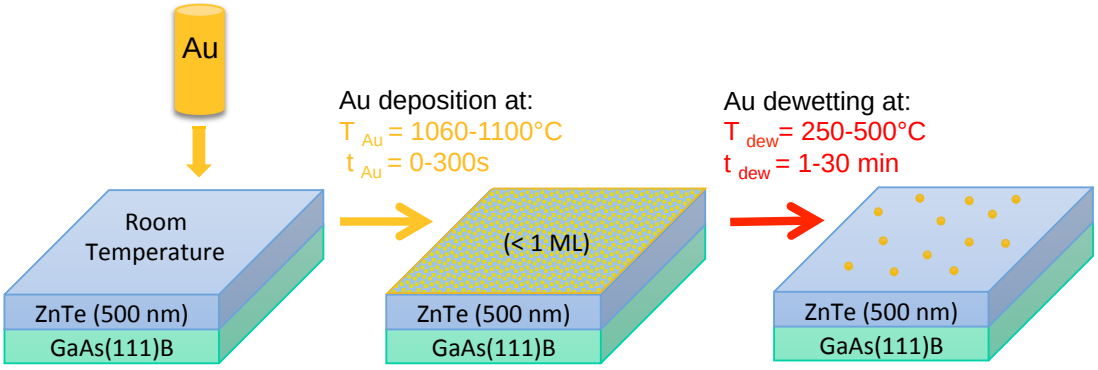

Figure 2.12 – Schema of the Au deposition and dewetting process. The range of the temperature of the Au effusion cell (T_{Au}), the Au deposition time (t_{Au}), the dewetting temperature (T_{dew}) and the dewetting time (t_{dew}) explored in this chapter are indicated.

The temperature at which the dewetting of Au starts depends on the amount of Au deposited on the surface. For "high" Au thickness ($>$ 1 ML), the formation of Au droplets can even start at RT. It is possible that in that case, the Au particles are formed by direct nucleation of nanocrystals instead of dewetting of Au over the ZnTe surface, resembling the case of Au/$SrTiO_3$ systems [17]. In the sub-monolayer regime, which we consider in the present study, the first evidence of the dewetting process (RHEED diffraction spots) appears at around 150°C. To complete the dewetting process, the samples are annealed up to temperatures in the $[250 - 500°C]$ range for periods of time between $[1 - 30$ min$]$. In this work, the final annealing temperature will be refered to as "the dewetting temperature" and the time the sample spends at that temperature as "the dewetting time".

The influence of three main parameters are explored to understand how the Au dewetting process works:

- The dewetting temperature (T_{dew}) and the dewetting time (t_{dew})
- The amount of gold deposited over the surface. This parameter can be adjusted by changing the temperature of the Au effusion cell (T_{Au}) or by the Au deposition time (t_{Au})
- The quality of the ZnTe buffer layer: impact of the surface roughness, defects and surface reconstructions

To obtain unambiguous results on the impact of these parameters, we have prepared several sets of samples. Each set is composed of 4 to 6 samples grown under the as-close-as-possible conditions and where only one parameter is varied by set. Each step of the sample growth is performed on the same day and using an identical step-by-step procedure (same growth times and temperatures, same and stable cell pressures for the same cell temperature, same surface preparation, same cell deburst before growth, same Au deposition made one after another, etc.)

We monitor the behavior of the Au dewetting *in situ* by RHEED and *ex situ* using SEM images. Moreover, for a set of samples, Rutherford Backscattering Spectrosopy was performed to measure the amount of Au deposited on the sample. Bear in mind that, even if the SEM images reveal clearly the density and diameter of the droplets, the growth of NWs will not begin on exactly the same surface as the surface imaged by SEM. NW growth starts immediately after the dewetting time finishes, while the SEM images of the Au droplets are taken from surfaces that have been previously cooled down to RT. Hence, the main difference is that the period of time the sample stays at temperatures where the dewetting process is still active is higher for samples where there is no NW growth.

Beside this, a second annealing to about 200°C is performed under open-air conditions to remove samples from the sample-holder (fixed using molten In). This additional annealing is done for all samples (with or without NWs), however, the dewetting process will be finished once the Au droplets have catalyzed the NWs. Consequently, rising the temperature a second time, has a greater influence over samples without NWs. In spite of those differences, a reliable control of the NW surface density and the diameter of the Au droplet sitting on top of the NWs can be reached by optimizing the parameters that govern the Au dewetting process (listed above).

2.3.2 Thermodynamic phase of the Au catalyst

An important parameter for the growth of NWs is the thermodynamic phase of the Au catalyst droplet. Not only the requirements to stabilize a solid or a liquid catalyst are different, but also the NW growth kinetics change (different NW yield, morphology, orientation, etc.) [35]. The NW growth mechanism are different: Vapor-Liquid-Solid (VLS) for liquid catalyst and the Vapor-Solid-Solid (VSS) for solid catalyst. The difference between these growth mechanisms will be discussed in chapter 3.

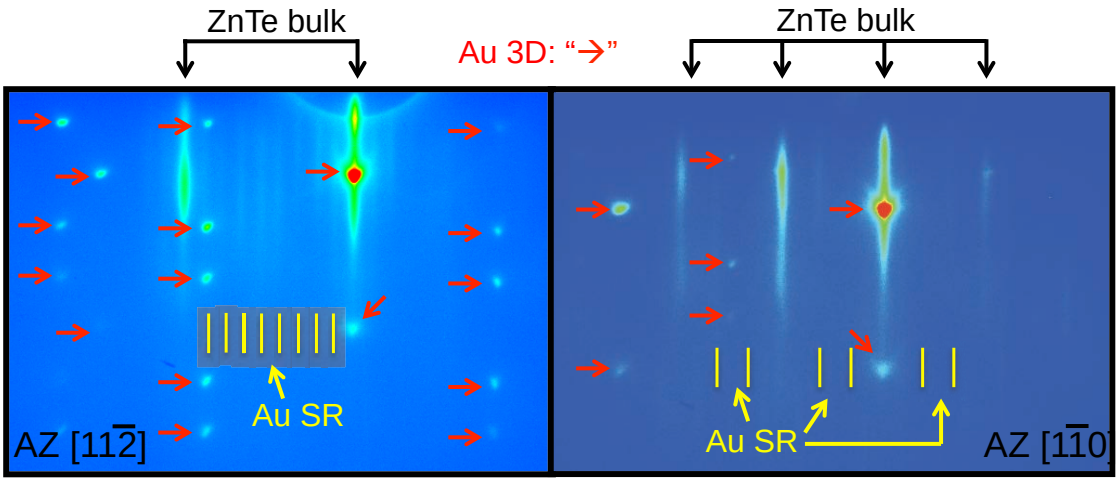

Figure 2.13 – Typical RHEED diffraction pattern of a ZnTe(111)B layer covered with Au particles dewetted at T_{dew} = 375°C. Both [11$\bar{2}$] and [1$\bar{1}$0] azimuths are presented. The spots indicate the presence of solid crystalline Au particles on the surface (indicated with red arrows). In addition to the spots, we observed streaks corresponding to the bulk ZnTe (arrows in black) and to a surface reconstruction (SR indicated in yellow). The Au-induced SR will be discussed in detail on section 2.3.5.

The melting point of bulk Au is 1064°C. This is a very high temperature when compared to the annealing temperatures explored in this study (T_{dew} = 250°C −400°C). Nevertheless, forming liquid Au catalyst may be possible for two reasons. First, the incorporation of elements from the substrate such as Zn or Te into the Au particles, may decrease the melting temperature. The Au-Zn phase diagram presents an eutectic point at 682°C when there is 35 at% of Zn inside the Au and the Au-Te phase diagram presents an eutectic point at 447°C when there is 53 at% of Te inside the Au [36]. Second, the Gibbs-Thomson effect predicts that the melting temperature of small crystals may be much lower than large crystals due to variations in the chemical potential[6].

[6]The size effect on the melting temperature of gold particles has been studied by Buffat and Borel since 1976 [37]. The effects are mostly for particles with diameters below 10 nm.

Hence, it is plausible that the nanometric sized droplets of Au used to catalyze the NWs have a much lower melting point than bulk Au. Moreover, the majority of the metal-catalyzed NWs in the literature are grown by the VLS mechanism, hence with a liquid metal catalyst. Then, the question of the phase of the Au catalyst is not evident.

The RHEED diffraction patterns observed during the Au dewetting show us that, for all the samples presented in this work, the Au catalysts seem to be solid. We observe diffraction spots when the ZnTe buffer layers covered with a thin layer of Au are annealed. These spots are observed at $T_{substrate} = 170°C$ and are continuously seen when the sample temperature is increased to attain the dewetting temperature (T_{dew}) and during the time the samples are kept at this temperature (t_{dew}). In Figure 2.13 we present the typical RHEED diffraction pattern for a sample annealed at $T_{dew} = 375°C$.

2.3.3 Calibration of the quantity of Au deposited

To understand how the dewetting of Au-droplets takes place in the sub-monolayer regime, a precise control of the amount of Au available to form the droplets is needed. To obtain a precise calibration of the quantity of Au deposited on the ZnTe surface, Rutherford Back-scattering Spectroscopy analysis (RBS) were performed on five different samples. For this set of samples, the Au exposure time was changed (t_{Au} = 0, 25, 50, 100, 200s), while the Au-cell temperature was kept constant at $T_{Au} = 1090°C$ (hence the Au vapor pressure at which all the samples were exposed). The samples were annealed at $T_{dew} = 350°C$ for $t_{dew} = 5$ min. The results obtained are shown in Table 2.1.

t_{Au} (s)	Quantity of Au ($\times 10^{15}$ atomes/cm^2)	ML of ZnTe	ML of Au
25	0 ± 0.04	0 ± 0.07	0 ± 0.03
50	0.17 ± 0.04	0.27 ± 0.07	0.12 ± 0.03
100	0.30 ± 0.03	0.48 ± 0.05	0.21 ± 0.02
200	1.05 ± 0.04	1.69 ± 0.07	0.75 ± 0.03

Table 2.1 – Quantity of Au deposited over ZnTe(111)B buffer layers measured by RBS. Four samples are presented: $t_{Au} = 25, 50, 100, 200$s. 1 ML of Au = 1.39×10^{15} atomes/cm^2 and 1 ML of ZnTe = 6.21×10^{14} atomes/cm^2 ($a_{ZnTe} = 0.610$ nm and $a_{Au} = 0.408$ nm).

In Figure 2.14, the quantity of Au used to form the droplets, obtained by RBS, is plotted (vertical axis) versus the amount of Au sent to the surface (horizontal axis). This last quantity is calculated as the vapor pressure of the Au cell (corresponding to a

certain T_{Au})[7] times the time the sample is exposed to the Au flux (t_{Au}). Note that the amount of Au sent to the surface can be tuned with two different parameters: T_{Au} or t_{Au}. Here, we chose to vary the t_{Au} instead of the T_{Au} due to the long stabilization time of the Au cell (the cell needs to be kept at a constant temperature for several hours to obtain reproducible results).

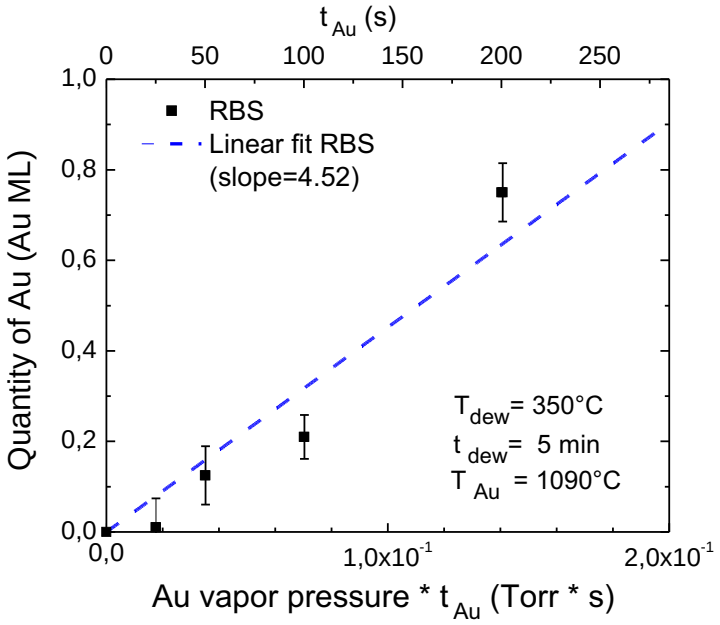

Figure 2.14 – The amount of Au deposited on the surface (in Au ML) obtained from Rutherford Backscattering Spectrosopy (RBS) versus the quantity of Au sent to the surface (lower horizontal axis). The quantity of Au sent to the surface is calculated as the Au vapor pressure times the exposition time. In the upper horizontal axis, we indicate the exposure time. Four different samples were measured at $t_{Au} = 25, 50, 100, 200$s. The Au cell temperature was kept constant at $T_{Au} = 1090°C = 7 \times 10^{-4}$ torr while the exposure time was changed. All samples where annealed at 350°C for 5 minutes. The blue line is a linear fit of the data fixing y = 0 at x = 0. The slope of the fit is 4.52 ± 0.37.

The slope of the linear fit (line in blue) of the data presented in Figure 2.14, gives an equivalence between the actual quantity of Au on the surface (in Au ML[8]) and the quantity of Au sent to the surface. The latest is calculated using the time the sample is exposed to a certain Au flux times the value of that flux quantified as the vapor pressure from the cell (at a certain constant temperature). This means that the slope

[7]The equivalence between the Au temperature and the vapor pressure is calculated using the following equation [38]: $logP = 14.158 - 19343/T - 0.7479\,log(T)$. The units are Pascal and Kelvin. This equation reproduce the observed pressures [39] to an accuracy of at least ±5%.

[8]1 ML of Au in the $< 111 >$ direction $= d^{111} = 2.35\mathring{A}$.

(4.52 ± 0.37) is a quantity with units of Au ML/torr×s. Therefore, we can translate the quantity of Au sent to the surface (torr×s) to the thickness of a fraction of a layer of Au deposited on the surface (in Au ML) by calculating $4.52 \times P_{vap}$ (at T_{Au}) $\times t_{Au}$. Keep in mind that this calibration is limited by the incertitude of the fit presented in Figure 2.14, which we take as the standard deviation: ±0.37 Au ML/torr×s. Although this incertitude is not negligible, taking the slope obtained from the fit of the RBS results to calibrate the quantity of Au deposited on the surface remains very useful, as long as its corresponding error is taken into account.

2.3.4 Shape of the Au droplets

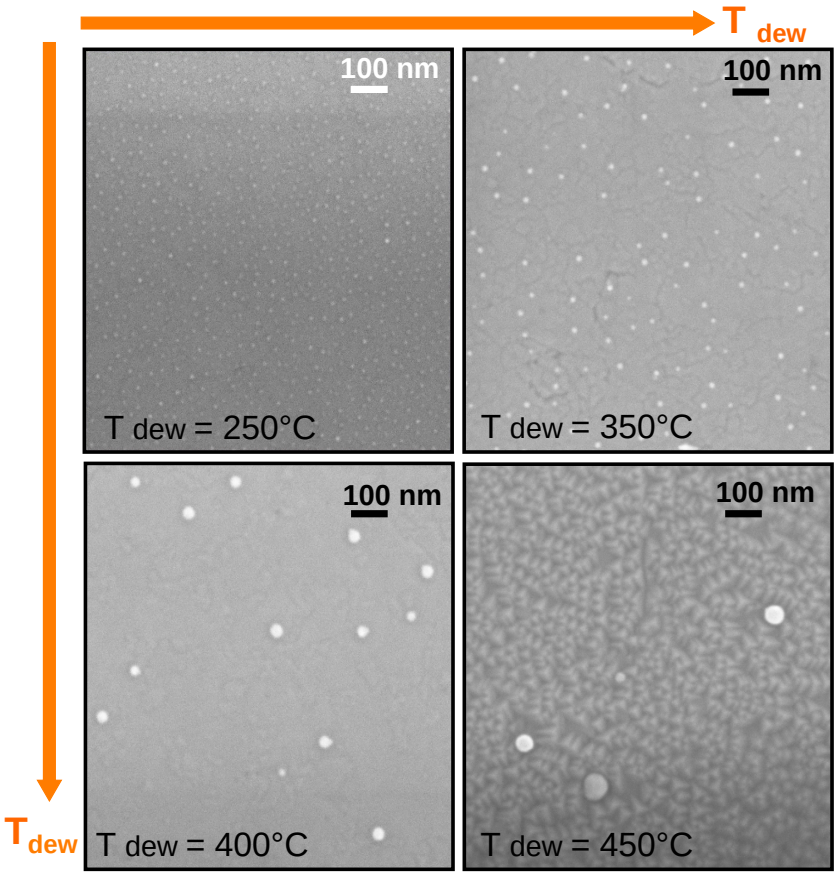

Figure 2.15 – SEM images of the ZnTe(111) surface covered with Au particles (taken from the top). Dewetting temperature varies from 250°C to 450°C. The orange arrow indicates increasing T_{dew}. Only for the sample dewetted at $T_{dew} = 250$°C, the ZnTe buffer layer was not smoothed at 420°C under Te flux. For all samples: $t_{dew} = 5$ min, $T_{Au} = 1100$°C and $t_{Au} = 50$ s.

The dewetting temperature has a major influence over the diameter and the surface density of the Au-droplets. To reveal the impact of this parameter, two sets of samples where grown where the T_{dew} was varied from 250°C to 500°C. In each of these samples, the growth of the ZnTe buffer layer and the Au deposition were identical (same T_{Au} and t_{Au}). On one of the sets, the ZnTe buffer layer was smoothed at high temperature (420°C) under Te flux and on the other not (for details of the smoothening process see section 2.2.5). SEM images of the surface of four samples with different dewetting temperatures are shown in Figure 2.15. The evolution of the samples when T_{dew} increases (orange arrows) is clear: the droplet density decreases and the diameter increases. Statistics on the samples shown in Figure 2.15 along with all samples made in the two sets are shown in Figure 2.16.

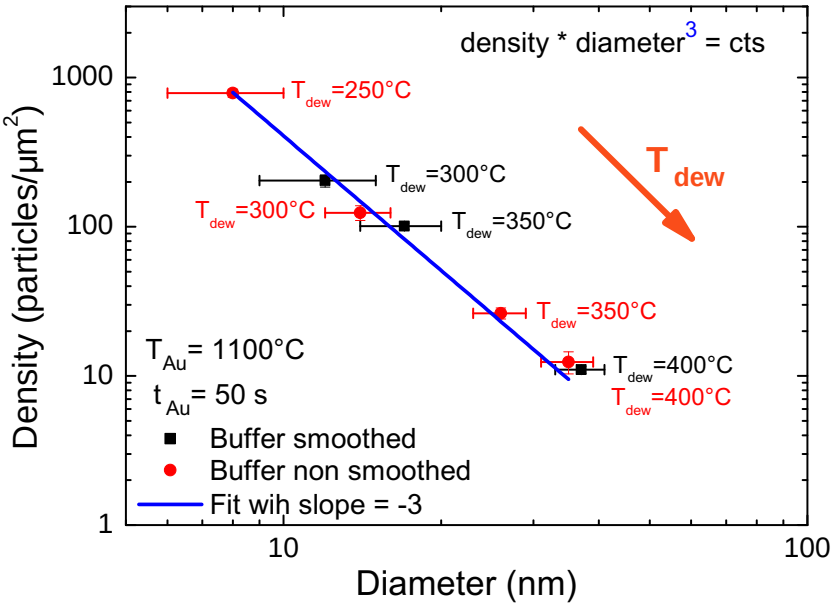

Figure 2.16 – Au-particles surface density (in logarithmic scale) as a function of the Au-particles average diameter for samples with different dewetting temperatures: T_{dew} = [250°C−400°C]. For all samples: t_{dew} = 5 min, T_{Au} = 1100°C and t_{Au} = 50 s. In black: samples where the ZnTe buffer layer was smoothed at 420°C prior to the Au deposition at RT. In red: samples where the ZnTe buffer layer was not smoothed. The blue line is a fit of the data with a constant slope of -3. The data are obtained from SEM images of the surface.

The density of each sample is calculated by counting the number of Au particles in one image and then dividing this number by the surface of that image. In general, we use SEM images with a magnification enough to observe around 100-200 objects by image. The sample's density is obtained by calculating the average value of the

densities from 3 to 5 different images. These images are taken over different zones of the sample to observe differences on the homogeneity of the samples. The error is taken as the standard deviation of the densities calculated for several images. This error is in general smaller than the random distribution of particles $\pm\sqrt{N}$ for images with N particles. This means that the difference between the density obtained from images taken in different zones of the samples is smaller than the interval given by the random distribution of the number of particles in each sample. Hence, there is not a significant difference between the images taken from different zones on the sample (if they are far away from the edges) and we can conclude that the samples have a homogeneous surface density given by the average density from several images.

The diameter is measured from SEM images with much higher magnification, typically from images where around $\sim 10-20$ particles are observed. The number of objects measured by sample is at least > 50. The average diameter and its corresponding error (standard deviation) are calculated from all the particles measured. Again, we used several images from different zones on the sample to obtain the average diameter from Au droplets from all the sample surface. Hence, the error calculated for the average value of the density and the characteristic diameter of each sample takes into account local variations of these parameters.

The surface density *versus* the average diameter of the Au particles is plotted in logarithmic scale. Both sets of samples (with a ZnTe buffer smoothed or not) follow a clear linear trend. The different results from the two sets of samples, higher diameter for non-smoothed samples, will be discussed in section 2.4.3. It is worth mentioning that the data presented in Figure 2.16 can be fitted with a linear -3 slope curve (in blue) indicating that the following relation is valid:

$$\text{density} \times \text{diameter}^3 = \text{constant} \tag{2.1}$$

This result indicates that the aspect ratio of the Au particles is preserved: the proportion between the height and the diameter is constant. In other words, the shape of the droplets is uniform for all the samples. It seems plausible, considering that the Au particles seem to have circular contour line, that the shape of the particles is a fraction of sphere. This is a significant characteristic of the Au/ZnTe system, which differentiates it from other systems like Au/ZnSe(100) where the exponent of the diameter is 2 [25]. Figure 2.16 shows that for $T_{dew} \leqslant 400°C$, the amount of Au in the droplets is equal from sample to sample. When the Au particles surface density increases (or decreases), the average diameter of the Au particles decreases (or increases), preserving constant the total quantity of Au spread over the ZnTe surface.

2.3.5 Volume of the Au catalyst droplets

Now that we have established that aspect ratio of the Au droplets is conserved, we can go further by determining the explicit aspect ratio (hence the volume) of the Au droplets. The set of samples presented previously in section 2.3.3 consists of ZnTe(111)B layers covered with small amounts of Au deposited at $T_{Au} = 1090°C$ during different exposure times for each sample. Here we explore a bigger interval of Au deposition times ($t_{Au} = 0 - 300s$). The dewetting conditions for all samples were $T_{dew} = 350°C$ for $t_{dew} = 5$ minutes.

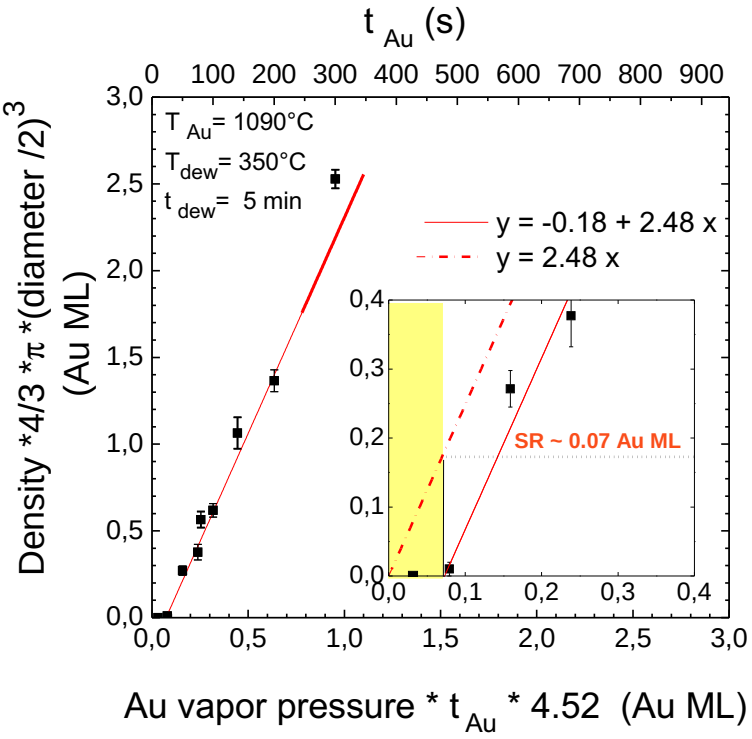

Figure 2.17 – Quantity of Au used to form the droplets as a function of the total amount of Au sent to the surface. The quantity of Au used to form the droplets is calculated as the product of the density of droplets and the volume of one droplet (complete sphere with the average droplet diameter of the sample). The amount of Au sent to the surface is taken as the vapor pressure (at $T_{Au} = 1090°C = 7 \times 10^{-4}$ torr) $\times t_{Au} \times 4.52$ (the calibrating constant obtained from the RBS results with an error of ± 0.37). In the upper axis the exposure time is shown. All samples were annealed at 350°C for 5 min. The red line is a fit of the data.The inset shows a zoom of the same graph at low Au exposures. The yellow region shows the amount of Au sent to the surface before the Au droplets start to form.

In Figure 2.17 we plotted the quantity of Au used to form the droplets (in Au ML) versus the amount of Au sent to the surface (also in Au ML). The first quantity (y-axis), is calculated assuming that the Au particles are complete spheres and using the average density and diameter obtained from the size statistics measured on SEM images of the samples. To obtain the quantity of Au consumed to form the droplets, we multiply the density of Au droplets on the surface [particles /μm^2] by the volume of one complete sphere [μm^3]:

$$\text{droplets density} \times \frac{4}{3} \cdot \pi \left(\frac{\text{diameter}}{2} \right)^3 \tag{2.2}$$

As a result, we calculate the thickness (in μm) of a layer of Au, containing the total volume of Au in the droplets, spread over a surface. This thickness is then transformed in Au monolayers. The second quantity (x-axis), is calculated as the vapor pressure of the Au cell P_{vap} (corresponding to a certain T_{Au}) $\times\, t_{Au} \times 4.52$ (the calibrating constant obtained from the RBS results in section 2.3.3, the error associated to this constant is ± 0.37). The inset is a zoom of the same graph at low t_{Au}.

As expected, the amount of Au used to form the droplets increases linearly with the amount of Au sent to the surface. The slope of the fit gives us a relation between the two quantities of Au, x is the total quantity of Au sent to the surface (measured) and y is the quantity of Au in the droplets if they are a complete sphere (calculated). The equation of the fit can be stated as $x = 0.072(\pm 0.007) + 0.4(\pm 0.05)y$. Since the slope of the curve is not one, we know that the Au droplets are not complete spheres but their volume is equal to a fraction of a sphere given by the slope of the fit. So we can conclude that 0.4 ± 0.05 is the ratio between the real volume of the Au droplets and the volume of a complete sphere. Keep in mind that this value is obtained using the calibrating constant obtained in Fig. 2.17, and as we mentioned before, the error related to this calibration is not negligible. Nevertheless, we can most probably conclude that the volume of the droplets are very close to the volume of half-spherical particles.

Contact angle

The volume of a spherical cap is given by $V_{cap} = \frac{\pi h^2}{3}(3R - h)$ where R is de radius of the sphere and h is the height of the cap. The volume of the spherical cap can be written in terms of its contact angle θ since h=R(1-cos θ). This relationship is represented in Equation 2.3 and plotted in Figure 2.18.

$$V_{cap} = V_{sphere} \times \frac{(1 - cos\theta) \times (2 - cos\theta - cos^2\theta)}{4} \tag{2.3}$$

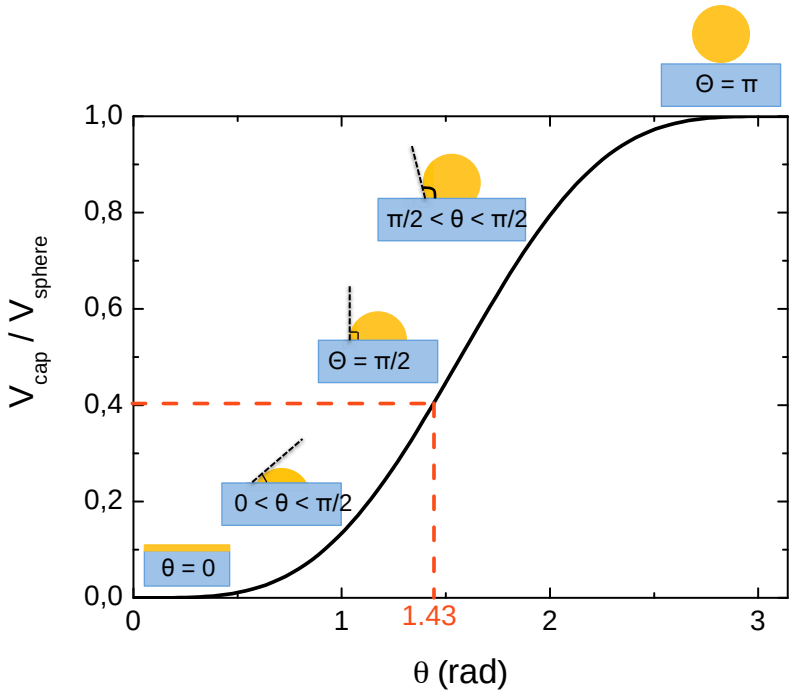

Figure 2.18 – Ratio between the volume of a cap spheric and the volume of a complete sphere versus the contact angle (in radians). For the samples presented here, we obtained $V_{cap}/V_{sphere} = 0.4 \pm 0.05$ hence $\theta = 1.43 \pm 0.007$ rad $= 80° \pm 4°$ (indicated in orange).

Since $V_{cap}/V_{sphere} = 0.4 \pm 0.05$, we can deduce a contact angle of $\theta = 1.43 \pm 0.07$ rad $= 80° \pm 4°$. This is a relevant information due to Young's relation that links the contact angle θ and the surface tensions γ between different phases. It states: $\gamma_{12} = \gamma_{13} + \gamma_{32}\cos(\theta)$ where 1, 2 and 3 may be three different phases (solid, liquid and gas). This analysis allows us to gain information concerning the surface energies involved in this system that can be used for further studies. Keep in mind that we suspect the Au catalyst to be solid, if it is the case, it is possible that the surface energy also depends on the orientation of the Au droplet facets. Finally, we should mention again that the contact angle calculated at $80° \pm 4°$ must be interpreted taking into account the fact that it has an error related to the calibration of the quantity of Au sent to the surface (obtained with the RBS results). Notice that this value is fairly close to 90°, which is the value expected for the volume of exact half-spheres.

Formation of a Au-induced surface reconstruction

In Figure 2.17 we observe that a threshold is attained at weak Au exposure ($t_{Au} < 25$s). This implies that when the surface is exposed to a weak quantity of Au (zone in yellow

in the inset of Figure 2.17), the amount of Au sent do not result in the formation of Au droplets. We found that this is most probably related to the formation of a $3\sqrt{3} \times 3\sqrt{3}$ R30° surface reconstruction (SR) induced by Au adatoms on the ZnTe(111)B surface. This Au-induced SR is clearly observed *in situ* by RHEED and to our knowledge has not been reported before in the literature. Similarly, Au-induced surface reconstructions have been observed for other materials like Au/Si [22] and Au/GaAs(111)B [16].

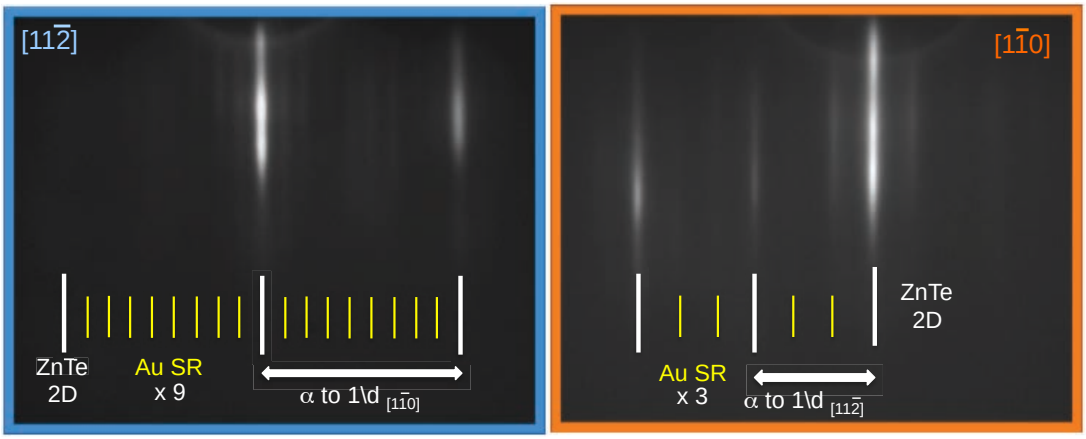

Figure 2.19 – $3\sqrt{3} \times 3\sqrt{3}$ R30° surface reconstruction (SR) observed by RHEED along [11$\bar{2}$] and [1$\bar{1}$0] azimuths. This SR is induced by Au over the ZnTe(111)B surface at temperatures above 300°C.

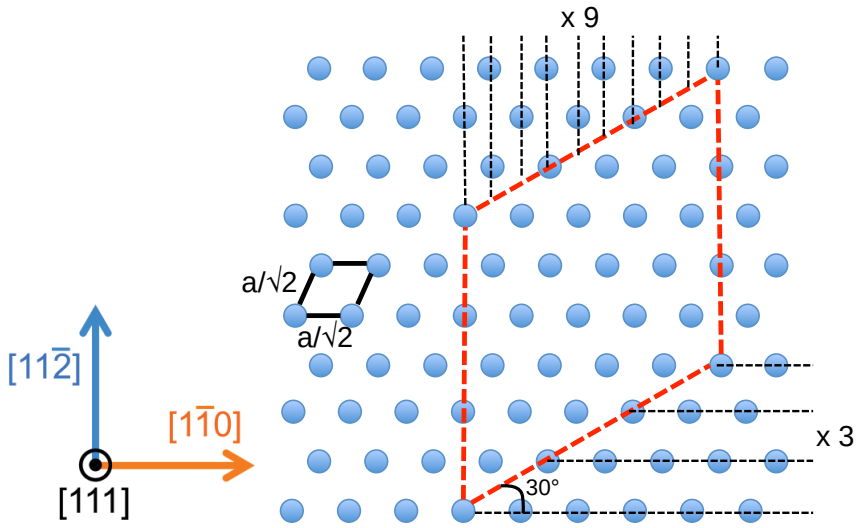

Figure 2.20 – The Au-induced surface reconstruction cell, $3\sqrt{3} \times 3\sqrt{3}$ R30°, is shown in red over the surface structure of ZnTe(111). In black we indicate the ZnTe unit cell. Only the last layer of Te atoms is shown.

Photos of the RHEED diffraction patterns are shown on Figure 2.19, for a sample were the Au exposure is very weak (we did not observe points related to the formation of 3D Au particles). Although this SR can be simultaneously observed with the diffraction spots of Au particles as shown in Figure 2.13. This means that depending on the amount of Au available on the surface and on the quality of the ZnTe layer, Au adatoms can form a SR in addition to the formation of Au particles.

In Figure 2.20 we indicate the Au-SR cell (in red) and the ZnTe unit cell (in black). Notice that the surface is composed of Te atoms since the ZnTe layer is [111] oriented and **B** type. The surface of the SR cell is 4.35 nm^2= $4.35\times10^{-14}cm^2$ and there are 27 Te atoms within the Au-SR cell. The primitive cell of ZnTe has a surface of 0.16 nm^2 (1 ML of ZnTe = 6.21×10^{14} atoms/cm^2) and the primitive cell of Au has a surface of 0,07 nm^2 (1 ML of Au = 1.39×10^{15} atoms/cm^2). Using the fit presented in Figure 2.17 we can deduce the quantity of Au involved in the SR. We found a coverage of 0.072 ($\pm$0.007) ML of Au which corresponds to 9.7×10^{13}atoms/cm^2. According to this calculation, there are 4.4$\pm$0.5 Au atoms in the $3\sqrt{3}\times3\sqrt{3}$ R30° SR cell [9].

This information is crucial to determine the motif of the SR in a future study. Note that it was not possible to directly measure the amount of Au present in Au-SR by RBS. In the sample where t_{Au} = 25s, it was not possible to detect a RBS signal while the SR was clearly visible by RHEED during growth. The amount of Au used to form the SR is below the measurement limits of the RBS. Therefore, it is necessary to use the fits of both Fig. 2.14 and Fig. 2.17. The number of Au atoms in the SR cell has a significant error associated to method used to calculate that value. Even if we cannot affirm the exact number of atoms inside in the Au-induced SR cell, we can say that there are minimum 4 and maximum 5 atoms involved.

In the Au/GaAs system, Hilner et al. [16] have calculated that the $\sqrt{3}\times\sqrt{3}$ R30° Au-induced SR (called Au wetting layer) has a Au coverage of 1/3 ML. They stated that Au atoms are adsorbed at every third threefold hollow hcp (hexagonal close-packed) site of the Ga lattice. Their results are based on scanning tunneling microscopy and low energy electron diffraction/microscopy measurements, as well as, on density functional theory calculation performed to establish a model for the structure of the Au SR of GaAs(111)B surfaces. Here, we propose to copy this motif to our system in order to propose a possible structure for the SR that we observed on the ZnTe(111)B surface. This method has already been used to find the motif of the CdTe(111)B SR under Te rich conditions with success [33, 40]. Since these two surfaces behave very similarly to the ZnTe(111)B surface, it is plausible that the motif is alike. If we assume that there

[9] We can also convert these values from Au ML units to ZnTe ML units: 0.072 ML of Au = 0.16 ML of ZnTe and 4 Au atoms / 27 Te atoms correspond to a coverage of 0.15 ML (in units of ZnTe).

are 4 Au atoms involved in the $3\sqrt{3} \times 3\sqrt{3}$ R30° SR cell, we can propose a possible motif (shown in figure 2.21).

The motif proposed in Fig. 2.21 takes the same arrangement of atoms as the one proposed by Hilner et al. for Au on a GaAs(111) surface, which is a Au atom surrounded by 3 Te atoms, this block is completely surrounded by bare Te. We propose to take this motif at the angles of the SR cell (counts for 1 atom), another 4 of this Au blocks on the edges (count for 2 more Au atoms) and one Au-block completely inside the cell. We present the blocks at the edges and at the interior rotated by 180°, but several possibilities are possible. To reveal the real geometry of the surface reconstruction, STM measurements must be performed. Nevertheless, Fig. 2.21 shows a possible configuration of Au atoms in the $3\sqrt{3} \times 3\sqrt{3}$ R30° SR cell.

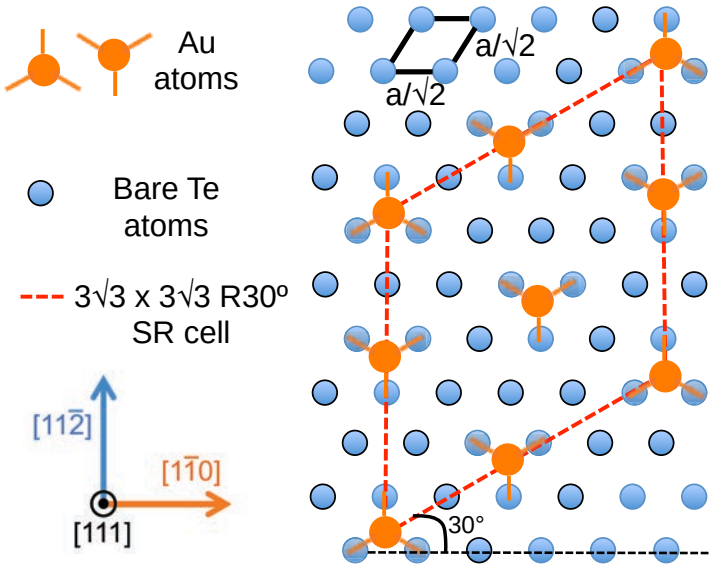

Figure 2.21 – A possible motif for the Au-induced $3\sqrt{3} \times 3\sqrt{3}$ R30° surface reconstruction cell is shown over the ZnTe(111)B surface. In black we indicate the ZnTe unit cell, in red the SR cell, in blue de Te atoms and finally, in orange the Au atoms.

The existence of this Au-induced SR may have an important impact on how the Au adatoms diffuse during the dewetting process. Hilner et al. [16] have already mentioned that the Au-SR (Au wetting layer) was necessary for the thermodynamic stability of the Au particles on the GaAs surface. Here, we also observed that it plays a role in the formation of the Au particles. For example, this effect is demonstrated by an increase of the Au-droplet surface density on samples grown over a ZnTe(111)A pseudo-substrates (Zn at the surface). On those surfaces, we do not observe the formation of a SR under

the same annealing conditions. This could be explained by a different diffusion of the Au adatoms over surfaces where the SR is present or not. It is plausible that in the first case, an arriving Au atom will rather diffuse over the Au atoms building the SR (acting as a wetting layer) than over the Te atoms on the surface. Under those circumstances, the dewetting of Au particles will involve the diffusion of Au over Au and not of Au over Te, therefore changing the characteristic diffusion length of the process.

In brief, in this section we conclude that to control the total amount of Au available to form the Au catalyst it is necessary to subtract the small part that goes into forming the SR:

$$\begin{array}{ccc} \text{Au available to} & = & \text{Au sent to the surface} \; - \\ \text{form the droplets} & & \text{Au consumed to form the SR} \end{array}$$

2.3.6 Quantity of Au incorporated in the droplets

In the previous sections we have established that the aspect ratio of the Au droplets is conserved and calculated that their volume is $\sim 0.4 \times V_{sphere}$. For simplicity and due to the incertitude related to the volume calculated, from this point on, we will consider the Au-droplets as half-spheres. We have studied the impact of varying the amount of Au sent to the surface (controlled by t_{Au} and T_{Au}), now we present results on how the quantity of Au incorporated in the droplets changes with the dewetting temperature and time.

Influence of the dewetting temperature

One particularity is that for $T_{dew} > 400$°C, the ZnTe surface between the Au droplets becomes rough. This is indicated by the disappearance of the SR probably due to higher evaporation rates at this temperature that do not allow the SR stability. At $T_{dew} \gtrsim 450$°C, there is strong surface damage characterized by a 3D RHEED diffraction pattern and confirmed by the presence of cubic-type structures on the surface (as observed by SEM and shown in Figure 2.22). There are almost no Au particles visible on the surface for samples dewetted at $T_{dew} = 500$°C. As a matter of fact, the few Au particles observed are located inside holes on the surface (indicated with red circles in Figure 2.22b). Moreover, deep cracks on the surface (possible twin boundaries, see section 2.2.4) defining regions of the surface with different symmetry are observed. This behavior suggests that the Au droplets migrate inside the ZnTe buffer layer at high annealing temperatures.

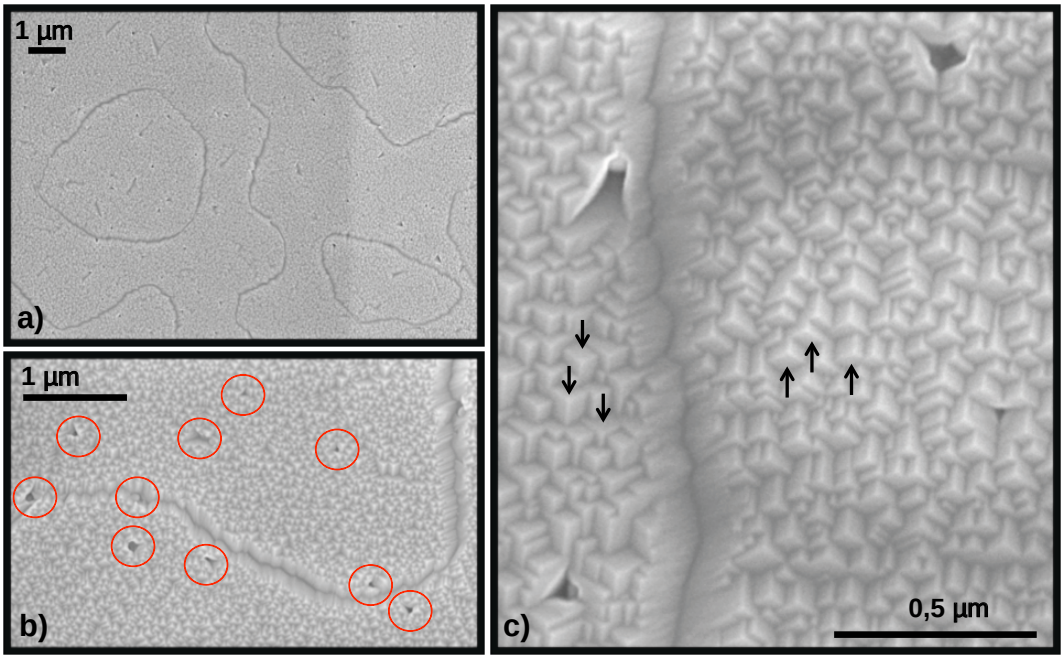

Figure 2.22 – SEM images of the surface of a thick ZnTe(111)B layer after depositing a thin layer of Au for $t_{Au} = 50$s at $T_{Au} = 1100$°C and annealing it at $T_{dew} = 500$°C for $t_{dew} = 5$ min. Three images with different magnification are shown to illustrate a) large surface regions delimited by cracks (possible twin boundaries); b) that the few Au particles observed are sited inside holes on the surface and c) details on the structure of the ZnTe surface, in particular the arrows indicate the inversion of symmetry (180° rotation) between the two sides of the surface separated by a crack.

In Figure 2.23, we plot the quantity of Au used to form the droplets as a function of the dewetting temperature. For $T_{dew} \lesssim 400$°C, the amount of Au in the droplets is relatively constant at around 0.5 ± 0.15 ML. At $T_{dew} > 400$°C, it decreases until vanishing at $T_{dew} = 500$°C (zone marked in orange in Figure 2.23). These quantitative data confirm the migration of small amounts of Au, in the form of droplets, into the ZnTe(111) layer at high annealing temperatures ($T_{dew} > 400$°C). This is consistent with previous demonstrations of Au diffusing in ZnTe [41,42,43]. With these results in mind, dewetting of Au for the following samples was always kept below $T_{dew} = 400$°C to avoid diffusion of Au below the surface, hence to keep constant the amount of Au deposited on the surface (at a fixed T_{Au} and t_{Au}).

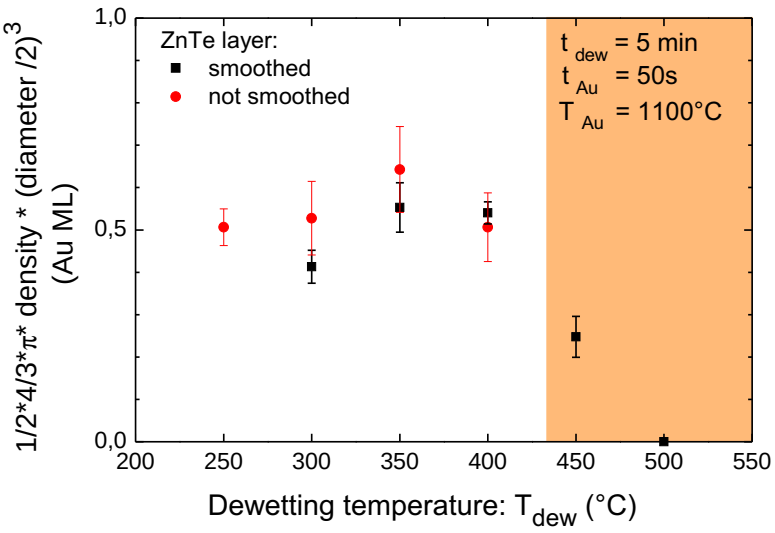

Figure 2.23 – Thickness of Au incorporated in the droplets (taken as half-spheres) as a function of T_{dew}. The quantity in the vertical axis is calculated with the data shown in Figure 2.16. The zone where there is possible Au migration into the ZnTe layer is indicated in orange ($T_{dew} > 400$°C). In black, samples where the ZnTe buffer layer was smoothed at high temperature prior the Au deposition and in red samples without smoothing. For all samples: $t_{dew} = 5$ min, $T_{Au} = 1100$°C and $t_{Au} = 50$ s.

Influence of the dewetting time

Correspondingly, we have also investigated the effect of the dewetting time on the diffusion of Au droplets on the surface. In Figure 2.24 the quantity of Au used to form the droplets is plotted for samples with different t_{dew} but with the same T_{dew} (350°C). Remarkably, the quantity of Au in the droplets is constant at 0.1 ± 0.03 ML for $t_{dew} \geqslant 10$ min (line in green). Note that this quantity is smaller than the one found in Figure 2.23 due to a different amount of gold sent to the sample (lower T_{Au} and t_{Au}).

In Figure 2.25 we present separately the density and the diameter of the samples shown in Figure 2.24. We conclude that for $t_{dew} \geqslant 20$ min, the Au particle formation has saturated (density and diameter are constant) hence indicating the absence of a clear Ostwald ripening[10]. In this system, Ostwald ripening states that with increasing time, Au atoms from small particles should diffuse to be incorporated into bigger ones. Accordingly, the average Au-diameter should increase and the average density of Au-

[10]Oswald ripening is a spontaneous process, thermodynamically-driven, where small particles are less energetically favored than large ones (since atoms at the interior of a particle are more energetically stable than on the surface). It dictates that with increasing time, small particles will be incorporated into bigger ones.

particles decreases with time. This is not what we observed between the samples at $t_{dew} = 20$ and 30 min. We observed that both density and diameter of the Au particles are constant for high t_{dew}, indicating that the Au dewetting process has stabilized and that there is not an evident Ostwald ripening for samples where the stabilization time (t_{dew}) is higher than 20 min.

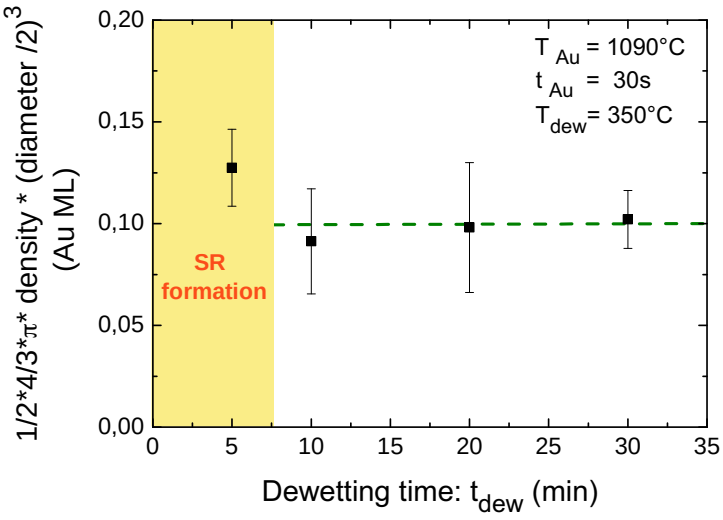

Figure 2.24 – Quantity of Au in the droplets calculated using Eq. 2.2 as a function of t_{dew}. The zone in yellow indicates the time where the formation of the Au-induced surface reconstruction (SR) may still be active ($t_{dew} \lesssim 10$ min). For all samples: $T_{dew} = 350°C$, $T_{Au} = 1090°C$ and $t_{Au} = 30$ s.

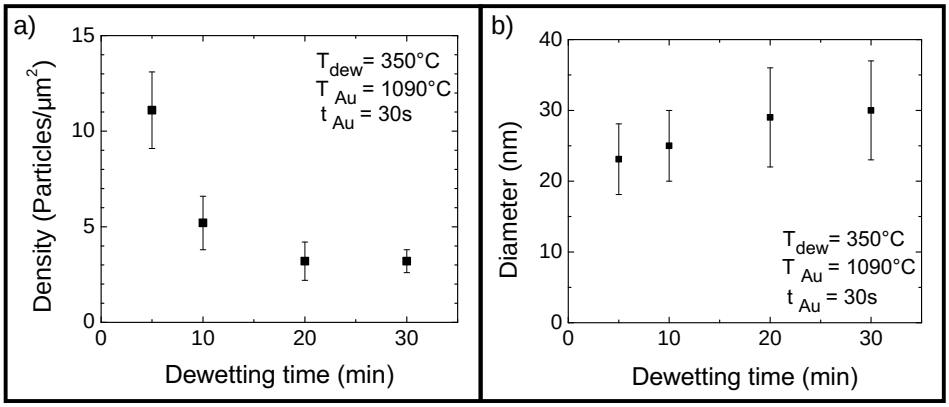

Figure 2.25 – Sample's average Au-droplet a) density and b) diameter as a function of the the dewetting time. The total amount of Au sent to the surface is constant: for all samples $T_{Au} = 1090°C$, $t_{Au} = 30$s and $T_{dew} = 350°C$.

For $t_{dew} = 5$ min, the quantity of Au incorporated in the droplets is slightly bigger. A possible explanation for this behavior at low dewetting times, is the formation of the Au surface reconstruction. According to our RHEED observations, the formation of the SR occurs after the droplets start to appear. This could be explained by considering that part of the Au in the initial islands will contribute to the formation of the SR. In other words, when the sample is heated at a certain temperature, between RT and 300°C depending on the amount of Au deposited on the surface, there will be droplets that form. At around 300°C the formation of the SR is energetically favored, hence part of the Au incorporated in the droplets is used to form the SR. Once the SR is completely formed, the Au remaining in the surface will continue to diffuse and the Au-dewetting process will go on forming droplets until this process is completed. We can assume that for the sample at $t_{dew} = 5$ min in Figure 2.24 and Figure 2.25, the amount of Au is higher than for the others because the SR is not completely build over the whole surface under those conditions. At longer dewetting times, the quantity of Au in the droplets decreases in comparison with the sample at $t_{dew} = 5$ min and it remains stable, showing that the SR has completely covered the surface.

In short, at $t_{dew} = 5$ min: the formation of the SR is not finished and is still consuming a part of the Au deposited on the surface; at $t_{dew} = 10$ min: the SR is almost completely formed and the assembling of Au particles is nearly stabilized. Finally, at $t_{dew} \geqslant 20$ min: the SR and Au droplets seem to be completely stabilized and we do not observe any evolution in the density or in the diameter of the Au particles. Note that we strongly suspect that the Au particles are solid (indicated by a spotty RHEED pattern). This could explain why samples dewetted for 20 min or more, at a constant dewetting temperature, do not seem to follow the typical Ostwald ripening. The solid phase of the catalyst may diminish the Ostwald ripening or eventually stop it.

In conclusion, Figure 2.24 shows that at $T_{dew} \leqslant 400$°C and $t_{dew} \geqslant 10$ min (for a Au deposition of $t_{Au} = 30s$ at $T_{Au} = 1090$°C), the quantity of Au available to form the droplets is constant. Hence, once the amount of Au sent to the surface is fixed, the Au-droplet diameter and density remain almost at a constant value, determined by the dewetting temperature, for all dewetting times. There is no significant effect of the dewetting time. Therefore, if the annealing of Au is performed at dewetting temperatures $\leqslant 400$°C for $t_{dew} \geqslant 10$ min, there is no observable migration of Au droplets inside the ZnTe(111)B layer and the Au droplet formation process is stabilized. Note that in section 2.4.1, we will show that for higher Au depositions (at $t_{Au} \geqslant 50s$ and $T_{Au} = 1090$°C), the diameter is constant even for $t_{dew} = 5$ min (shown in Figure 2.27).

2.4 Control of the Au-dewetting process

In the last paragraphs we have established two main ideas: that the quantity of Au incorporated in the droplets can be easily controlled, once the SR is completely constructed, and that there is a correlation between the diameter and the surface density of Au droplets. Now the questions are: what is the influence of the key parameters involved in the dewetting of Au particles on the diameter and on the surface density? And how can we experimentally tune those parameters to obtain the ideal surface to start the growth of NWs? To answer those questions, first we will discuss the evolution of the Au-droplet diameter for different dewetting conditions and second, the evolution of the particle surface density.

2.4.1 Control of the Au-catalyst diameter

When the quantity of Au sent to the surface is changed, while all other dewetting parameters are kept constant, we observe two response regimes. This behavior is presented in Figure 2.26 for weak Au depositions and in Figure 2.27 for stronger ones. At low Au coverage, the diameter decreases, until a critical diameter is attained. Then, at higher Au coverage, the diameter saturates at constant value independently of the amount of Au deposited on the surface.

In Figure 2.26, the temperature of the Au cell was varied whereas the Au exposure time was kept constant and quite small ($t_{Au} = 50$ s for all samples). Correspondingly, in Figure 2.27 the temperature of the Au cell was kept constant ($T_{Au} = 1090°C$) and the exposure time was widely changed for each sample. Notice that both figures have the same horizontal axis: the vapor pressure of the Au cell at a certain temperature multiplied by the exposure time multiplied by 4.52 (the RBS calibration constant that allows to passe from torr×s to the equivalent Au quantity in Au ML). That quantity represents the total amount of Au sent to the surface.

We observe that from zero to $\sim$ 0.2 ML, the diameter decreases linearly and from $\sim$0.2 ML to 1 ML the diameter remains constant at $\sim$ 15 nm. Accordingly, the negative slope of the curve shown in Figure 2.26 corresponds to the initial part of the curve presented in Figure 2.27 (marked in purple). The range where the amount of Au sent to the surface modifies the particles diameter is quite short: $0 < t_{Au} < 60$s. As a result, this parameter is not very practical to use for exploring systematically the growth of NWs.

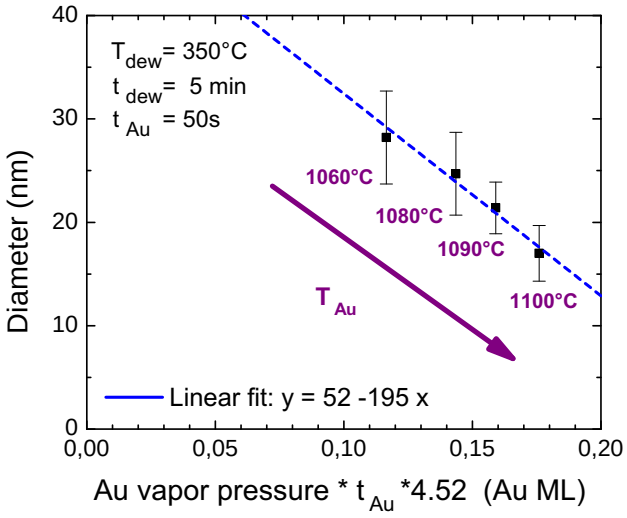

Figure 2.26 – Sample's average Au-droplet diameter as a function of the total amount of Au sent to the surface. This quantity is calculated as the Au cell vapor pressure times the exposure time times 4.52 (RBS calibration constant). The parameter that was varied in this set of samples was T_{Au}, indicated next to each data point. The Au cell was left for 1 hour at each different temperature to stabilize the flux. For all samples the exposure time was of 50s and the annealing was performed at 350°C for 5 minutes.

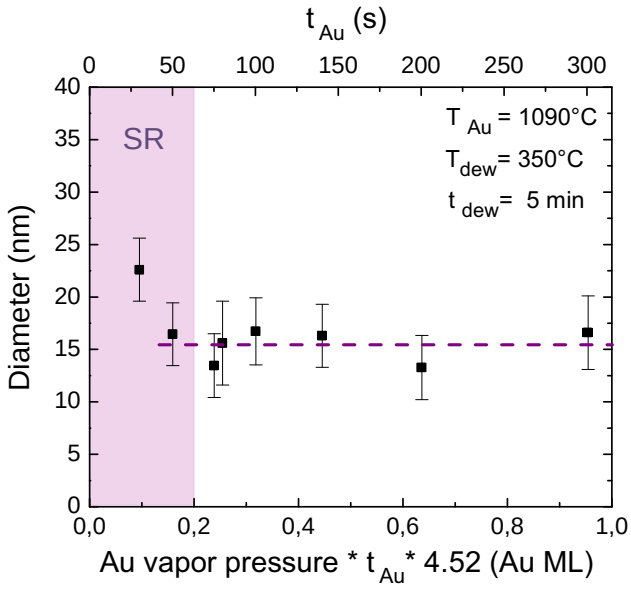

Figure 2.27 – Sample's average Au-droplet diameter as a function of the total amount of Au sent to the surface (lower axis). This quantity is calculated as the Au cell vapor pressure times the exposure time times 4.52 (RBS calibration constant). In this set of samples, the time the sample was exposed to a fixed Au cell flux was varied (shown in the upper axis). For all samples: $T_{Au} = 1090$°C, $T_{dew} = 350$°C and $t_{dew} = 5$ minutes. The region colored in purple corresponds to the region explored in Figure 2.26.

The existence of these two regimes can again be explained by the fact that at low Au coverages the surface reconstruction is still in formation. For the samples presented in Figure 2.26 and Figure 2.27, the annealing time was 5 minutes. We observed that the diameter stabilizes only at Au coverages > 0.2 ML. In section 2.3.6 (see Figure 2.24), we found exactly the same behavior: from 0 to 0.2 Au ML ($t_{dew} = 5$ min), there is a domain where the diameter and density are not yet stable. Here, we find the same result and we additionally observe that even for low dewetting times ($t_{dew} = 5$ min) when the Au coverage is high enough the diameter saturates to a constant value. This means that size-stable Au droplets can be obtained either at low Au coverage if the dewetting time is high enough or at low dewetting times if the Au coverage is high enough. The last one can be due to a faster formation of the SR when there is more Au available on the surface.

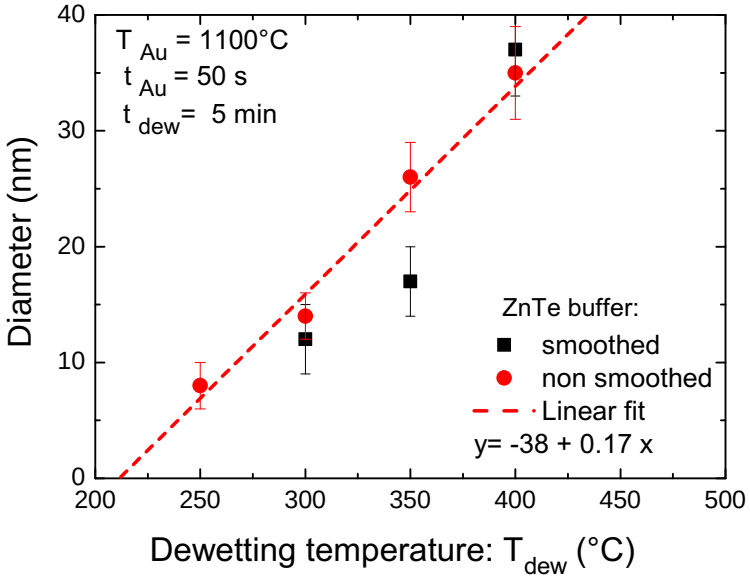

Figure 2.28 – Sample's average Au-droplet diameter as a function of the dewetting temperature. The total amount of Au sent to the surface is constant: for all samples $T_{Au} = 1100$°C, $t_{Au} = 50$s and $t_{dew} = 5$ minutes. In black squares samples where the ZnTe buffer layer was smoothed and in red circle samples where the buffer was not smoothed.

In Figure 2.28 the impact of the dewetting temperature on the Au particles diameter is presented (the influence of the dewetting time was shown in Figure 2.25). We observe that when the dewetting temperature is increased, the diameter of the Au droplets increases linearly. By changing T_{dew} from 250°C to 400°C, the droplet diameter increases 4 times its size, going from 10 nm to 40 nm. The effect of this parameter is sharp, hence it is the most efficient way for adjusting the diameter of the catalyst droplets.

2.4.2 Control of the Au-catalyst density

The same analysis is done to determine the behavior of the droplets surface density. In Figure 2.29 we present the variation of the density of Au droplets on the surface when the quantity of Au deposited on the surface is changed. We plotted the results from samples where the exposure time changed and where the temperature of the Au cell was kept constant. We observe that the density varies linearly with the amount of Au deposited on the surface. This is compatible with the results presented on Figure 2.17 and on Figure 2.27: since the droplet-diameter is constant, the density should increase when more Au is deposited on the surface.

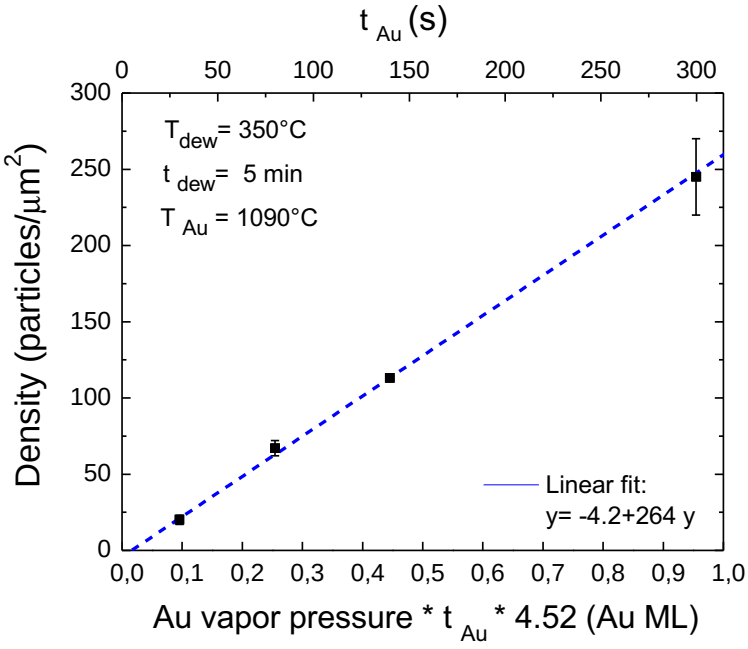

Figure 2.29 – Au-droplets surface density as a function of the total amount of Au sent to the surface. This quantity is calculated as the Au cell vapor pressure times the exposure time times 4.52 (RBS calibrating constant). The parameter that was changed in this set was the exposure time (t_{Au}). For all samples: $T_{Au} = 1090°C$, $T_{dew} = 350°C$ and $t_{dew} = 5$ minutes. The blue line is a linear fit of the data.

The amount of Au deposited on the surface can also be controlled by the temperature of the Au cell. Samples where t_{Au} was kept constant at 50s and the temperature of the Au cell (T_{Au}) was changed are presented in Figure 2.30. We plotted the droplet surface density as function of the inverse of the temperature of the Au cell. Notice the semi-logarithmic scale. From this data, we can deduce that an activation energy law is followed with $E_a = 7.4$ eV.

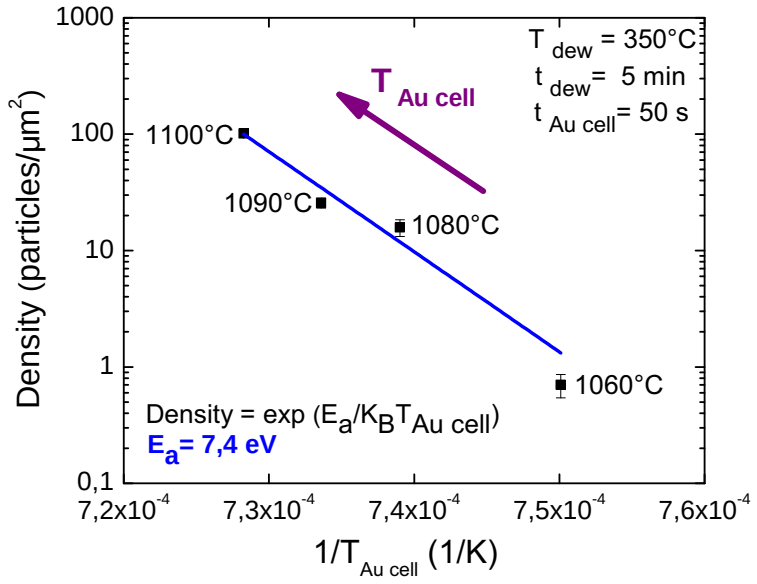

Figure 2.30 – Au-droplet surface density as a function of the inverse of the Au cell temperature. For all samples $t_{Au} = 50$ s, $t_{dew} = 5$ min, and $T_{dew} = 350$°C.

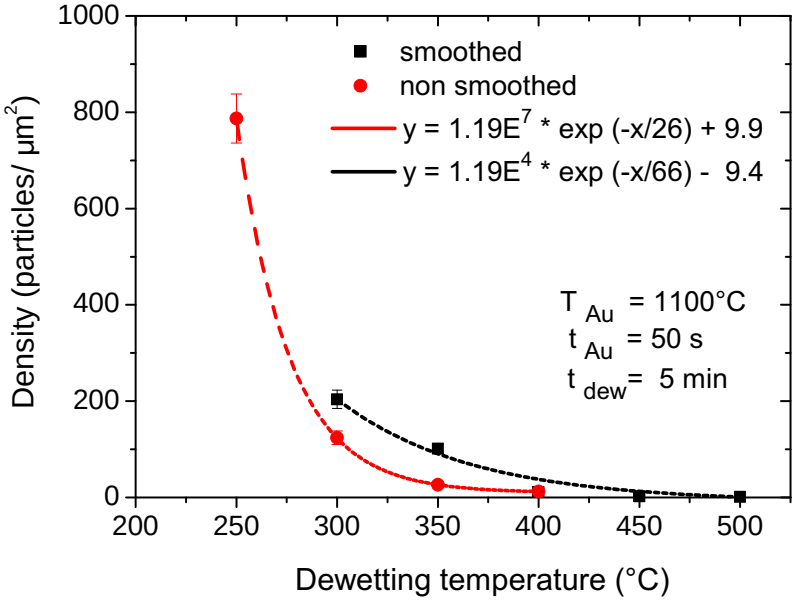

Figure 2.31 – Au-droplet surface density as a function of the dewetting temperature. For all samples: $t_{dew} = 5$ min, $t_{Au} = 50$ s and $T_{Au} = 1100$°C. In black squares samples where the ZnTe layer was smoothed and in red circle samples where the buffer was not smoothed. The lines are exponential fits of the data.

Finally, the variation of the density with the dewetting temperature is presented in Figure 2.31. We observe again an important variation of the density, decreasing exponentially when the dewetting temperature increases. This is a second approach to control the density of Au droplets. Keeping in mind, that when we vary the dewetting temperature we simultaneously change the diameter as shown in Figure 2.16.

In conclusion, we have found that the droplet density can be controlled by varying t_{Au} (Figure 2.29) or T_{Au} (Figure 2.30) and the diameter by varying T_{dew} (Figure 2.28). Again, it is important to keep in mind that the density and the diameter are dependent of each other. Note that the diameter can also be tuned using the T_{Au} (Figure 2.26), each T_{Au} stabilizes a different value for the droplet diameter. According to these results, the ideal conditions to obtain Au droplets with a diameter in the $[20 - 30$ nm$]$ range with ultra low density (< 10 droplets $/\mu m^2$), are chosen as follows: $t_{Au} = 30 - 40$s, $T_{Au} = 1090$°C, $T_{dew} = 350$°C and $t_{dew} \geqslant 5$ min. With these conditions and taking into account the SR, we expect to deposit around one third of a Au ML. In Figure 2.32 the surface of a sample prepared under those conditions is shown.

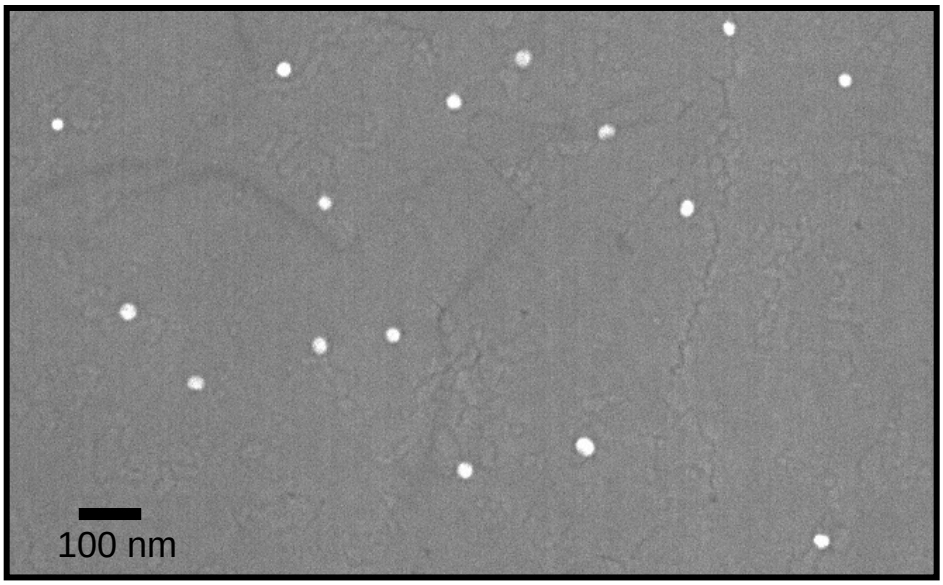

Figure 2.32 – SEM image of the surface of a ZnTe(111)B layer with Au deposited at $T_{Au} = 1090$°C for $t_{Au} = 30$s and annealed at $T_{dew} = 350$°C for $t_{dew} \geqslant 5$ min.

2.4.3 Influence of the quality of the ZnTe(111)B buffer layer

In Figures 2.16, 2.23, 2.28 and 2.31 we show results on two sets of samples where the Au deposition has been done on ZnTe surface with (points in black) or without (points in red) a "smoothening" process at high temperature. This process consists in rising the temperature of the ZnTe buffer layer at 420°C under a Te rich atmosphere, then decreasing the temperature to 380°C where the Te flux is stopped and finally cooling down the sample to RT under vacuum. Note that after this particular process, surface reconstruction of the ZnTe buffer layer are observed only under Te flux and they immediately disappear as soon as the Te flux was cut off at 380°C (details of the SR evolution during this process are presented in section 2.2.5).

For these sets of samples, we observe a different behavior for samples dewetted at $T_{dew} = 300$°C and 350°C. The droplet density is smaller and the diameter is bigger for samples grown over layers that were not "smoothed". The most striking difference is for the sample dewetted at $T_{dew} = 350$°C, where the density is one order of magnitude smaller and the diameter is double when there is no "smoothening" process performed on the surface. SEM images of these two samples are shown in Figure 2.33.

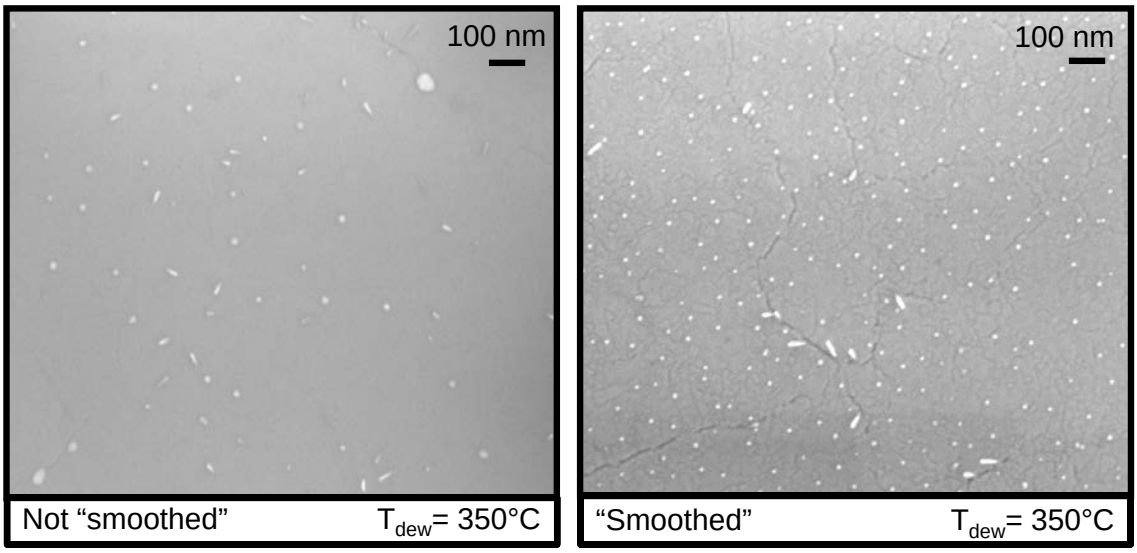

Figure 2.33 – SEM images of the ZnTe(111) surface covered with Au particles (taken from the top). The sample where the "smoothening" of the buffer layer was performed is shown in the right image and the samples where the buffer was not "smoothed" in the left image. For both samples: $T_{dew} = 350$°C, $t_{dew} = 5$ min, $T_{Au} = 1100$°C and $t_{Au} = 50$ s.

The difference in the droplet density and in the quality of the surface between the particles is severe. The sample that has been "smoothed" has many cracks and seems rougher. This is consistent with the *in situ* information given by the RHEED pattern: the c(8×4) surface reconstruction disappears when the Te flux is stopped at 380°C. Another signature of this roughness is the absence of the Au-induced SR during the Au dewetting process. These results are surprising because they indicate that the diffusion is higher for samples that did not had their ZnTe surface previously "smoothed". The fact that the density is smaller and the diameter bigger when there is no "smoothening" of the surface means that in that case, the Au particles diffused faster and hence formed (less) particles with bigger diameter. It seems that the conditions taken for this "smoothening" process are no optimal.

Nevertheless, even for the two samples dewetted at $T_{dew} = 350$°C (biggest difference in droplet density and diameter), we keep a clear trend when changing the dewetting temperature. The "smoothening" process seems to only shift the data. In other words, when we observe each set of samples independently, we observe the same behavior: linearly increasing diameter and exponentially decreasing density when T_{dew} increases. These significant differences in the droplet density and diameter due to the "smoothening" process of the ZnTe layer, do not question this tendency.

The "smoothening" process performed on the ZnTe buffer layer at high temperature, was done to smooth the surface in order to enhance diffusion of adatoms of Au during the dewetting process and of Zn and Te during NW growth. Since that was not the case, we modify the initial "smoothening" process to obtain that effect, by keeping the Te flux during the cooling down until 300°C. This new process, allowed us to observe the c(8×4) surface reconstruction even at room temperature. Afterwards, when the Au is deposited and the sample dewetted, the Au-induced surface reconstruction is observed only on samples that have been smoothed with the new recipe. Samples without smoothening of the ZnTe layer or with the initial "smoothening" process (Te flux was cut off at 380°C), do not show so clearly the formation of a Au-induced SR. This is a significant difference that is consistent with the results presented in section 2.2.5. We conclude that the (111)-ZnTe surface diffusion is bigger under Te rich conditions.

2.5 Conclusions

To summarize this chapter, we present a list of the main points treated and the informations that we have established concerning the growth of 2D ZnTe (111)B layers and the Au dewetting on this surface.

- The optimal conditions to grow a high quality ZnTe(111)B layer over a deoxidized GaAs(111)B substrate are: $T_{sample} = 260°$C under stoichiometric flux ratio conditions. Under those growth conditions, the roughness of a 200 nm-thick ZnTe layer is equivalent to the one of the GaAs substrate (the root mean square roughness is 0.3 nm over a 5 x 5 μm^2 surface).

- Strain relaxation during the growth of a ZnTe(111)B layer over a GaAs(111)B substrate starts after depositing only 1 ML of ZnTe. This process is very fast: after 5 ML of ZnTe the surface is almost completely relaxed. The existence of twins on the ZnTe surface is shown.

- The surface reconstruction diagram is explored and established for ZnTe(111)B layers. We mainly observed the c(8x4) and $2\sqrt{3} \times 2\sqrt{3}$ R30° SR. Additionally, we found large regions of the SR diagram where we observed a mix of those two SRs. Under those conditions, both SR can be stabilized, hence we may have regions on the surface with a c(8x4) SR and others with a $2\sqrt{3} \times 2\sqrt{3}$ R30° SR. The SR diagram found for ZnTe(111)B surface is very similar but shifted towards higher temperatures compared to the one found for CdTe(111)B surfaces.

- The Au catalyst seems to be in a solid phase according to the spotty RHEED pattern observed at the dewetting temperatures and during the NW growth.

- The amount of Au deposited on the surface is mainly controlled by the vapor pressure of the Au cell (equivalent to a fix Au cell temperature) times the exposure time: $P_{vap} \times t_{Au}$. The proportionality constant is determined by RBS measurements and it is found to be 4.52 ± 0.37 Au ML/torr×s.

- The formation of a $3\sqrt{3}\times3\sqrt{3}$ R30° Au-induced surface reconstruction is observed. This SR is stable at our typical Au dewetting conditions and consumes around 0.072 ±0.007 Au ML (∼0.16 ML of ZnTe). Using this value, we expect that the SR cell involves 4-5 atoms of Au for 27 atoms of Te (the exact value calculated is 4.4±0.5 Au atoms).

- The aspect ratio of Au particles after dewetting is constant. We found that ratio of volumes is: $V_{catalyst} = 0.4(\pm0.05) \times V_{complete\ sphere}$, which corresponds to a contact angle of $80° \pm 4°$. Hence, the Au particles are very close to half-spheres once the Au-induced SR is completed.

- At dewetting temperatures higher than 450°C, the ZnTe layer becomes very rough and there is most probably migration of Au inside the ZnTe layer.

- The dewetting time does not influence the surface density or the diameter of the Au particles at $t_{dew} \geqslant 20$ min. Once the Au-induced SR is completely formed, the dewetting of catalyst seems to reach a saturation point where the number of particles and the diameter of those particles remains stable. For $t_{dew} \geqslant 20$ min, Ostwald ripening is either very slow or absent. Further investigation is needed to confirm this fact and to explore if this phenomena is related to the possible solid phase of the Au droplets in this system.

- This study allowed us to determine the optimal conditions to prepare samples with small-diameter Au particles (10-20 nm) and ultra low surface density (< 10 particles/μm^2) to catalyze NWs. The droplets density and diameter are mostly determined by the dewetting temperature T_{dew}. Note that, only the density and not the diameter can be controlled by the amount of Au sent to the surface (once the SR is completed). This means that we are able to vary the Au catalyst surface density without changing the diameter of the particles. This allowed us to have ZnTe surfaces covered with an ultra-low density of Au particles with a homogenous diameter.

CHAPTER 3

Growth and properties of ZnTe nanowires

Contents

3.1 State of the art & purpose of this study 76
3.2 Sample preparation 80
3.3 Influence of different stoichiometric conditions on the nanowire growth 82
3.4 Cone-shaped and cylinder-shaped ZnTe NWs 86
3.4.1 Lateral *versus* axial growth 86
3.4.2 Crystal structure of the nanowires 91
3.4.3 NW polarity 93
3.4.4 Discussion 95
3.5 Early stages of the nanowire growth 97
3.5.1 Surface densities 99
3.5.2 Morphological characteristics of the NWs 101
3.6 Influence of the temperature on the NW growth 109
3.7 Diffusion-driven nanowire growth model 114
3.8 Conclusions 127

3.1 State of the art & purpose of this study

As stated in the introduction, nanowires present many attractive properties, for instance: the prominent role of surfaces due to a high surface/volume and length/radius ratio, the possibility to grow heterostructures (axial or radial), various opportunities for quantum confinement, the efficient relaxation of stress on sidewalls but also the easy tailoring of strain in core-shell NWs, etc. To develop and use this appealing characteristics, NW-based research needs to deeply investigate the different mechanisms involved in the growth of NWs. Understanding and controlling the mechanism of NW growth is a necessary condition to develop optimized NW-based structures.

With this intention in mind, a main objective of this work is to gain knowledge on how the growth of II-VI semiconductor NWs occurs and to determine which, how and why certain conditions affect the growth of NWs. To begin this chapter, we will present a general overview of the main results published for selenide and telluride SC NWs.[1]

ZnSe and ZnTe NWs can be grown by various methods from vapor phase transport [44], metal organic vapor phase epitaxy [45,46,47], electro-chemical deposition [48], solution-phase growth [49] and MBE [50, 51]. The MBE growth of NWs is particularly interesting since it allows to explore the NW growth at lower growth temperatures in comparison to other growth techniques and the growth of radial and axial heterostructures with sharp interfaces. Additionally, it is possible to observe the growth in-situ using reflection high-energy electron diffraction.

The growth of **ZnSe NWs** by MBE has been reported by several groups, in particular we can mention the work reported by N. Wang's group at the Hong Kong University of Science and Technology [52, 53, 54, 55], the contribution from Colli et al. [56] from the University of Cambridge and the work of our group in the Nanophysics and Semiconductors group of the CEA/CNRS at Grenoble [25, 57]. The growth of ZnSe NWs has been explored on different substrates (GaP, GaAs, pseudo-substrate of ZnSe, amorphous SiO_2) and along different orientations: $< 111 >, < 112 >, < 110 >$. In most of the cases the NW growth is catalyzed by Au droplets through the VSS mechanism (solid Au catalyst). The NWs diameters can vary between 9 and 80 nm. These NWs usually have very few defects when their diameter is below 20 nm [25]. For thicker NW (diameter $>$ 20 nm), staking faults are systematically observed. The crystal structure is usually ZB, but some observations of ultra-thin NWs (diameter $<$ 10 nm) show a WZ structure. Depending on the growth temperature and II/VI flux ratio, the NWs are reported to be tapered (when grown at $\sim 300°C$ under Zn- rich flux ratio conditions) or

[1] Extensive reviews of the growth, properties and applications of Si-Ge and III-V SC NWs have been published in [1, 58, 59, 60, 61].

not (constant NW diameter at growth temperatures $\sim 400°C$ under excess of Se). The NWs grow preferentially along the $< 111 >$ direction independently of the orientation of the substrate.

The literature on the growth of **ZnTe NWs** by MBE is very concise. The MBE growth of ZnTe NWs has been reported previously by the Polish Academy of Sciences in Warsaw [4, 26, 50, 62]. This group reported the growth of high density ZnTe NWs directly on GaAs and Si substrates (along different orientations) by using a Au catalyst and the vapor-liquid-solid mechanism (VLS). These conditions correspond to the formation of a Ga-Au or Au-Si eutectic alloy in the catalyst droplet (observed ex-situ by EDX) which are a source of impurities during the growth. The NW growth is performed under Zn-rich flux ratio conditions at temperatures between 360 and 450°C, using elemental cells: Zn and Te sources. The ZnTe NWs reported have the ZB structure and many stacking faults. They grow preferentially along the $< 111 >$ axis independently on the substrate orientation.

The NW growth conditions used in this work are very different. First, we take advantage from the congruent nature of the evaporation of tellurides to explore the growth of ZnTe NWs near stoichiometric flux ratio conditions. It is possible to obtain a stoichiometric molecular beam flux from a Knudsen cell loaded with the compound semiconductor (ZnTe, CdTe), and to precisely tune the cation-anion balance thanks to additional elemental cells (Zn, Te, Cd). Our ZnTe NWs are grown either under Te-rich or under stoichiometric flux ratio conditions. Second, we chose to grow a thick ZnTe(111)B buffer layer (250-500 nm) to separate the GaAs(111)B substrate from the Au catalyst particles. This isolating buffer layer along with the low dewetting temperature responsible for solid phase of the Au catalyst particles, reduces the incorporation of impurities in the NW (Ga or As). Third, the density of NWs (determined by the Au droplet density) is very low in our samples ($\sim$ 1-5 μm^2), which is ideal to study the influence of the growth conditions on the NW morphology without shadowing or competition effects from NWs growing close to each other. Finally, the NWs are grown at a low temperature (350°C) using the ZnTe, Te and Zn effusion cells.

Low temperature and a control of the flux ratio conditions allows us to grow NW with different morphology (cone and cylindric-shaped NWs) and crystal structure (ZB/WZ).

Purpose of this study

In this chapter, the growth of pure gold-catalyzed ZnTe NWs by molecular beam epitaxy (MBE) under different growth conditions is explored. Particularly, the growth of NWs under different flux ratio conditions (II/VI ratio) and at different growth temperatures is studied. The idea is to determine the effect of the growth conditions on the morphology and crystal structure of the NWs and to understand the growth mechanisms that govern the NW growth.

A particular observation was made during the first stages of this work: two different types of ZnTe NWs can be grown (SEM image shown in Fig. 3.1). The first type are cone-shaped NWs (tapered) with a crater at their base and the second type are cylinder-shaped NWs with a pyramid at their base. We will show that they have different crystal structures (ZB and WZ respectively). These different types of NWs can be obtained by varying the growth conditions, but the originality of this observation is the fact that not only we have observed these two types of NWs on the same sample at different regions, but more interestingly they can be found homogeneously distributed over the whole sample. Even if these two types of NWs are grown under the same growth conditions, their morphology, crystal structure and length distributions are very different.

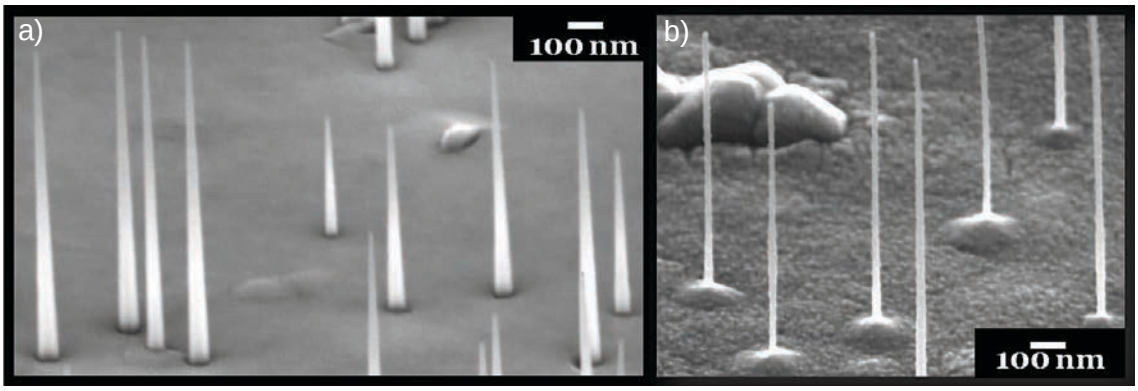

Figure 3.1 – SEM image of ZnTe NWs: a) cone-shaped and b) cylinder-shaped.

These distinct characteristics motivated a more-detailed investigation of the origin of the two types of NWs, including the evolution of the growth from the very early stages and the presence of radial growth (observed thanks to the growth of CdTe markers). Understanding the mechanisms involved in the growth of these two types of NWs is a central part of this chapter. It is for that reason that we believe the results presented in this work are not only of interest for the II-VI scientific community, but can also be transferred to unravel NWs growth phenomena in other semiconductor systems.

This chapter is divided in five main parts:

- In the first part, we begin by a general description of how the NWs are grown. Then we introduce the results on the NW growth under different II/VI flux ratios (section 3.3). The growth conditions at which the two types of NW grow simultaneously on the same sample are described.

- In the second part, a detailed study of the different characteristics of the two types of ZnTe NWs is presented (sections 3.4). This study includes various TEM measurements to assess the crystal structure,wurtzite *vs.* zinc-blende, and the polarity of the NWs. EDX measurements are also performed to detect, or not, the presence of lateral growth.

- In the third part, we investigate the early stages of the growth of ZnTe NWs under different flux ratio conditions (section 3.5). In particular, the appearance and the evolution of the growth of the two types of NWs are studied.

- In the fourth part, the growth of ZnTe NWs at different sample temperatures is explored (3.6). Different conditions for the growth of the two types of NWs is also explored.

- Finally, in the fifth part, a diffusion-driven NW-growth model is presented (section 3.7). Values of the diffusion length on the substrate and along the NWs are discussed.

3.2 Sample preparation

The whole NW growth process takes place in an ensemble comprising two MBE chambers connected under ultra high vacuum, one for II-VI elements and the second one for III-V elements and Au. Details concerning the GaAs deoxidation, the growth of the ZnTe buffer layer, the Au deposition and the Au dewetting have been extensively described in Chapter 2. Once the Au catalyst droplets are formed, the shutters from the effusion cells are opened and the fluxes are sent to the surface initializing the growth of NWs. The sample holder is rotated around its axis during growth to obtain an homogenous incident flux from the cells.

We have explored the growth of NWs at different sample temperatures, from 300°C to 400°C and under different II/VI flux ratios. The stoichiometry of the flux can be precisely controlled thanks to the congruent evaporation of a binary ZnTe cell and the use of two single element cells for Zn and Te [2]. A scheme of the NWs growth process is given in Figure 3.2.

[2] According to reference [1], the signal of the ion gauge I_k, also called Beam Equivalent Pressure (BEP), for each element (k= Zn, Te, ZnTe) can be written in terms of: the cell flux J_k, the absolute temperature T_k, the molecular weight of the species M_k and a ionization coefficient $\eta(Z_k)$. This coefficient depends on the atomic number Z_k of the species and it is relative to nitrogen: $\eta(Z_k) = \eta(Z_{N_2}) * [(\frac{0.4Z_k}{14}) + 0.6]$. The expressions used to calculate the Te/Zn ratio are:

$$\begin{aligned} I_{Zn} &= J_{Zn}\sqrt{\frac{M_{Zn}}{T_{Zn}}}\,\eta(Z_{Zn}) \\ I_{Te} &= \frac{1}{2}J_{Te}\sqrt{\frac{2M_{Te}}{T_{Te}}}\,\eta(2Z_{Te}) \\ I_{ZnTe} &= I_{Zn} + I_{Te} \end{aligned}$$

So for example, if we use the ZnTe cell plus the Zn cell, we obtain:

$$\begin{aligned} J_{Te} &= \frac{I_{ZnTe}\sqrt{T_{ZnTe}}}{\sqrt{M_{Zn}}\,\eta(Z_{Zn}) + \frac{1}{2}\sqrt{2M_{Te}}\,\eta(2Z_{Te})} \\ J_{Zn} &= \frac{I_{ZnTe}\sqrt{T_{ZnTe}}}{\sqrt{M_{Zn}}\,\eta(Z_{Zn}) + \frac{1}{2}\sqrt{2M_{Te}}\,\eta(2Z_{Te})} + \frac{I_{Zn}\sqrt{T_{Zn}}}{\sqrt{M_{Zn}}\,\eta(Z_{Zn})} \\ \frac{J_{Zn}}{J_{Te}} &= 1 + \frac{I_{Zn}\sqrt{T_{Zn}}}{I_{ZnTe}\sqrt{T_{ZnTe}}}\left[1 + \frac{\frac{1}{2}\sqrt{2M_{Te}}\,\eta(2Z_{Te})}{\sqrt{M_{Zn}}\,\eta(Z_{Zn})}\right] \end{aligned}$$

The same equation is valid when we use the ZnTe cell plus the Te cell:

$$\frac{J_{Te}}{J_{Zn}} = 1 + \frac{I_{Te}\sqrt{T_{Te}}}{I_{ZnTe}\sqrt{T_{ZnTe}}}\left[1 + \frac{\sqrt{M_{Zn}}\,\eta(Z_{Zn})}{\frac{1}{2}\sqrt{2M_{Te}}\,\eta(2Z_{Te})}\right]$$

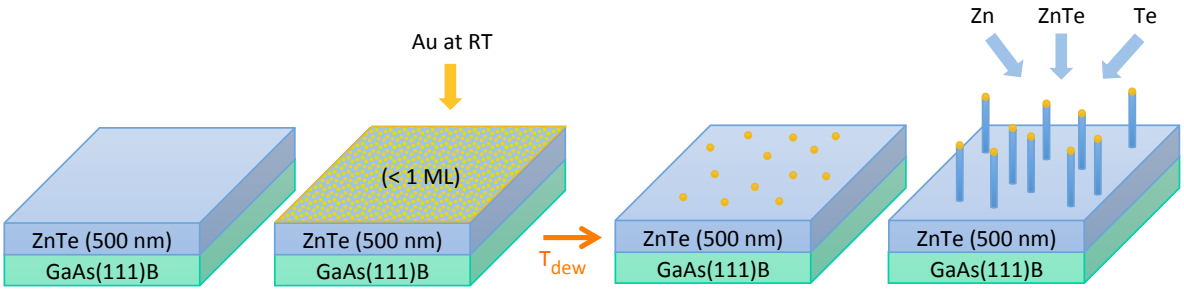

Figure 3.2 – Scheme of the NW growth process.

To begin with, we chose to fix the Au dewetting temperature at 350°C. SEM images of the Au-particle formation at T_{dew} = 350°C, t_{dew} = 5 min, T_{Au} = 1090°C and t_{Au} = 40s, reveal droplets with a diameter in the 10-20 nm range, homogeneous over all the sample, with an ultra-low density (for details see Chapter 2).

The NW growth temperature was chosen to remain at 350°C for three main reasons:

- First, this temperature is low enough to grow CdTe insertions. At this temperature Cd incorporates into the droplets and allows axial growth of CdTe axial sections, whereas at higher temperatures the evaporation rate is much higher hence the growth of this type of insertions is not optimal.

- Second, keeping the same temperature for the Au dewetting and the NW growth allows to stabilize the size of the catalyst particles, hence to obtain more uniform diameter distributions and reproducible NW samples. We have shown in Chapter 2, that for a fixed dewetting temperature (T_{dew} = 350°C) after 10 min of stabilization time, there is no ripening by diffusion (see Figure 2.23).

- Finally, at this temperature the Au catalyst particles are solid (shown by RHEED observations). This means that most probably the growth of NWs will occur through the Vapor-Solid-Solid (VSS) mechanism. The main advantage of the VSS NW growth with respect to the VSL growth is to obtain more abrupt heterostructure interfaces [35]. Keep in mind that the axial growth of NW heterostructures is obtained by changing the element flux during growth. This process generally produces broad interfaces (broad compositional transitions), as atoms in the catalyst will deplete gradually from the droplet over time. This means that the Au droplet acts as a reservoir: when we change the flux from Zn to Cd, for a certain time there will be both Zn and Cd incorporating thought the catalyst, until all the Zn atoms are incorporated in the NW and only Cd (and Te) atoms remain in the catalyst. The length of this transition (here the interface between the ZnTe/CdTe), depends on the solubility of the growth species in the catalyst droplet. The VSS growth mechanism induces lower solubilities of the atoms in the catalyst and reduces the NW growth rate [63, 64], therefore it is plausible to grow sharper interfaces.

3.3 Influence of different stoichiometric conditions on the nanowire growth

Figure 3.3 displays SEM images of NW samples grown with different Te/Zn flux ratios. The NWs were grown for 30 min, one sample after another on the same day, and adding a Zn or Te flux to the stoichiometric flux from the ZnTe cell. Flux ratios (atoms·cm^{-2}·s^{-1}) were calculated from beam equivalent pressures (BEP) using the growth conditions presented in Table 3.1. The flux ratio is calculated as explained in the footnote in section 3.2.

In Figure 3.3 we present NWs grown at: (a) strongly Te rich (Te/Zn : 4/1), (b) Te rich (Te/Zn : 1.7/1), (c) stoichiometric (Te/Zn : 1/1) and (d) Zn rich (Te/Zn : 1/2.3) flux ratio conditions.

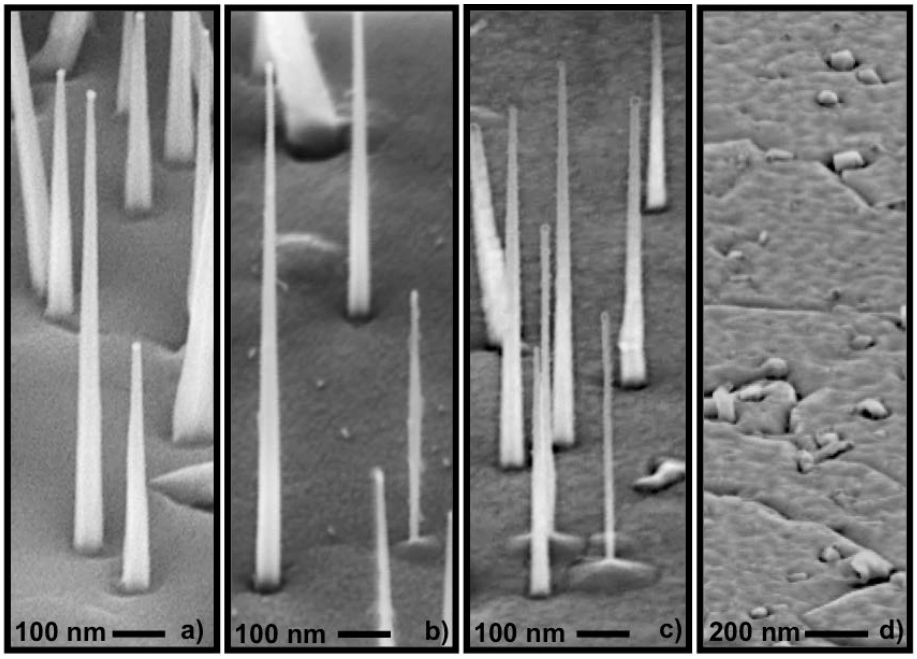

Figure 3.3 – SEM image of ZnTe NWs grown at 350°C under a) high Te rich conditions (Te/Zn : 4.1/1) , b) low Te rich conditions (Te/Zn : 1.7/1), c) stoichiometric (Te/Zn : 1/1) and d) Zn rich conditions (Te/Zn : 1/2.3). Samples are tilted at 65°.

As mentioned previously, this set of samples was grown at $T = 350$°C. At such temperature a 2D layer is also formed during the growth of the NWs. This layer can be observed by SEM. In Table 3.2, the typical sizes of the NWs above the 2D layer are given as well as the thickness of the 2D layer (buffer + re-growth layer).

Sample	Cell temperature (°C)			BEP ($\times 10^{-6}$ Torr)			Flux ratio
	ZnTe	Te	Zn	ZnTe	Te	Zn	(Te/Zn)
Fig. 3.3a	607	376	-	1.6	4.1	-	4.1/1
Fig. 3.3b	607	360	-	1.6	1.0	-	1.7/1
Fig. 3.3c	607	-	-	1.6	-	-	1/1
Fig. 3.3d	607	-	250	1.6	-	1.4	1/2.3

Table 3.1 – Growth conditions of the NWs shown in Figure 3.3.

	Fig. 3.3a (Te/Zn:4.1/1)	Fig. 3.3b (Te/Zn:1.7/1)	Fig. 3.3c (Te/Zn:1/1) Cone	Fig. 3.3c (Te/Zn:1/1) Cylinder
Height (nm)	440 ± 175	560 ± 200	590 ± 325	460 ± 50
Base diameter (nm)	46 ± 8	49 ± 6	40 ± 6	17 ± 2
Au diameter (nm)	17 ± 2	18 ± 2	17 ± 3	16 ± 3
2D ZnTe layer (nm)	500 ± 30	450 ± 20	475 ± 20	475 ± 20

Table 3.2 – Size statistics of the NWs shown in Figure 3.3 (average values ± standard deviations). In the last row, the values of the 2D layer (buffer and re-growth) measured by SEM are given.

Zn-rich flux ratio growth conditions: no nanowires

Under a strong Zn excess (Fig. 3.3d), the growth of NWs is totally inhibited. Even when the zinc excess is significantly reduced (1:1.2) (not shown here), the conditions for catalyzed NW growth are not fulfilled.

High Te-rich flux ratio growth conditions: cone-shaped nanowires

Under strongly Te rich conditions (Fig. 3.3a), in contrast to the Zn-rich conditions, the growth of NWs is highly enhanced. The NW density, about 7 NW/μm^2, is significantly lower than the initial gold-droplet density under the same conditions (20 ± 3 Au particles per μm^2). This fact will be discussed in section 3.5. Most of the NWs are vertical. They are cone-shaped (tapered): the diameter at the tip matches that of the gold particles, 17 ± 2 nm on this sample, while the base-diameter is larger. The NW length distribution is broad. A general trend is that the base diameter increases with the NW length, as shown in Fig. 3.5 (circles in red). However, we observed several NWs with a quite high difference in length, up to 500 nm, and the same base diameter. Another characteristic of these cone-shaped NWs is the presence of a crater around the NW base, with a diameter smaller than the average distance between the NWs.

Stoichiometric flux ratio growth conditions: cone-shaped and cylinder-shaped NWs

The most interesting observation is made on the sample grown under stoichiometric flux conditions: two sorts of wires are seen, homogeneously distributed throughout the same sample (Fig. 3.3c). The majority of the NWs are cone-shaped with a crater at the base (like the ones grown under Te rich growth conditions), however about 20% of the total have a cylinder shape (non-tapered). The cylinder-shaped NWs sit at the top of an hexagonal pyramid. In fact, when observed them from the top, we can distinguish pyramids with 6 facets as show in Fig. 3.4. Remark that, the gold-particle diameter is in the same range for both types of NWs (see Table 3.2).

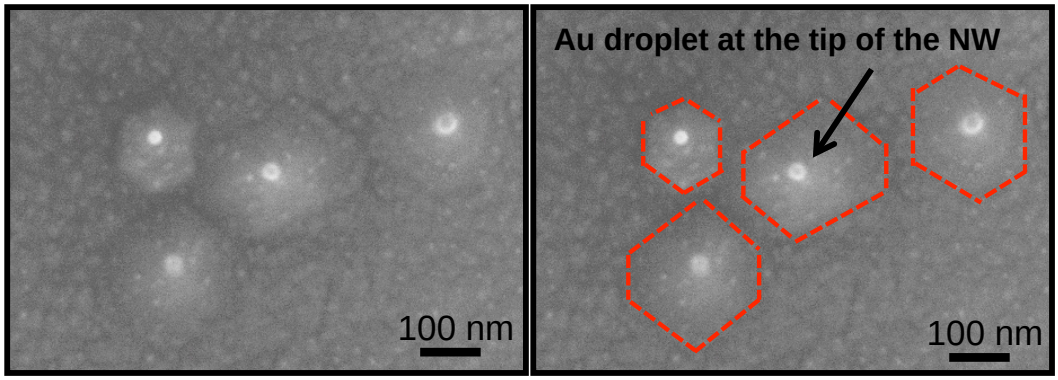

Figure 3.4 – SEM image of a few cylinder-shaped ZnTe NWs taken from the top (exceptionally grouped together). The Au droplet at the tip of the NWs is observed as well as the pyramid's facets. These facets are illustrated with red-dotted lines in the right image.

The two kinds of NWs also coexist in a sample grown with a moderate Te excess (to Te/Zn flux ratio 1.7/1), shown in Fig. 3.3b. When compared to the stoichiometric sample, the percentage of cylinder-shaped NWs is smaller and the base pyramid has a smaller diameter in average.

In figure 3.5, we show the size statistics for the NWs presented in Fig.3.3. We observe that:

– **Cylinder-shaped NWs** are grouped together on figure 3.5. They present an almost constant diameter (with a variation of at most 10 nm from the base to the tip), mainly determined by the diameter of the gold droplets and a narrow length dispersion (in comparison with cone-shaped NWs).

– **Cone-shaped NWs** from the three different samples show a strong dispersion in the NW length and in the base diameter. Nevertheless, it is possible to distinguish a trend among them: the base diameter increases rapidly for low height values and saturates for large height values. The NW radius versus length behavior is very different than for cylinder-shaped NWs. When comparing cone-shaped NWs with similar height, we observed that the ones grown under stoichiometric conditions are thiner at the base than the ones grown under Te-rich conditions.

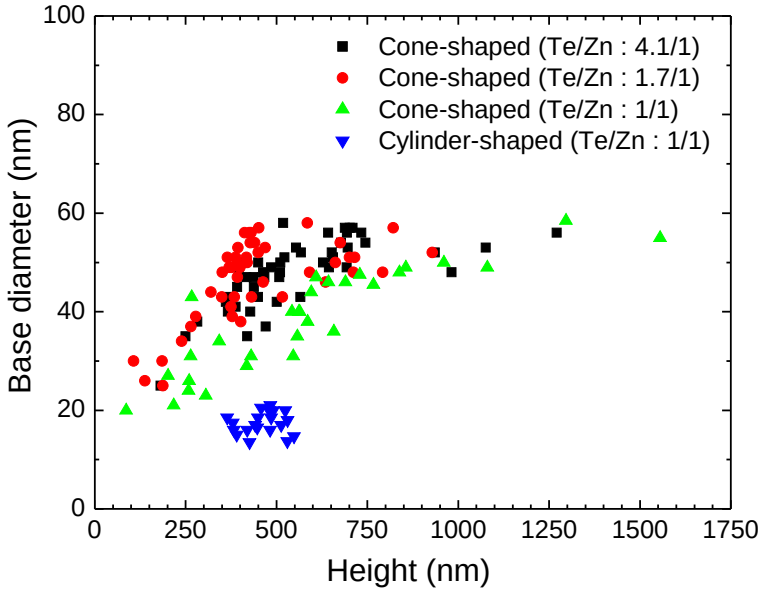

Figure 3.5 – Base diameter versus height distribution of ZnTe NWs grown under different stoichiometric conditions. Note that the values of the height measured are of the part of the NW above the total 2D ZnTe layer.

Keep in mind that there is a 2D ZnTe layer (simultaneously) growing between the NWs. The thickness of this re-growth layer depends on the Te/Zn growth ratio, hence it needs to be taken into account when comparing the difference of height of the cone-shaped NWs from samples grown under different flux ratio conditions. We looked at SEM images from the edge (samples tilted at 90°) and we observed that there is only a very small difference in the thickness of the re-growth layer: the sample grown at Te/Zn:4.1/1 has a re-growth layer only 25 nm thicker (on average) than the sample grown at Te/Zn:1/1 (see Table 3.2). Note that the measurements of the thickness of the 2D layers have a significant error. This is due to non-optimal 2D layer growth conditions at the temperature where the NWs are grown causing inhomogeneities on the re-growth layer.

3.4 Cone-shaped and cylinder-shaped ZnTe NWs

Complementary observations were performed to unravel the mechanisms involved in the growth of the two types of ZnTe NWs. We aimed to gain information on the structural characteristics of these NWs to understand the origin of such different behaviors. For that, 1) we checked the possible presence of lateral growth using EDX to detect a CdTe marker (section 3.4.1); 2) we used high-resolution transmission electron microscopy (TEM) to determine the NW crystal structure (zinc-blende or wurtzite; section 3.4.2) and 3) we reveal the polarity of the two types of NWs using high angle annular dark field (HAADF) scanning transmission electron microscopy (STEM; section 3.4.3).

3.4.1 Lateral *versus* axial growth

The growth of NWs can be both axial (through the Au catalyst) and lateral (radially along the NW side walls). The existence of these two different growth directions determines the morphology of the NWs. The predominance of one direction of growth with respect to the other, gives us an indication of the different diffusion contributions involved in the growth (atoms arriving directly to the Au-catalyst, or to the NW side wall or to the 2D layer). Hence, it is interesting to determine the presence, or not, of lateral growth for both types of NWs.

To establish that, we have studied the incorporation of a CdTe insertion in a ZnTe NW. The main idea is to use Cd as diffusion marker within the NWs. This is obtained by growing a sample of ZnTe NWs under the same conditions as the sample presented in Fig. 3.3c, except for a 2 min interruption under vacuum at $t = 25$ min, and the subsequent insertion of CdTe (for 30s). ZnTe growth was then resumed for 5 more minutes. In photoluminescence such a CdTe insertion acts as a quantum dot [65]. The two types of NWs, cylinder-shaped and cone-shaped, are also found to coexist on this sample (under stoichiometric flux ratio conditions) as shown in Fig. 3.6. Note that some NWs, of both types, may kink during the growth of a CdTe insertion (not all of them) and that there are also 3D objects on the surface corresponding to Au droplets that have not succeeded to catalyze a well formed-vertical NW. Again, here we confirmed that when a sample is grown using the same recipe as the sample shown in Fig. 3.6 but only changing to Te-rich flux ratio conditions, we do not observed cylinder-shaped NWs, only cone-shaped NWs are present (sample shown in Figure 3.7).

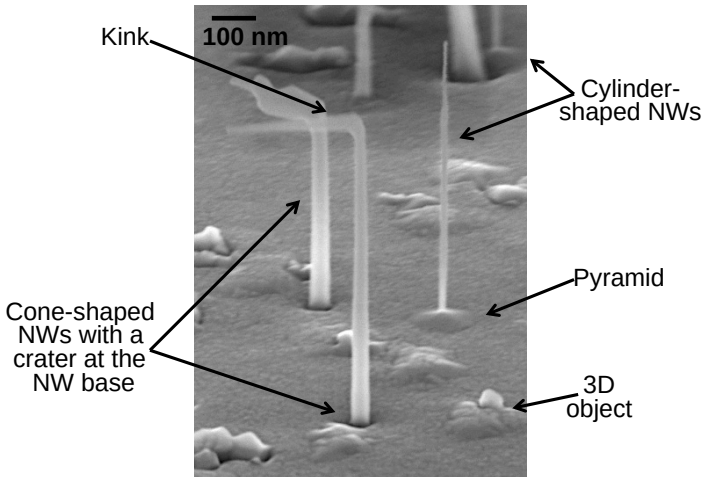

Figure 3.6 – SEM image of ZnTe NWs with a CdTe insertions grown under stoichiometric flux conditions. Cone-shaped NWs and cylinder-shaped NWs are observed on the sample and are indicated on the image. We also observed other objects crumbling on the surface, they are indicated as "3D objects".

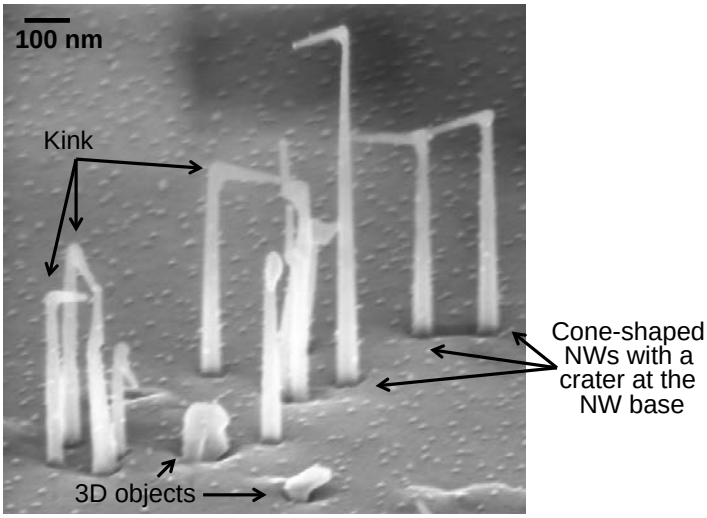

Figure 3.7 – SEM image of ZnTe NWs with a CdTe insertions grown under Te-rich flux conditions. Only cone-shaped NWs are observed on the sample (no cylinder-shaped NWs). We also observed objects crumbling on the surface, they are indicated as "3D objects".

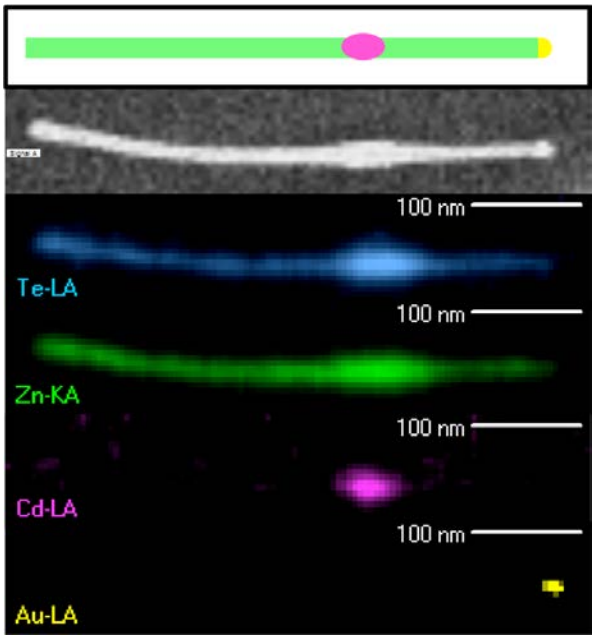

Figure 3.8 – Energy-dispersive-X-ray spectroscopy map of a cylinder-shaped ZnTe NW with a CdTe insertion. The Te, Zn, Cd and Au distribution are obtained from the intensity of the Lα or Kα lines as indicated.

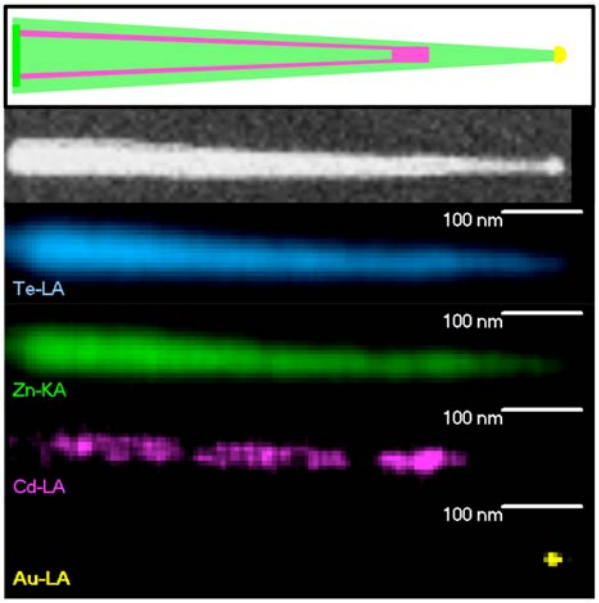

Figure 3.9 – Energy-dispersive-X-ray spectroscopy map of a cone-shaped ZnTe NW with a CdTe insertion. The Te, Zn, Cd and Au distribution are obtained from the intensity of the Lα or Kα lines as indicated.

The EDX maps coupled to a SEM were performed for a cylinder-shaped NW (Fig. 3.8) and a cone-shaped NW (Fig. 3.9). The distribution of Te, Zn, Cd and Au on the NW is shown. The localization of Cd along the NW is strikingly different depending on the type of NW. Cd is detected only at the position of the CdTe insertion for the cylinder-shaped NWs, whereas it is detected also along the lower part of the NW up to the CdTe insertion in cone-shaped NWs.

These EDX maps are a useful tool to illustrate the distribution of an element along the NW. Nevertheless, they must be taken with precaution. In these type of images, the intensity of each color is independent for each element: the intensity of the colors of the image is not normalized. This means that the intensity of each element can be adjusted independently, hence the threshold to observe the presence -or not- of an element is different for each element[3]. In conclusion, we need to remember that these images are not quantitative: the intensity observed is not related to the concentration of one element with respect to another. It only indicates the presence -or not- of a certain element in a certain position. Also, the intensity is proportional to the irradiated volume, as a consequence it is normal to observe brighter intensity when the NW is thicker. For example, in Fig. 3.9 we see that for Te or Zn, the intensity is higher at the base of the NW (the thicker part) than near the Au droplet (the thinner part).

A better resolution, of the order of 1 nm, can be obtained by performing EDX maps coupled to a S/TEM. This technique was used to study thicker cone-shaped NWs from a sample grown under Te rich conditions (same growth temperature and growth time). A SEM image of this sample is shown in chapter 4 in Fig. 4.3. As expected, all the NWs are cone-shaped. The EDX image of a typical NW of this new sample is shown in Fig. 3.10. We observe from right to left: the tip of the NW with a Au-catalyst in yellow[4]; then the NW diameter gets thicker and we observed a pure ZnTe section (in green) that finishes after a change in the growth direction (kink). More to the left, the composition map clearly reveals a CdTe insertion (in pink) surrounded by a ZnTe shell. In this part the diameter of the NW decreases. For the rest of the NW (to the left of the CdTe insertion), we observe a core of ZnTe surrounded by a Cd-rich inner shell surrounded by a ZnTe exterior shell. Once more we observe that the diameter of the NW increases when moving farther from the CdTe insertion. Keep in mind, that the image presented is a projection of the structure of the NW in a plane. Hence, we observe the response from electrons going through a complex core-shell structure as illustrated in the upper part of Fig. 3.10.

[3]Quantitative results of the EDX maps will be presented in chapter 4.

[4]Note that, we do not detect a peak associated to the presence of Ga in the spectra taken at the position of the Au catalyst particle. Additionally, Au is not detected anywhere else that in the tip of the NW.

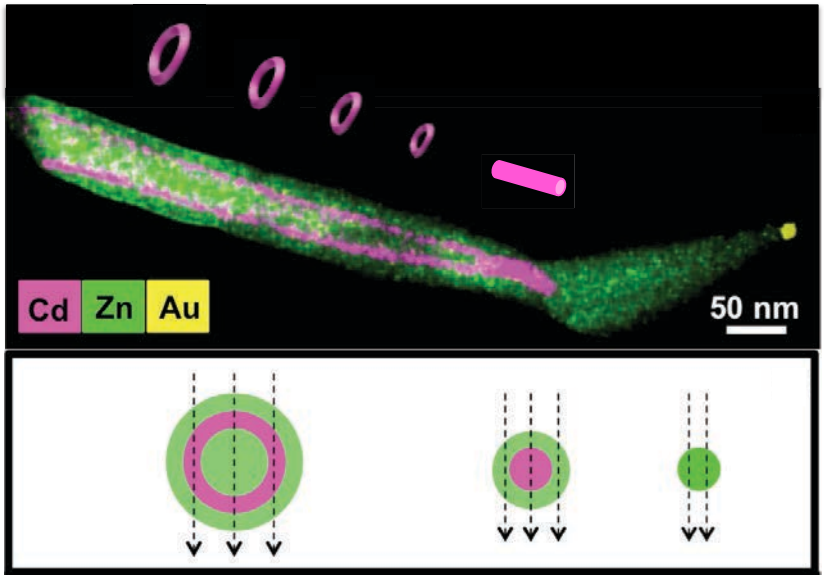

Figure 3.10 – Energy-dispersive-X-ray spectroscopy image showing the Cd, Te and Au content of a kinked cone-shaped ZnTe NW with a CdTe insertion. Above the EDX image, a representation of the Cd-rich segments of the NW are indicated: the QD as a compact cylinder and an inner Cd-rich shell as spherical rings. Slices of this structure are also represented below the EDX image.

Many of the NWs grown on the sample,but not all, present a kink located at 150-300 nm from the tip (SEM image of the sample surface is presented in Fig. 4.3). Note that the change in growth direction takes place just after the CdTe insertion has been grown. A possible relationship between the insertion of a different material and the formation of a kink is not fully understood [58]. Some authors have also reported kinking in Si NWs grown by chemical vapor deposition, induced by changes of the growth conditions, such as a temperature gradient [66] or a change in the total pressure [67,68].

Nevertheless, the shape of the NW follows a clear cone-shaped trend from the base to the CdTe insertion. Since the growth direction changes, the NW shape also changes. It is reasonable to observe a thicker part (higher diameter) after the direction has changed due to an inhomogeneous impinging flux: there are more atoms arriving to one side of the NW than to the other (see Fig. 3.11). This causes not only a higher lateral growth of ZnTe at one side of the NW but also a shadowing effect. The effect of the shadow of the upper part of the NW on the lower part clearly manifest in two ways: a) the ZnTe shell at the level of the QD and b) the Cd rich inner shells are both thinner from one side of the NW than from the other. A quantitative analysis of this effect will be developed in chapter 4.

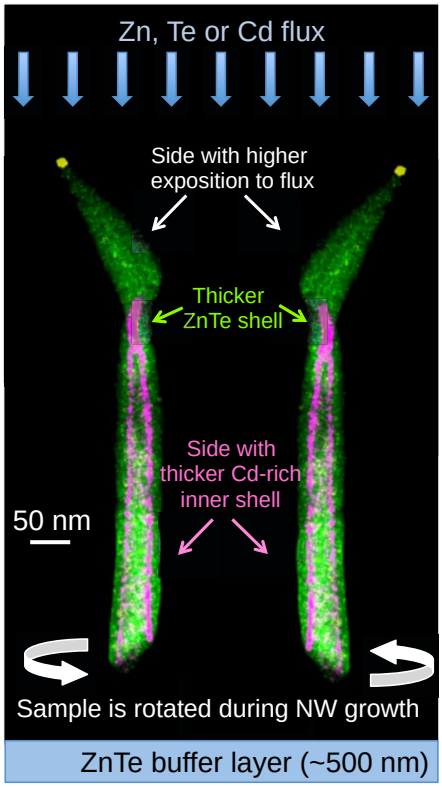

Figure 3.11 – Schema showing the side of the NW exposed to a higher flux due to the kinking of the NW. The NW is represented using a EDX-TEM map.

The EDX images (showing the presence of CdTe below the insertion, in the form of an inner-shell, and also of a ZnTe outer shell) demonstrate that lateral growth of CdTe and ZnTe takes place on the cone-shaped NWs, while it is not the case on the cylinder-shaped NWs. These results clearly indicate a distinct growth mechanism between the two types of NWs, where only cone-shape NWs present lateral growth.

3.4.2 Crystal structure of the nanowires

High Resolution TEM (HRTEM) images were realized on both types of ZnTe NWs. We found that the cone-shaped NWs have a cubic zinc-blende structure (shown in Fig. 3.12) and that the majority of them are oriented along the $\langle 111 \rangle$ axis. Some cone-shaped NWs are defect free but most of them feature twins, as frequently observed in $\langle 111 \rangle$ oriented NWs. Many of these twins are perpendicular to the $\langle 111 \rangle$ NW axis, but some are on $\{111\}$ diagonal planes as shown in Fig. 3.12b. Very few cone-shaped NWs have a short WZ section embedded in the ZB phase. Note that the Au particles no longer has a half-spherical shape but an almost complete spherical shape. This leads to a narrow contact area (diameter $\sim$ 8 nm) between the NW and the Au particle.

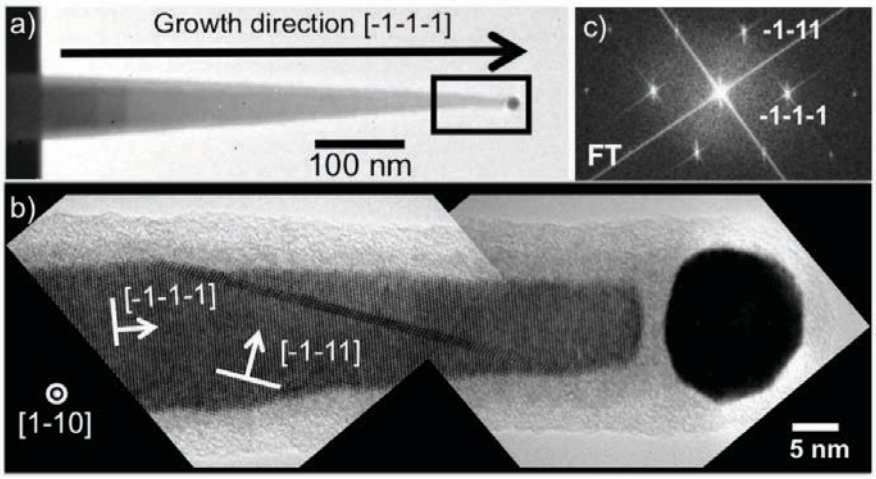

Figure 3.12 – a) Low magnification and b) High Resolution TEM image of a cone-shaped ZnTe NW grown for 30 min under stoichiometric growth conditions. The crystal structure is zinc-blende. A pair of twins along the (-1-11) plane (diagonal plane to the growth axis) is clearly visible. c) Fourier transform of b). Courtesy of R. Vigliaturo and M. den Hertog.

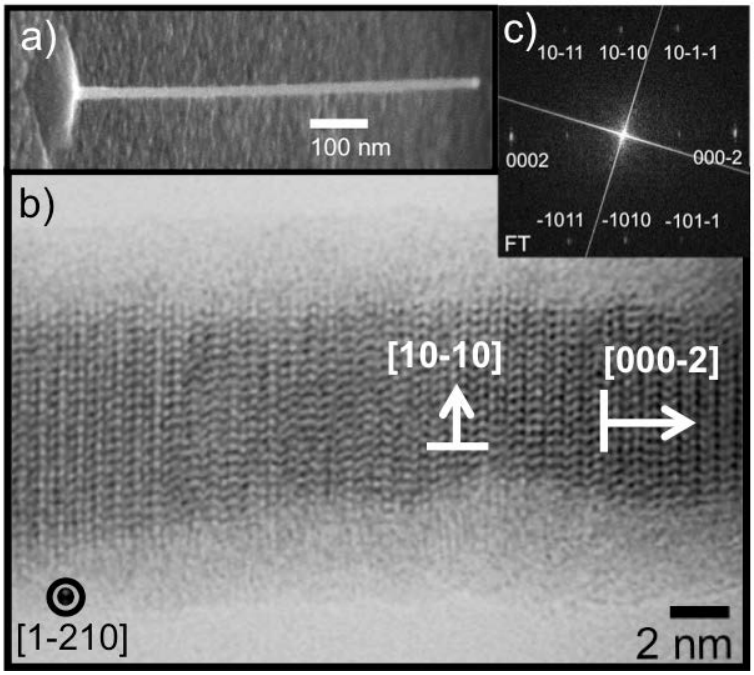

Figure 3.13 – a) SEM and b) Bright field (BF) STEM image of a cylinder-shaped ZnTe NW grown under stoichiometric flux conditions. The crystal structure is wurtzite and we observed no stacking faults. c) Fourier transform of b).

In contrast, cylinder-shaped NWs have a homogeneous hexagonal wurtzite crystal structure (shown in Fig. 3.13). These NWs are mostly defect-free or with a very small number of stacking faults. Note that ZnTe NWs are proned to beam damage, especially the cylinder-type due to their very small diameter, and can easily move under the beam due to charging effects. In spite of these difficulties, more than 10 NWs (of each type) were observed.

3.4.3 NW polarity

High-Angle Annular Dark-Field (HAADF) STEM measurements were performed to determine the polarity ($< 111 >$A or $< 111 >$B) of each type of ZnTe NWs. The more heavy element (Te with Z=52) scatters more electrons on the annular HAADF detector and appears therefore brighter in the HAADF STEM image than the lighter element (Zn with Z=30), providing a chemical contrast that allows identification of Te and Zn columns respectively in the HAADF STEM image. Therefore, this technique allows to reveal the orientation of the Zn-Te dumbbell, where for $< 111 >$B the heaviest atom (Te) is up along the growth axis in the dumbbell. The results are shown in Fig.3.14 for a cone-shaped NW (and it's substrate) and in Fig. 3.15 for a cylinder-shaped NW (including its pyramid and the substrate). All presented STEM images are raw data and no filtering or image processing was done.

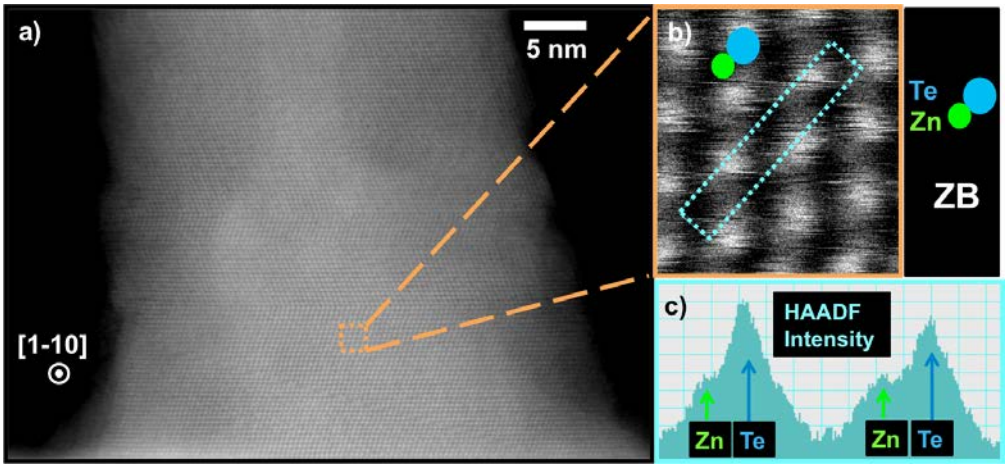

Figure 3.14 – HAADF STEM images of a cone-shaped NW. a) HAADF STEM of a cone-shaped NW. Twins perpendicular to the ⟨111⟩ direction are visible. b) Zoom on the marked region in a. The inset identifies the atoms in the image. c) Intensity profile along the marked box in b. We observed that the polarity found is Te-ended along the growth axis.

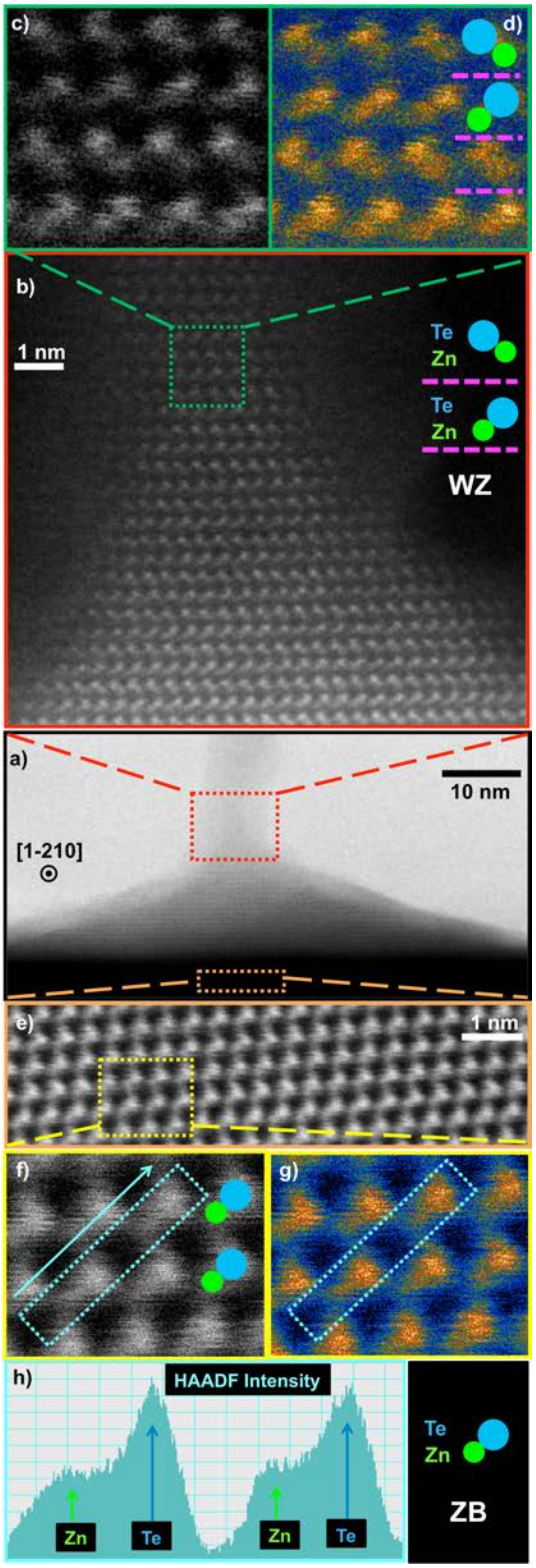

Figure 3.15 – STEM images of a cylinder-shaped NW. a) BF STEM of the ZnTe buffer layer, the pyramid and the lower part of a cylinder-shaped NW. b) HAADF STEM zoom on the region marked with a red rectangle in a. The inset identifies the atoms in the image. c) Zoom on the marked region in b in gray scale and d) in color scale with the indicated atomic structure. We have illustrated the Zn (in green) and Te (in blue) atomic columns. e) HAADF STEM zoom on the region marked with the orange rectangle in a. f) Zoom on the marked region in e) in gray scale with the indicated atomic structure and g) in color scale. h) Intensity profile along the marked box in f). The inset identifies the atoms in the image.

As shown in Figure 3.14, the polarity of the cone-shaped NWs remains Te polar. A zoom of the ZnTe lattice is presented in Fig.3.14b along with its corresponding HAADF intensity profile in Fig.3.14c.

Figure 3.15 shows the results for a cylinder-shaped NW. The central image, Fig.3.15a, is a bright field STEM image where the pyramidal base is clearly visible. Fig.3.15b is a zoom of the area marked in red, which contains the base of the NW and the top of the pyramid. Fig.3.15c and d are a closer zoom of the Zn-Te lattice where we can clearly distinguish both Zn and Te columns in the zone marked in green, both in grey and in color scale. These HAADF STEM images show that the polarity is Te-ended along the growth axis, and that it does not change at the intersection between the pyramid and the NW. The polarity is the same for the ZnTe buffer layer, the pyramid and the cylinder-shaped NW (Fig.3.15 e-g). An HAADF STEM intensity profile shown in Fig.3.15h confirms our results: substrate, pyramid and cylinder-shaped NW are Te-polar (Te facing the growth direction, which is the $[\bar{1}\,\bar{1}\,\bar{1}]$ axis of the substrate: $<111>$B oriented).

Clearly there is no polarity inversion for ZnTe NWs. Whatever the crystal structure, both NWs and substrate are Te-polar. These results agree with those previously observed [69] on ZnTe NWs. They completely differ from cylinder-shaped ZnO NWs grown by metalorganic vapor phase epitaxy over O-polar ZnO substrates. Like the present ZnTe NWs, these ZnO NWs have the wurtzite structure and feature a pyramid at their base. In that case however, the pyramids are O-polar whereas the NWs are Zn-polar [70].

3.4.4 Discussion

To summarize, we observe two types of ZnTe NWs: (1) cone-shaped NWs, with zinc-blende structure, with the presence of a crater at the base, and the occurrence of lateral growth as confirmed using a CdTe insertion; (2) cylinder-shaped NWs, with wurtzite structure, with a pyramid at the base, and no lateral growth detected. In both cases the polarity is identical to that of the (111)B buffer layer. Both types of NWs are grown simultaneously under stoichiometric ZnTe flux and can be found homogeneously distributed over the same sample. Notice that increasing the Te/Zn flux ratio progressively suppresses the formation of cylinder-shaped NWs and decreasing Te/Zn flux completely inhibits the growth of (any type) of NW.

Different crystallographic structures have been reported for both III-V and II-VI semiconductor NWs, and relations between the NW crystal structure and other growth parameters have been proposed. A connection between the NW diameter and the crys-

tal phase was shown for GaAs and InAs NWs [71,72]. In these studies, the NW diameter is determined by the diameter of the gold droplet. In general, NWs with a large diameter have the zinc-blende structure, as in bulk, albeit with twins or even wurtzite inclusions, whereas those with a small diameter tend to have the wurtzite structure. The contribution from the lateral surface energy to the total free energy can determine the crystal phase: in narrow NWs, the low energy of the facets in the wurtzite structure can compensate for a higher bulk energy [73].

Nucleation models have been proposed which take into account the influence of the sidewall surface reconstruction on the NW crystal phase [73] or relate the crystallographic phase of the NWs to the interface energies involved in the formation of 2D nuclei at the vapor-liquid-solid triple phase line [74].

In the present case, the size of the gold droplet, and hence the NW diameter in the initial stage of growth, spans a rather narrow range on each sample, identical for all samples described here. We never observed a bi-modal distribution of these diameters, and both cone-shaped and cylinder-shaped NWs are found over the whole range of gold droplets diameters. Hence the growth conditions of Fig. 3.3c - low growth temperature and stoichiometric flux - are those for which the two growth modes coexist for this range of droplet diameters.

With that in mind, we can point out that we observe a clear relation between the crystallographic phase of the NWs and the presence - or not - of lateral growth. We observe radial growth only on ZB NWs (cone-shaped), never on WZ (cylinder-shaped) NWs. This behavior has been also observed for the growth of an InAs shell over GaAs NWs containing both ZB and WZ sections. T. Rieger and al. [75] showed that the shell will only grow over the ZB parts of the NW. This point will be fourthly discussed in chapter 4 where the growth of ZnTe/ZnMgTe core-shell NWs will be addressed. Moreover, spacial correlations between ZB and WZ segments in the same NW have been demonstrated for III-V NWs [76]. They suggest a short range interaction between the newly formed ML and the underlying MLs which influence stacking during growth. They propose to model that interaction within the classical nucleation theory. In that case, the step energy of the 2D nucleus not only depends on the structure (cubic or hexagonal) of the nuclei but also, on the crystal structure of the preceding MLs.

Nevertheless, surface energies may play a role in favoring the formation of only zinc-blende NWs under a strong Te excess. A similar trend was observed in arsenide NWs grown under As excess [73]. The nucleation mechanism involves the supersaturation in the gold droplet: the supersaturation in Zn and Te is governed by the diffusion rate of each species on the substrate and on the sidewalls.

3.5 Early stages of the nanowire growth

To understand the formation of different types of ZnTe NWs, we investigated the morphological evolution of the NWs with growth time. The idea is to observe the different stages, in particular the beginning, of the formation of nanowires by interrupting the NW growth at short growth times (t_{growth}). We have grown a set of 6 samples, 2 of them are grown during only 2 min, 2 other for 10 minutes and finally, the 2 remaining are "control-samples" grown for 30 min (same time as previous samples). From each pair of samples, one is grown under Te-rich conditions (Te/Zn:2/1) and the other under stoichiometric flux ratio (Te/Zn:1/1). The Au deposition and dewetting conditions were: $T_{Au} = 1090$°C and $t_{Au} = 40$ s, $T_{dew} = 350$°C and $t_{dew} = 10$ min. The growth temperature was kept at 350°C. SEM images of these 6 samples are presented in Figure 3.16.

This set of samples allowed us to observe three clearly different stages in the growth of ZnTe NWs. After **2 min of growth**, the first signs of NW-growth started to appear (from both RHEED and SEM measurements). We observe no striking difference between the 2 min-samples grown under different flux ratio conditions. Furthermore, we see that only some of the Au particles start to catalyze ZnTe NWs (height > diameter) while the others remain in a half-sphere morphology (height $\sim$ diameter). This indicates the existence of an "incubating" time prior to the NW growth that is not equal for all Au particles. This is a relevant issue since it may explain why we observed a big NW-height dispersion.

For the **10 min-grown samples**, the formation of NWs is clearly visible. We observe different NWs on the two samples. The NWs observed when the growth is Te-rich, are already slightly cone-shaped while the majority of the NWs present on the stoichiometric-grown sample are not. Most of the NWs that we see in the images of the stoichiometric-grown sample have a cylinder-shape (diameter of the base of the NWs is the same as the diameter of the tip). We also observed in this sample the beginning of the formation of a pyramid under the cylinder-shaped NWs.

Finally, for the **30-min grown samples** the SEM images correspond to our previous observations. Under Te-rich conditions we observe only NWs with a clear conic shape. Whereas, under stoichiometric conditions two families of NWs are present: cone-shaped NWs with a crater at the base and cylinder-shaped NWs with a well-formed pyramid at the base. Again, we observe that both types of NWs are homogeneously distributed over the surface. Notice the enlargement of the pyramid from the 10 min to the 30 min-stoichiometric grown samples. This proofs that the pyramids are not formed prior the growth of cylinder-shaped NWs.

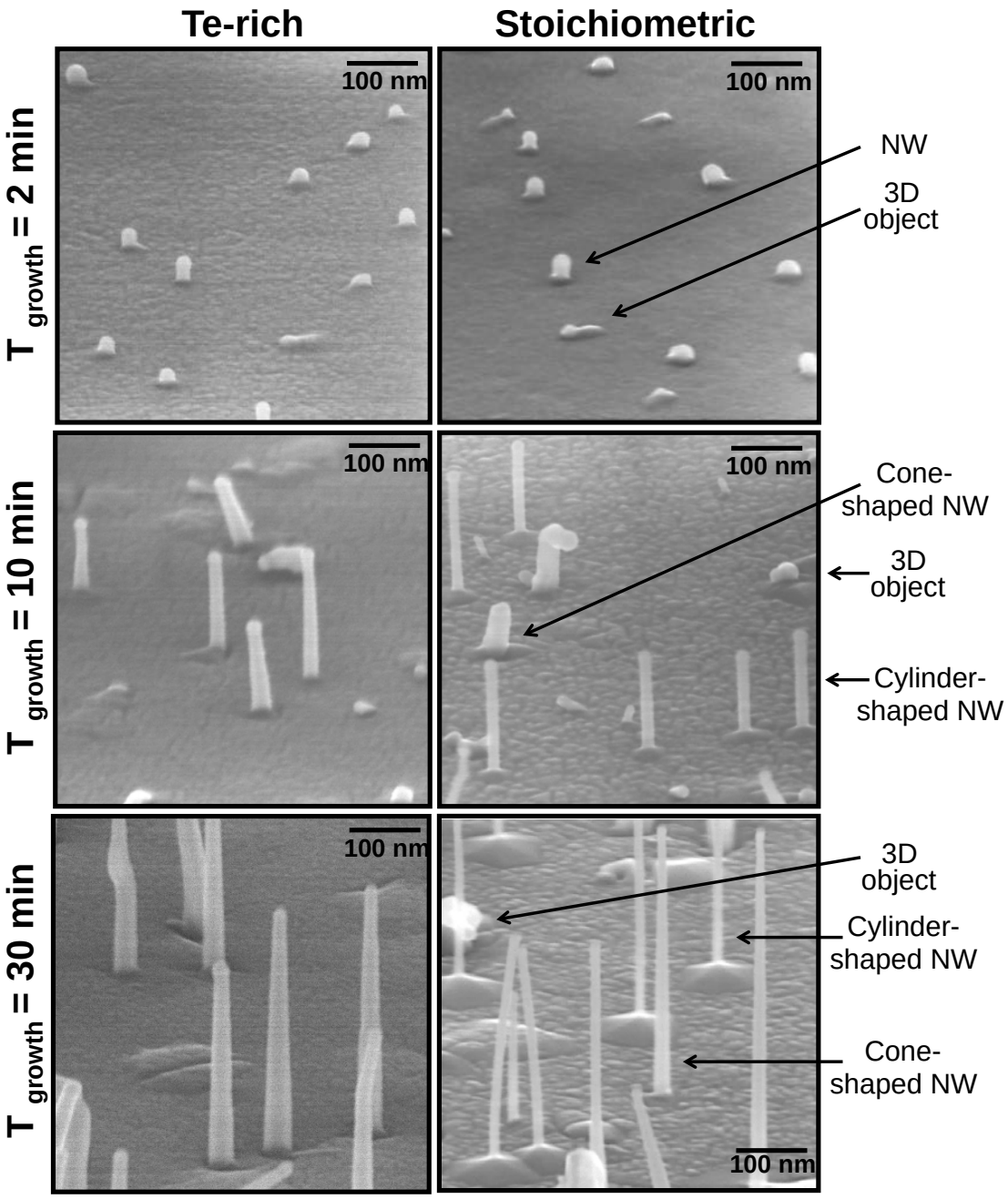

Figure 3.16 – SEM images of NW samples grown under Te-rich (first column) and stoichiometric (second column) flux ratio conditions and during different growth times: 2 min (first row), 10 min (second row) and 30 min (third row). All images have the same length scale.

In Table 3.3 the thickness of the 2D layer (buffer layer+ regrowth) for the 6 samples is presented.

	2D ZnTe layer	
t_{growth} (min)	Te rich	stoichiometric
2	195 ± 10 nm	255 ± 10 nm
10	260 ± 10 nm	250 ± 10 nm
30	360 ± 10 nm	310 ± 10 nm

Table 3.3 – Values of the 2D layer measured by SEM for the 6 samples presented in this section.

3.5.1 Surface densities

In Table 3.4, we present statistical results on the average density (ρ) for all the 6 samples shown in Fig. 3.16.

t_g (min)	VI/II ratio	$\rho_{\,totat}(\mu m^{-2})$	$\rho_{\,3D\ objects}$ (μm^{-2})	ρ_{NW} (μm^{-2})	
2	Te rich	36 ± 1	27 ± 1	9 ± 1	
2	stoichiometric	34 ± 1	23 ± 1	11 ± 1	
10	Te rich	36 ± 1	19 ± 3	17 ± 3	
10	stoichiometric	42 ± 2	21 ± 1	21 ± 1	
				cones	cylinders
30	Te rich	24 ± 3	6 ± 1	18 ± 2	0
30	stoichiometric	29± 3	11 ± 4	9 ± 2	8 ± 1

Table 3.4 – Population density of 6 different samples where the growth conditions (growth time and VI/II ratio) are varied. We present the density (average values ± standard deviations) of: total objects, 3D objects growing on the ZnTe layer, NWs or different type of NWs (cone or cylinder-shaped).

In Figure 3.17 we have plotted the results presented in Table 3.4. We count independently: 1) the density of 3D objects growing over the ZnTe layer (objects emerging from Au droplets that do not catalyze NWs or other) and 2) the density of NWs (different types of NWs are also counted separately if present on the sample). The total density is the sum of these two parts. All densities are calculated by counting the number of objects (3D or NWs) over one image and then dividing this number by the surface of that image. In general, we use SEM images with a magnification suitable to observe around 100 objects by image. This calculation is performed for 3 to 8 images. These are taken over different zones of the sample to observe differences on the homogeneity of the samples (but never very close to the edges of the sample). The

densities presented in Table 3.4 and in Fig. 3.17 are the average values of the densities calculated for single images and the error is the standard deviation of the average value.

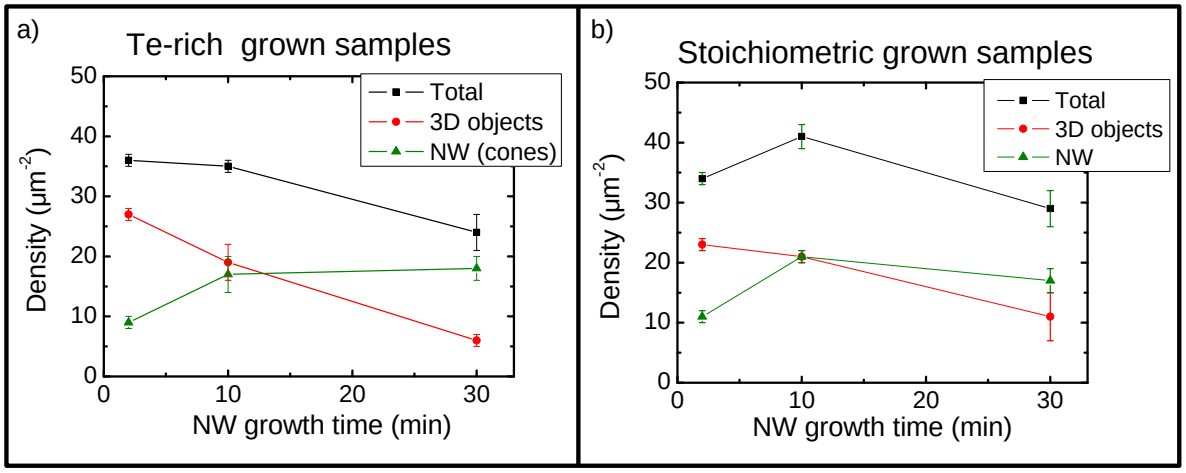

Figure 3.17 – Plot of the density statistics presented in Table 3.4. Density (total, NW and 3D objects on the layer) versus the growth temperature at a) Te-rich and b) stoichiometric flux ratio conditions.

We observe that the total densities are very close for samples grown for 2 and 10 minutes. For the 30 min-grown samples, the total density values are clearly smaller than for lower growth times, but nevertheless close for both samples. This means that there is a large part of the initial Au particles (around 25-30%) that are no longer visible after 30 min of growth (neither on the surface nor at the tip of a NW). Probably the Au particles that do not catalyze the growth of a NWs or other type of 3D objects were buried in the 2D ZnTe layer that grows at the same time, and in between, the NWs. This behavior is independent of the flux ratio conditions.

Another important point that should be mentioned when analyzing closely the proportion of NWs with respect to other 3D objects, is that the percentage of NWs (from the total density) increases with t_{growth}. For both samples grown at $t_{growth} = 2$ min, we see that the population is divided in: 1/3 NWs and 2/3 other 3D objects (Au particles that have not yet - or will not - catalyze a NW). When increasing t_{growth} to 10 min, this proportion changes (for both samples): more NWs are catalyzed and we observe 1/2 of NWs and 1/2 of 3D-objects. Finally, at $t_{growth} = 30$ min, we observe (again for both samples) that the NWs proportion has continued to increase up to: roughly 2/3 of NWs and only 1/3 of 3D objects. In summary, after 30 min of growth: 30% of Au particles have disappeared, 20% have become some kind of 3D objects and 50 % end up being NWs. This means that half of the initial Au droplets will not lead to the growth of NWs.

Beside this, we observe no cylinder-shaped NWs in the samples grown under Te-rich conditions (as expected) and 1/2 of cone-shaped - 1/2 of cylinder-shaped NWs on the 30 min-stoichiometric sample. This is a different result from the sample presented in Fig. 3.3c, where only 20% of the NWs were cylinder-shaped. Keep in mind that the Au deposition and dewetting conditions are slightly different, but more importantly, that the treatment to smooth the ZnTe buffer layer before the Au deposition was modified. In section 2.4.3, we demonstrated that the smoothening process performed over the samples shown in Fig. 3.3 was not optimal. This step in the growth process was then optimized to decrease the roughness of the ZnTe layer by exposing it to a Te flux while decreasing the sample temperature from 420°C to 300°C (previously the Te flux was cut off at 380°C). This improved smoothing method was used during the growth of the 2D layer for the set of samples presented in Fig. 3.16. This difference may explain why the percentage of cylinder-shape NWs augmented from 20 to 50 %. It surely indicates that the proportion of one type of NW with respect to the other is linked to the quality of the 2D buffer layer (better diffusion of adatoms).

3.5.2 Morphological characteristics of the NWs

In the following paragraphs, we discuss the informations we obtained by performing a statistical analysis of the morphology of the objects observed on the 6 samples shown in Figure 3.16. The height, the diameter at the base and at the tip (Au-diameter) are measured for each NW, from SEM images taken at high magnification, and then the average value is calculated with its corresponding standard deviation. In Table 3.5, we present statistical results on the morphological characteristics of the NWs and in Fig. 3.18 and Fig. 3.19, we show histograms of the height of the objects measured on the samples grown with Te-rich and stoichiometric flux ratio conditions for $t_{growth} = 2, 10, 30$.

- *Samples grown for 2 min:*

  When we compare the 2 min-samples, we observe objects with the same average height and the same diameter. This shows that, at this point of the growth process, there is no observable distinction between the Au-particles that will catalyze one or the other type of NW. For each sample, the height and diameter are very similar between them. Comparing with the results obtained in chapter 2, the average diameter is in the range that we expected (20-30 nm). Nevertheless, there is a high diameter and height dispersion for both samples. This corresponds to the fact that we have two kinds of populations on these samples: some "flatter" particles (low height and high diameter, in red in Fig. 3.18 and Fig. 3.19) and some other particles that are more "NW-typed" (higher height than diameter, in

t_g (min)	VI/II ratio	height (nm)		diameter (nm)			
2	Te rich	24 ± 10		25 ± 5			
2	stoichio.	27 ± 11		26 ± 7			
				Au		NW base	
10	Te rich	123 ± 59		19 ± 4		19 ± 4	
10	stoichio.	138 ± 63		19 ± 3		18 ± 4	
		cone	cylinder	cone	cylinder	cone	cylinder
30	Te rich	372 ± 93	–	18 ± 3	–	37 ± 7	–
30	stoichio.	600 ± 200	444 ± 47	16 ± 8	16 ± 2	38 ± 16	16 ± 2

Table 3.5 – Size statistics from the 6 different samples of Fig. 3.16 where the growth time and VI/II flux ratio were varied. Average values ± standard deviations of the NW height, diameter of the NWs base and of the Au droplets for cone and cylinder-shaped NWs. Note that for the 2 min-samples the statistics were performed over all the objects.

purple and yellow in Fig. 3.18 and in black in Fig. 3.19). We observe quite clearly the existence of at least 2 populations (for both 2 min-samples): one is centered at 20-25 nm and the other around 45 nm.

- *Samples grown for 10 min:*

  The height statistics of the 10 min-grown samples show that the NWs have been successfully catalyzed and that the average values and distribution of NW height for both samples are very close. This means that on average the NWs of both samples are growing at the same rate for the first 10 minutes. We observe a clear change from the histograms of the 2 min samples to the 10 min samples. For the Te-rich sample, we no longer see two separate populations, but we observe a very broad single distribution [$0 < H < 275$ nm]. Among this broad distribution, we can find 3D objects (low height, marked in red) and NWs of all heights between 50 and 300 nm (with a large majority of NWs between 50 and 175 nm). As an example, in the SEM image in Fig. 3.18, we marked the shorter NWs in purple and the longer ones in yellow. The broad single distribution can be explained by the fact that more NWs were catalyzed during the 8 minutes of additional growth (we observed in Table 3.4 that the NW density was double).

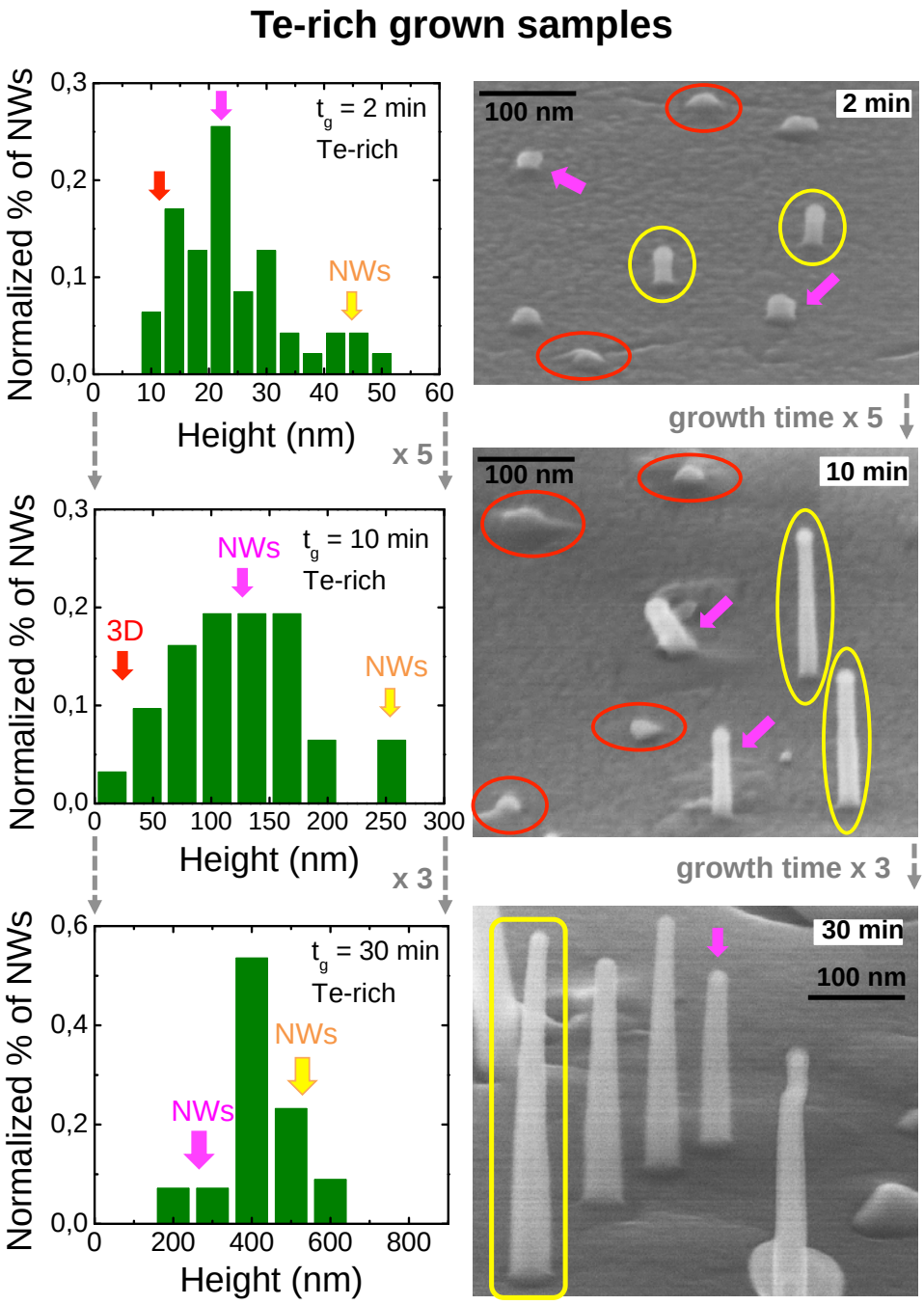

Figure 3.18 – Height histograms of samples grown at Te-rich flux conditions (Fig. 3.16 on the left column). Height statistics of three different samples are presented: $t_{growth} = 2$ min, $t_{growth} = 10$ min and $t_{growth} = 30$ min. For each samples, one SEM image is shown illustrating the different objects. We marked in red the 3D objects (low height) that are mostly present in the samples grown for 2 and 10 min. For the samples grown for 30 min, the statistics were performed only on vertical NWs. Cone-shaped NWs are marked in purple (lower height) and in yellow (higher height).

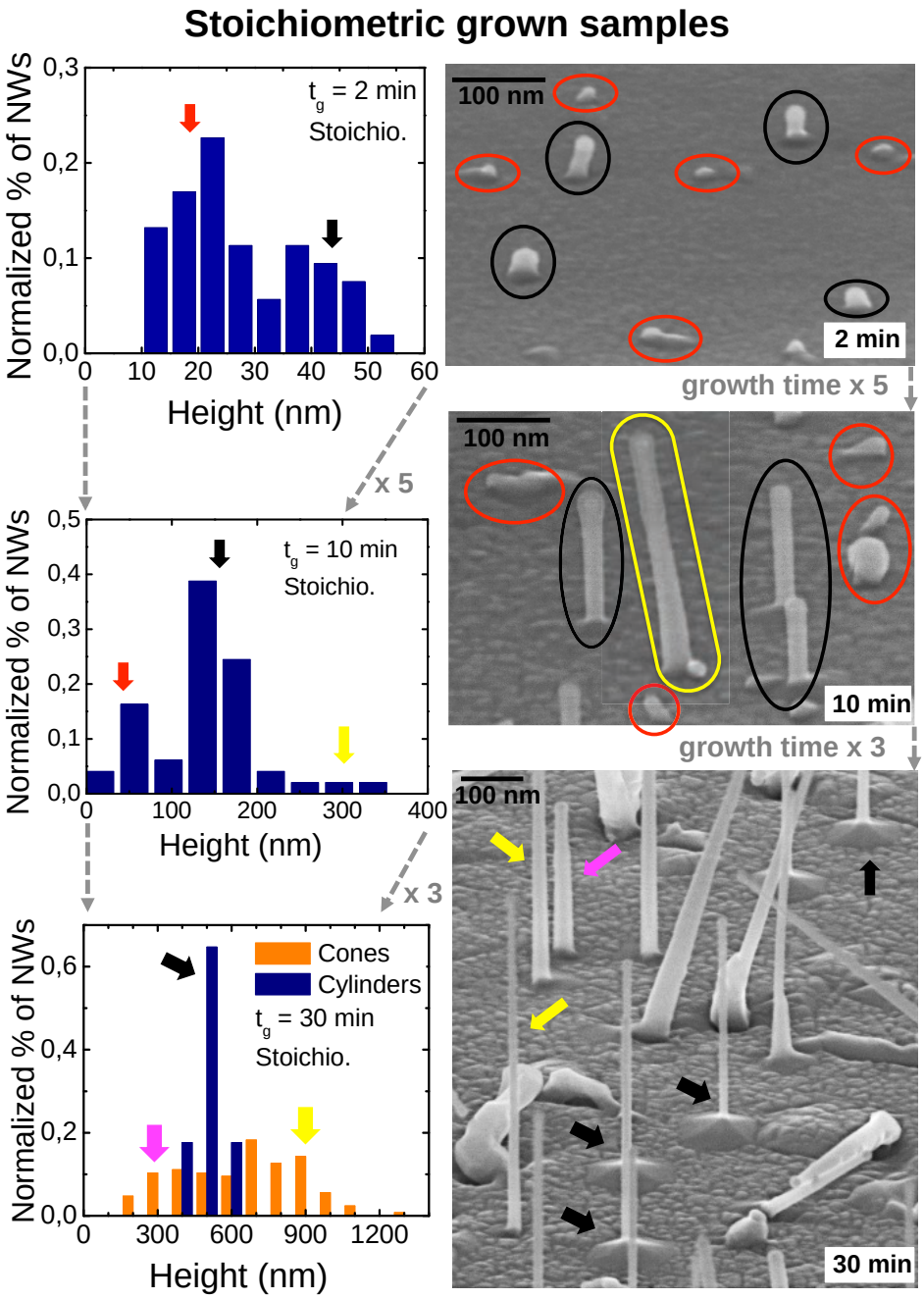

Figure 3.19 – Height histograms of samples grown at stoichiometric flux conditions (Fig. 3.16 on the right column). Height statistics of three different samples are presented: $t_{growth} = 2$ min, $t_{growth} = 10$ min and $t_{growth} = 30$ min. For each samples, one SEM image is shown illustrating the different objects. We marked in red the 3D objects (low height) that are mostly present in the samples grown for 2 and 10 min. Cone-shaped NWs are marked in purple (low height values) and in yellow (high height values). Cylinder-shaped NWs are marked in black.

For the 10 min-stoichiometric-grown sample, we also see a broadening of the height distribution [$0 < H < 350$ nm], but we clearly observe 2 peaks in the distribution: one centered at 50 nm and the other at 150 nm. Again, in the SEM image 3D objects are marked in red and the NWs corresponding to the peak at 150 nm in purple. Additionally, we observe some NWs in the [$275 < H < 350$ nm] range of heights (marked in yellow), that we do not observe on the Te-rich sample. At $t_{growth} = 10$ min, the average values of the diameter at the NW base and at the NW tip are the same (for both samples). This means that at $t_{growth} = 10$ min, we cannot observe from the measurements performed on the SEM images, *on average*, two morphologically different populations. Nevertheless, when we observe the NWs on the SEM images (Fig. 3.16), we verify that some of the NWs from the 10 min-Te-rich samples are slightly cone-shaped whereas the NWs from the stoichiometric-sample are not. Additionally, we observe that for the stoichiometric-sample, it is possible to distinguish a pyramid at the base of some nanowires (the cylinder-shaped ones).

- *Samples grown for 30 min:*

  Statistics on the 30 min-growth samples show a clear difference in the average height of the NWs present on the Te-rich sample (cone-shaped) and the 2 types of NWs present on the stoichiometric sample (Table 3.5). On average, the cone-shaped NWs grown at stoichiometric conditions are the longest (exactly like what we have presented previously in section 3.3). The cone-shaped NWs are on average ~ 200 nm longer when they are grown at stoichiometric flux ratio conditions than at Te-rich conditions. They are also longer than the cylinder-shaped NWs grown over the same sample. The average height values of the cylinders is 150 nm lower than the average height values for the cones of the same sample but still 80 nm longer than the cones from the Te-rich sample.

  Since the height distribution of the NWs is very large, these results need to be compared to the height distributions of the three populations. In Fig. 3.20 these height distributions are plotted together. We observe that the information obtained by the average values does not represent completely the behavior of the height of the NW population. Indeed, the cylinder-shaped NWs (in blue) and the Te-rich cones (in green) have peaks in the distributions that are close (between 400-500 nm), but the cylinder-shaped NWs distribution is much narrower.

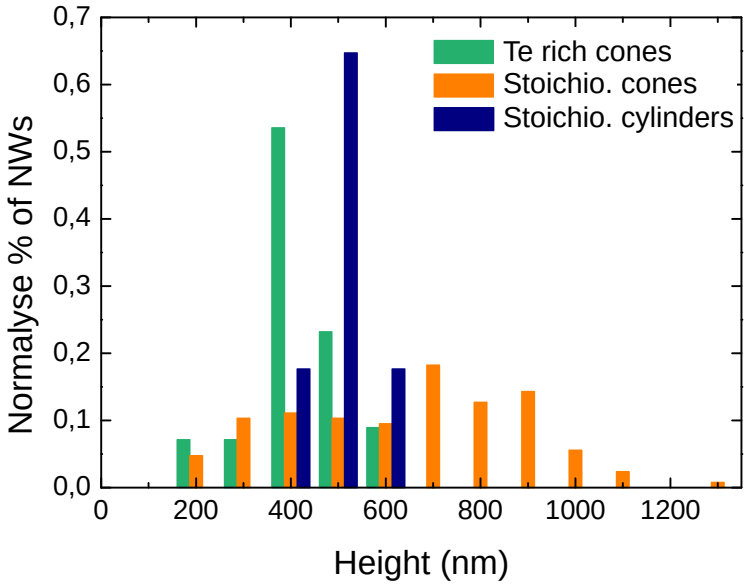

Figure 3.20 – Height histograms of the 2 NW samples grown at t_{growth} = 30 min presented in Fig. 3.16, one of them is grown at Te-rich and the other at stoichiometric flux conditions. We show independently the two types of NWs present on the stoichiometic sample.

The cone-shaped NWs grown in the stoichiometric sample (in orange) have a distribution that its extremely large (200-1300 nm) compared to the other two population of NWs. In general we can conclude that, under stoichiometric flux ratio conditions, the growth of cylinder-shaped (WZ) NWs starts quite easily while, a part of cone-shaped (ZB) NWs do not start to grow easily. The fact that some of the cone-shaped NWs seem to have a hard time to start growing under stoichiometric conditions explains why their height distribution is so big. Under Te-rich conditions, the (cone-shaped) NWs grow without problem from the beginning hence their height distribution after 30 min is much narrower than under stoichiometric conditions (but is still larger than for cylindrical NWs).

- *Statistics of the NW base and tip*

  In Fig. 3.21, we present the diameter at the base of the NWs versus the diameter at the tip. These statistics confirm that both cone-shaped NWs are tapered (Te-rich and stoichiometric flux ratio conditions correspond to the orange and green points respectively), since the base diameter is about the double of the tip diameter (at the level of the Au particle). For cylinder-shaped NWs, the diameter at the base and tip remains the same: their distribution (in blue) follows the black line at base diameter = Au diameter.

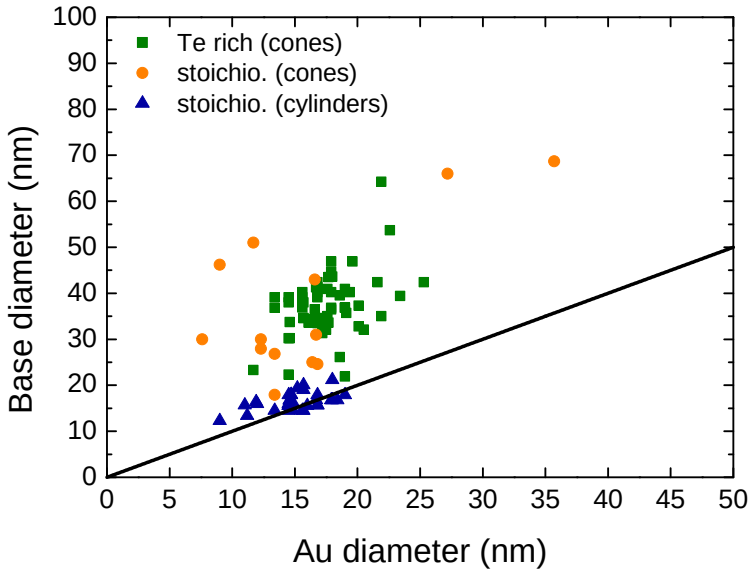

Figure 3.21 – NW base diameter versus diameter of the Au (at the NW tip) for samples presented in Fig. 3.16 and grown at $t_{growth} = 30$ min. We show independently the two types of NWs present on the stoichiometic sample. The black line corresponds indicates when the base diameter = Au diameter.

We clearly observe that the diameter of the Au particles for a large majority of NWs (cylinder and both Te-rich and stoichiometric cones) are in the [10-25 nm] range (same as presented before in section 3.3). This is a strong indication supporting the idea that the 2 types of NWs do not originate from Au droplets of different sizes. We have observed that the Au droplets are very similar for all the NWs, hence the existence of different types of NWs is probably not related to a different nucleation on the Au droplet, but more probably, to a different mobility of the adatoms on the surface.

Finally, we observe that the average diameter of the Au particles sitting on the NW's tip for the 30 min-grown samples (∼18 nm) is smaller than the average diameter of the Au particles measured on the sample grown for only 2 min (∼25 nm, see Table 3.5). This is a considerable difference since the change in the volume is proportional to the diameter^3. A possible explanation for this difference in diameter is the fact that Au droplets over ZnTe surface are formed as almost half-spheres (in chapter 2 we showed that $V_{catalyst} = 0.4 \pm 0.05 \times V_{complete\ sphere}$) while Au droplets at the tip of the NW may have a different shape. This is a reasonable explanation since the diameter of the Au catalyst is the same for the

samples grown during 10 and 30 minutes. We can compare: the volume of a $0.4 \times V_{complete\ sphere}$ with 25 nm of diameter is 3270 nm^3 and of a complete sphere with a diameter of 18 nm is 3060 nm^3. Given the error of the SEM measurements, the two volumes are very close. Hence, it is plausible that Au droplets at the tip of the NWs have a volume close to a complete sphere. In the TEM image of a cone-shaped NW presented in Fig. 3.12, we observe that the Au catalyst at the tip of the NW has a shape close to a complete sphere, which suggests that this explanation is probably correct. In figure 3.22, a scaled schema of three different cases is presented: the Au droplet over a ZnTe substrate, the Au droplet over a short NWs (2 min of growth time) and the Au droplet over a long NW. In the last case, the contact surface between the Au droplet and the NW has a diameter of 8 nm.

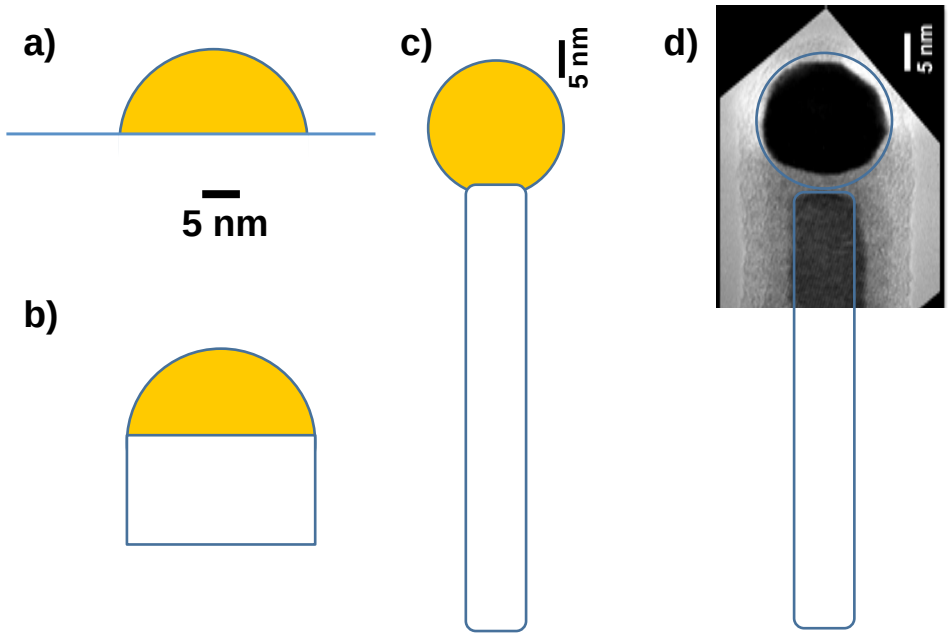

Figure 3.22 – a) Au particle with a volume of 0.4 × the volume of a complete sphere of 25 nm of diameter, over a flat 2D surface. b) Au particle at the tip of a short NW with the same volume as in a. The contact surface between the NW and the Au droplet is the same as in a. c) Au droplet at the tip of a long NW with a volume almost equal to a complete sphere of 18 nm of diameter. The diameter of the NW is 8 nm. d) Superposition of c and the TEM image of a cone-shaped NW (presented in Fig. 3.12).

From the evolution of the NW growth with time we can conclude that:

- Nearly 50% of the Au droplets formed on the surface do not give rise to nanowires.
- All nanowires do not start to growth at the same time. This effect is particularly evident for cone-shaped NW grown under stochiometric flux ratio conditions, where the distribution of the nanowire height after 30 minutes spreads from
  200 nm to 1.2 μm.
- Distinguishing cone-shaped NW from cylinder-shaped NW from the SEM images of the sample grown for 2 minutes is not possible, and it remains quite difficult for the sample grown for 10 minutes. A complementary TEM study to determine the crystal structure of the nanowires could provide valuable information.
- The shape of the Au catalyst particle seems to change from a nearly half-spherical volume at the beginning of the growth, to the volume of an almost complete sphere after 30 minutes of growth.

3.6 Influence of the temperature on the NW growth

In this section we will present preliminary results on the growth of ZnTe NWs at different growth temperatures. Until this point, we have explored the growth under different II/VI flux ratio conditions for a fixed NW growth temperature (T_{growth} = 350°C). As mentioned previously, this temperature was chosen to optimize the insertion of CdTe segments in the ZnTe NWs. However, now we will investigate the morphological evolution of the ZnTe NWs when increasing the growth temperature. The idea is to gain information on the growth mechanisms by observing the effect on the shape of the NWs when they are grown under conditions of faster surface diffusion and higher evaporation rates.

In Figure 3.23 we present SEM images of four different NW-samples. All of them start from a ZnTe buffer layer grown under the same conditions (described in section 2.2). The Au deposition and dewetting is also performed following the same recipe for all samples. The conditions were: T_{Au} = 1090°C, t_{Au} = 40 s, T_{dew} = 350°C and t_{dew} = 10min.

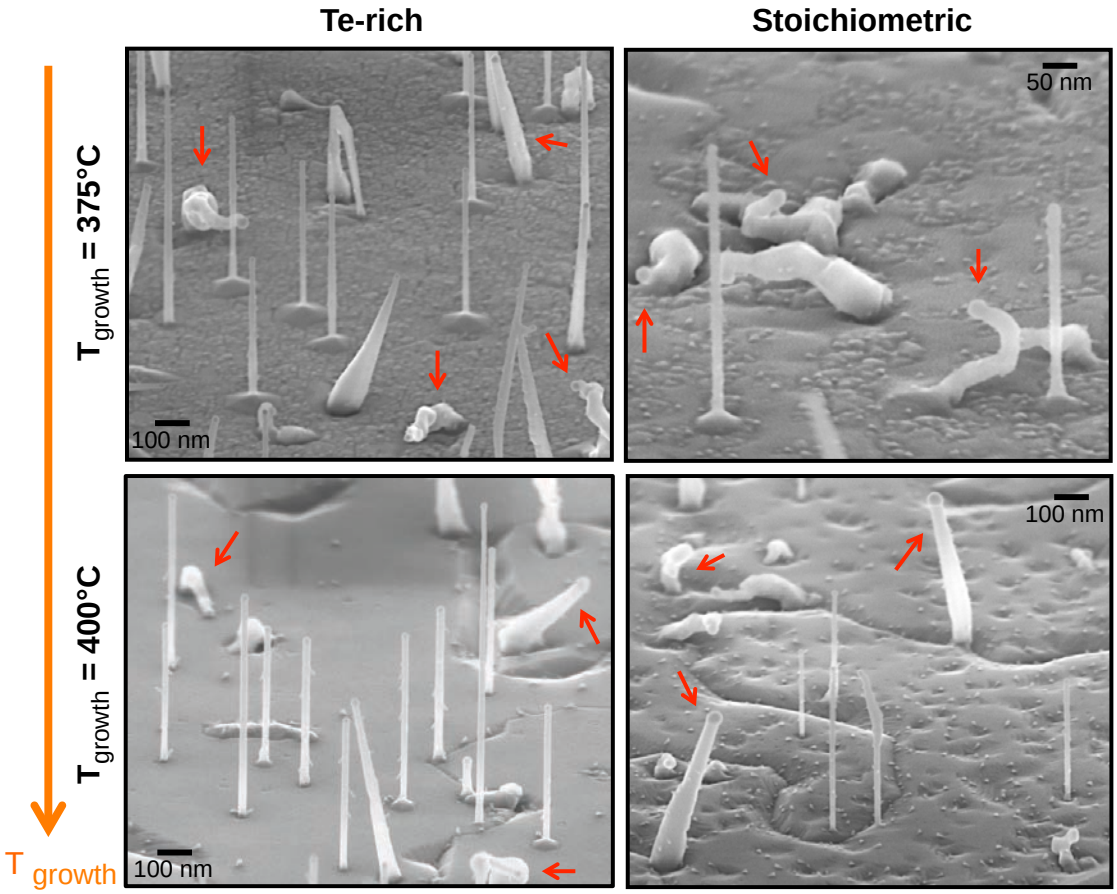

Figure 3.23 – SEM images of samples grown at $T_{growth} = 375°C$ and $T_{growth} = 400°C$ under both stoichiometric and Te rich conditions. Notice that the scale of the image of the sample grown at $T_{growth} = 375°C$ and stoichiometric conditions is twice bigger than the others.

To start the growth of NWs, the sample temperature was rapidly increased (ramp of 40°C per min) from the Au dewetting temperature up to the NW growth temperature, and immediately after, a ZnTe (or ZnTe+Te) flux was sent to the surface. Notice that we keep the dewetting temperature as before hoping that the size of the Au particles will remain similar. If the T_{dew} is increased, we will form Au droplets of higher diameter hence NWs with a diameter above our goal (see chapter 2). From the 4 samples of these set, we grew two of them at $T_{growth} = 375°C$ and the other two at $T_{growth} = 400°C$. For each pair of samples, one was grown under stoichiometric conditions (Te/Zn:1/1) and the other under Te-rich conditions (Te/Zn:2:1).

In figure 3.23, we clearly observe that the Au catalyst, at the tip of the NWs grown at higher temperatures, have very different sizes. This shows that it is not possible to keep a narrow distribution of Au droplets diameter by the process describe above. Even if the step where we have increased the temperature (to 375°C or to 400°C) was done very fast, and after 10 min of stabilization time at 350°C, we see that it is unavoidable to activate the dewetting process again and to obtain Au droplets of higher diameter. Nevertheless, since the NW growth started immediately after the sample reaches the NW growth temperature (without a stabilization time), some of the Au-catalyst remained in the $10 - 30$ nm range.

In general we observe that:

- There are vertical NWs, inclined NWs and 3D objects on the surface.
- Au-droplets with diameters below 30 nm catalyze vertical NWs. The density of vertical NWs decreases with the growth temperature, specially for the NWs grown under stoichiometric flux ratio conditions.
- Au-droplets with diameters above 30 nm catalyze inclined NWs or objects that remain crumbling near the surface. Clearly, under these conditions, the growth of NWs using Au particles of high diameter is unfavorable. This kind of NWs are indicated in red in figure 3.23 and will not be considered in the sample description that follows.

ZnTe NWs grown at 375°C

In the samples grown at 375°C, the NW diameter is in the 10-15 nm range. For most of the vertical NWs, the diameter at the base is nearly the same as the diameter at the tip. Formation of a pyramid at the base of the NW is observed for the two samples grown at 375°C.

The sample grown under **Te-rich conditions at 375°C** is similar to the sample grown previously under stoichiometric conditions at 350°C (presented in Figure 3.16). The growth of cylinder-shaped NWs and few cone-shaped NWs was observed. This indicates that the increase of the sample temperature is compensated by a higher Te flux. In other words, the fact that more Te atoms are evaporated from the surface (since it is a Te-ended surface) is balanced by a higher flux of Te atoms, then preserving similar growth conditions.

For the sample grown under **stoichiometric conditions at 375°C**, we observe that the density of vertical NWs is very low. There are few cylinder-shaped NWs. This is understandable since at a higher sample temperatures the evaporation rate is higher, hence there will be more Te atoms evaporating from the surface (surface type B). This makes the surface become Zn-rich which inhibits NW growth (shown in Figure 3.3d).

ZnTe NWs grown at 400°C

At T_{growth} = 400°C and under **Te-rich conditions**, the vertical nanowires exhibit a cylindrical shape, with a slightly higher diameter (in the 20-25 nm range) than the vertical nanowires described in the previous cases. Only a few of these nanowires show a pyramid at the base.

Again under **stoichiometric conditions**, the density of vertical NWs is very low. A few cylinder-shaped NWs of small diameter (10-15 nm range) are observed. As observed for samples grown at T_{growth} = 375°C, here we notice that the sample grown under Te rich conditions has more vertical well-formed NWs than the sample grown under stoichiometric conditions.

2D layer

The thickness of the buffer layer and the re-growth layer (growing between the NWs) are shown in Table 3.6 for the four samples presented on figure 3.23. These values are obtained from SEM images taken from the side (90° tilt from the top view). Keep in mind that this measurements are not very precise due to the low magnification of the SEM images used. The values of the buffer layer[5] are obtained from test samples where the same recipe is used but instead of growing NWs after the sample reaches T_{growth}, the temperature is decreased. The values of the re-growth layer are simply calculated by subtracting the values of the buffer layer from the total 2D layer thickness measured from the samples with NWs.

We observe that the thickness of the regrowth layer is always higher at the lowest temperature and for the same temperature is higher for Te-rich conditions. This is due to the sublimation rate which increases with the temperature, and that can be reduced when there is an additional Te flux arriving at the surface. This explains why the thinnest layer is the one grown at higher temperature and under stoichiometric conditions.

[5]Note that the buffer layer was grown at 260°C. For more details see section 2.2.

	Buffer layer (nm) (sample without NWs)	Total layer (nm) =buffer + re-growth		Re-growth layer (nm) =total layer- buffer	
$T_{\text{NW growth}}$		Te rich	stoichio.	Te rich	stoichio.
375°C	185 ± 10	300 ± 10	280 ± 10	115 ± 10	95 ± 10
400°C	215 ± 10	310 ± 10	280 ± 10	95 ± 10	65 ± 10

Table 3.6 – On the first column: values of the ZnTe buffer layer measured by SEM on two samples grown following the recipe of the samples in Fig. 3.23. Second column, measure of the thickness of the total layer (buffer + re-growth layer) for the 4 samples presented in Figure 3.23. Third column, calculated re-growth layer of the same 4 samples using the first two columns.

The roughness of the 2D layer grown between the NWs increases with the growth temperature. Keep in mind that during the growth of NWs we are well above the optimal growth temperature for 2D layer (around $250 - 280$°C) hence it is not surprising to obtain rough surfaces. At 400°C, we observe deep cracks on the surface, most probably these are twins that are revealed at this temperature (see section 2.2). They are formed by the preferential evaporation of atoms at the twin boundaries. Apart from these cracks, we remark that the surface seems smoother for Te-rich conditions, which is consistent with the results presented in chapter 2.2 and with the fact that the growth of NWs is enhanced. At 375°C under stoichiometric conditions, we observe less cracks on the surface and the ones present are less deep. Finally, for the sample grown at 375°C under Te-rich conditions, the surface seems very similar to the one observed for the previous set of samples (grown at 350°C under stoichiometric conditions). The regrown layer shows that at high NW growth temperature, there is a higher adatom diffusion feeding the Au particle when there is a Te-rich environment. Hence, it is normal to observe that the NWs prefer to grow under Te rich conditions at high temperature.

In summary:

- Exploring the NW growth at high temperature (> 350°C) without modifying the size of the Au catalyst particle is complicated. The method tested in this set of samples didn't completely succeed at this task. Nevertheless, some quantitative information was gained from the NWs that where catalyzed with Au particles of "normal" size (< 30 nm).

- The optimized growth of vertical cylinder-shaped NWs can be obtained at higher temperatures under Te-rich conditions: a) at 400°C, we obtain NWs with a "big" diameter in the 20-25 nm range and sometimes with a pyramid at the base; b) at 375°C, we obtain NWs with "small" diameter in the 10-15 nm range and with a pyramid at the base.

- Well-formed vertical cone-shaped NWs preferentially grow at low temperature (350°C) under Te-rich conditions.
- At 350°C under stoichiometric conditions, we found an intermediate point where both types of NWs (cone and cylinder-shaped) can be simultaneously found.
- To further understand the effect of both the growth temperature and flux ratio conditions, a quantitative analysis of the NW's dimensions when they are grown at high temperature is needed. Additionally, TEM measurement need to be perform to retrieve the crystal structure of those NWs.

3.7 Diffusion-driven nanowire growth model

The growth of nanowires is strongly influenced by two parameters: the nucleation at the Au catalyst particle, and the diffusion of species on the surfaces. On one hand, complex models based on growth kinetics, involving the interaction of atoms in various thermodynamic states at the Au-NW interface, have been proposed for the VLS growth of III-V NWs [77]. These models relay on transition state kinetics driven by the minimization of the free energy of the total system. On the other hand, diffusion-dependent nanowire growth models has also been stated [78]. In these type of models, the morphology (length and shape) of the nanowires is directly related to different values of the diffusion length on the substrate and along the NW sidewalls. These models are also known to apply to a wide range of growth conditions of III-V and Si NWs [79] and even to CdTe NWs [80].

In this section we focus on the role of adatom diffusion in the growth of some of the NW-samples presented in this chapter. We examine a part of our results using a purely diffusion-driven growth model to extract characteristic physical parameters of our system. This attempt to model the formation of ZnTe NWs is clearly not complete: the effect of the nucleation on the growth is yet to be introduced. However, it is beyond the scope of this work to accomplish that task.

With that in mind, several assumptions can be made to describe the growth of the nanowires presented here:

1. The density of Au droplets (and hence the density of NWs on the substrate) is low enough that we can consider a single NW.
2. The NW is perpendicular to the substrate surface.

3. The temperature is low enough that re-evaporation is negligible: that implies that the diffusion length is defined by the incorporation of adatoms on the substrate or on the NW facets.

4. We observe a NW growth rate enhanced by one order of magnitude with respect to that of the 2D layer, hence we neglect the effect of the direct flux on the Au droplet.

A diffusion-based nanowire growth model is built from the general solution of the diffusion equations: for the nanowire side walls in 1D and for the substrate surface in 2D (circular symmetry). The flux arriving onto the substrate (here the ZnTe buffer layer) induces the presence of adatoms and results in the growth of a quasi-2D layer on the surface between the nanowires.

The local densities of adatoms (number of adatoms by surface unit), $n_s(r)$ on the substrate, and $n_f(z)$ on the NW sidewall facets, are solutions to the diffusion equations and can be written as follows:

$$n_f(z) = n_f^0 + c_f^+ \exp(\frac{z}{\lambda_f}) + c_f^- \exp(-\frac{z}{\lambda_f}) \tag{3.1}$$

$$n_s(r) = n_s^0 + c_s^+ \mathrm{I}_0(\frac{r}{\lambda_s}) + c_s^- \mathrm{K}_0(-\frac{r}{\lambda_s}) \tag{3.2}$$

- r is the radial coordinate increasing when moving away from the NW and z is the coordinate axis perpendicular to the substrate increasing in the direction of the tip of the nanowire.

- I_0 and K_0 are the modified Bessel functions. Note that for a weak density of NWs, $n(\infty) \sim 0$ then $c_s^+ = 0$.

- λ_s and λ_f are the diffusion lengths on the substrate and on the NW facets. They are defined assuming identical values of the diffusion coefficients D, as:

$$\lambda_s = \sqrt{D\tau_s} \tag{3.3}$$

$$\lambda_f = \sqrt{D\tau_f} \tag{3.4}$$

- τ_s and τ_f are the resident times of an adatom on the substrate and side wall facets before incorporation or desorption.

– n_s^0 is the value of the uniform adatom density far from the NW and n_f^0 is the same value on the NW facets:

$$n_s^0 = J_s \tau_s \tag{3.5}$$

$$n_f^0 = J_f \tau_f \tag{3.6}$$

– J_s and J_f are the incident flux on the substrate and the facets. The flux ratio is:

$$\frac{J_f}{J_s} = \frac{\tan \alpha}{\pi} \tag{3.7}$$

where α is the angle in incidence of the flux: the angle of the cells with respect to the substrate normal. In the case of the ZnTe cell in our MBE chamber: $\frac{J_f}{J_s} = 0.15$ (see Table 1.2). This definition takes into account the homogenisation of the flux due to the rotation of the substrate or by diffusion.

– The adatom density ratio can be written as:

$$\frac{n_f^0}{n_s^0} = \frac{J_f}{J_s} \left(\frac{\lambda_f}{\lambda_s} \right)^2 = \frac{\tan \alpha}{\pi} \left(\frac{\lambda_f}{\lambda_s} \right)^2 \tag{3.8}$$

The simplest **boundary conditions** are:

- The adatoms hopping probability from NW to substrate and from the substrate to the NW are symmetric:

$$n_f(z = 0) = n_s(r = R) \tag{3.9}$$

R is the nanowire radius at the base.

- The adatom current at the vicinity of the NW-substrate interface are in equilibrium (conservation of the adatom currents):

$$\frac{dn_f}{dz}(z = 0) = -\frac{dn_s}{dr}(r = R) \tag{3.10}$$

- Complete trapping at the tip of the NW: catalyst droplet acting as perfect sink.

$$n_f(z = L) = 0 \tag{3.11}$$

L is the height of the nanowire.

Note that this condition is valid for a purely diffusion-driven model [78]. In the more complex case of kinetic-driven growth [77] (not treated here), where the thermodynamical mechanisms in the catalyst droplet limiting the axial growth need to be taking into account, this condition is modified to:

$$\frac{n_f}{dz}(z = L) = \Delta\Gamma \tag{3.12}$$

where $\Delta\Gamma$ is the net state transition flux.

In case of complete trapping in the droplet, the boundary conditions presented in equations 3.9, 3.10 and 3.11, allow us to determine the constants in equations 3.1 and 3.2 and to obtain the following expression for **the NW adatom density**:

$$n_f(z) = n_s^0\,\omega_s + n_f^0\,\omega_f \tag{3.13}$$

$$\text{with} \quad \omega_s = \frac{\sinh(\frac{L-z}{\lambda_f})}{\sinh(\frac{L+\tilde{\lambda}_s}{\lambda_f})} \tag{3.14}$$

$$\text{and} \quad \omega_f = \left[1 - \frac{\sinh(\frac{z}{\lambda_f})}{\sinh(\frac{L}{\lambda_f})} - \frac{\sinh(\frac{L}{\lambda_f}) + \frac{\tilde{\lambda}_s}{\lambda_f}}{\sinh(\frac{L+\tilde{\lambda}_s}{\lambda_f})}\frac{\sinh(\frac{L-z}{\lambda_f})}{\sinh(\frac{L}{\lambda_f})}\right] \tag{3.15}$$

An effective diffusion length $\tilde{\lambda}_s$ is defined as:

$$\tilde{\lambda}_s = -\lambda_s \frac{\mathrm{K}_0(\frac{R}{\lambda_s})}{\mathrm{K}_0'(\frac{R}{\lambda_s})} \tag{3.16}$$

Note that if the diffusion equation in the substrate was in 1D instead of in 2D, $\tilde{\lambda}_s$ would simply be λ_s. By definition $\tilde{\lambda}_s$ depends on R and varies with the growth time. However, when we supposed a fixe value of λ_s and we calculate the values of $\tilde{\lambda}_s$ for R from 10 to 35 nm (corresponding to the range of NW base radius found for the ZnTe NWs grown at 350°C, shown in figure 3.5), we find that the variations of $\tilde{\lambda}_s$ are not very high. In particular, $\tilde{\lambda}_s$ influences mainly the NWs when they are short (i. e. when $R \simeq R_0$, with R_0 being the radius of the catalyst particle which remains constant). When the NWs are longer, it is $\tilde{\lambda}_s + L$ that dominates the growth, hence the variations of $\tilde{\lambda}_s$ are masked by the values of L. In brief, when we calculate $\tilde{\lambda}_s$, we realize that the values are small, for example for $\lambda_s = 60$ nm and $R = 10$ nm we obtain $\tilde{\lambda}_s = 19$ nm and for $\lambda_s = 60$ nm and $R = 35$ nm we obtain $\tilde{\lambda}_s = 36$ nm. Since $\tilde{\lambda}_s$ can be taken as a small value, we can supposed that $\tilde{\lambda}_s << \lambda_f$. This approximation was used to determine equation 3.13.

Equation 3.13 has two main parts: the contribution from flux arriving to the substrate (ω_s) and the contribution from the flux arriving laterally (ω_f). In figure 3.24 and 3.25, this contributions are plotted for $\lambda_s = 60$ nm, $\tilde{\lambda}_s = 20$ nm and $\lambda_f = 200$ nm.

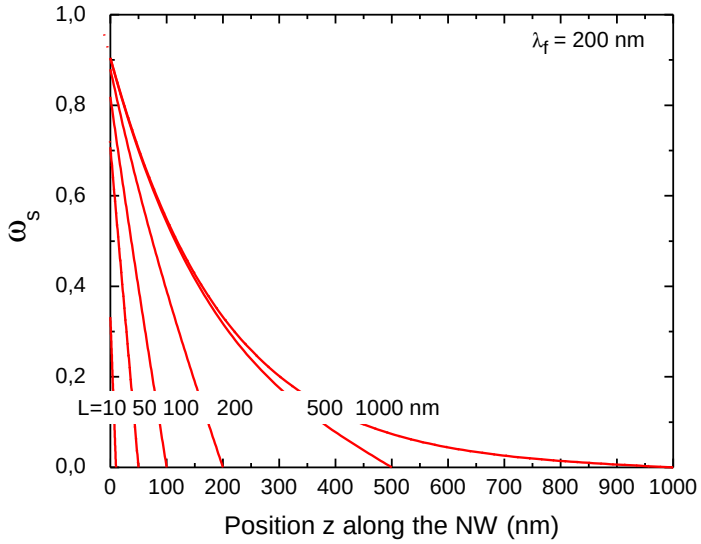

Figure 3.24 – Contribution to the NW density of adatoms diffusing from the substrate (equation 3.14): $\omega_s(z)$ is plotted for different values of L (L=10, 50, 100, 200, 500 and 1000 nm. We fixed: $\lambda_s = 60$ nm, $\tilde{\lambda}_s = 20$ nm and $\lambda_f = 200$ nm.

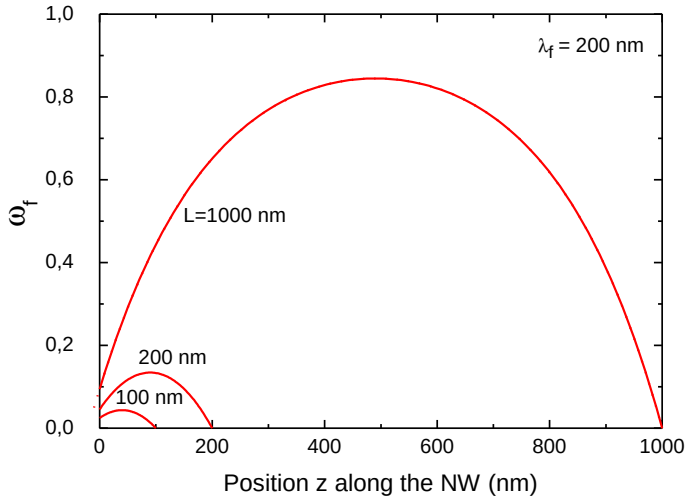

Figure 3.25 – Contribution to the NW density of adatoms from the lateral flux (equation 3.15): $\omega_f(z)$ is plotted for different values of L (L= 100, 200 and 1000 nm. We fixed: $\lambda_s = 60$ nm, $\tilde{\lambda}_s = 20$ nm and $\lambda_f = 200$ nm.

The growth rates for the NW length L (axial growth), for the NW radius at the base R (lateral growth) and for the 2D pseudo-substrate with height h are given by:

$$\frac{dL}{dt} = -\alpha_L \frac{2D\Omega_0}{R_0} \frac{d}{dz} n_f(z = L) \tag{3.17}$$

$$\frac{dR}{dt} = \alpha_f \frac{n_f(z = 0)}{\tau_f} \Omega_0 \tag{3.18}$$

$$\frac{dh}{dt} = \alpha_s \frac{n_s^0}{\tau_s} \Omega_0 = V_s \tag{3.19}$$

In these equations, Ω_0 is the volume occupied by an atom in the crystal; α_s, α_f and α_L are the incorporation rate at the substrate, the NW facets and at the tip of the NW (at the interface with the Au catalyst particle). In Eq. 3.19, V_s is the growth speed on the substrate. At the end of the growth, the final thickness of this re-grown layer will be $h = V_s t$.

From equation 3.17 and figure 3.24 we conclude that the contribution to the growth from adatoms diffusing from the substrate is: i) important for short NWs (low L): it shows an almost linear decreasing dependence with z, and ii) weak for long NWs (high L): it decreases exponentially with z.

Figure 3.25 indicates that the contribution to the growth from the lateral flux is proportional to L. For short NWs (low L): the majority of the adatoms arriving from the lateral flux diffuse to the substrate ($z = 0$) or into the catalyst ($z = L$). For long NWs (high L): the adatoms arriving at the middle part of the NW are incorporated. This is indicated by the formation of a plateau (at almost constant $\omega_f(z)$) between $z \sim 400 - 600$nm for the case at $L = 1000$nm. This plateau is longer for larger L.

Axial growth

Using equation 3.13 and 3.17, the NW axial growth rate is described by the following expression:

$$\frac{dL}{dt} = \frac{\alpha_L}{\alpha_s} \frac{2\lambda_f^2}{R_0 \lambda_s} V_s \frac{1 + \frac{n_f^0}{n_s^0} \left[\cosh(\frac{L+\tilde{\lambda}_s}{\lambda_f}) - 1 \right]}{\sinh(\frac{L+\tilde{\lambda}_s}{\lambda_f})} \tag{3.20}$$

Additionally, if we supposed that $\tilde{\lambda}_s$ is constant, equation 3.20 can be integrated. We obtain an expression of the **nanowire length in terms of the thickness of the re-grown layer:**

$$\frac{h}{R_0} = \frac{J_s}{J_f}\frac{1}{2}\ln\frac{1+\frac{J_f}{J_s}\left(\frac{\lambda_f}{\lambda_s}\right)^2\left[\cosh(\frac{L+\tilde{\lambda}_s}{\lambda_f})-1\right]}{1+\frac{J_f}{J_s}\left(\frac{\lambda_f}{\lambda_s}\right)^2\left[\cosh(\frac{\tilde{\lambda}_s}{\lambda_f})-1\right]} \tag{3.21}$$

This dependence of L with h is plotted in figure 3.26 for different contributions from the substrate (different values of λ_s):

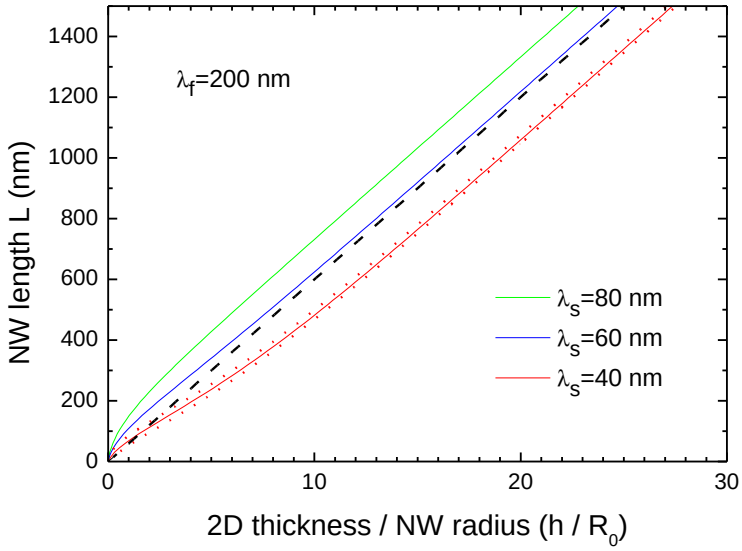

Figure 3.26 – Nanowire length L as a function of the thickness of the re-grown layer h divided by the radius of the catalyst particle R_0 (equation 3.21). The continuous curves are plotted for: $J_f/J_s = 0.15$, $\lambda_f = 200$ nm, $\tilde{\lambda}_s = 20$ nm and three different values of $\lambda_s = 40, 60, 80$ nm (in red, blue and green). The dotted red curves have the same parameter except for λ_s with is changed to: $\tilde{\lambda}_s = 10$ nm and 50 nm. Finally, the black dashed line is the asymptotic line due to lateral flux.

For short NWs ($L < \lambda_f$), the contribution from the substrate determines how fast the NW starts to grow: the growth speed at $\lambda_s = 40$ nm is lower than at $\lambda_s = 80$ nm (slope of the red curve is lower than the slope of the green curve at low L in figure 3.26). Hence, the contribution from the substrate influences the axial growth of the NWs only at the early stages of the growth.

When the NW length starts to increase, the contribution from the substrates gets weaker and the one from the flux arriving laterally gets stronger. For the long NWs ($L \gg \lambda_f$), the contribution to the NW axial growth from the adatoms arriving to the substrate and diffusing up the NWs walls up to the catalyst droplets is very week (negligible). The contribution to the axial growth of the NW from the lateral flux is dominant. The slopes of the curves in figure 3.26 correspond to this contribution (dashed black line).

Finally, when we modify the values of $\tilde{\lambda}_s$ to 10 nm and to 50 nm (extreme values corresponding to the smaller and larger values of R measured for the samples shown in figure 3.5), we see that the behavior of the lines is almost the same (red dotted lines). This somehow validates the hypothesis of a constant $\tilde{\lambda}_s$ value.

Lateral growth

The lateral growth rate at the NW base ($z = 0$), in the case where $\tilde{\lambda}_s << \lambda_f$, is given by:

$$\frac{dR}{dt} = \frac{\alpha_f}{\alpha_s}\left(\frac{\lambda_s}{\lambda_f}\right)^2 V_s\, \omega_R(z=0) \tag{3.22}$$

$$\text{with} \quad \omega_R(z=0) = \frac{\sinh(\frac{L}{\lambda_f}) + \frac{J_f}{J_s}\frac{\lambda_f \tilde{\lambda}_s}{(\lambda_s)^2}\left[\cosh(\frac{L}{\lambda_f}) - 1\right]}{\sinh(\frac{L+\tilde{\lambda}_s}{\lambda_f})} \tag{3.23}$$

In figure 3.27 we plot the value of ω_R, for different contributions from the substrate (different values of λ_s). We observe that for small t values, the lateral growth is slow and that the lateral flux does not influence the growth (four lines are merged together). For higher t values, the lateral growth becomes constant and the contribution from the lateral flux remains relatively weak. Thus, the lateral growth at the NW base is a good measure of the NW growth time, which can be interesting in samples where the NWs start to grow at different times.

Finally, the variation of the NW radius at the base R with the NW length can also be determined:

$$\frac{dR}{dL} = \frac{\alpha_f}{2\alpha_L}\frac{R_0}{\lambda_f}\frac{\sinh(\frac{L}{\lambda_f}) + \frac{J_f}{J_s}\frac{\lambda_f \tilde{\lambda}_s}{(\lambda_s)^2}\left[\cosh(\frac{L}{\lambda_f}) - 1\right]}{1 + \frac{J_f}{J_s}\left(\frac{\lambda_f}{\lambda_s}\right)^2\left[\cosh(\frac{L+\tilde{\lambda}_s}{\lambda_f}) - 1\right]} \tag{3.24}$$

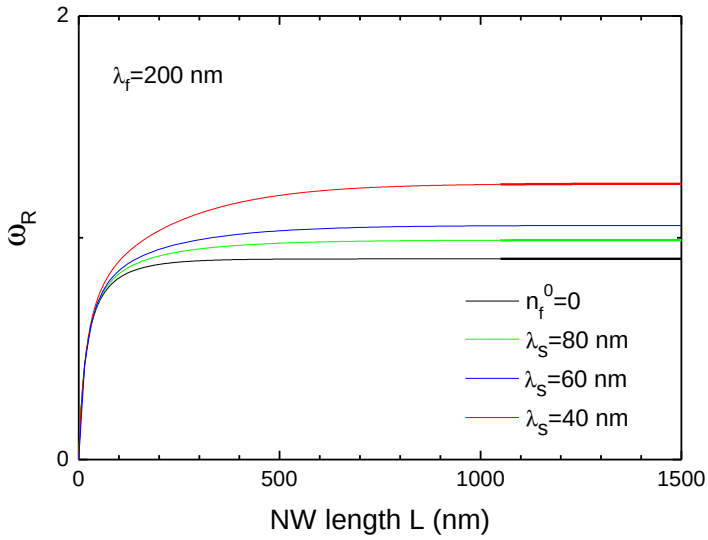

Figure 3.27 – ω_R as a function of L (equation 3.22). This value is proportional to the lateral growth rate at the NW base ($z = 0$). The curves are plotted for: $J_f/J_s = 0.15$, $\lambda_f = 200$ nm, $\tilde{\lambda}_s = 20$ nm and three different values of $\lambda_s = 40, 60, 80$ nm (in red, blue and green). The curve for the case where there is no contribution from the lateral flux ($n_f^0 = 0$) is plotted in black.

Application to ZnTe NWs at low temperature

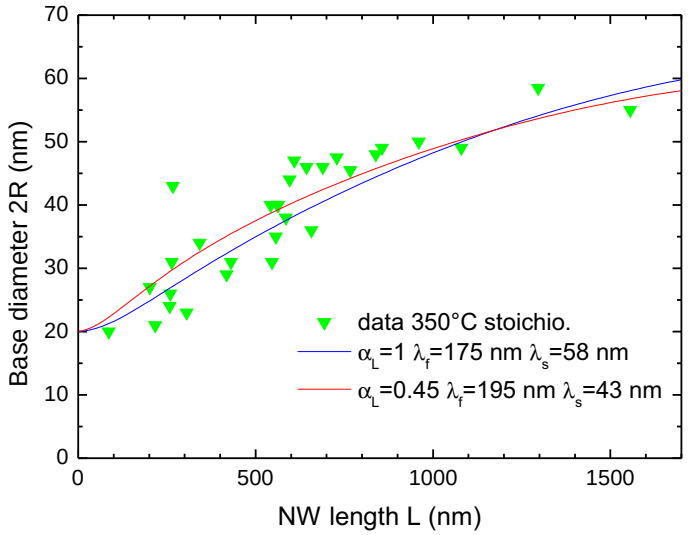

Figure 3.28 – NWs base diameter as a function of the NW length L for cone-shaped NWs growth at 350°C under stoichiometric flux ratio conditions. The fits are based on a purely diffusion-driven model. The red fit uses $\alpha_L = 1$, $\lambda_f = 175$ nm and $\lambda_s = 58$ nm and the blue fit uses $\alpha_L = 0.45$, $\lambda_f = 195$ nm and $\lambda_s = 43$ nm.

Let's consider the cone-shaped NWs from the sample presented in figure 3.3c: growth at 350°C **under stoichiometric flux ratio conditions**. We can use equation 3.24 to fit the behavior presented in figure 3.5. The result is shown in figure 3.28, assuming that:

- The incorporation rate at the substrate and the NW facets is close to 1 ($\alpha_s \approx 1$ and $\alpha_f \approx 1$).
- The effective diffusion length $\tilde{\lambda}_s$ is fixed to 20 nm.
- The thickness of the 2D layer growing in between the NWs is of the order of 200 nm at the end of the growth.
- Results presented previously in section 3.5, indicate that all the cone-shaped NWs do not start to grow at the same time. A part of them initialize the growth later than the others (different "incubation" times). Here we take this into account, and we use the radius of the NW at the base as a measure of the real growth time of each NW. Therefore, for a particular set of growth conditions (λ_f, λ_s and the incorporation rate at the tip of the NW: α_L) the height L of a nanowire depends on the initial radius R_0 and on the real growth time measured by $(R - R_0)$.
- In figure 3.5 we can see that the minimum radius of the base for the cone-shaped NWs coincides with the maximum radius of the cylinder-shaped NWs. Since the averaged values of the Au catalyst droplets for both populations of NWs are in the same range: $R_0 = 7-10$ nm (shown in table 3.2), we assume that the initial radius of the longer cone-shaped NWs of this sample (1550 nm) probably corresponds to the minimum radius (7 nm). We take into account the dispersion of the radius of the Au catalyst particles using: $R_0(L) = 10 - 3L/1550$. The length of the longest nanowire is adjusted supposing that it started to grow immediately. This initial weighting has a significant effect on the curve $R(L)$ for high values of L (saturation).

Two extreme sets of parameters give a good fit of the data. In one case, we assume complete trapping on the catalyst particle ($\alpha_L = 1$) and we obtain for the values of the diffusion length on the NW facet and on the substrate: $\lambda_f = 175$ nm and $\lambda_s = 58$ nm (blue fit). On the other case, we decrease the trapping coefficient of the catalyst to $\alpha_L = 0.45$, and we obtain a higher diffusion length on the NW facets $\lambda_f = 195$ nm and a smaller diffusion length on the substrate $\lambda_s = 43$ nm. The data presented in this work do not allows to distinguish from this two cases. Nevertheless, the values of λ_s and λ_f calculated in both situations are not that different and give a first order of magnitude of these values for ZnTe NWs.

We can also consider the set of NW samples presented in section 3.5 grown under **Te-rich flux ratio conditions and for different growth times** (2, 10 and 30 min). Preliminary results on this three samples can be obtained using the same method and by considering that:

- The incorporation rate at the substrate, the NW facets and at the NW tip is close to 1 ($\alpha_s \approx 1$, $\alpha_f \approx 1$ and $\alpha_L \approx 1$).
- The effective diffusion length $\tilde{\lambda}_s$ is fixed to 20 nm.
- The thickness of the 2D layer grown in between the NWs is 11, 57 and 170 nm for the samples grown at 2, 10 and 30 min, obtained from table 3.5.
- The NW with maximum height in each sample has: $L_{max} = 52, 260$ and 640 nm (for 2, 10 and 30 min of growth). We assume that these nanowires start to grow immediately after the cell shutters are opened.
- The values of the catalyst particle are taken as: $R_0(L) = 12.5 - 5L/L_{max}$ for the 2 min sample, $R_0(L) = 9.5 - 4L/L_{max}$ for the 10 min sample and $R_0(L) = 9 - 3L/L_{max}$ for the 30 min sample. We attribute the extreme values of the error bars to the longer NWs.

In figure 3.29 we plotted the NW of the sample with highest height versus the 2D regrowth thickness divided by the radius at the tip. The error bars represent the dispersion of the Au particle radius. The fit plots equation 3.21 by adjusting the values of the diffusion lengths on the substrate and on the NW facets. We obtain $\lambda_s = 45$ nm which is a slightly lower value than the one obtained under stoichiometric flux ratio conditions ($\lambda_s = 58$ nm). For λ_f we obtain 100 nm using the average value of the radius at the tip and 85 nm using the minimal value of the radius at the tip. Both values obtained for λ_f are much lower than the value obtained under stoichiometric flux ratio conditions ($\lambda_f = 175$ nm).

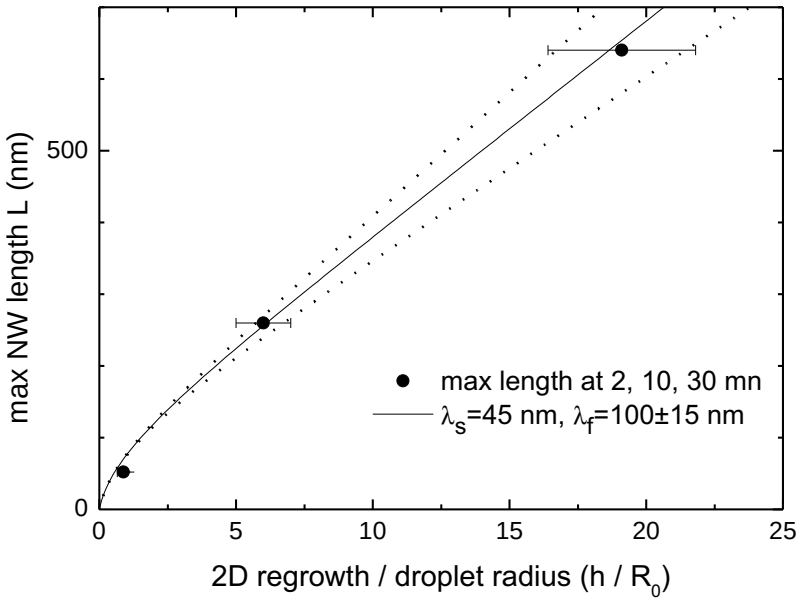

Figure 3.29 – Maximum NW length L versus the 2D regrowth thickness divided by the radius at the tip h/R_0. The 3 points are the experimental data obtained from the longest NW of each sample (samples are grown under Te-rich flux ratio conditions and for 2, 10 and 30 min). The fit is based on a purely diffusion-driven model. The fit takes $\lambda_f = 100 \pm 15$ nm and $\lambda_s = 45$ nm.

Discussion

- We clearly observe the effects of diffusion on the growth of cone-shaped ZnTe nanowires.
- By supposing that the growth is purely diffusion-driven we succeeded at finding quantitative values of λ_s and λ_f. These values set a reference of the order of magnitude of diffusion lengths for ZnTe surfaces. The value obtained for λ_s roughly corresponds to the radius of the crater at the base of the nanowires, thus validating our approximate approach.
- The condition stating that the NWs start to grow at different times has an important influence on the fit. Hence, it needs to be understood and verified for other growth conditions.
- The values of the diffusion lengths under Te rich flux ratio conditions are lower than under stoichiometric flux ratio conditions. This finding suggests that it is the diffusion of Zn adatoms that limits the growth (when more Te_2 molecules

are sent to the surfaces, adatoms of Zn are incorporated more rapidly, thus they diffuse for a lower distance on the surface).

- The NW length-radius statistics can also be fitted with a low incorporation rate at the tip using $\alpha_L = 0.45$ (catalyst particle does not act a perfect sink). This suggests that the nucleation mechanisms in the Au droplet starts to play a role in the growth. To take into account this kinetic processes, the boundary condition at the NW tip must be changed (equation 3.11 to equation 3.12). The complete model (including the nucleation mechanism in the catalyst), needs the knowledge of several physical parameters (e. g. the surface, interface and step energies) that have been determined for III-V SC but are presently unknown for II-VI materials.

- The cylinder-shaped NWs show that there is no lateral growth on the sidewall facets, which is not surprising for WZ nanowires. It is plausible that the diffusion length at the facets is much higher for this type of nanowires. The NW height seems to be limited after a certain growth time. Saturation of nucleation at the Au droplet-NW interface probably limits the growth. An evaluation of the chemical potentials for II-VI semiconductors (as it was done for III-V semiconductors [81]) would be helpful to understand this effect. Consequently, the description of the growth of this type of NWs is not included in this study.

- This model has not been tested for ZnTe NWs grown at higher temperatures. Further analysis on those samples needs to be performed.

3.8 Conclusions

In this chapter we focused on gaining knowledge on the effect of different growth conditions on the NW morphology and on the NW crystal structure to understand the mechanisms that govern the growth of pure ZnTe NWs. A summary of the results found in this chapter is presented in this section.

Nanowire growth at low temperature (350°C)

The low-temperature growth of Au-catalyzed ZnTe nanowires on a ZnTe(111) B buffer layer was explored under **different II/VI flux ratio conditions**.

- *Under stoichiometric conditions*, we observed that zinc-blende and pure wurtzite nanowires can be found homogeneously spread on the same sample surface.

  - **Wurtzite nanowires** are cylinder-shaped. This morphology probably results from a diffusion length along the NW sidewalls larger than the NW length. No lateral growth was detected on the facets of these nanowires. They present a pyramid structure around their base, which is favored in the presence of a strong flux on the NW sidewalls. Their height distribution is very narrow and probably limited by nucleation mechanisms at the NW-catalyst interface. Their morphology cannot be explained by a purely diffusion-driven model.

  - **Zinc-blende nanowires** are cone-shaped with a crater at their base. Their shape indicates a lower diffusion length on the sidewalls giving rise to lateral growth which was clearly detected by EDX measurements. Their large height distribution suggests that some nanowires start to grow later than the others. A diffusion-driven model is proposed to interpret the morphology on this type of nanowires. This model shows the importance of the lateral flux and allows us to determine values for the diffusion length at the substrate ($\lambda_s = 58$ nm) and at the NW facets ($\lambda_f = 175$ nm), assuming that the catalyst particle acts as a perfect sink. The value obtained for λ_s matches approximatively the radius of the crater at the NW base. Influence of the nucleation process at the catalyst-NW interface is not rule out for the growth of this type of nanowires, nevertheless its inquiry is out scope of this work.

- *Under Te-rich flux ratio conditions* the growth of zinc-blende cone-shaped nanowires is favored (suppressing the growth of wurtzite nanowires). This nanowires are in majority well-formed and perpendicular to the substrate. Values of the diffusion length

on the substrate and on the NW sidewalls are also determined using a purely diffusion-dependent growth model: $\lambda_s = 45$ nm and $\lambda_f = 100 \pm 15$ nm. These values are smaller than the ones found for the stoichiometric growth conditions indicating that the diffusion of Zn adatoms is probably limiting the growth.

- *Under Zn-rich flux ratio conditions* the growth of nanowires is completely suppressed.

The morphological evolution of the ZnTe NWs, grown at low-temperature, with the **growth time** was also studied. We found that:

- *At low growth times* (2 min), we observed that some nanowires started to grow but not all of them. Two populations are identified: "NW-typed" with a bigger height than diameter and "flatter particles" with lower height than diameter. Whats more, the normalized percentage of NWs found on this sample is lower than for samples grown for higher times. The fraction of NWs increases with the growth time: 1/3 at 2 min,1/2 at 10 min and 2/3 at 30 min. This agrees with the existence of a different "incubating time" that can also explain the large height distribution observed for cone-shaped nanowires grown for longer times.

- *At medium growth times* (10 min), both types of nanowires can be identified (when the growth is under stoichiometric flux ratio conditions) by their different morphology and the presence of a crater or a hexagonal pyramid at their base. The size of the pyramids is smaller for medium growth times than for larger growth times (30 min) evidencing the fact that it is formed during the nanowire growth.

- *The evolution of the surface density* was studied for the samples grown at different times. The quantitative analysis of these samples showed that in total, only 50% of the initial Au droplets catalyzed the growth of nanowires; the other 20% of the Au droplets gave rise to 3D objects on the surface and the last 30% were buried in the 2D layer.

- *The origin of the growth of two types of NWs* remains unknown. We investigated the polarity of both types of nanowires and of their respective substrate and we found that all of them have the same polarity. Additionally, quantitative analysis on the Au catalyst at the NW tip showed that the distribution of diameters is almost the same. Which goes against the hypothesis that two populations of different sized Au particles catalyzed two different types on NWs.

A possible hypothesis is that the growth of these two types of nanowires is induced by the simultaneous presence of surface domains with different surface reconstructions

(stoichiometry) on the 2D buffer layer (as shown section 2.2). This may lead to a surface composed of domains leading to different diffusion lengths of the adatoms. This hypothesis has not been proved -nor ruled out- and needs to be fourthly investigated.

Nanowire growth at high temperature ($>$ 350°C)

The growth of ZnTe NWs at 375°C and 400°C, under both stoichiometric and Te-rich flux ratio conditions, was qualitatively investigated. Three main results were found:

- Au-droplets with diameters below 30 nm catalyze vertical NWs, whereas Au-droplets with diameters above 30 nm catalyze inclined nanowires or nanowires that remain crumbling near the surface.
- Few straight cone-shaped NWs were observed on the sample grown at 375°C in excess of Te. None were observed on the other samples grown at high temperatures. Clearly, our results show that their growth is highly enhanced at a lower growth temperature (350°C).
- The optimized growth of vertical cylinder-shaped NWs can be obtained at high temperatures under Te-rich conditions.

  - At 375°C: the nanowires have a diameter in the 10-15 nm range (small with respect to the cylinder-shaped NWs found at 400°C) and they present a pyramid at the base. The nanowires found in this sample are similar in morphology and size to the ones obtained at 350°C under stoichiometric flux ratio conditions.

  - At 400°C: the nanowires have a diameter in the 20-25 nm range (high with respect to cylinder-shaped NWs grown at 350°C and at 375°C) and sometimes a pyramid at the base is observed.

To further understand the effect of the growth temperature, additional TEM measurements and a quantitative analysis of the morphology of the nanowires from samples grown at high temperatures needs to be performed.

CHAPTER 4

Axial and radial NW-based heterostructures

Contents

4.1 State of the art & purpose of this study . . . 132
4.2 Sample growth . . . 135
4.2.1 Growth of a ZnMgTe shell over ZnTe NWs . . . 135
4.2.2 Growth of a Cd(Mn)Te QD in a ZnTe(/ZnMgTe) NW . . . 137
4.3 EDX analysis and modeling . . . 144
4.4 Results . . . 152
4.4.1 EDX of sample A: ZnTe NWs with a ZnMgTe shell . . . 152
4.4.2 EDX of sample B: ZnTe NWs with a CdTe QD insertion . . . 154
4.4.3 EDX of sample C: ZnTe NWs with a CdMnTe QD insertion and a ZnMgTe shell . . . 165
4.4.4 Spectroscopy results . . . 175
4.5 Discussion . . . 182
4.5.1 Quantum dot insertion . . . 182
4.5.2 Core-multi shell NW structures . . . 185
4.6 Conclusion . . . 192

4.1 State of the art & purpose of this study

The objective of this chapter is to investigate the growth of NW-based semiconductor heterostructures. Chemical modulation can be obtained along the nanowires axis and/or from the interior to the exterior of the NW. Both axial and radial NW heterostructures have been developed using a large variety of SC materials. Some examples are: Si/Ge group IV SC [82, 83, 84], III-V SC compounds such as: GaAs, AlGaAs, GaP, InAs, InP, III-Sb, III-N [85,86,87,88,89,90,91] and II-VI SC compounds like ZnSe(Te), CdSe(Te) and ZnO [47,92,51,65,93]. Hybrid NWs combining different SC group materials have also been explored, for example: Si-GaAs heterostructures [94,95], GaP segments on top of Si NWs and Ge segments on top of GaAs or GaP NWs [64]. The literature on nanowire-based heterostructures is large and rich. Several extensive reviews on this topic have been published (for instance in [1, 58, 59, 61]). The goal of this section is to present a brief summary of the published results on II-VI SC heterostructures to establish the context of the results presented in this chapter.

As described in the general introduction, the growth of QD in NWs present several advantages. Among those, the possibility to control the QD size and position and the excellent spectroscopy properties due to the absence of a wetting layer are particularly appealing. The investigation of core-shell nanowires (NWs) with magnetic quantum dot (QD) axial insertions is a step forward in the search of novel properties and new possibilities for functional devices. Mastering the growth and properties of these complex structures is required. Four main goals need to be developed: 1) the control of the size and the position of the QD inside the NW; 2) the growth of as-sharp-as-possible interfaces between the QD and the barrier (NW); 3) the introduction and tuning of small concentration ($< 10\%$) of magnetic atoms such as Mn inside the QD and 4) the growth of a homogenous shell that passivates efficiently the surface and that allows to tailor the strain in the QD. The results presented in this chapter are a step towards obtaining this goal.

The growth of CdSe QDs in ZnSe NWs on a ZnSe peudo-substrate grown on a GaAs substrate has been developed by our group [24,25]. The ZnSe NWs obtained have a homogeneous diameter and can be grown at very low densities. The NW growth direction is preferentially along the $< 111 >$ and $< 100 >$ axis. The growth was demonstrated to take place via the Vapor-Solid-Solid (VSS) mechanism (solid Au catalyst particle). In spite of this, the QD insertion only contained about 50% of Cd. Nevertheless, the optical study of such nanowires showed exciting results, such as sharp excitonic lines with over 85% linear polarization and single photon emission on the biexciton measured up to room temperature [96, 51].

The growth of optically active CdTe QD in ZnTe NWs over GaAs substrates have been reported by Wojnar et al. [65]. The growth process takes place via the Vapor-Liquid-Solid mechanism (VLS). The CdTe insertions are grown using the Cd and Te cells and the temperature is decreased from 420°C (temperature for the ZnTe section) to 380°C. The NW diameters varied from 30 to 70 nm and the length amounts to 2 μm. A change of the growth direction is observed at the upper part of the NW and is attributed to the presence of a CdTe insertion. Energy-Dispersive X-ray spectroscopy (EDX) measurements were performed on those NWs and showed "significant intermixing of Cd and Zn at the interfaces" which they attributed to the VLS growth mode. They observed sharp emission lines associated to individual QDs and low temperature antibunching in the photon correlation measurements indicating the zero dimensional character of the QD.

In this work we are interested in the growth and properties of CdTe QDs and $Cd_{1-x}Mn_xTe$ (Mn concentration of few %) in core-shell ZnTe/ZnMgTe NWs. We will consider different growth conditions for the QD insertions and a different approach for the growth of a shell. In general the growth conditions used are very different than those presented by Wojnar et al. [65]. The major differences are: i) a lower growth temperature (70°C less) which is not changed during the growth of all the heterostructure (QD and shell); ii) solid Au catalyst particles indicating that the NWs growth takes place in the VSS mode; iii) the NWs are grown in homoepitaxy over a ZnTe buffer layer. This avoids defect formation at the NW base and allows a greater control of the Au particle formation, leading to a narrow diameter distribution and to possibility of tuning the density to minimize the interaction between NWs. Furthermore, we study in detail the structure and optical properties of the QD and of the core-shell NWs. We aim to characterize: 1) the growth of different axial insertions: size, shape and composition of the QD; and 2) the growth of core-multishell structures: lateral growth, thickness and composition of the shells.

EDX characterization of NW-based heterostructures is frequently performed. In most cases, it is employed to study the interface between two materials, to detect and localize the position of a QD or to study NW doping. For example, Si-Ge-Si core-multi shell NWs [82], hybrid Si-GaAs NWs [95] and GaAs/AlGaAs core-shell NWs [97] have been measured by EDX. Highly complex structures have also been studied by EDX, for example QD in the apex of the GaAs/AlGaAs interface in core-shell GaAs/AlGaAs NWs [85]. Usually, a profile of the EDX counts as function of the position and/or a map showing the distribution of elements are presented. These raw profiles give an *average* of the composition of each element along the beam path, therefore information on the local compositions is not available. Also, these profiles include an averaging along the interfaces hence they do not provide exact information on the shape of QDs.

In this chapter we develop a new approach to obtain *quantitative and local* information on the composition and shape of the QDs and of the core-shell NWs. A quantitative analysis is particularly useful when complementary studies are conducted on the same NW. We performed structural and optical characterization *on the same nanowire* by combining EDX measurements (coupled to a TEM) and cathodoluminescence and magneto-optical spectroscopy study.

This chapter is composed of four main parts:

- First, the conditions for the growth of different heterostructures are presented (section 4.2). We begin by describing the growth of a ZnMgTe shell over cone-shaped ZnTe NWs by lateral growth (sample A). Following on, we present two different samples where a QD insertion has been included. The first sample contains bare ZnTe NWs with a CdTe QD insertion (sample B) and the second one, ZnTe NWs with a ZnMgTe shell and a CdMnTe QD insertion (sample C). These last two samples have been characterized and compared in detail.

- Second, the method used to analyze the EDX data is presented. A quantitative model is proposed to study the composition, size and position of the QD and of the core-shell NWs. In particular, this model allows to obtain *quantitative and local* concentrations in complex NW heterostructures (section 4.3).

- Third, the results obtained for these samples are shown (section 4.4). This part includes the EDX characterization of the NWs and their corresponding spectroscopy results.

- Finally, in the fourth part, the analysis of all the results and a discussion on the informations obtained from combining the structural and optical results is performed (section 4.5).

4.2 Sample growth

4.2.1 Growth of a ZnMgTe shell over ZnTe NWs

Sample A: ZnTe NWs with a ZnMgTe shell

This section summarizes a series of results which where obtained indifferently on simple core-shell NWs grown on a GaAs(111)A substrate (sample A) and on more complex cone-shaped NWs grown on GaAs(111)B substrate (under both cases there was a ZnTe buffer layer grown prior to the Au deposition). We kept the same NW growth conditions as in chapter 3. In Fig.4.1 we present a SEM image of sample A. Note that the NW growth direction is no longer perpendicular to the surface.

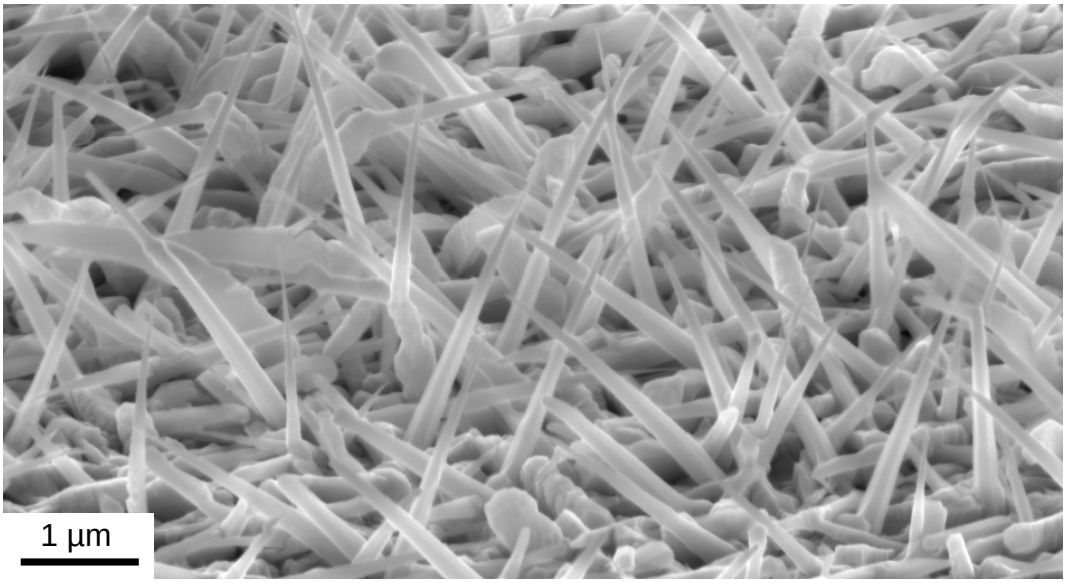

Figure 4.1 – SEM image of sample A: ZnTe coned-shaped NW grown under Te rich flux ratio conditions with a ZnMgTe shell. The image is taken with a 65° angle.

The growth of a shell is usually done by interrupting the NW growth, then decreasing the sample temperature to favor 2D growth conditions and proceeding by growing a conformal layer that covers the whole surface including the NW sidewalls. In this work, we preferred to take advantage of the cone-shaped geometry of the NWs. The conic shape of the NWs is the effect of lateral growth taking place while the axial growth under the Au catalyst is undergoing. Hence, to grow a shell over the cone-shaped NWs on sample A, we simply opened the Mg flux during the last 10 minutes of the ZnTe NW growth. The Zn/Mg flux ratio was 1/0.08. With this method, we do not decrease

the sample temperature to grow the shell, but it is kept constant at the NW growth temperature (350°C). We found that this method of growing a ZnMgTe shell works very well to passivate the surface of the ZnTe NWs. Results from the Mg distribution over the NW and the enhanced spectroscopy response of these NWs will be presented in section 4.4.

We have also started to explore the growth of a ZnMgTe shell on samples with both cone and cylinder-shaped ZnTe NWs. This appears to be more of a challenge. Preliminary results from SEM images presented in Figure 4.2 show that under those conditions the ZnMgTe shell only covers the cone-shaped NWs. The diameter of the cylinder-shaped NWs has not increased with respect to cylinder-shaped NWs grown without a shell, indicating that they are probably not surrounded by a ZnMgTe shell.

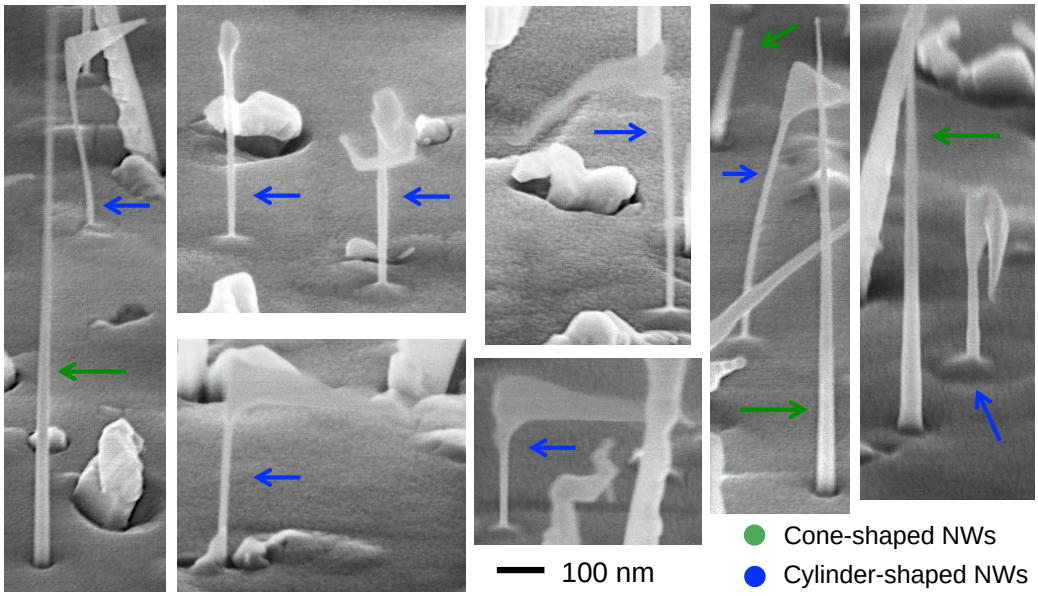

Figure 4.2 – SEM images of ZnTe NW grown under stoichiometric flux ratio conditions. ZnMgTe was sent to the surface to obtain a ZnMgTe shell over the ZnTe NWs. It seems that the shell was only grown over coned-shaped NWs and not over cylinder-shaped NWs. The images is taken with a 65° angle.

We observed that both types of NWs start to grow properly, with a nice and clear base where we distinguish a crater at the base of cone-shaped NWs and a pyramid for cylinder-shaped NWs. In contrast, when we introduce ZnMgTe at the end of the growth (instead of ZnTe), the typical morphology of the upper part of cylinder-shaped NWs is completely lost. It is clear that the ZnMgTe did not cover all the NW, but is incorporated at the top in the form of asymmetric non-conformal objects. A second

attempt was done to cover the cylinder-shaped NWs, but this time the growth temperature was reduced to 300°C before the deposition of ZnMgTe. The SEM images are not conclusive (not shown), it seems that some of the cylinder-shaped NWs are covered since their diameter is thicker. Nevertheless, an EDX analysis needs to be done to obtain more information on these samples and probably, the growth conditions for the shell of cylinder-shaped NWs still need to be optimized. In section 4.5, we will discuss a possible hypothesis to explain these findings.

4.2.2 Growth of a Cd(Mn)Te QD in a ZnTe(/ZnMgTe) NW

To grow a QD inside a NW, we keep the optimal growth conditions found for the growth of cone-shaped[1] ZnTe NWs (see chapter 3) and we explored only how to grow the CdTe insertion. The size of the QD is determined by i) a "vertical" dimension (the height), that can be controlled by changing the growth time, and ii) by "horizontal" directions (in the plane perpendicular to the NW growth axis), which are linked to the diameter of the Au catalyst droplet.

The QD height can be controlled by modifying the growth speed. To tune the height of the insertion, we can either change the growth time or the incident flux. The growth time is advantageous since it is proportional to the growth speed. The incident flux can be more tricky, since it changes the amount of material sent to the surface and trapped by the Au droplet in a certain time. Since the growth speed behaves differently whether the phase of the Au catalyst is solid (slower growth by steps) or liquid (faster and continuous growth), as shown by Ross et al. for Si NWs [63], the relation between the incident flux and the height of the QD can be more complex. By varying those parameters, we are able to grow ZnTe NWs with Cd(Mn)Te insertions with heights in the 18 to 100 nm range (measured by EDX). So far, we have not tested the growth of QD with a smaller height but we believe that this remains possible since the growth time (1 min) can be reduced.

Concerning the control of the QD diameter (in the plane perpendicular to the growth axis), we studied how to control the Au droplet diameter in chapter 2 and here, we present results that confirm that the diameter of the QD insertion is close to the diameter of the Au particle at the intersection between the Au particle and the NW tip. As a result, we managed to grow QD insertions with small diameters in the 6-8 nm range (shown in section 4.4).

[1] We chose to explore the growth of QD on this type of NWs since the growth of a ZnMgTe shell on cone-shaped NWs was simpler to perform and had shown good spectroscopy results.

To grow QDs with a larger diameter, we could grow NWs with a higher Au catalyst diameter. Nevertheless, the limiting factor is that most of the NWs catalyzed from Au particles with a diameter larger than 40 nm do not efficiently rise from the surface, and the ones that succeed are non-vertical (see section 3.6). However, this limitation does not affect us since our intention is to grow small insertions of CdTe to have a larger carrier confinement.

Other parameters were also chosen to optimize the growth of the QDs. For instance, we have grown Cd(Mn)Te segments without changing the sample temperature used for the ZnTe NW growth. This is possible since the growth of ZnTe NWs is performed at a temperature allowing the growth of Cd(Mn)Te. The advantage of keeping constant the temperature is that we may reduce possible perturbations during the growth of the Cd(Mn)Te insertions and limit the inter-diffusion between Cd(Mn)Te et ZnTe.

With that objective in mind, we also avoided to keep the sample under vacuum at temperatures above 350°C where the evaporation of surface atoms (Cd, Te) begins to have a significant effect. Therefore the growth of the QD was simply performed by changing the flux of ZnTe by CdTe straight away and vice versa. This method allows us to minimize evaporation effects and is favored by the fact that we probably grow the NWs by the vapour-solid-solid mechanism (solid catalyst).

Actually, liquid catalysts are known to act as reservoirs of atoms, which means that when the flux of atoms sent to the surface is stopped, the growth below the catalyst can continue until the Au droplet is emptied. This is a problem when we try to grow abrupt interfaces, since there are large sections of ternary compounds grown (here CdZnTe). To avoid this, the sample can be left under vacuum for a small period of time between the end of the ZnTe flux and the beginning of the CdTe one. This may allow to finish the growth of the ZnTe part and then to start the growth of CdTe, however this may also disturb the growth. The advantage of a solid catalyst is that the crystal structure does not allow to stock as much of foreign atoms, hence there is no need to keep the sample under vacuum to have a sharp interface. Nevertheless, there is also inter-diffusion of atoms that can affect the steepness of the interface that are not linked to the phase of the catalyst particle.

Having established the general conditions for the growth of the QD and the shell we focus our attention on two samples that show very different QD insertions and core-shell structures.

Sample B: ZnTe NWs with a CdTe QD insertion[2]

In figure 4.3 we present a SEM image of ZnTe NWs with a CdTe QD insertion from sample B. The growth recipe used is indicated in figure 4.4.

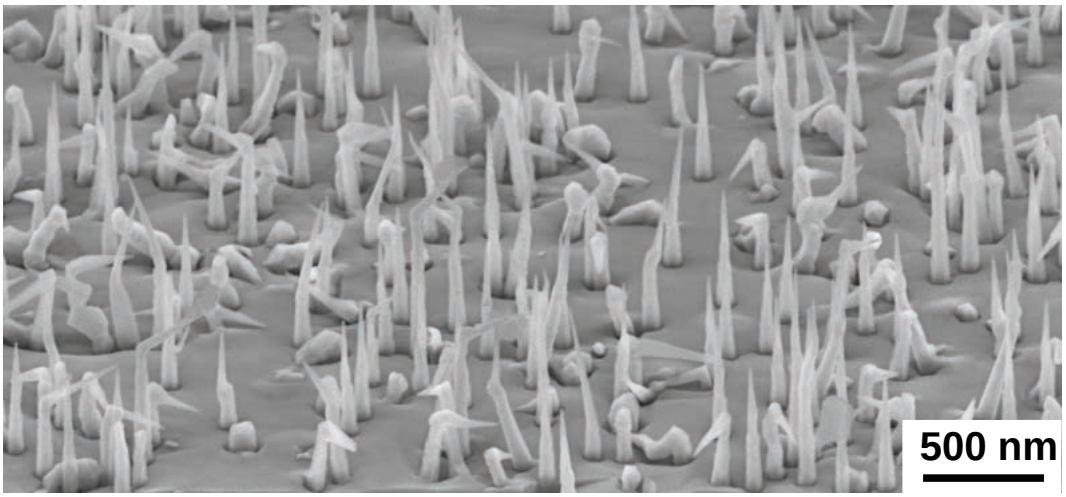

Figure 4.3 – SEM image of **sample B**: cone-shaped ZnTe NWs with a CdTe insertion. The growth conditions are written in the text.

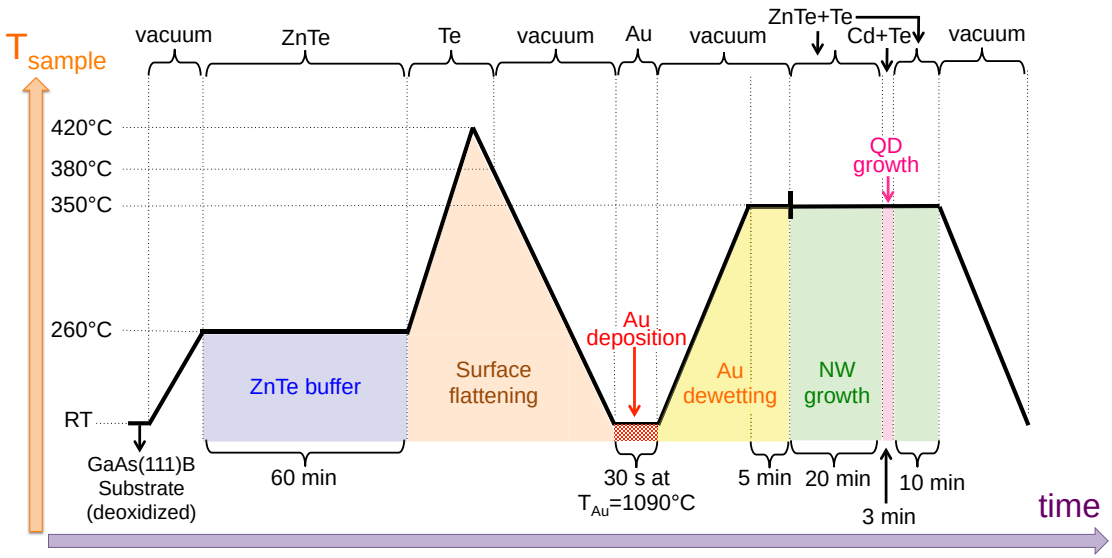

Figure 4.4 – Scheme of the growth process of **sample B**: cone-shaped ZnTe NWs with a CdTe QD insertion. These NWs are grown under Te-rich conditions.

[2] Note that this sample has been presented previously in chapter 3 in section 3.4.1 where a EDX-TEM image of a kinked NW is shown in Fig.3.10.

Details of the NW's growth conditions (see figure 4.4):
The substrate preparation and the growth of a ZnTe(111)B buffer is performed with an excess of Te as indicated in section 2.2. The Au dewetting conditions are chosen according to the analysis performed in chapter 2. The NWs are grown under Te rich flux ratio conditions: Te/Zn : 2.3/1. The beam equivalent pressure (BEP) used was 5.7×10⁻7 torr for ZnTe and 6.2×10⁻7 torr for Te.

Details of the CdTe QD growth conditions (see figure 4.4):
The QD insertion is placed at 2/3 of the total ZnTe growth time and it is grown using the Cd and Te effusion cells for 3 min. The CdTe section is also grown under Te-rich flux ratio conditions (Te/Cd: 1.2/1). The temperature is kept constant at 350°C. We calibrated the CdTe growth speed using RHEED oscillations to 0.3 ML/s (in the (001) direction) over a CdTe(100) layer at 280°C.

Sample C: ZnTe/ZnMgTe core-shell NWs with a CdMnTe QD insertion

Sample C also consists of ZnTe cone-shaped NWs but with a CdMnTe QD insertion and a ZnMgTe shell. In Figure 4.5 a SEM image of sample C is presented. Also, a scheme illustrating the growth recipe of this sample is presented in Figure 4.6.

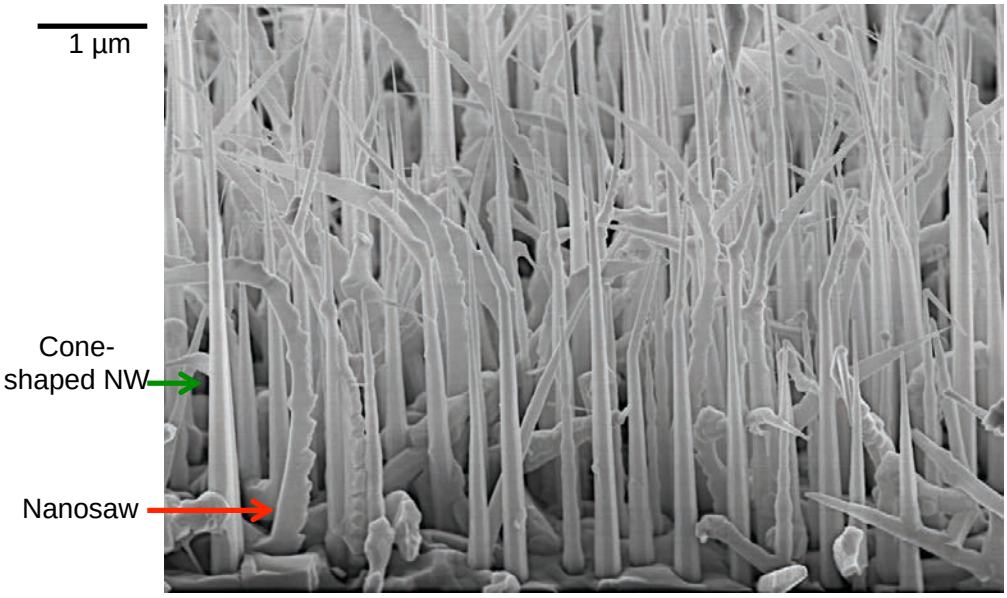

Figure 4.5 – SEM image of sample C: ZnTe NW with a CdMnTe QD insertion and a ZnMgTe shell. The tilt of the image is 65°.

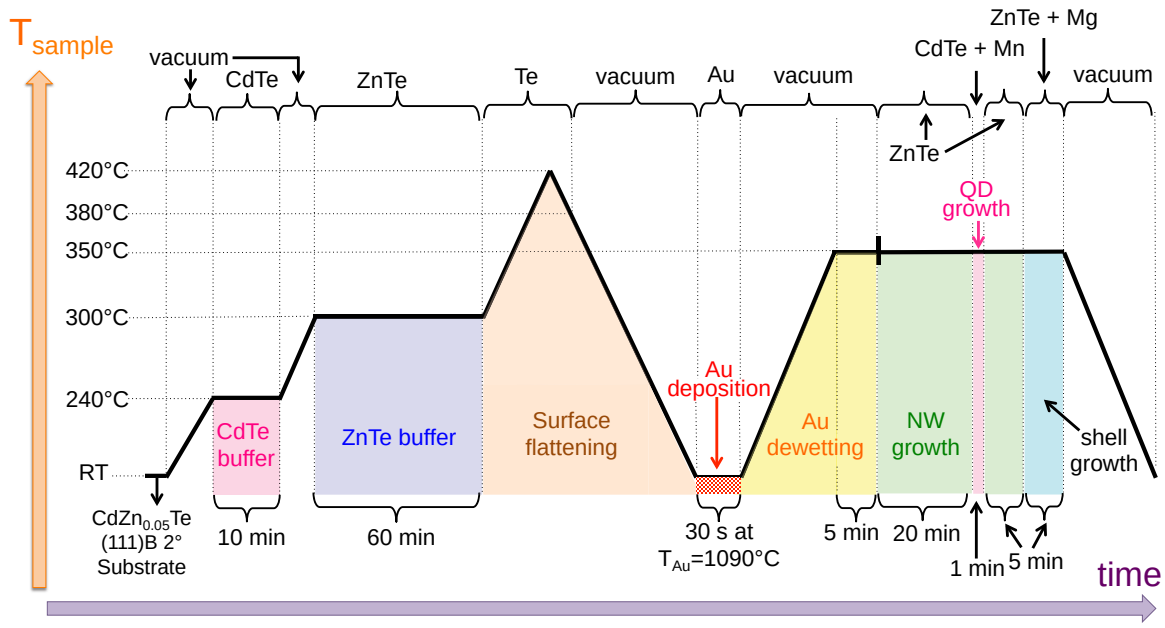

Figure 4.6 – Scheme of the growth process of sample C: ZnTe NW with a CdMnTe QD insertion and a ZnMgTe shell.

Details of the buffer layer and NW's growth conditions (see figure 4.6):
For this sample, the growth is directly performed on a II-VI substrate[3]: CdZnTe(111)B with 5% of Zn and misoriented of 2°. The advantage of using a misoriented substrate is that the formation of twins is reduced. The growth over a CdZnTe(111)B substrate is slightly different than for a GaAs substrate: before the growth of a ZnTe layer, we have grown a CdTe buffer at 240°C for 10 min to smoothen the surface. Then, the ZnTe buffer is grown at 300°C for 1h under stoichiometric flux ratio conditions. The flattening process of the surface of this buffer layer is unchanged, as well as the Au dewetting conditions. The NWs are grown under stoichiometric flux ratio conditions: Te/Zn : 1/1. The BEP of the ZnTe effusion cell is highly increased to $2.2\times10^{-}6$ torr (for sample B the BEP of the ZnTe cell was $5.7\times10^{-}7$ torr).

Details of the CdMnTe QD growth conditions and ZnMgTe shell (see figure 4.6):
The QD insertions are grown at the same temperature but for a shorter time than sample B (1 min instead of 3 min) and using simultaneously the CdTe and Mn effusion cells. The position of the QD inside the NW was kept at 2/3 of the total height. In this sample the QD is not grown under Te-rich flux ratio conditions. The Cd/Mn BEP ratio was 1/0.1. We calibrated the CdTe growth speed by using RHEED oscillations to 0.5 ML/s over a CdTe(100) layer. Finally, the shell is grown using the ZnTe and Mg cells, the Zn/Mg BEP ratio was 1/0.06.

[3]This change of substrate is due to a break in the stock of GaAs(111)B. Since a thick-ZnTe(111)B layer is then grown over this substrate, we believe the influence of this change of substrate is minimal.

As expected, in Fig.4.5 we observe that the NWs are much bigger than the ones in sample B (Fig.4.3). Their height is in average between $3-5\,\mu$m and their base diameter in the $150-250$ nm range. Remarkably, the Au droplet diameter is kept very low at $10-20$ nm. SEM images of the base and of the top of some NWs of sample C are presented in Figure 4.7. We clearly observe the 6-fold symmetry facets at the base of the NWs.

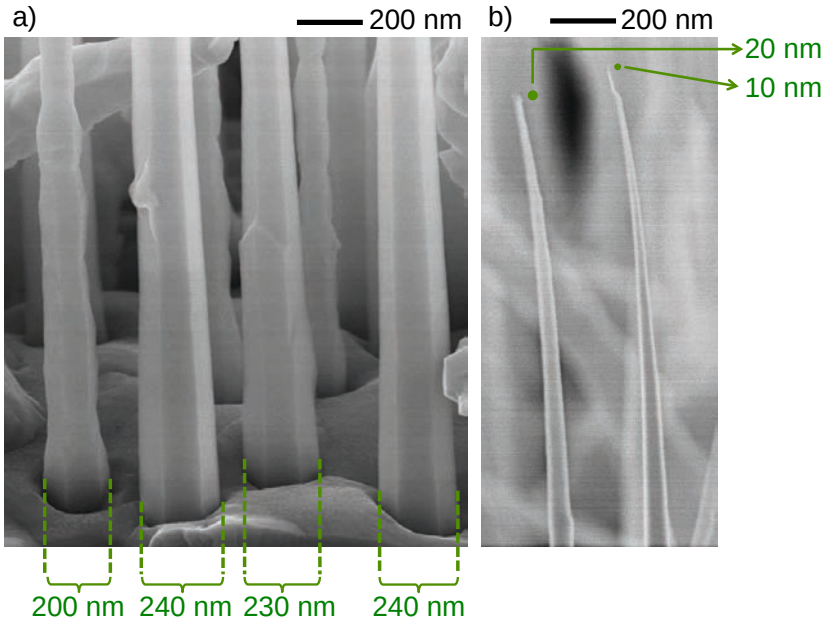

Figure 4.7 – SEM image of sample C. In a) the base of four NWs are shown with their correspondent diameter indicated in green. The facets are clearly seen. In b) the tips of two NWs are shown, the Au-droplet diameter is around $10-20$nm. The tilt of the images is 65°.

The roughness of the re-grown layer between the NWs is very high (see Figure 4.5). This probably indicates that the 2D growth of ZnMgTe is not optimized at 350°C. Note that the NW density seems higher for sample C than for the samples presented previously, but this is not the case. In fact, as the NWs are much bigger, the global image gives that impression but when we look in detail, there are only around 7 NWs/μm^2.

Remark that sample C is grown under stoichiometric flux ratio conditions, however, we do not observed any cylinder-shaped NWs. Instead, we observe that some of the cone-shaped NWs have at least one of their facets in a zig-zag shape. This type of NWs are generally referenced in the literature as "nanosaws" (one of them is indicated in red in Fig. 4.5). This NW morphology has been previously reported on the growth of II-VI semiconductor systems using thermal evaporation process and va-

por phase growth [98, 99]. The nanosaws found in this sample (and in other samples grown at high growth speed) are never straight, since they have one side larger than the other. Hence, they curved but in a random direction. They have been observed by TEM and their structure are zinc-blende with many defects. The nanosaws reported by Wang's group [98] present frequently a wurtzite structure. They suggested that the nanosaw morphology is a result of "atomic-termination induced asymmetric growth" due to the cation-terminated, catalytically active (0001) surface compared to the anion-terminated (000-1) surface which is chemically inactive. Even more, they propose that: "phase transformation from wurtzite to zinc blende could also be a factor in initializing the growth of the saw teeth". For the MBE grown ZnTe nanosaws observed in this work we have not clear evidence of a phase transformation. Clearly a detailed study of this structures will be necessary to obtain more information on the origin of the nanosaw morphology.

The reason why we do not observed cylinder-shaped NWs and why we observed the emergence of "nanosaws" in this sample is unknown to us. Nevertheless, we believe that it is not linked to the different substrate (CZT instead of GaAs) but to the fact that the flux of ZnTe is much higher. We have grown pure ZnTe NWs, under stoichiometric conditions using the same (high) ZnTe flux, over GaAs(111)B substrates (with the intermediate growth of a ZnTe buffer layer as usual) and we do not observed the growth of cylinder-shaped NWs.

A first explanation could be that they are hidden inside "forest" of NWs and we are not able to see them from the edge of the sample. This first hypothesis seems improbable since several samples, grown at high growth speed and under stoichiometric ZnTe flux ratio conditions, have been observed and no cylinder-shaped NWs have been spotted. A second explanation may be that given the size of the cone-shaped NWs, the NW density is not low enough, hence it creates competition between the NWs that do not favor the growth of cylinder-shaped NWs. This explanation can be ruled out since samples grown under a high flux and with a lower Au droplet density only show cone-shaped NWs. A third possibility could be that the diffusion length on the surface is reduced for a high ZnTe flux (high growth speed) favoring the formation of cone-shaped NWs. Further investigation needs to be done to unravel the correct reason for the absence of the cylinder-shaped NWs on this type of samples.

4.3 EDX analysis and modeling

In this section we describe the method used to analyze the EDX[4] measurements and we introduce a geometrical model used to quantify the local concentration of elements in the QD/core-shell NWs.

EDX measurements of a NW deposited over a microscopic grid are made in the form of hypermaps. An hypermap[5] is a data based map composed of a spectrum for each pixel. This means that we have access to a distribution map of each element detected (in the NWs presented in this work, we mainly detect: Te, Zn, Cd, O, Mg, Mn, C, Si and Cu). At this point we can only know if we detect -or not- an element (detection of a peak at a specific energy in the spectrum) in each pixel of the map. When possible, several hypermaps of a single NW are taken at different angles (rotation around the NW axis) to gain more information about the 3D structure and composition of the NWs.

Once the hypermaps are acquired, the raw data need to be processed to obtain quantitative information about the sample. The first step in quantification method is to attribute to each line detected in the spectrum an element and to determine the background. Once the background is subtracted from the raw spectrum, a deconvolution of each peak is performed. The area under each peak allows to obtain a first *relative* quantification: we can quantify how much more of one element is detected in one pixel than in another. This is done using the ESPRIT- QUANTAX software from Braker. In Figure 4.8 we show what a typical spectra from a CdTe QD inserted in a ZnTe NW looks like. The background to be subtracted is indicated in gray. In Figure 4.9 we observe the peaks used for the quantification after the deconvolution is performed.

To obtain an *absolute* quantification of the concentration of each element, a calibration of the EDX signal [counts/s] is needed. The measured EDX signal from a NW can be written as[6]:

$$I_i = I_0 \, N_0 \, \sigma_i \int \mathrm{x}_i(y) \, dY \tag{4.1}$$

[4]This characterization technique is introduced in section 1.3.3.

[5]Hypermap imaging was achieved using a FEI Tecnai Osiris S/TEM equipped with four silicon 157 drift detector and operated at 200 kV.

[6]To simplify, we suppose that there are no absorption effects. In that case, the measure intensity is equal to the generated intensity. The correction needed to take into account the absorption of X-rays is treated later in this section.

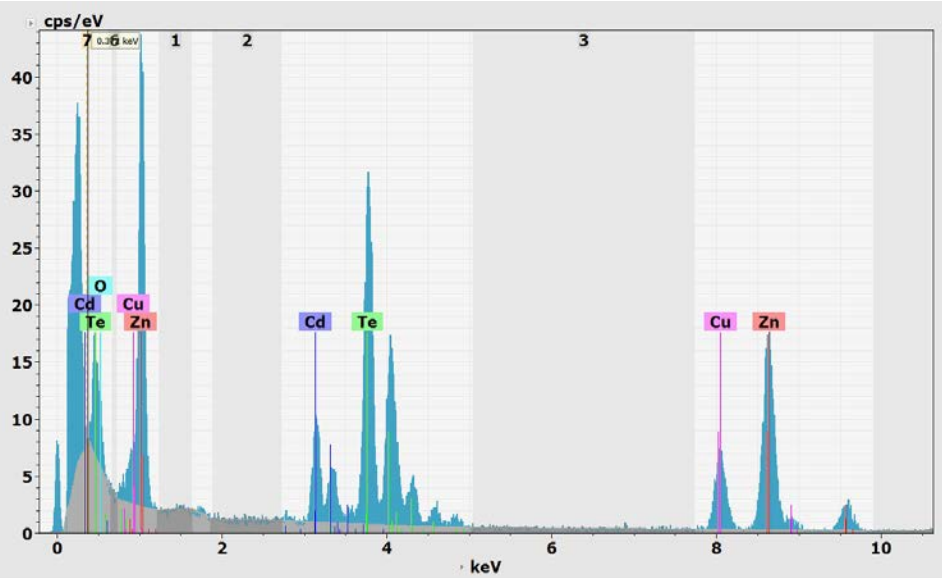

Figure 4.8 – The typical EDX point spectrum from a CdTe QD inside a ZnTe NW (measured at 30kV for a few seconds). For this measurement the EDX was coupled to a SEM. The background to be subtracted is marked in gray.

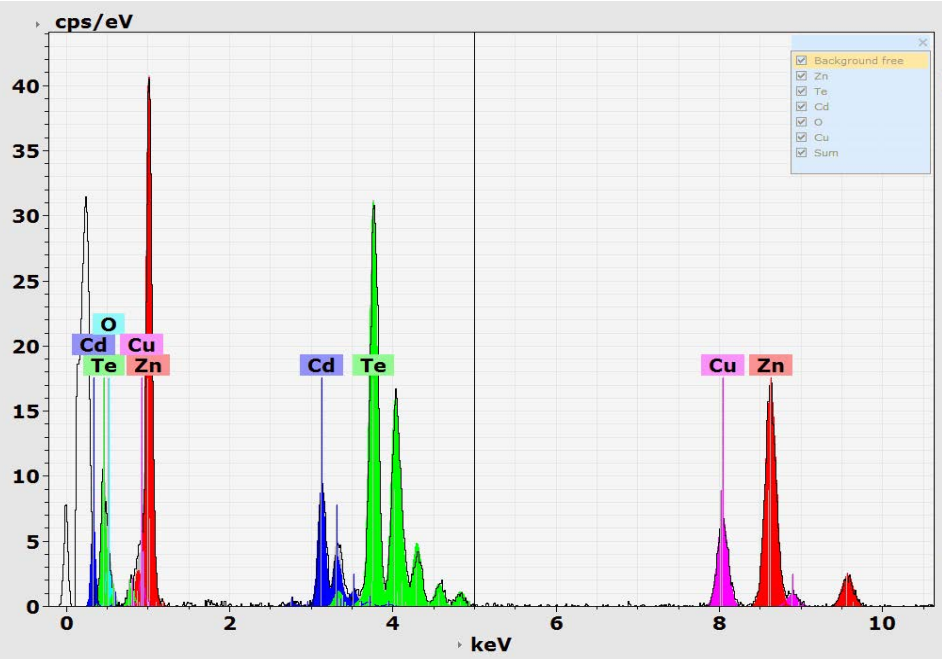

Figure 4.9 – The same EDX point spectra after deconvolution. Only the colored peaks will be used to quantify the concentration of each element.

In eq.4.1: i represents a particular element (e.g. Cd, Zn, Te...); I_0 is the excitation current [electrons/s]; σ_i is the scattering cross section (of atoms of element i that are proved) [cm^2]; N_0 is the density of available sites for atom i (for zinc-blende: $N_0 = 4/a^3$ [cm^{-3}], with a being the lattice parameter) and x_i is the proportion of an element i (from 0 to 1). We take the Z-axis along the NW growth axis, the Y-axis as the incident e-beam direction and the X-axis crossing the NW and perpendicular to Y and Z (see Figure 4.10). The maps of the distributions of elements are a projection of the composition in the X-Z plane.

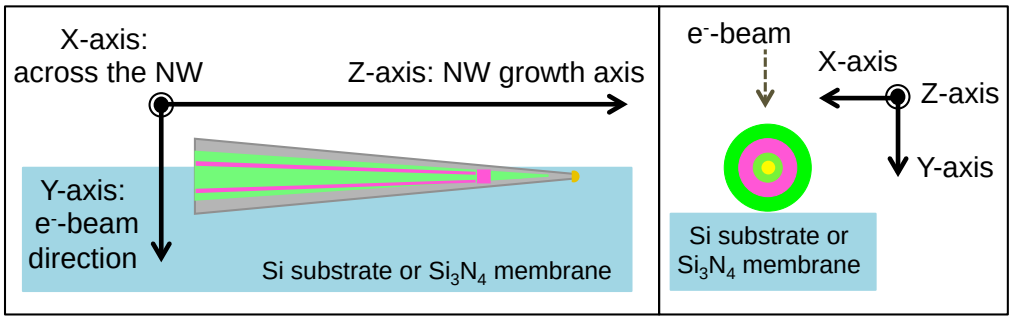

Figure 4.10 – Scheme of the orientation convention used in this chapter. The X, Y and Z direction are indicated.

If the measure is from a sample with uniform concentration, e.g. the case of a uniform layer or of a simple bare uniform NW, we can simplify eq. 4.1 to:

$$I_i(x) = I_0\, N_0\, \sigma_i\, x_i\, t(x) \quad (\text{If } x_i(y) \text{ uniform over } t) \tag{4.2}$$

where $t(x)$ is the thickness of material proved by the electron beam (varying from 0 to the NW diameter depending on the position along the X-axis). If the proportion of element x_i is uniform over the e-beam path, we can integrate eq. 4.1 over the whole length at each x position: $\int dY = t(x)$. The quantity $N_0 \times x_i$ is the number of atoms of element i per unity of volume. Hence, $N_0 \times x_i \times \sigma_i$ [cm^{-1}] is the number of scattering events per unity of length and per incident electron (related to the element i). Then, $N_0 \times x_i \times \sigma_i \times t(x)$ is the number of scattering events related to the element i per incident electron at each x position. And finally, the last quantity multiplied by I_0 gives us the EDX signal measured for element i at position x, which is the expression given in equation 4.2.

The EDX signal can be calibrated in order to translate the number of counts of element i detected per second to the total number of atoms of element i along the e-beam path. It is also possible to calculate the thickness (in length units) using the

ζ-factors [100]. The ζ-factors are calibration factors that allow us to calculate the thickness of material crossed by the e-beam from the EDX intensity. They are calculated using standard samples of each element [101]. These are samples where the thickness and the concentration of elements are well known. The ζ-factor for element i: ζ_i (i = Zn, Te, Cd, O, Mn, Mg) are defined from the expression of the EDX signal (equation 4.2) as:

$$I_i^{generated} = \frac{I_0\, \rho\, C_i\, t}{\zeta_i} \quad \text{with} \quad \zeta_i = \frac{m_i}{\sigma_i\, N_A} \tag{4.3}$$

where ρ is the mass density: $\rho = \sum_i x_i\, m_i \times N_0/N_A$ with N_A being Avogadro number and C_i is the mass concentration of the element i taken as: $C_i = \frac{x_i\, m_i}{\sum_i x_i\, m_i}$.

Since we know: C_i, ρ, t for the standard sample as well as I_0 and I_i, we can calculate the ζ-factor for each element. Once the ζ-factor of the elements detected in the NW are known, they give us access to the thickness crossed by the beam at each scanned position $t(x)$:

$$t_i(x) = \frac{I_i^{generated}\, \zeta_i}{C_i} \times \frac{1}{\rho\, I_0} \quad \text{with} \quad t(x) = \sum_i t_i(x) \quad \text{and} \quad \sum_i C_i = 1 \tag{4.4}$$

In addition, the absorption corrections related to the attenuation of the X-ray after crossing the sample thickness need to be taken into account. These corrections are different for each element and need to be calculated independently. It allows us to convert the *measured* EDX intensity to the *generated* EDX intensity.

$$I^{generated} = I^{measured} \times A(\rho, t, C) \tag{4.5}$$

The absorption correction depends on the sample density, the concentration and the thickness. Hence, it also depends on the path of the emitted X-ray to the detector (take-off angle). In this work we have calculated these absorption corrections for each element detected on each NW and found that for Zn, Te, Cd, Mn and Mg it is negligible and for O, the maximum correction is 5%. Note that even if the corrections are very small, they are included in all quantitative results presented in this chapter.

Finally, there are other parameters that need to be taken into account. For example, the beam resolution (taken as $\Delta x = 3$ nm) and the statistical error: $\pm\sqrt{N}$. N is the number of counts hence it depends on the measuring time. Keep in mind that the NWs are scanned for as-long-as-possible, to maximize the measuring time, in order to

acquire an amount of counts allowing to gain quantitative information. However, the measuring time is always limited by the drifting of the NW (probably due to charging effects) and by a strong beam damage induced on the NW[7].

Once the points mentioned previously are taken into account, we are able to obtain an *absolute* quantification of the EDX signal measured at each position of the hypermap. This means that we can calculate the number of atoms per unit of length or the % of atoms of element i ***averaged*** over the beam path. It is important to understand that the EDX signal that we measure, and that the analysis software translates to at.%, is *not the local* concentration of atoms i but it is the % of atoms i averaged over the sample thickness at the measuring position $t(x)$. Therefore, this analysis is not sufficient to study non-homogenous samples where the composition of elements is distributed differently over different volumes (e. g. heterostructures like QDs inserted in NWs and core-shell NWs). To quantify the *local* concentration of elements in a volume of the sample (for example in the QD), a geometrical model is needed to disentangle the contributions from each part of the structure (QD, core and shell).

It is useful to examine what type of profile we expect to obtain from the EDX signal of simple core-shell NWs. By considering different structures of ideal cylindrical NWs we set a reference point to help us understand the kind of EDX signal profile we can obtain from a complex core-multi shell NW that is not a perfect cylinder. The expected EDX profile of 4 different ideal NW-based structures is plotted in Fig. 4.11.

Case 1: a bare cylinder-shaped ZnTe NW

Let's start by considering the simplest scenario: the EDX imaging of a bare circular cylinder-shaped ZnTe NW. In Figure 4.11a, we show the profile of the EDX signal that we expect to obtain from a bare ZnTe NW. We expect to observe a projection of the NW, with the horizontal axis giving a measure of the radius of the cylinder and the vertical axis giving the NW thickness (since the intensity has been calibrated).

Case 2: a cylinder-shaped ZnTe NW with a CdTe QD

If we consider a CdTe cylindrical insertion inside the cylindrical ZnTe NW, we expect to see a Cd profile (in pink) equivalent to the one presented in case #1 but with a smaller diameter (horizontal axis) and with a smaller vertical axis since the thickness of the CdTe part is smaller than of the ZnTe part (profile shown in Fig. 4.11b). In this case, the Zn profile (in green) will be the same as in case #1 for $-r_1 > x > r_1$ and for $-r_1 < x < r_1$, the Cd part is subtracted since in this ideal case Cd+Zn=Te.

[7]The measuring time depends of the e-beam energy, on the NWs dimensions and on the position of the NW on the grid. For example, for a NW with 50 nm-thick base we can normally measure the EDX signal for less than 10 min at 200 KV before it moves or it is damaged.

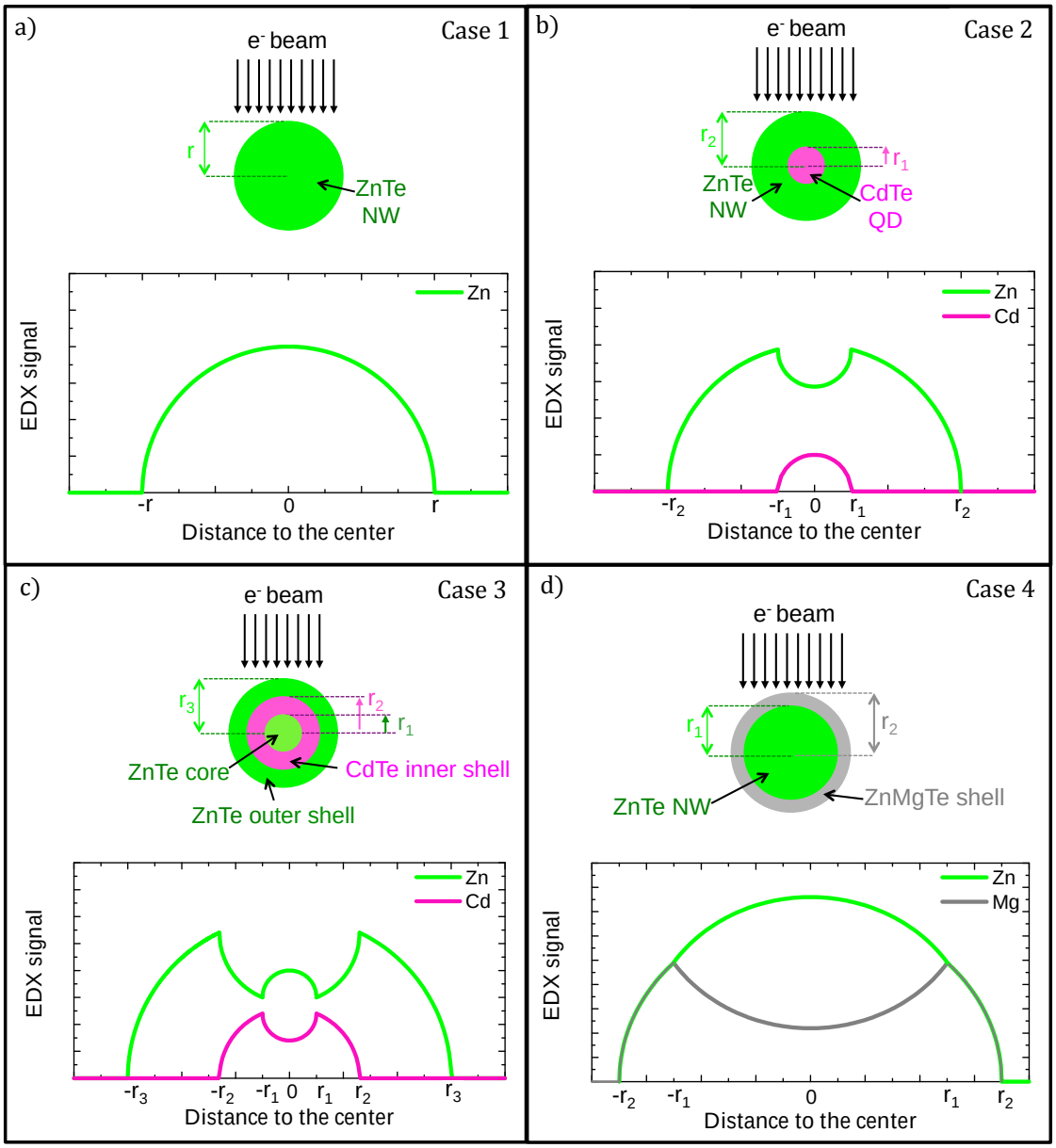

Figure 4.11 – Expected EDX signal profile for a) a bare cylinder-shaped ZnTe NW of radius r; b) a bare cylinder-shaped ZnTe NW of radius r_2 with a cylinder-shaped CdTe QD insertion of radius r_1; c) a cylinder-shaped ZnTe NW of radius r_1 with a cylinder-shaped CdTe inner shell of radius r_2 and an outer ZnTe shell of radius r_3; and d) a cylinder-shaped ZnTe NW of radius r_1 with a cylinder-shaped ZnMgTe shell of radius r_2.

Case 3: a cylinder-shaped ZnTe NW with a CdTe inner shell

When considering a ZnTe cylindrical core of radius r_1 surrounded by a cylindrical CdTe inner shell of external radius r_2 and covered again by a ZnTe outer shell of radius r_3, we expect to see a Cd and Zn profile as the ones shown in Fig. 4.11c. In this case, the Zn profile (in green) will be circular at the exterior part ($-r_2 > x > r_2$) and it will decrease in the zone $-r_2 < x < r_2$ where Cd is detected. The difference between the previous case is that in the center zone $-r_1 < x < r_1$ the Zn contribution increases again due to the ZnTe core. For the Cd profile (in pink), we expect the complementary behavior: no signal at the exterior, and a circular profile in the zone $-r_2 < x < r_2$ that diminishes at the center zone ($-r_1 < x < r_1$).

Case 4: a cylinder-shaped ZnTe NW with a ZnMgTe shell

Finally, a ZnTe cylindrical core of radius r_1 surrounded by a cylindrical ZnMgTe shell of radius r_2 should have the same circular profile for Zn and Mg at the exterior part $-r_1 > x > r_1$. At the interior part ($-r_1 < x < r_1$), the Mg content decreases (like for all the shells) and the Zn profile increases even more than in the case #1, since there is the additional contribution of Zn from the ZnMgTe shell.

To model a real NW, we use a simple geometrical model that uses a set of ellipses[8] placed one inside the other to simulate the QD insertion and the core-shell structure (software developed by E. Robin). In practice the software was limited to 5 ellipses. An homogenous concentration of elements is attributed to each ellipse. Five parameters can be adjusted for each ellipse: their axes length a and b[9], their tilt-angle θ and the X_0 and Y_0 position of their center (see Fig. 4.12).

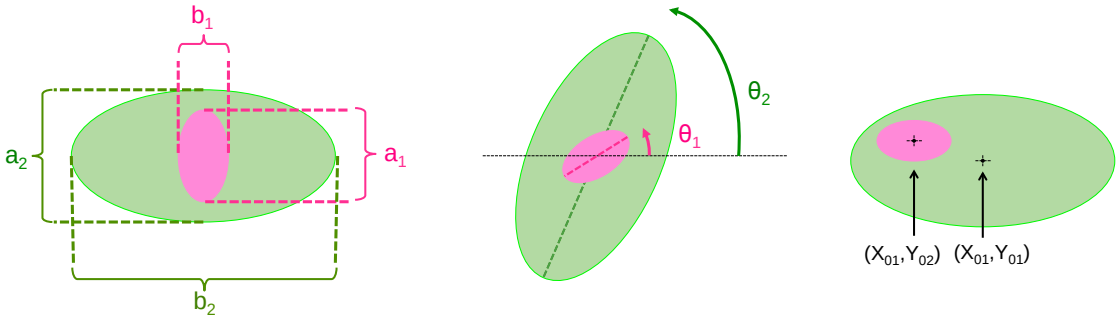

Figure 4.12 – The ellipse has five parameters that can be adjusted: their axes a and b, their tilt-angle and the position of the center (X_0, Y_0).

[8]Ellipses allowed us to fit better the EDX profile than circles. Nevertheless, a more precise (and complicated) approach would have been to use hexagons to take into account the facets of the NW.

[9]The equation of the ellipse is defined as: $\frac{4x^2}{a^2} + \frac{4y^2}{b^2} = 1$.

The quantification model is based on simultaneously tuning the parameters of the ellipses to achieve the best fit for the EDX signal from each of the elements present in the NW. This is done by tuning the composition (atomic concentration of Zn, Mg, Cd, Mn, Te and O), the zero position (X_0, Y_0), the tilt angle (Θ) and axes length of each ellipse used to model the NW. For example, for a ZnTe NW with a CdTe QD and a ZnMgTe shell, we can use one ellipse to model the QD insertion, another that corresponds to the ZnTe core of the NW and a third one that represents the ZnMgTe shell. Then, we need to define a set of parameters (for each ellipse) and then calculate the expected averaged EDX signal (projection of the composition of all the ellipses) for each element to compare it to the measured EDX profiles. To obtain a more detailed and realistic image of the NW, more ellipses can be used in order to reproduce variations on the concentration in each part of the NW (in this work we took up to 5).

The key point of this geometrical model is to succeed at finding a unique set of parameters that simultaneously fit the measured signal of all of the elements. To discriminate amongst possible solutions, not only all elements should be well fitted, but also the solution must also fit the elements from EDX measurements taken at different angles. Several hypermaps of the same NW, measured at different angles (rotation around the NW growth axis), need to be acquire to be able to reproduce the 3-dimensional shape and composition of the NW. The need of EDX measurements at several angles to obtain a single set of parameters that can describe completely the NW structure, is proven by the fact that ellipses with the same area, but different orientation and ellipticity, can have the same projection in the plane[10]. This means

[10] A simple demonstration shows this fact: an ellipse drawn inside a rectangle Δx, Δy is described by $x = \Delta x\, cos\Theta$, $y = \Delta y\, sin(\Theta - \Theta_0)$ where Θ_0 is the phase shift angle. A vertical cord is defined by opposite values of the parameter, Θ and $-\Theta$, giving the same value of $x = \Delta x\, cos\Theta$, and the thickness is $t(x) = y(\Theta) - y(-\Theta) = \Delta y\, sin(\Theta - \Theta_0) - \Delta y\, sin(-\Theta - \Theta_0)$. The projection is thus $x = \Delta x\, cos\Theta$, $t(x) = 2\Delta y\, cos\Theta_0\, sin\Theta$, which describes an ellipse aligned on the axes. Hence all ellipses defined by Δx, Θ_0 and $\Delta y = \frac{A}{\pi \Delta x\, cos\Theta_0}$ have the same projection of width Δx and area A. Here are three examples:

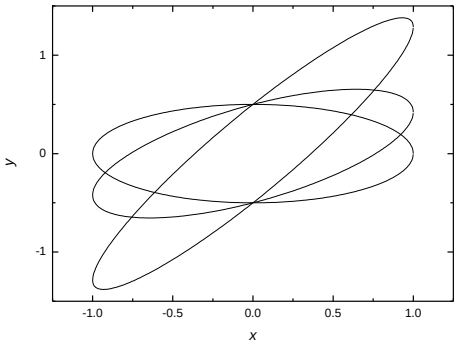

that if we measure only one projection of the NW, we can only determine: the position X_0, the apparent length projected along the x-axis and the total intensity (determined by the area of the ellipse). In that case, we won't be able to determine the Y_0 position (along the beam) nor the orientation of the ellipses. Therefore, we need to choose a set of parameters that also fits the elements of the hypermaps taken along different angles. In conclusion: the solution that fits the best *all of the elements from all the EDX hypermaps*, will be the closest representation of the NW.

4.4 Results

This section is divided into two main parts. In the first one we present the EDX results obtained for: i) a ZnTe/ZnMgTe core-shell NW (sample A); ii) a ZnTe NW with a CdTe QD insertion (sample B); and iii) a ZnTe/ZnMgTe NW with CdMnTe QD insertion (sample C). For the NW from sample A, the EDX data are obtained from uncalibrated measurements coupled to a SEM (instead of a TEM), therefore the results presented here are exploited using the usual EDX analysis software. For the other two NWs (sample B & C), the structure of the QD and of the core-shell structure is determined using the quantitative results obtained from the model developed to fit the signal measured on the hypermap (model presented in the last section).

In the second part, we briefly summarize the results of the optical properties of each sample. These NWs were studied by cathodoluminescence (CL), photoluminescence (PL), photon auto-correlation and magneto-optical techniques. In particular, several characterization measurements (EDX, CL, PL and magneto-spectroscopy) were performed on *the same* NW from sample C. The interpretation of the results presented in this section will be developed in section 4.5.

4.4.1 EDX of sample A: ZnTe NWs with a ZnMgTe shell

A first EDX measurement coupled to a SEM was performed on a NW from sample A to confirm the incorporation of Mg in the shell. In figure 4.13a we observe a map of the distribution of Mg in the NW. This map is obtained from an hypermap measurement, where only the EDX intensity of a single element (in this case Mg) is selected. By setting a fixed threshold of the measured intensity of that particular element, we can illustrate the distribution of the element in the region measured. Note that a map where the distribution of several elements are illustrated can also be obtain by independently choosing a threshold for the measured intensity of each element.

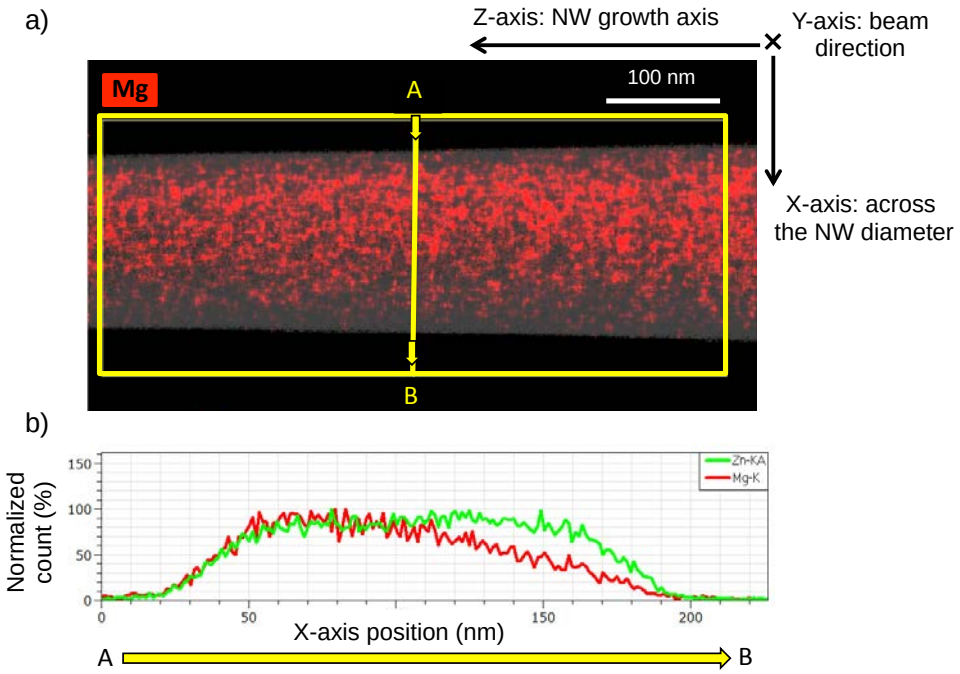

Figure 4.13 – a) EDX map of the Mg distribution in a ZnTe NW with a ZnMgTe shell from sample A. b) Normalized count of Mg (in red) and Zn (in green) as a function of the position across the NW diameter. The line scan is shown in yellow (averaged over the yellow rectangle).

In figure 4.13b, the Mg and Zn counts (normalized independently) are shown for a line scan crossing the NW's diameter (indicated on the map by a central yellow line which is averaged over the zone marked by the yellow rectangle). We observe that Mg is detected all around the NW, verifying that a ZnMgTe shell has been grown. However, we observe that the Mg content is not homogeneously distributed around the NW: one side of the NW has a higher Mg concentration than the other. Comparing the Zn profile, which represents the shape of the NW, with the Mg profile clearly shows that there is a considerable difference of Mg content in the two sides of the NW. Precise quantitative information about this EDX measurement is hard to obtain due to the low EDX signal and the absence of calibration on this particular microscope, therefore we cannot obtain a trustworthy percentage of Mg in the shell[11] or a reliable quantitative estimation of the difference of concentrations at the sides[12]. Despite the non-homogeneous Mg content in the ZnMgTe shell, the growth of this shell efficiently passivates the surface of ZnTe NWs (results shown in section 4.4.4).

[11] The expected Mg percentage calculated from the BEP measure of the ZnTe and Mg cell is 8%.

[12] Note that the ZnMgTe shell present on the NWs from sample C is measured by an EDX coupled to a TEM and a detailed quantitative study of the NW structure, including the shell, is presented in this chapter.

4.4.2 EDX of sample B: ZnTe NWs with a CdTe QD insertion

An EDX hypermap of a NW from this sample has already been shown in Fig. 3.10. That NW allowed us to determine the position of the QD inside the NW and to demonstrate the existence of CdTe inner-shell grown laterally on the cone-shaped NWs. Here, we study another NW from the same sample which is less kinked (the change of growth direction is less abrupt). In Figure 4.14 an HAADF image of the ZnTe NW with a CdTe insertion and it's corresponding hypermap showing the composition of Zn, Cd and O is presented. We clearly observe an elongated Cd-rich zone (Cd in pink) completely surrounded by a Zn-rich part (Zn in green), showing the QD insertion in the ZnTe NW. Below the insertion, we observe a core-shell structure composed of a Zn-rich core (ZnTe NW) enclosed by a Cd-rich part (CdTe inner shell), which is also surrounded by Zn-rich part (ZnTe shell). In brief, we detect a Cd-rich shell sandwiched in between a ZnTe core and shell. These data confirm the results presented previously in chapter 3.

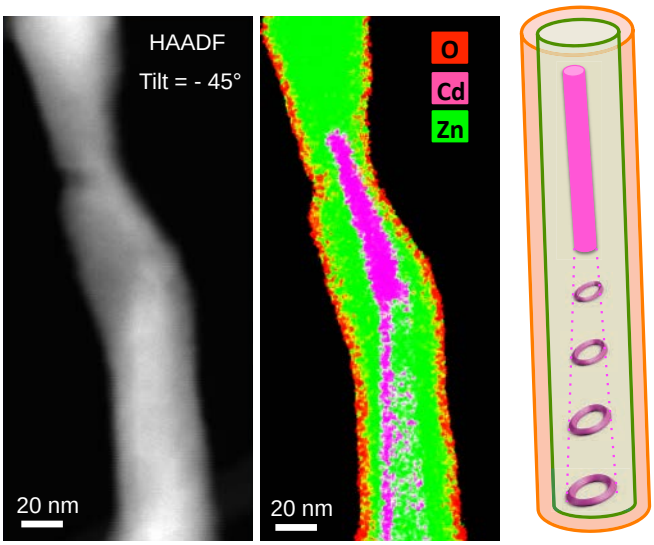

Figure 4.14 – EDX hypermap of a ZnTe NW with a CdTe QD insertion from sample B (tilt angle = −45°). On the left we show the HAADF image of the NW. On the middle, the EDX hypermap of the NW is shown with the distribution of Zn, Cd and O illustrated. Finally, on the right a simple scheme of the NW structure is presented. We clearly identify in the EDX map: the CdTe QD, the Cd-rich inner shell embedded between a ZnTe core and an exterior ZnTe shell and an oxygen-rich zone around all the NW.

Furthermore, an oxygen-rich shell surrounding all of the NW surface is observed (O in red). It corresponds to the oxidation of the ZnTe NWs, that occurs as soon as the sample is in contact with air when it is taken out of the MBE chamber to be transferred

to the microscope[13]. A simplified scheme of the structure of the NW is also presented in Fig. 4.14. In this section, we estimate quantitatively the composition of the three parts: the QD insertion, the Cd-rich shell and the native oxide on the surface.

At the level of the quantum dot insertion

In Figure 4.15 we present four hypermaps from the NW shown in Fig. 4.14. These were taken at different tilt angles (−75°, −45°, +45° and +62°)around the NW axis. We see that the QD is much larger in one direction (85 nm along the NW growth direction) than in the other two directions (in the plane perpendicular to the NW growth axis). Note that the QD follows the direction of growth, hence in the map at −75° and −45°, the NW slightly changes direction to the left and the QD follows this change. The same observation is made for the +45° and +62° map, but in those cases the change of direction is to the right, which is consistent with a rotation around the NW axis. Likewise, the shape of the QD seems to mimic the shape of the NW with a conic shaped: larger diameter at the lower part and a smaller diameter near the tip.

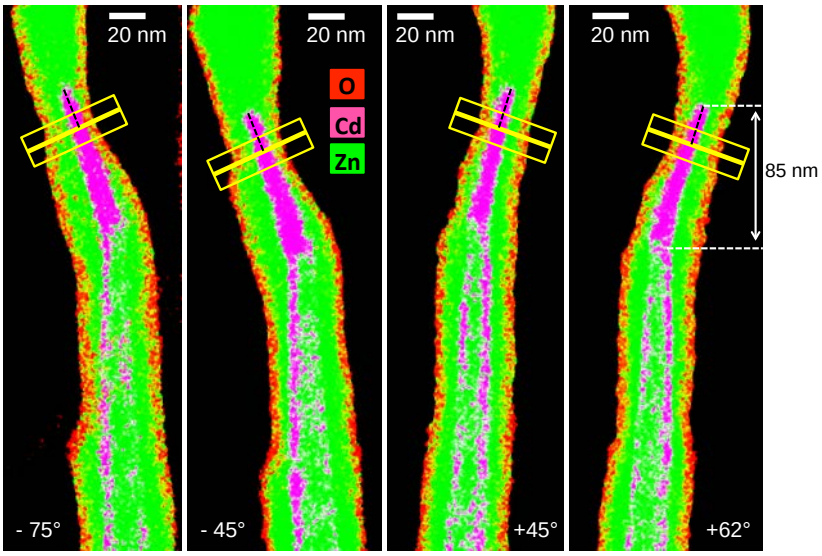

Figure 4.15 – EDX hypermaps of a ZnTe NW with a CdTe QD from sample B. Each hypermap is taken at a different tilt angle around the NW axis. We show hypermaps rotated at angles of −75°, −45°, +45° and +62° with respect to the initial (zero) position of the NW. The distribution of Zn, Cd and O are shown for each hypermap. The thicker yellow lines indicate the positions where the line scans (figure 4.16) were taken and the rectangle around it the zone where the line scan was averaged.

[13]More information on the strain effects produced by this native oxide shell on the luminescence of ZnTe NWs are discussed in appendix A.

Four line scans (one for each hypermap) were made at the level of the QD to quantify the concentration of the elements present in the NW. The position of these line scans was taken near the thinner part of the QD insertion and is indicated with yellow lines in Fig. 4.15. Each line scan is averaged inside the rectangle surrounding the central line. This averaging was made to have a higher count to obtain better statistical results. Note that the line scan changes of direction for negative and positive tilts in order to scan the same (as-close-as-possible) part of the NW.

The projected EDX signal, measured for Cd (in pink), Zn (in green), Te (in blue) and O (in red) with the line scan made at tilt = +45° are plotted in Figure 4.16 (the experimental data are represented with hollow circles linked with a thin line). Keep in mind that the projected EDX signal is an *average* concentration of an element detected over the whole NW thickness. The Cd profile shows a clear peak indicating the existence of a Cd-rich insertion (maximum at 4 nm to the left of the NW center). Correspondingly, at the same position, we observe a depression in the Zn profile. In the exterior zone of the NW, two peaks are observed for the O and Zn profile. These indicate the existence of a shell containing both elements. Note that the Te signal does not follow this typical "shell" profile. We observed that the Te signal decreases near the NW edge, indicating a low content of Te in the exterior of the NW.

Along with the experimental results, we present two different models to fit the data (represented with thick continuous lines in Fig. 4.16): model A in the left column and model B in the right one. Each model uses a set of parameters to *simultaneously* fit the profiles of the four elements for the four hypermaps made at different tilts. In Figure 4.17 the values of the parameters used in each model are given: horizontal and vertical axis (H-axis and V-axis) are given in the tilted coordinate system, X_0, Y_0 and the atomic concentrations[14] (at.%) for each ellipse. The ellipses of each model are also plotted in Fig. 4.17 (filled points) to illustrate the structure of the NW according to each model. Additionally, the thickness at each point of the line scan is calculated using equation 4.4 and plotted in Fig. 4.17 (black line).

Description of model A (see figure 4.17):
Model A considers the QD as a pure CdTe center of 5-6 nm in diameter (ellipse #1) surrounded by a 3-5 nm-thick CdZnTe zone with 26% of Cd and 24% of Zn (ellipse #2). This QD is embedded in an almost pure 4 nm-thick ZnTe zone (Cd 1.5%, ellipse #3). The exterior zone of the NW is modeled with two ellipses, an intermediate 3.5-5 nm-thick shell with 45% Zn, 35% Te and 30% O (ellipse #4) and a purely 2.5 nm-thick ZnO (50-50%) exterior shell (ellipse #5).

[14]Note that in EDX characterization the concentrations are usually given in at.% (total % of all elements is equal to 100%). This notation should be distinguished from the traditional notation for SC compounds where only one sub-lattice is taken into account (for example: $Cd_xZn_{1-x}Te$).

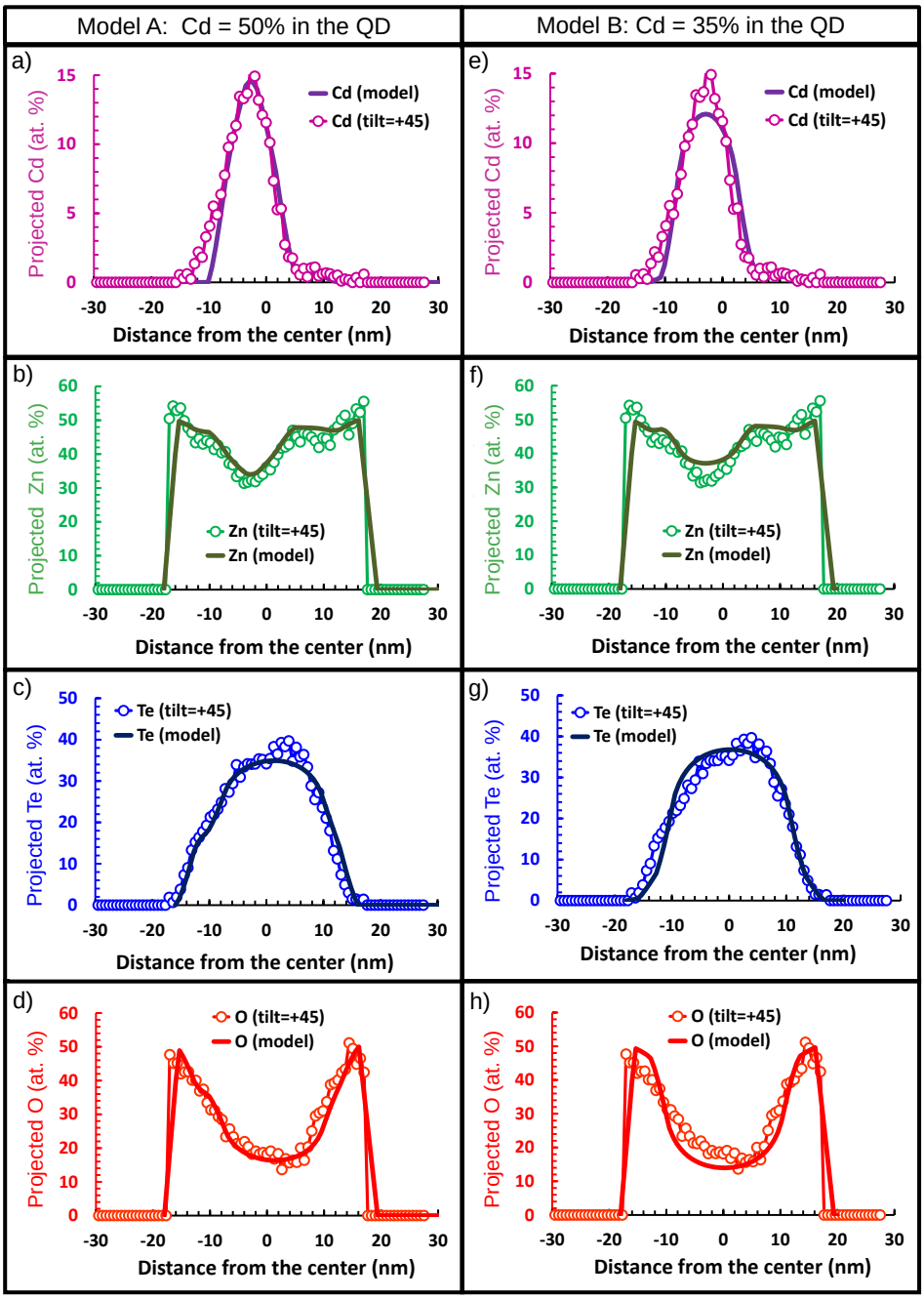

Figure 4.16 – Cd, Zn, Te and O compositions (at.%) averaged over the NW thickness obtained from the EDX signal of a NW from sample B using the line scan of the hypermap taken at tilt= +45°. The EDX data (measured) is plotted with empty circles. Note that the data outside the NW are set to zero. The color code is: Cd in pink, Zn in green, Te in blue and O in red. Two different models are used to fit the data (continuous line). The left column shows the data fitted with model A (QD with 50% of Cd, i.e., pure CdTe) and the right column fitted with model B (QD with 35% of Cd).

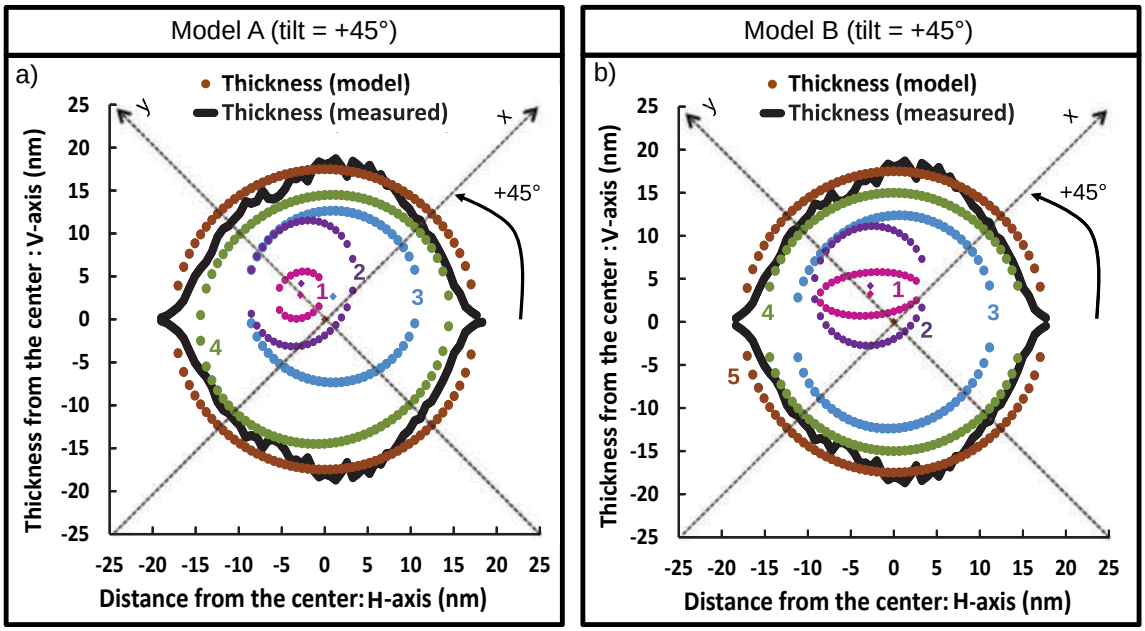

c) Model A	Local concentration (at.%)				Size (nm)		Position (nm)		Orientation
Ellipse	Zn	Cd	Te	O	H-axis	V-axis	X_0	Y_0	Θ (deg)
1	0	50	50	0	6	5	0	4	0
2	24	26	50	0	12	15	1	4.9	-25
3	48.5	1.5	50	0	20	23	2.5	1	25
4	45	0	10	45	30	30	0	0	0
5	50	0	0	50	35	35	0	0	0

d) Model B	Local concentration (at.%)				Size (nm)		Position (nm)		Orientation
Ellipse	Zn	Cd	Te	O	H-axis	V-axis	X_0	Y_0	Θ (deg)
1	15	35	50	0	12	5	0.4	4.2	40
2	24	26	50	0	13	14	1	4.9	25
3	48.5	1.5	50	0	25	23	0	0	-25
4	45	0	25	30	30	30	0	0	0
5	50	0	0	50	35	35	0	0	0

Figure 4.17 – The NW structure is presented according to model A (left column) and B (right column). In a and b: plot of the ellipses used for each model (filled points) and of the thickness calculated from the measurement (black continuous line). Each ellipse has a number increasing from the interior of the NW to the exterior and is identified by a different color. In c and d: the set of parameters used in each model is shown for each ellipse (same color). The parameters for each ellipse are: the concentration of each element (Zn, Cd, Te and O), the horizontal H-axis and the vertical V-axis (in the tilted coordinate system), the center position (X_0, Y_0) and the orientation (last two parameters are given in the non-tilted coordinate system).

Description of model B (see figure 4.17):
Model B takes the QD as a ternary alloy with a center part containing 35% of Cd and 15% of Zn, which is represented as an elongated ellipse of axis length: 12 and 5 nm (ellipse #1). This central part is surrounded by a less Cd-rich shell containing 26% of Cd and 24% of Zn (ellipse #2). This ellipse has almost the same value for the horizontal axis (H-axis) and a thickness of 4.5 nm along the vertical axis (V-axis) diameter. Notice that this ellipse is almost equal in model A. The ZnTe zone (ellipse #3) has the same composition and similar thickness (6-4.5 nm) as in model A. Finally, there is a ZnTeO inner shell (ellipse #4) of 2.5-3.5 nm-thickness with higher O content (in comparison to model A): 45% O and 10% Te and an exterior pure ZnO shell which is identical for both models.

It is clear that model A fits better the data than model B. This is also true for all the profiles of the remaining three hypermaps (not shown here). Nevertheless, we present both models to show how the parameters in the model can be varied to represent the structure of the NW and to obtain a fit that follows well the trend of all the data. The interpretation of the results presented here will be discussed in section 4.5.

A third model is proposed (model C) to focus on the structure of the QD. In Figure 4.18, the projected Cd EDX signals are shown for two different hypermaps (tilt= $+45°$ and $-75°$) along with the fit obtained from model C. The fit of the tails in the peak of the Cd signal is clearly improved with respect to the previous two models, which indicates a closer representation of the QD structure.

Description of model C (see figure 4.18):
The NW structure is modeled using 4 ellipses for the Cd-rich zone (QD) and one for the NW. This model ignores the native oxide (since it does not impact the QD) and takes the exterior zone of the NW as a single ellipse (#5) composed of only ZnTe (50-50%). Hence, the O and Te concentration are fixed to 0% and 50% for all the ellipses. The rest of the ellipses are used to model the QD, with increasing Cd concentration when we get closer to the center of the QD. This means that this model fits very well the Cd profile (for all the tilts) in comparison to model A and B (see the left tail of the peak) but it does not fit the O and Te signal (they are taken as constants). The fit of Zn is relatively good at the level of the QD but at the exterior zone is overestimated since the Te is taken as 50% which is not the reality. Despite this, model C is interesting since it is useful to model the structure of the QD insertion.

Model C represents the QD with a first ellipse (circle of 6 nm of diameter) containing pure CdTe (50-50%). This central core is surrounded by three ellipses with decreasing Cd concentration: ellipse #2 with 35%, ellipse #3 with 16% and ellipse #4 with 7%. This is a smoother way to simulate de decrease of Cd content and the increase of Zn content from pure CdTe to pure ZnTe. The part that contains a mix of CdZnTe is about 9-14 nm thick. The structure of the NW presented in Figure 4.18 shows clearly that the QD is not centered at the middle of the NW.

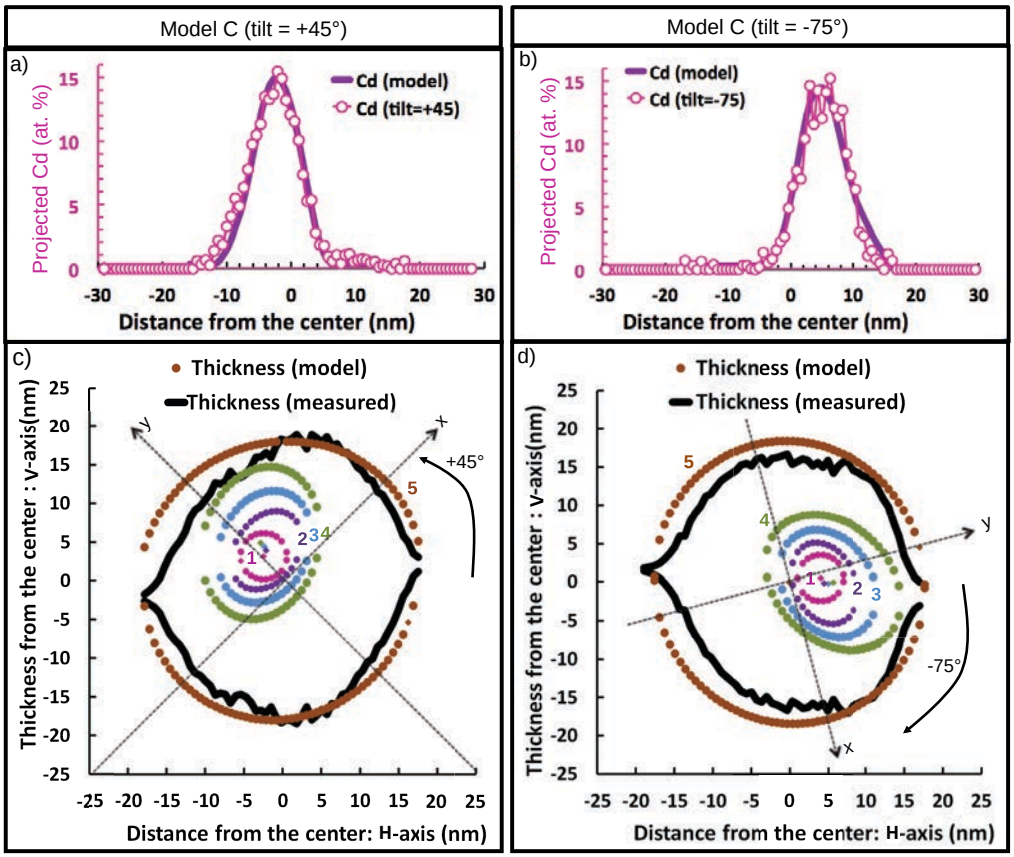

e)	Local concentration (at.%)				Size (nm)		Position (nm)		Orientation
Ellipse	Zn	Cd	Te	O	H-axis	V-axis	X_0	Y_0	Θ (deg)
1	0	50	50	0	6	6	0.5	4	0
2	15	35	50	0	8	11	1.28	4.29	10
3	34	16	50	0	11.5	15	1.45	4.78	20
4	43	7	50	0	15	20	1.46	5.46	30
5	50	0	50	0	35	37	0	0	0

Figure 4.18 – The Cd composition (at.%) averaged over the NW thickness is shown for 2 different hypermaps (pink hollow circles) taken at tilt =+45 (same as Fig. 4.15) and tilt = -75. The NW structure is presented according to model C for both hypermaps. The corresponding ellipses and the calculated thickness from EDX measurements (in a black continuous line) are plotted. Each ellipse has a number increasing from the interior of the NW to the exterior and is identify by a different color. The set of parameter used in each model is shown for each ellipse (same color). The parameters for each ellipse are: the concentration of each element (Zn, Cd, Te and O), the horizontal H-axis and the vertical V-axis (in the tilted coordinate system), the center position (X_0, Y_0) and the orientation (last two parameters are given in the non-tilted coordinate system).

Structure of the CdTe QD insertion (sample B)

In summary, we used three different models to discern the structure of the QD insertion in a NW from sample B. Model A and B, propose two different QD/NW structures using a global approach that takes 2 ellipses to describe the QD and 3 to describe the oxidized NW. It is clear from Figure 4.16 that model A gives a closer representation of the NW than model B, since it provides a better fit of the data. We conclude that the Cd concentration in the central ellipse is not 35% (model B) but 50% as proposed from model A (see Figure 4.17). Keep in mind that when the Cd concentration is slightly reduced in model A, for example if in the most internal ellipse (#1) we take 45% of Cd and 5% of Zn instead of 50% of Cd and 0% of Zn, the fit does not reach the maximal height of the measured Cd peak. Therefore, it indicates a pure CdTe insertion in the zone determined by the size of the ellipse (#1).

In comparison, model C focusses on describing the structure of the QD and leaves aside the structure of the NW around it. It smoothly models the transition between a pure CdTe QD and a pure ZnTe NW around it by taking 4 ellipses to model the Cd-rich regions and only one for the ZnTe NW. Accordingly, model C certainly describes better the QD insertion which is proven by the fact that it fits better the Cd projected concentration (compare Fig.4.18 a/b to Fig.4.16 a/e). Therefore, the QD from a NW of sample B can be described according to model C as: a cone-shaped insertion of 85 nm of height, that in it's thiner part contains a circular pure CdTe core of 6 nm of diameter. This CdTe core is surrounded by an elliptical 4.5-7 nm thick ZnCdTe shell. The Cd content on the ZnCdTe shell decreases from the interior (50%) to the exterior (0%). Neither the pure CdTe core nor the Cd-rich shell are center at the middle of the NW. The QD is surrounded by a oxidized ZnTe NW of 70 nm of diameter.

Below the quantum dot insertion

Let's consider the Cd-rich shell grown by lateral growth. In Figure 4.19, we present the results from a line scan performed at the level of the Cd-rich shell just below the CdTe insertion. From the hypermap image (in d), we notice that the left side of the Cd-rich shell seems to be thicker and more continuous along the growth direction. The difference between the two sides is confirmed by the projected Cd signal, which shows two peaks[15] with a higher projected Cd content for the left peak. Actually, the same behavior is observed for all the hypermaps (Fig. 4.15): for $-75°$ and $-45°$ it is the left side and for $+45°$ and $+62°$ it is the right side. This behavior (higher projected Cd

[15]These peaks are the typical profile of a shell. They correspond to the exterior zone where the e-beam crosses the Cd-rich shell without traversing the core, see figure 4.19b and 4.11.

content in one side than in the other) was also observed from an another NW of sample B (shown in Fig. 3.11). Note that in between the two peaks, the projected at.% of Cd decreases but it does not reaches zero. This is normal because at the position of the core we still detect the Cd-rich shell on the top and bottom part (see central scheme in Fig.4.19b). In Fig.4.19d, the parameters for the model that fits best the data are given.

Model description: below and near the QD (see figure 4.19):
The model consists of a pure elliptical ZnTe core with axes length of 10-12.5 nm (ellipse #1) surrounded by a CdZnTe zone with 22% of Cd and 28% of Zn (ellipse #2) of thickness 4.2-6 nm and which is not centered with the core (to fit the left peak which is higher than the right one). This Cd-rich shell is surrounded by an almost pure ZnTe shell (Cd% is only 0.9%) with 4.5-7.5 nm of thickness (ellipse #3). The exterior zone of the NW is modeled with two ellipses, an intermediate 3.5 nm-thick shell with 34.1% Zn, 0.9% Cd, 50% Te and 15% O (ellipse #4) and a purely ZnO exterior shell (50-50%) of 4-5.5 nm (ellipse #5). Again, for this line scan we can calculate thickness (black continuous line in Fig. 4.19) using Eq. 4.4. Note that we clearly observe 6 facets.

In Figure 4.20, we present a new hypermap of the same NW but taken at the base, where the NW broke from the substrate. Once again, we took several hypermaps (four different angles) to validate the model used. In the figure, we show the projected Cd atomic % and the set of parameters used to model all the elements (for the four hypermaps), as well as a plot of the corresponding ellipses. The projected Cd profile at the base is similar to the one below the CdTe insertion, but here the peaks are further away from each other and we distinguish more clearly the plateau of Cd between the two peaks. Once more, the left peak has a higher average Cd concentration than the right one.

Model description: at the base of the NW (see figure 4.20):
The model takes the structure of the NW at the base as a thick pure ZnTe core with axis length 35-37 nm (ellipse #1) surrounded by a CdZnTe zone with 22% of Cd and 28% of Zn (ellipse #2) and of thickness 4.5-5 nm (the same as before). This Cd-rich shell is surrounded by a Zn-rich shell with 46% of Zn, 4% of Cd and 50% of Te which has 5.5-7.5 nm of thickness (ellipse #3). The intermediate shell that follows is only 1.5 nm thick in one direction and 8.5 nm in the other and has a composition of 38.5% Zn, 1.5% Cd, 40% Te and 20% O (ellipse #4). Finally, the exterior shell is quite thin: 3-3.5 nm and only contains Zn and O: 55% and 45% (ellipse #5). The coned-shaped of the NW is clearly shown by the much thicker dimensions of the ellipses at the base. The interpretation of the results presented here will be discussed in section 4.5.

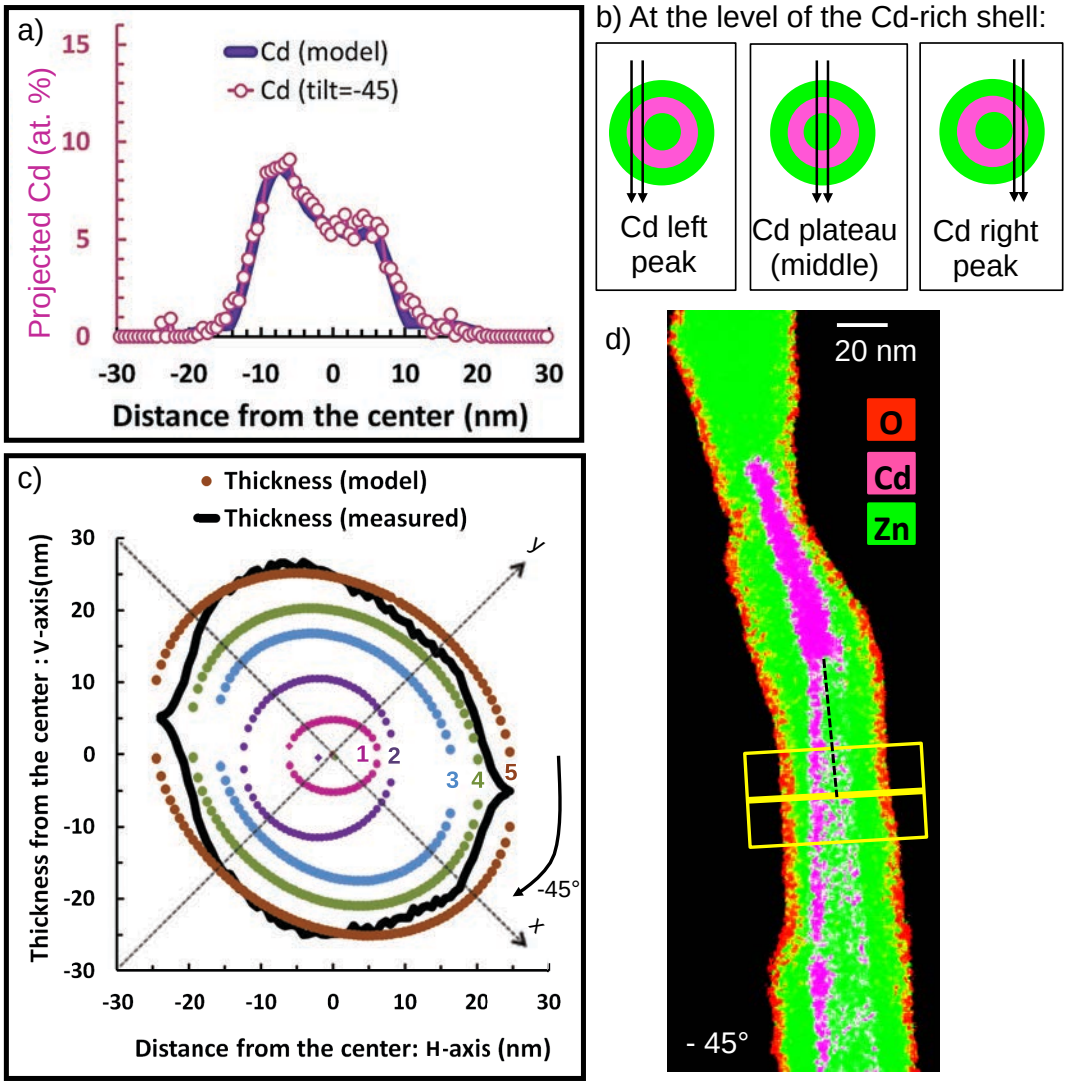

e)	Local concentration (at.%)				Size (nm)		Position (nm)		Orientation
Ellipse	Zn	Cd	Te	O	H-axis	V-axis	X_0	Y_0	Θ (deg)
1	50	0	50	0	10	12.5	0.2	0	-45
2	28	22	50	0	22	21	0.5	-2	-45
3	49.1	0.9	50	0	37	30	0.5	0	-5
4	34.1	0.9	50	15	44	37	0.5	0	-5
5	50	0	0	50	55	45	0	0	0

Figure 4.19 – a) Plot of the Cd composition (at.%) averaged over the NW thickness obtained from a line scan taken below the QD insertion with its corresponding fit (continuous line). b) Scheme of the different parts of the NW that are probed. c) Plot of the set of ellipses used to model the NW in order to fit all the data. d) Hypermap showing the position of the line scan (in yellow). e) Set of parameters that fit the signal of all the elements from the 4 hypermaps (lines scans at the same position).

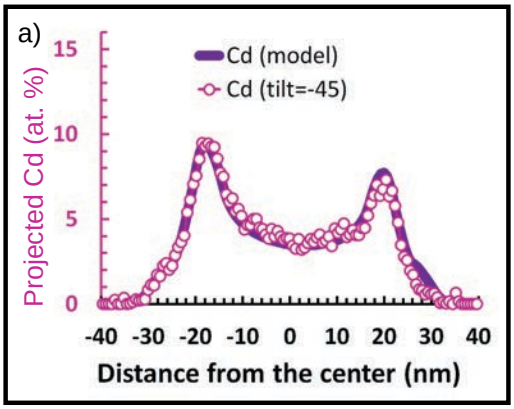

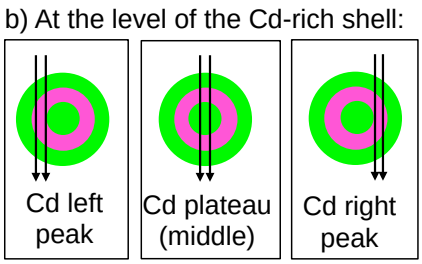

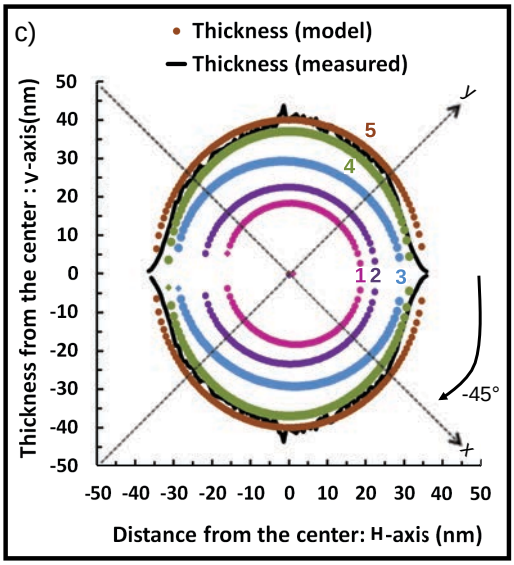

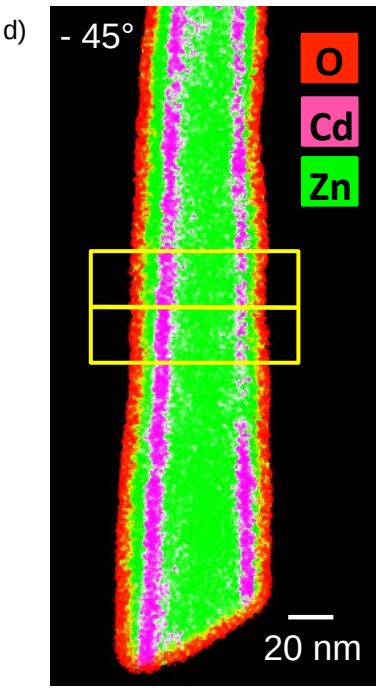

e)	Local concentration (at.%)				Size (nm)		Position (nm)	
Ellipse	Zn	Cd	Te	O	H-axis	V-axis	X_0	Y_0
1	50	0	50	0	35	37	0	0
2	28	22	50	0	45	46	0.13	-0.48
3	46	4	50	0	60	57	0	0
4	38.5	1.5	40	20	63	74	0	0
5	55	0	0	45	70	80	0	0

Figure 4.20 – a) Cd composition (at.%) averaged over the NW thickness obtained from a line scan taken at the base of the NW (marked in yellow in d) and a fit of the data is also plotted with a continuous purple line. b) Scheme of the different parts of the NW that are probed at different positions. c) Plot of the set of ellipses used to model the NW in order to fit all the data (parameters that fit the signal from all the elements from the lines scans taken from 4 different hypermaps at the same position). The thickness measured is also presented (in a black continuous line). Each ellipse has a number increasing from the interior of the NW to the exterior and is identified by a different color. e) Set of parameter used in each model is shown for each ellipse (same color).

4.4.3 EDX of sample C: ZnTe NWs with a CdMnTe QD insertion and a ZnMgTe shell

EDX imaging of a single NW of sample C (described in section 4.2) was performed under the same conditions as sample B but using a 50 nm-thick Si_3N_4 home-made microscopy membrane (courtesy of A. Artioli). Aluminum patterns on the membrane allowed to retrieve easily the position of the NW, hence to perform several characterization methods on the same NW: EDX, TEM, CL, micro-PL and magneto-optical measurements. To transfer a NW from the as-grown sample to the home-made membrane, we use a dual beam FIB/SEM machine (Zeiss NVision 40 DualBeam) equipped with a micro-manipulator (collaboration with J. F. Motte).

In this section, we treat the EDX measurements performed on a NW from sample C. The other measurements performed on the same NW will be treated in section 4.4.4. Unfortunately, it was not possible to measure several EDX hypermaps at different tilts from this NW (sample C) due to a technical problem of the substrate holder. Therefore, we only measured the NW along one orientation which limits the information on the distribution of elements along the beam direction (Y-axis). Thus, for this NW it is not possible to determine exactly the position of the QD along the beam direction (Y_0 position).

However, we acquired hypermaps of different zones of the NW, in particular one that zooms into the area where the QD is placed. A HAADF STEM image along with two EDX maps showing the distribution of Cd and Zn and of Mg and O independently are presented in Fig. 4.21. Notice that the NW shown was broken when removed from the as-grown sample at the base and also at the tip. Although this implies that we do not observe the Au droplet, fortunately in Fig. 4.21b we observe clearly a small Cd-rich insertion (in pink) placed below the breaking point of the tip. In Fig. 4.21c, an O-rich shell all around the NW is observed, showing clearly that an oxidation process takes place also when the last part of the NW growth is changed from ZnTe to ZnMgTe. Moreover, in the map we detected a distribution of Mg that differs from the oxygen one and that is stronger in one side (lower part) than in the other.

The results obtained from this NW are divided into three main parts: i) the Cd-rich insertion (results are taken from a zoomed hypermap on the zone); ii) the zone below the Cd-rich QD (using the data from the hypermap presented in Fig. 4.21) and iii) the base of the NW (results from a different hyper map taken at the NW base). The interpretation of all these results will be presented in section 4.5.

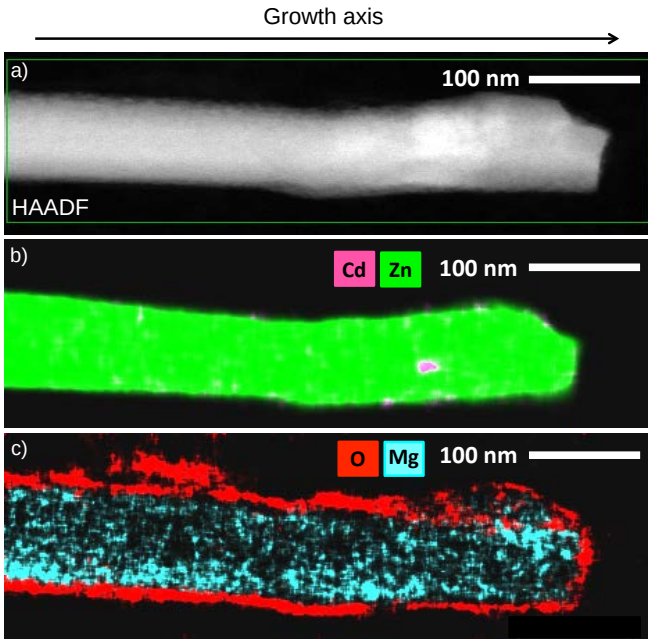

Figure 4.21 – a) HAADF STEM image of a ZnTe NW with a ZnMgTe shell and a CdMnTe QD insertion from sample C. b) EDX map of the NW is shown with the distribution of Zn and Cd. c) EDX map of the same NW is presented but with the distribution of O and Mg. We clearly identify the Cd-rich QD, the O-rich exterior shell around all the NW and the presence of Mg on the NW.

At the level of the quantum dot insertion

We are interested in the composition and size of the QD. To study it in details we made a zoomed hypermap of the zone where the QD insertion was detected (Fig. 4.23b) and a line scan crossing only the part where the Cd-rich insertion was visible (shown in yellow). In Fig. 4.22 we present the projected concentration of Cd, Zn, Mn and Mg obtained from the line scan. In Fig. 4.22a, the Cd-rich section is clearly observed (to the right of the NW center). In Fig. 4.22c, we distinguish a small Mn peak at the same position than the Cd peak (placed between 2 and 14 nm). Correspondingly, in Fig. 4.22b, we observe that the Zn distribution decreases at the same position. Finally, in Fig. 4.22d a Mg signal is homogeneously detected over all the line scan. To fit the results presented in Fig. 4.22 we use the same 5-ellipses model as for the NW from sample B. The parameters of the model and the illustration of the position and size of the ellipses are presented in Fig. 4.23a/c.

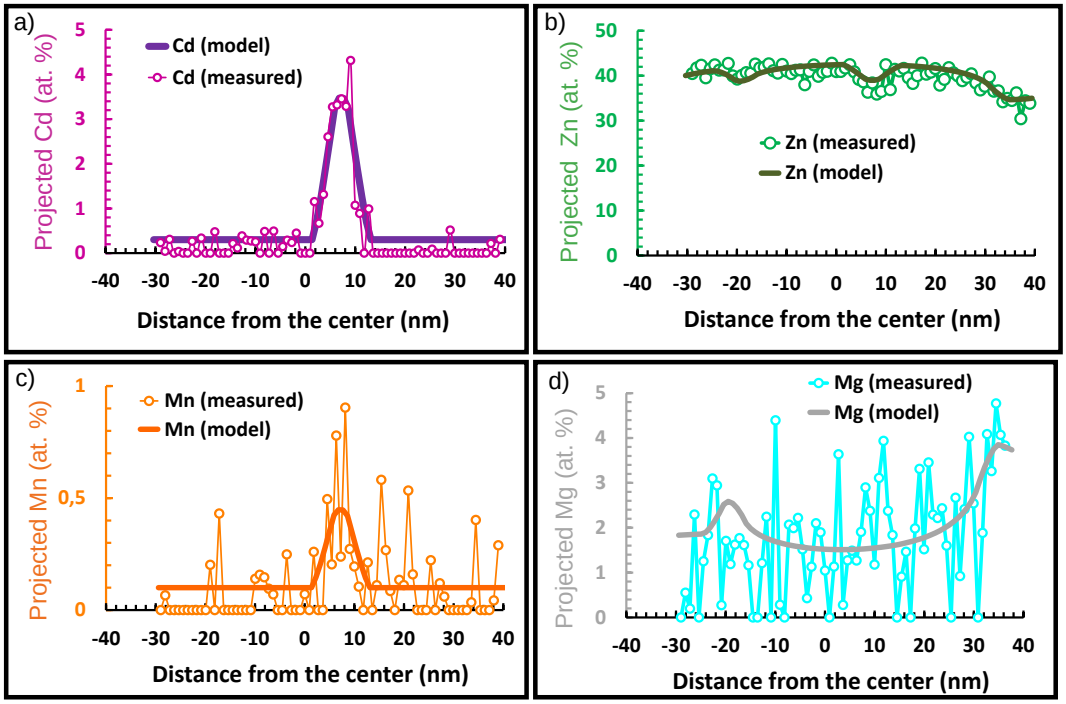

Figure 4.22 – Cd, Zn, Mn and Mg compositions (at.%) averaged over the NW thickness obtained from the EDX map shown in Fig. 4.23b (NW from sample C). The EDX data is plotted with empty circles. The fits of the data are also shown with continuous lines. The parameters of the model used for the fits are shown in Fig. 4.23c. The color code is: Cd in pink, Zn in green, Mn in orange and Mg in aquamarine and gray.

Model description: at the QD level (see figure 4.23):

According to this model, the NW structure consists of a CdMnTe center with 45% of Cd, 5% of Mn and 50% of Te, and with a diameter of 8 nm (ellipse #1). This center is surrounded by an almost pure ZnTe zone with 49.6% of Zn and 50% of Te with thickness of 25 nm (ellipse #2). This thick ZnTe part is centered around the CdMnTe QD and not around the center of the NW. The ZnTe core containing the CdMnTe QD inside it, is surrounded by a thinner zone of the NW (thickness 7.5-10 nm) that mainly contains 33.6% Zn, 50% Te, 5% Mg and 11% O (ellipse #3). The remaining two ellipses also contain Zn, Te, O and Mg. In this model, as we move further away from the center the Te and Mg content decreases and the O content increases.

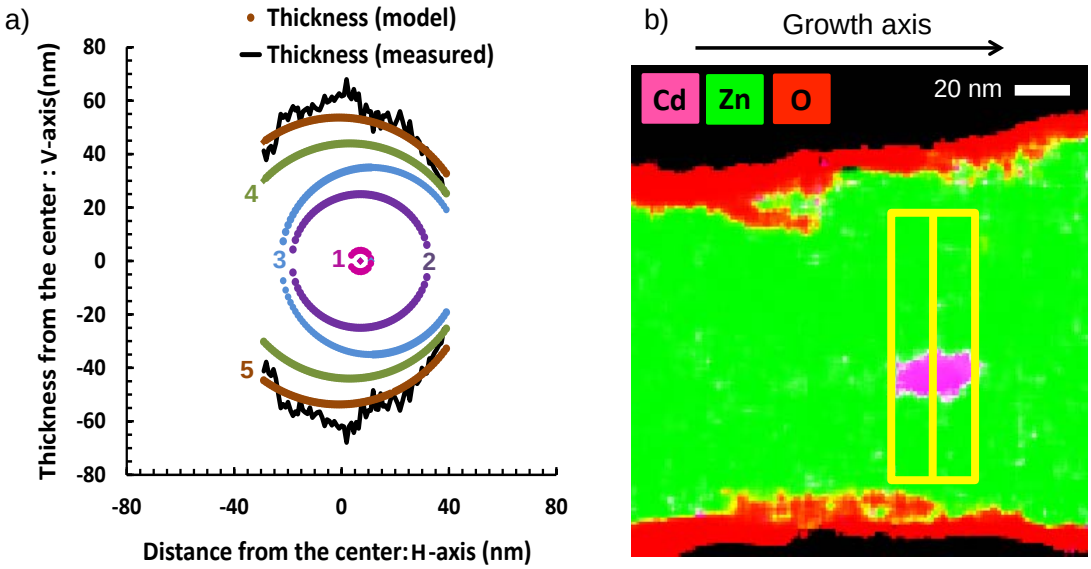

c)	Local concentration (at.%)						Size (nm)		Position (nm)	
Ellipse	Zn	Mg	Cd	Mn	Te	O	H-axis	V-axis	X_0	Y_0
1	0	0	45	5	50	0	8	8	7	-
2	49.6	0	0.3	0.1	50	0	51	50	7	-
3	33.6	5	0.3	0.1	50	11	67	70	11	-
4	45.6	2	0.3	0.1	41	11	88	88	3	-
5	29.6	1.5	0.3	0.1	41	27.5	101	107.4	-1	-

Figure 4.23 – a) The ellipses of the model used to fit the data shown on Fig. 4.22 are plotted with filled points. Each ellipse has a number increasing from the interior of the NW to the exterior and is identify by a different color. b) Image of the map taken from the zoomed zone of the NW where the Cd-rich insertion was detected. The line scan is marked in yellow. c) The set of parameters used to model the data for each ellipse. The parameters are: the concentration of each element (Zn, Mg, Cd, Mn, Te, O), the H- and V-axis of the ellipse and the center position along the horizontal axis (X_0). Note that since there were no tilted measurement of this NW, we can not determine the position of the ellipses along the vertical axis (Y_0).

Notice that since the line scan is limited to the zone around the QD insertion, we have no information about the outer part of the NW (that zone will be treated using a larger hypermap in the next paragraphs). This explains why the Mg profile does not show the two typical peaks corresponding to the shell. The fit taken for the Mg profile is not easy to choose since the trend is not clear. Here, the Mg profile is fitted to com-

plement the Zn profile (peak of Mg corresponding to depression of Zn). Nevertheless, the Mg profile retrieved from this hypermap can only tell us that there is Mg detected in this zone (normally coming from the top and bottom part of the shell) but nothing else. Therefore, this line scan is mainly useful to model the composition of the CdMnTe QD and of the pure ZnTe core in which it is embedded, which correspond to the ellipses #1 and #2.

Structure of the CdMnTe QD insertion (sample C)

In summary, the model presented in Fig. 4.22 and 4.23 proposes a QD with a concentration of 5% of Mn, 45% of Cd and 50% of Te and a diameter of 8 nm. This model fits very well the Cd, Zn and Mn EDX profile. The height of the QD measured from the hypermaps is 18 nm (dimension along the NW axis, Z-axis). This QD is embedded in a large ZnTe/ZnMgTe core-shell NW (100-110 nm of diameter).

The CdMnTe QD studied from sample C is more complicated to characterize than the CdTe QD from sample B since it is embedded in a bigger NW (the diameter of the NW at the level of the CdMnTe insertion is around 100-110 nm compared to a NW diameter of 70 nm for the CdTe insertion). This means that the QD is surrounded by a larger ZnTe matrix which attenuates the Cd and Mn signal detected by EDX. The statistical count is then much lower for the CdMnTe QD (sample C) than for the CdTe QD (sample B).

The fact that it was not possible to make EDX hypermaps at different tilts (rotation of the NW around its growth axis) makes it hard to determine exactly the structure of this QD. Here, we present the model that fits the best the data obtained from a single hypermap of this zone. However, it was not possible to continue further in this study to examine in detail the CdMnTe/ZnTe interface (like it was done for the CdTe QD from sample B). We can only consider the abruptness of the Cd peak (see Fig.4.22a) which shows us that Cd is detected over a region of 10-12 nm in total. This means that roughly the interface between the CdMnTe QD and the ZnTe NW is lower than 5-6 nm. Considering these remarks, we can say that it seems very plausible that the size and composition of the QD corresponds to the one proposed by the model. To gain more details on the structure of the QD, EDX hypermaps at different tilts need to be performed and analyzed.

Below the quantum dot insertion

Once the QD has been modeled, we can focus on the core-shell structure of the NW. We looked into two zones: below (but near) the QD insertion and at the base of the NW where it broke away from the substrate. The first analysis will give us the structure of the NW close to the QD insertion and the second one is useful to observe the structural difference between the base and center of the NW.

At the middle part of the NW:

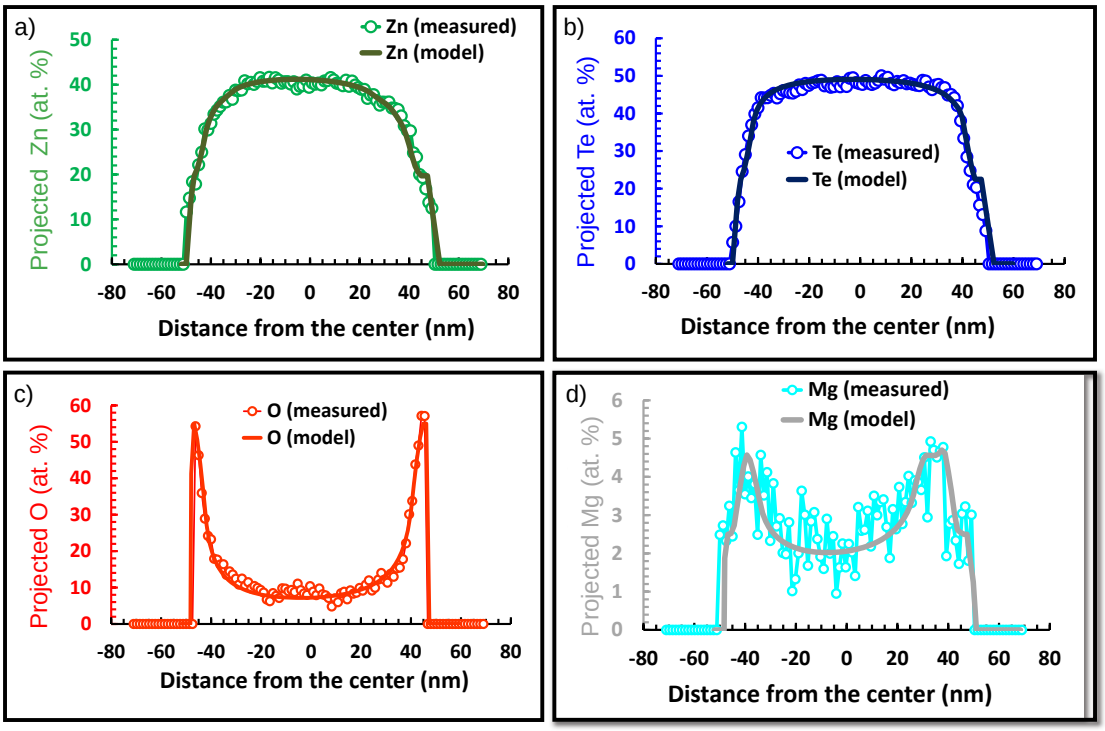

Figure 4.24 – Zn, Te, O and Mg compositions (at.%) averaged over the NW thickness obtained from the line scan shown in Fig. 4.25b (NW from sample C). The EDX data is plotted with empty circles and the fit with a continuous line.

In figure 4.25b a map of the NW is presented with the distribution Cd, Zn, O and Mg. The line scan chosen is marked in yellow: it crossed the NW along its diameter and it is averaged over a large zone (the rectangle around it) to obtain higher counts. In Figure 4.24, we present the EDX signal of Zn, Te, O and Mg obtained from the line scan with a corresponding fit for each element. The Te and Zn distributions are flat and homogenous inside the NW. Notice that the Zn profile is different from the previous one presented in Fig.4.22b: there is no decrease at the position where the QD was detected

since the line scan is chosen below the QD insertion. The O distribution shows two sharp peaks at exterior part of the NW and in between these two peaks, the projected O concentration does not decrease to zero but to around 10 at.%. This indicates that the NW is covered by a native oxide on the surface. The Mg signal shows a similar profile with two exterior peaks and a central plateau, again indicating the presence of a Mg-rich shell. In contrast to the NW from sample B, note that there was no Cd nor Mn detected above the noise level in this zone of the NW. The parameters used to fit the data presented in Fig.4.24 and a representation of the size and position of the 5 ellipses used on the model are plotted in Fig. 4.25.

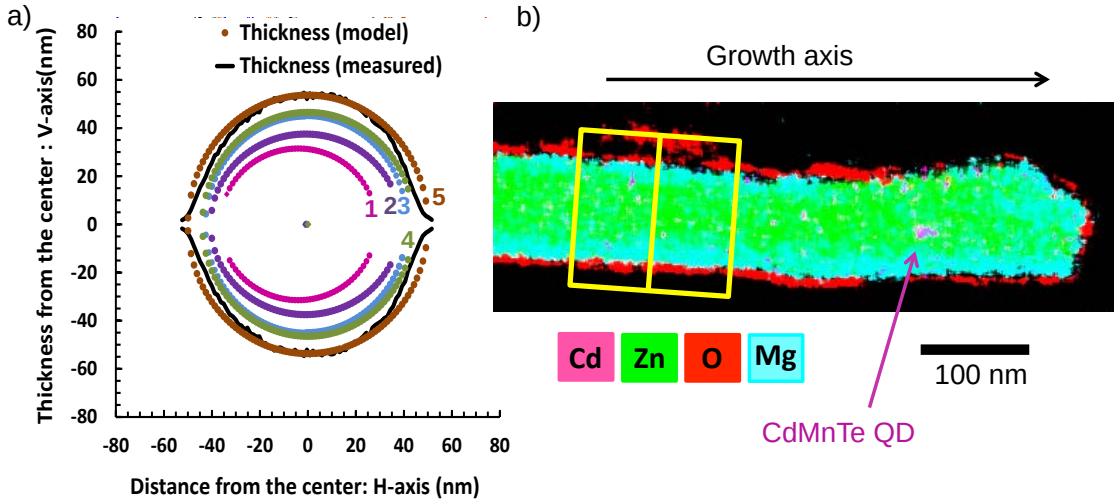

c)	Local concentration (at.%)						Size (nm)		Position (nm)	
Ellipse	Zn	Mg	Cd	Mn	Te	O	H-axis	V-axis	X_0	Y_0
1	49.7	0	0.3	0	50	0	65	63	-4	-
2	45.2	4.5	0.3	0	50	0	79	75	-1	-
3	41.7	8	0.3	0	50	0	84	90	-0.7	-
4	29.7	3	0.3	0	60	7	88	93	0	-
5	19.7	2.5	0.3	0	22.5	55	100	107.4	0	-

Figure 4.25 – a)The ellipses from the model used to fit the data shown on Fig. 4.24 are plotted with filled points. Thickness measured in a black continuous line is also shown. b) Image of an EDX map taken below the QD insertion, the line scan is marked in yellow. c) The set of parameters used in the model is shown for each ellipse. The parameters are: the concentration of each element (Zn, Mg, Cd, Mn, Te, O), the H- and V-axis of the ellipse and the center position along the horizontal axis (X_0). Note that since there were no tilted measurement of this NW, we can not determine the position of the ellipses along the vertical axis (Y_0).

Model description: below the QD insertion (see figure 4.25):
The structure of the NW in this zone is made of a central core of pure ZnTe (ellipses #1 with dimensions of 63-65 nm), surrounded by a ZnTeMg shell that we model with two ellipses. Ellipse #2 with a Mg content of 4.5% and of Zn of 45.2% (6-7 nm of thickness). Ellipse #3 with a higher Mg content of 8% and a lower of Zn of 41.7% (2.5-7.5 nm of thickness). In the last two exterior ellipses, the Mg and Zn content decreases and the O increases. In particular in ellipse #5, the O content is taken as high as 55%. Finally, the Mn content is zero and the Cd content is not only very low (0.3 at.%) but is also homogeneously distributed over the whole NW (same amount present in the 5 ellipses). This reflects the fact that we don't clearly detect a Cd-rich shell like in the previous NW, but only a very weak signal of Cd that is hardly higher than the background.

At the base of the NW:

The hypermap taken at the base of the NW is shown in Fig.4.27b. The EDX projected concentrations of Cd, Te, Zn, Mn and Mg are presented in figure 4.26 with the corresponding fit for each element. The Cd signal detected at the base of this NW (Fig. 4.26) is much lower compared to the one detected at the base of the NW from sample B (Fig. 4.20). Moreover, Mn is also detected and its signal is similar to the Cd profile: two peaks (at the same positions of the Cd peaks but with lower intensity) corresponding to the typical profile of a shell. A shell profile is also detected for the Mg and O signal, but their peaks are placed in the exterior part of the NW. These results indicate the presence of an inner Cd- and Mn- rich shell and an exterior shell rich in Mg and oxidized. The model used to fit the EDX data shown in Fig.4.26 is presented in Fig.4.27a/c.

Model description: at the base of the NW (see figure 4.27):
In this model the structure of the NW is build with a central almost circular 93-98 nm-thick core of pure ZnTe (ellipse #1), but at this position, it is surrounded by a 11-13.5nm thick shell containing mostly Zn and Te with a small concentration of Cd (1%) and of Mn (0.4%) (ellipse #2) . Ellipse #3, represents again a ZnTe shell (15 nm of thickness) but without Cd and Mn and instead, with a small percentage of Mg (0.4%). This ZnMgTe shell increases its Mg content (up to 1.5%) in ellipse #4 (18.5 nm of thickness) and also contains 6% of O. Finally the most exterior part of the NW (11.5 nm of thickness) contains 23% of O, 1.5% of Mg, 33.5% of Zn and 42% of Te.

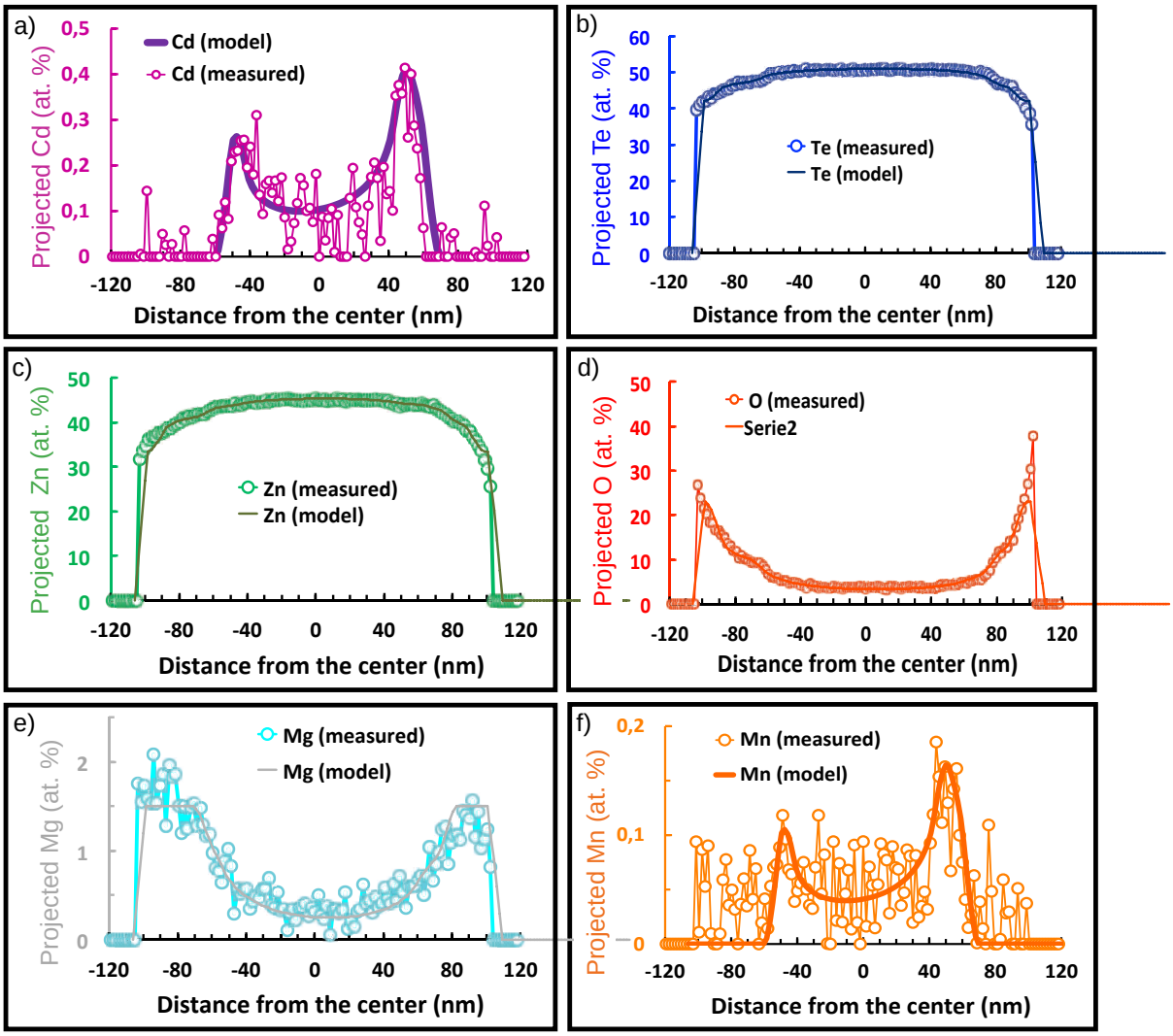

Figure 4.26 – Cd, Te, Zn, O, Mg and Mn compositions (at.%) averaged over the NW thickness obtained from the EDX map shown in Fig. 4.27 (NW from sample C). The EDX data is plotted with empty circles and the fit with continuous lines. The color code is: Cd in pink, Zn in green, Te in blue, O in red, Mn in orange and Mg in aquamarine and gray.

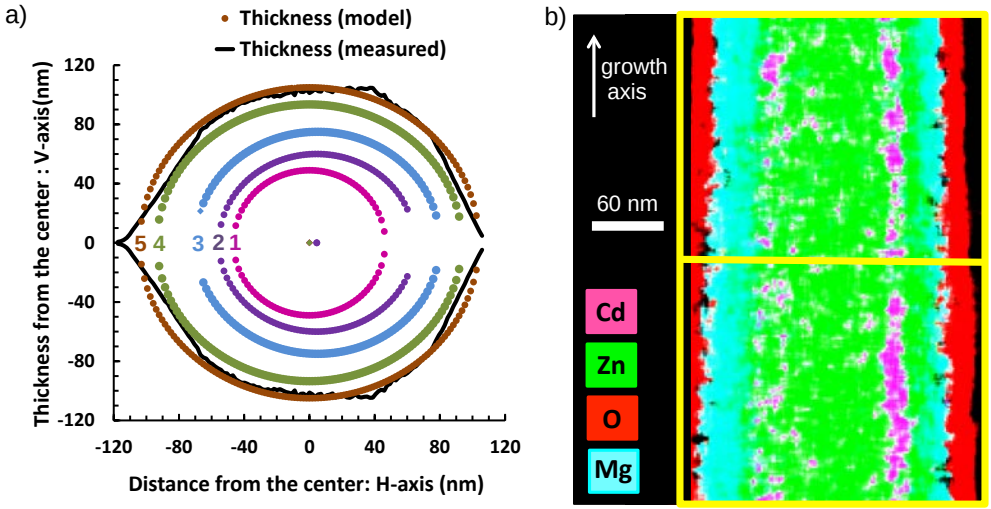

c)	Local concentration (at.%)						Size (nm)		Position (nm)	
Ellipse	Zn	Mg	Cd	Mn	Te	O	H-axis	V-axis	X_0	Y_0
1	47.5	0	0	0	52.5	0	93	98	0	-
2	46.5	0	1	0.4	52.5	0	120	120	4.5	-
3	47.1	0.4	0	0	52.5	0	150	150	5	-
4	43.5	1.5	0	0	49	6	187	187	0	-
5	33.5	1.5	0	0	42	23	210	210	0	-

Figure 4.27 – a)The ellipses from the model used to fit the data shown on Fig. 4.26 are plotted with filled points. Thickness measured in a black continuous line is also shown. b) Image of an EDX map taken from the base of the NW, the line scan is marked in yellow. c) The set of parameters used in each model is shown for each ellipse. The parameters are: the concentration of each element (Zn, Mg, Cd, Mn, Te, O), the H- and V-axis of the ellipse and the center position along the horizontal axis (X_0). Note that since there were no tilted measurement of this NW, we can not determine the position of the ellipses along the vertical axis (Y_0).

4.4.4 Spectroscopy results

In this section we present the optical characterizations performed on the core-shell NWs and on QD inserted in core-multi shell NWs that we have consider in this chapter. These measurements were performed by Alberto Artioli, Petr Stepanov and David Ferrand.

Sample A: ZnTe/ZnMgTe core-shell NWs

In Chapter 3, we presented results of the optical properties of single cone-shaped bare ZnTe NWs (with a native oxide shell). Low temperature cathodoluminescence (CL) of single NWs deposited on a Si substrate was recorded and a photoluminescence (PL) emission peak was observed near the bulk ZnTe band edge (details of these measurements are given in the published article joint in the appendix). Here, we present the results obtained from core-shell ZnTe/ZnMgTe NWs and compare them with the previous ones from bare ZnTe NWs.

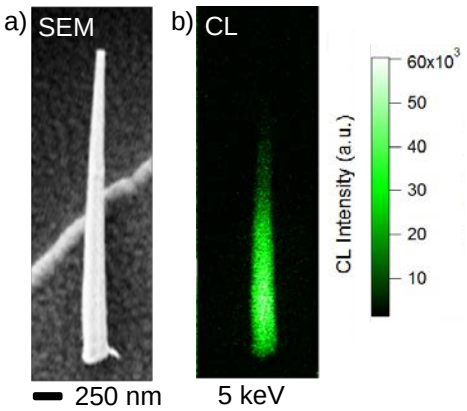

Figure 4.28 – a) SEM image of a ZnTe NW with a ZnMgTe shell deposited on a Si substrate. b) Low temperature cathodo-luminescence monochromatic image of the same NW taken at the maximum of the CL spectrum (at 2348.2 meV). The image was recorded at 5K and using an electron beam excitation of 5 KeV and a spot size aperture of 3.

Figure 4.28 shows a low temperature monochromatic cathodo-luminescence image[16] of an isolated core-shell ZnTe/ZnMgTe NW (sample A). The NWs were removed from the as-grown sample and deposited over a patterned Si substrate. The CL image shows that the emission is homogeneously distributed from the whole NW but the intensity

[16]The image of the NW was recorded using a FE-SEM FEI Inspect F50 equipped with a CL accessory and a low temperature Gatan stage which is able to cool down the sample to 5 K. The CL emission was collected by a parabolic mirror and sent to an avalanche photo diode synchronized with the electron beam scan.

decreases from the base to the tip. The same behavior was observed for bare ZnTe NWs and was reported in the article joint in the appendix. In that paper, we showed that the CL intensity integrated across the NW diameter at different positions along its axis is proportional to the square of the diameter. This suggests that the radiative efficiency remains constant along the NW. Moreover, the most significant observation is that a stronger CL emission was systematically observed for these NWs compared to the one observed for bare ZnTe NWs.

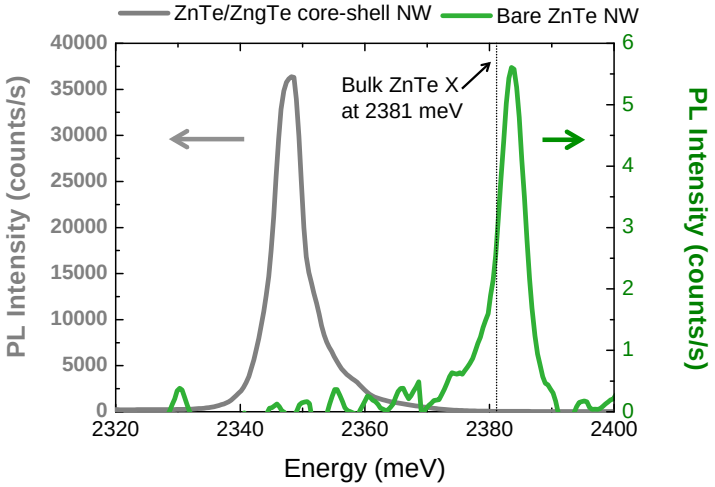

Figure 4.29 – Micro-photoluminescence spectra of a single ZnTe/ZnMgTe core-shell NW is plotted in gray (scale at the left) and of a single bare ZnTe NW, plotted in green (scale at the right). The emissions were recorded in the same conditions: at 5K with a laser excitation wavelength of 488nm and a power of 100 μW. The ZnTe bulk emission (2381 meV) is indicated with a dotted line.

The photoluminescence spectrum of a single ZnTe/ZnMgTe core-shell NW (sample A) and of a single bare ZnTe NW (with a native ZnO shell on the surface) are plotted in Fig. 4.29. Again, we observe that a stronger emission is obtained from single ZnTe NWs covered with a ZnMgTe shell than for bare ZnTe NWs. The intensity is 10.000 times higher when the ZnMgTe shell is present. Additionally, we clearly observe a significant red shift (33 meV) on the emission of the ZnTe/ZnMgTe NWs[17] and a small blue shift (3 meV) for the oxidized bare ZnTe NWs when compared to the band edge of bulk ZnTe[18]. These shifts are most probably related to the strain induced by the presence of a ZnMgTe shell or a ZnO shell around the NW [3, 62].

[17]This result has also been observed by P. Wojnar et al. [62]. They have explored the influence of the Mg concentration and of the thickness of the shell on the position of the PL emission peak.

[18]The bulk ZnTe band edge emission is 2381 meV, the bare ZnTe shows a peak at 2383.7 meV and the ZnTe/ZnMgTe core-shell NW at 2348.2 meV.

Sample B: ZnTe NWs with CdTe QD insertions

Single ZnTe NWs with CdTe insertions of sample B have been also characterized by CL and PL. In Fig. 4.30 we show a monochromatic CL image taken at 661 nm (1872 meV) of an isolated NW deposited over a Si substrate. This wavelength corresponds to the emission of the CdTe quantum dot. The CL image reveals a region around the middle part of the broken NW where the luminescence emission is localized.

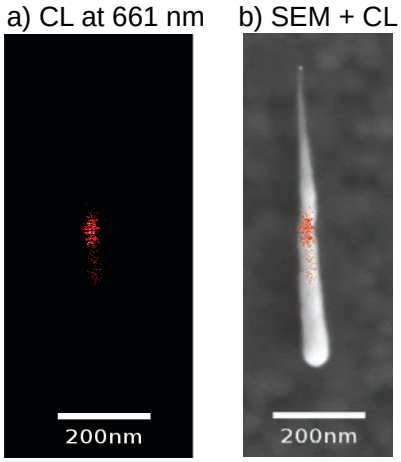

Figure 4.30 – a) Low temperature CL monochromatic image of an isolated ZnTe NW with a CdTe QD (sample B) deposited on a Si substrate. The image was taken at 1872 meV (661nm) corresponding to a CdTe emission. The image was recorded at 5K and using an electron beam excitation of 30 KeV. b) SEM image of the same NW with the CL image superposed.

Keep in mind that CL image does not show exactly where the emission originates (where the QD is localized). First, the CL image that we detect does not only correspond to the excitation of the beam on the QD volume but also from the excitation near the QD due to the electron beam spot size (30 nm). Second, the detected photons can also be generated from diffusion of electron-hole pairs. Hence, even if this technique does not give the exact position of the QD, we know that the emission is localized and an analysis of its spatial distribution could give information about the diffusion length of the electron-hole pair.

In Fig. 4.31 the PL spectrum of the same NW from sample B is shown (Fig. 4.30). The exciton and biexciton lines are attributed using the PL intensity power dependence (not shown here). The full width half maximum for the exciton line is 2 meV. The emitted light is polarized along the NW axis as shown in Fig. 4.31b.

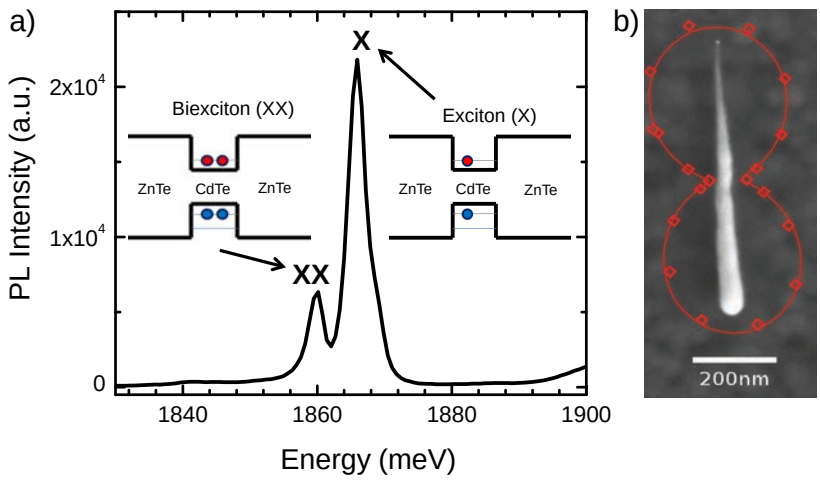

Figure 4.31 – a) Micro-photoluminescence spectrum of the ZnTe NW with a CdTe QD shown in Fig.4.30 (sample B). The emission was recorded at 5K with a laser excitation wavelength of 532 nm and a power of 7 μW. The exciton and biexciton lines are indicated.
b) The intensity of the PL exciton emission line as a function of the polarization.

Photon correlation measurements can be performed with a Hanbury-Brown and Twiss set-up [103]. In this measurement the emitted photons go through a monochomator and a beam splitter with a detector place for each branch (Figure 4.32). Each photon of the selected emission line can trigger either detector with equal probability. The idea is that a detection of a photon at detector 1 triggers the chronometer to start the time count and it will be stopped by the detection at detector 2. Therefore, it is a measure of the time τ between two emitted photons. A histogram of such events can be plotted as a function of the time between the two succeeding photons. This curve gives the number of coincidences as a function of the delay time. It represents the probability to detect a photon at time τ if a photon has been detected at time zero.

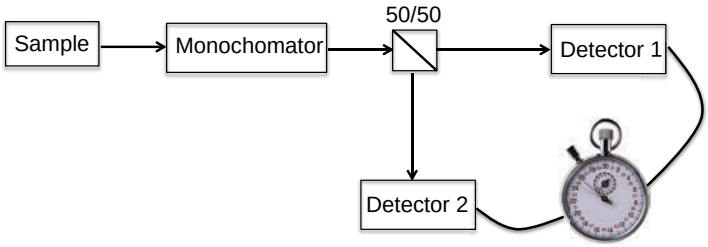

Figure 4.32 – Scheme of Hanbury-Brown and Twiss set-up for photon autocorrelation measurement.

Photon autocorrelation measurements were performed on a NW from sample B to confirm that the X-line observed originates from an exciton confined inside the QD (0D confinement). Fig.4.33 shows the characteristic antibunching curve of a single photon source indicating that the CdTe insertion on the ZnTe NW acts as a single photon emitter and that the excitons are confined inside the QD[19]. A detailed study of the spectroscopy properties of these ZnTe NWs with CdTe QD insertions can be found in [6].

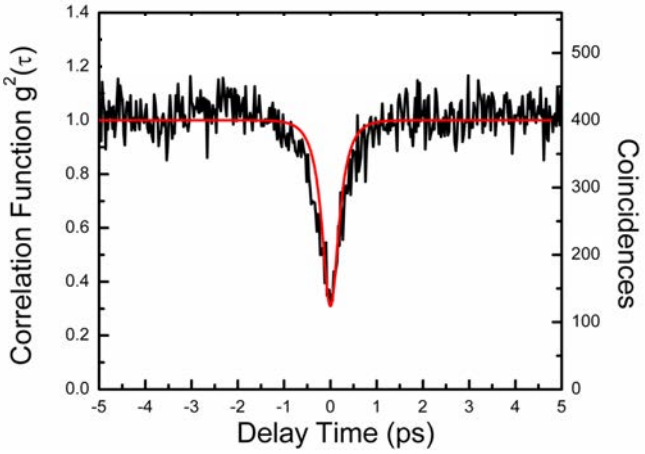

Figure 4.33 – Autocorrelation measurements performed at 5K on the exciton line of a single ZnTe NW with a CdTe QD (sample B). The emission was recorded at 5K with a laser excitation wavelength of 532 nm and a power of 2.5 μW.

Sample C: ZnTe NWs with CdMnTe QD insertions and a ZnMgTe shell

The same NW presented in Fig. 4.21 (sample C) and studied using EDX was characterized with CL, PL and Magneto-optical measurements. In Fig. 4.34 we present two CL images taken at 530 nm (corresponding to the CdMnTe emission) and at 630 nm (corresponding to the ZnTe emission shifted due to the presence of a ZnMgTe shell). The CL images reveal two emission zones, one located at the tip of the NW corresponding to the QD and other from the whole NW corresponding to the ZnTe core covered with a ZnMgTe shell. The image shown in Fig.4.34e shows that the luminescence emission from the QD is localized in the zone where the QD was detected by EDX.

[19]This measurement was made using two avalanche photo diode detectors that combined make the temporal resolution of the set up of 90 ps. This explains why the intensity of the correlation function $g_{(2)}$ is 0.35 and not 0.

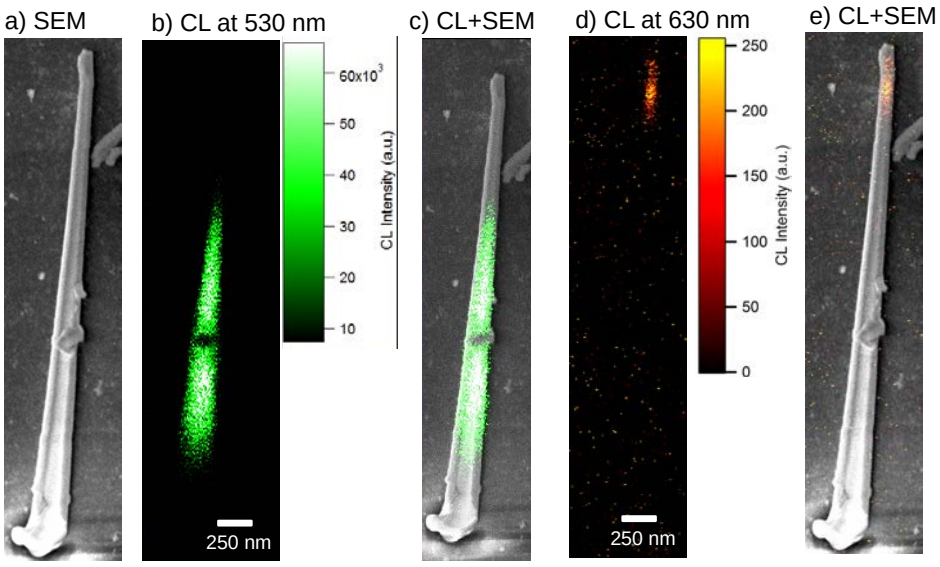

Figure 4.34 – a) SEM image of an isolated ZnTe NW with a CdMnTe QD and a ZnMgTe shell (sample C) deposited on a home-made microscopy membrane. b)Low temperature CL monochromatic image taken at 530 nm (corresponding to the ZnTe emission). c) SEM image superposed with the CL image shown in b. d) Low temperature CL monochromatic image taken at 630 nm (corresponding to the CdMnTe emission). e) SEM image super imposed with the CL image shown in d. The CL images were recorded at 5K and using an electron beam excitation of 5 keV.

Figure 4.35 shows the PL spectrum of the QD of the same NW. The exciton and charged exciton lines are indicated. Notice that the width of the exciton line is broader for CdMnTe QD than for the CdTe QD presented in Fig.4.31 (sample B). The full width half maximum for the exciton line related to the CdMnTe QD is 6 meV and for the QD without Mn from sample B is 2 meV. This broadening can be explained by the magnetic fluctuations at zero field. Furthermore, the position of the exciton line is blue-shifted with respect to the position of the exciton line from the QD without Mn, this is related to at least 3 contributions: i) strain on the QD is different due to a thicker ZnTe matrix; ii) the presence of Mn in the QD changes the band gap; and iii) the smaller size of the QD results in a larger energy of the electrons.

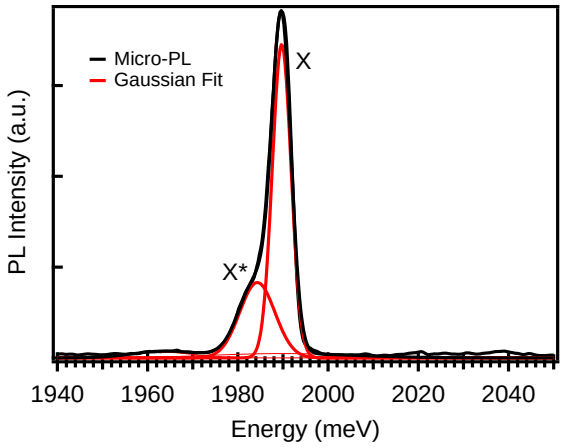

Figure 4.35 – a) Micro-photoluminescence spectrum of a CdMnTe QD embedded in a ZnTe/ZnMgTe core-shell NW(sample C) at zero field. The emission was recorded at 5K with a laser excitation wavelength of 488 nm and a power of 0.1 μW. The exciton and charged exciton lines are indicated.

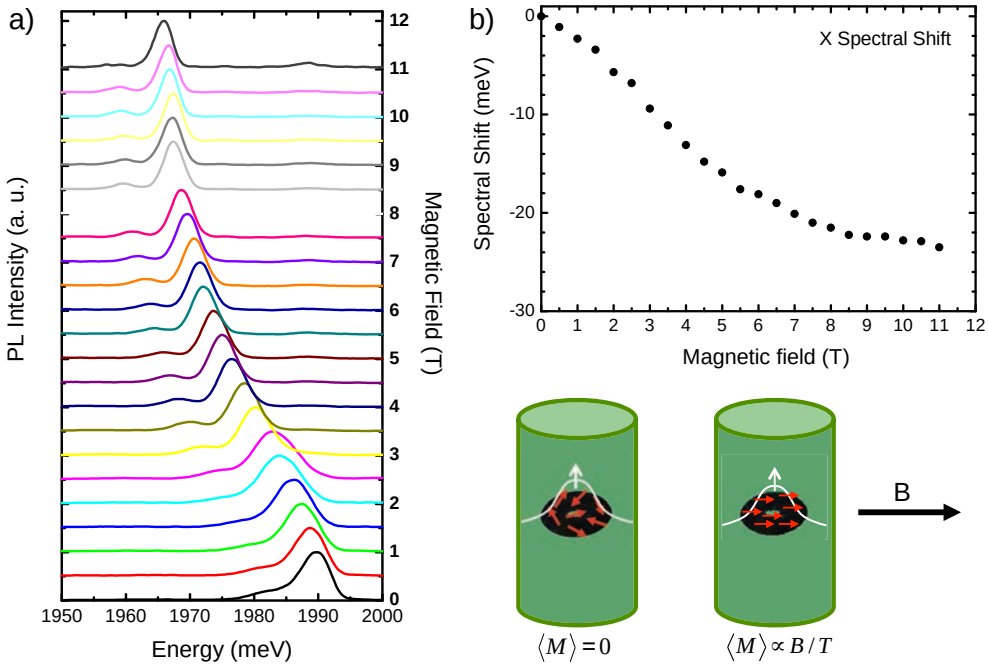

Figure 4.36 – a) Micro-photoluminescence spectra of a CdMnTe QD embedded in a ZnTe/ZnMgTe core-shell NW (sample C) in external magnetic field from zero to 11T. The emission was recorded at 6K with a laser excitation wavelength of 488 nm and a power of 2 μW. b) Spectral shift of the exciton line versus applied magnetic field.

Finally, the behavior of this QD was studied under external magnetic field. In figure 4.36a, the PL spectra of the CdMnTe QD under different external magnetic field conditions is presented. The magnetic field is applied from zero up to 11 T. We clearly observe a shift of the position of the main peak which is the trade mark of a giant Zeeman effect (plotted in figure 4.36b). This shift to low energies with high magnetic field is observed because the splitting of the conduction and valence band induced by the Giant Zeeman effect is proportional to the Mn magnetization. The shift observed in this NW confirms the incorporation of Mn in the QD.

4.5 Discussion

In this chapter we have considered two different QDs from sample B and C. The EDX and spectroscopy results obtained from these NWs were presented in the previous sections. In this part, we discuss the knowledge gained on the structure, morphology and properties of each NW. We treat separately the Cd(Mn)Te QD insertion, the Cd-rich inner shell, the Mg incorporation on the exterior shell and the overall shape of the NWs.

4.5.1 Quantum dot insertion

The QD composition and size retrieved from the EDX measurements and from the quantitative model for the NW from sample B and C are illustrated in Figure 4.37.

- The NWs measured confirmed the growth of a pure CdTe or (Cd,Mn)Te dot. Our results indicate that there is no Zn incorporation inside a central zone of the NW: 6 nm of diameter for the pure CdTe QD and 8 nm for CdMnTe QD. The diameter of the QD is a fraction of the Au droplet size. The diameter distribution of Au particles is between 10 to 20 nm for both samples (measured by SEM). This result is coherent with the TEM observations of Au particles at the NW tip with a shape larger than half-sphere (result presented in figure 3.22). In that case, the area of contact between the NW and the Au particle will have a diameter smaller than the Au particle. Keep in mind that in spite of the complicated external shape (bigger Au droplet diameter than NW diameter, faceting, native oxidation, growth of a shell) it is possible to control the diameter of the QD by modifying the diameter of the Au catalyst.

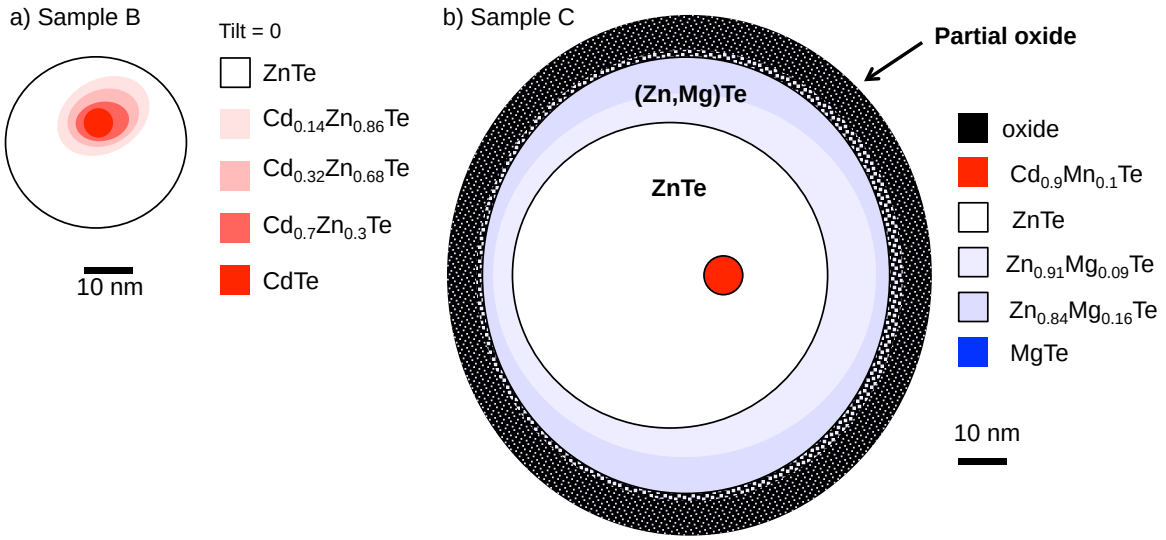

Figure 4.37 – a) Scheme of the QD structure (composition and size of each layer) for the NW studied from sample B (model C). b) Scheme of the NW structure (composition and size of each layer, including the QD) for the NW from sample C. Both structures represent the results presented in section 4.4. The concentration in each layer is illustrated by a quantitative color code: in a) pure CdTe in red and pure ZnTe in white; in b) CdMnTe with 5% of Mn in red, pure ZnTe in white, MgTe in blue, and O in black.

- The quantum dots studied in this chapter have an elongated shape. The aspect ratio (diameter over length), determined by the EDX measurements, for the CdTe QD from sample B[20] is 0.07:1 and for the CdMnTe QD from sample C is 0.4:1. The dot from sample B has an aspect ratio 5,7 times larger than the dot from sample C.

  The growth time of the CdMnTe insertion is 1/3 shorter (QD from sample C) than the growth time for the CdTe insertion (QD from sample B) but the flux is stronger for sample C (calibrated to 0.5 ML/s on a CdTe(100) layer) than for sample B (0.3 ML/s on a CdTe(100) layer). This corresponds to an amount of CdTe sent to the surface which is around 1.8 times larger for sample B than for sample C. Therefore the amount of CdTe sent to the surface does not fully explain the difference of lengths between the QDs (85 nm and 18 nm).

[20]Calculated using the diameter of the dot obtained from a line scan performed on a thin part of the insertion. Note that the diameter of the insertion seem to be bigger in the lower part (near the base) of this dot than on the upper part (near the tip).

We attribute the difference of QD lengths to the fact that the QD from sample B was grown using the Cd and Te cells whereas the QD from sample C by using the CdTe cell. In our MBE chamber, the position of the Cd and Te cell has a higher angle with respect to the sample's normal direction (the NW growth axis for NWs that grow perpendicularly to the surface) than the CdTe cell, which is almost aligned to the samples normal. Therefore, the contribution to the axial growth of the QD is higher when we use the Cd+Te cells than the CdTe cell. This is due to the extra contribution to the growth from the adatoms impinging the NWs facets and diffusing up to the Au droplet. Note that the contribution of the adatoms arriving directly to the Au droplet is almost the same for both cases.

In the case where the diffusion length of CdTe is larger than the one measured for ZnTe (see section 3.7), a second explanation can be given to the fact that the QD from sample B is longer than the one from sample C. Since the NWs from sample B are in average shorter (height between 430-530 nm) than the ones from sample C (height between 3-5 μm), the position of the QD insertion is much farther away from the substrate for the NW from sample C than for sample B. This implies that the contribution to the growth of the dot from the adatoms impinging the substrate and diffusing along the NW wall to reach the Au droplet is much lower (negligible) for the dot from sample C in comparison to the dot from sample B. This is possible if the diffusion length of CdTe is of the same order of magnitude as the distance between the position of the QD and the base of the NWs from sample B.

- The Mn content (QD from sample C) according to the model is 5% (45% of Cd and 50% of Te) which corresponds to the expected value deducted from the ratio of BEP: Cd/Mn=1/0.1. For this dot the contribution to the growth of CdTe and Mn cell are equivalent since both cells are almost aligned on the NW axis (normal to the surface). Hence, the ratio of concentration in the QD depends on the flux sent by each cell, provided that the diffusion on the sidewall is the same.

4.5.2 Core-multi shell NW structures

In this section we focus on the core-multi shell structure of the NWs presented in this chapter. In figure 4.38 and figure 4.39, we present the structure (composition, shape and size) of the NWs from sample B and C obtained from the EDX measurements and the geometrical model. We divide the discussion in three parts: i) the CdTe inner shell observed in the NWs from sample B and C; ii) the ZnMgTe shell present in the NWs from sample A and C; iii) the native oxidation observed in bare ZnTe NWs (sample B).

Cd-rich inner shell

At the NW's base:

- A Cd-rich shell is detected at the base for both NWs. The projected Cd profiles showed a different averaged Cd content at the right and left peaks (different intensity). This observation can be explained by two approaches: either there is a higher Cd content in one side of the NW than in the other or one side of the NW has a Cd-rich shell which is thicker than at the other. The geometrical models strongly suggests that the second explanation is more probable: it proposes an asymmetric Cd-rich shell where the center of the ellipse is not aligned with the center of the NW (see Fig.4.20 and Fig.4.27). This observation could be explained by at least 3 different reasons: a) an inclined NW (NW growth direction is not perpendicular to the surface) has one of its sides more exposed to the incident flux than the other (the side facing the substrate is less exposed to the incident flux) even if the sample is rotated during the growth; b) a shadowing effect of a kinked part of the NW (at the tip) over the lower trunk of the NW[21] ; or c) NW-facets with different diffusion or sticking coefficients (growth speed). For the moment, we have no evidence to indicate that one of these hypothesis is correct.

- The concentration of Cd in the inner-shell at the NW base is much higher for the NW from sample B (22 at.% over 4.75 nm, 4% over 6.5 nm and 1.5 over 5 nm) than for the NW from sample C (1 at.% over 12.3 nm of thickness). To compare this values we can translate the percentage of Cd found in the shells to a thickness of pure CdTe: we obtain 2.8 nm of CdTe (4.3 ML) for sample B and 0.25 nm of CdTe (0.39 ML) for sample C.

[21] This possibility was described in section 3.4.1 in Fig. 3.11.

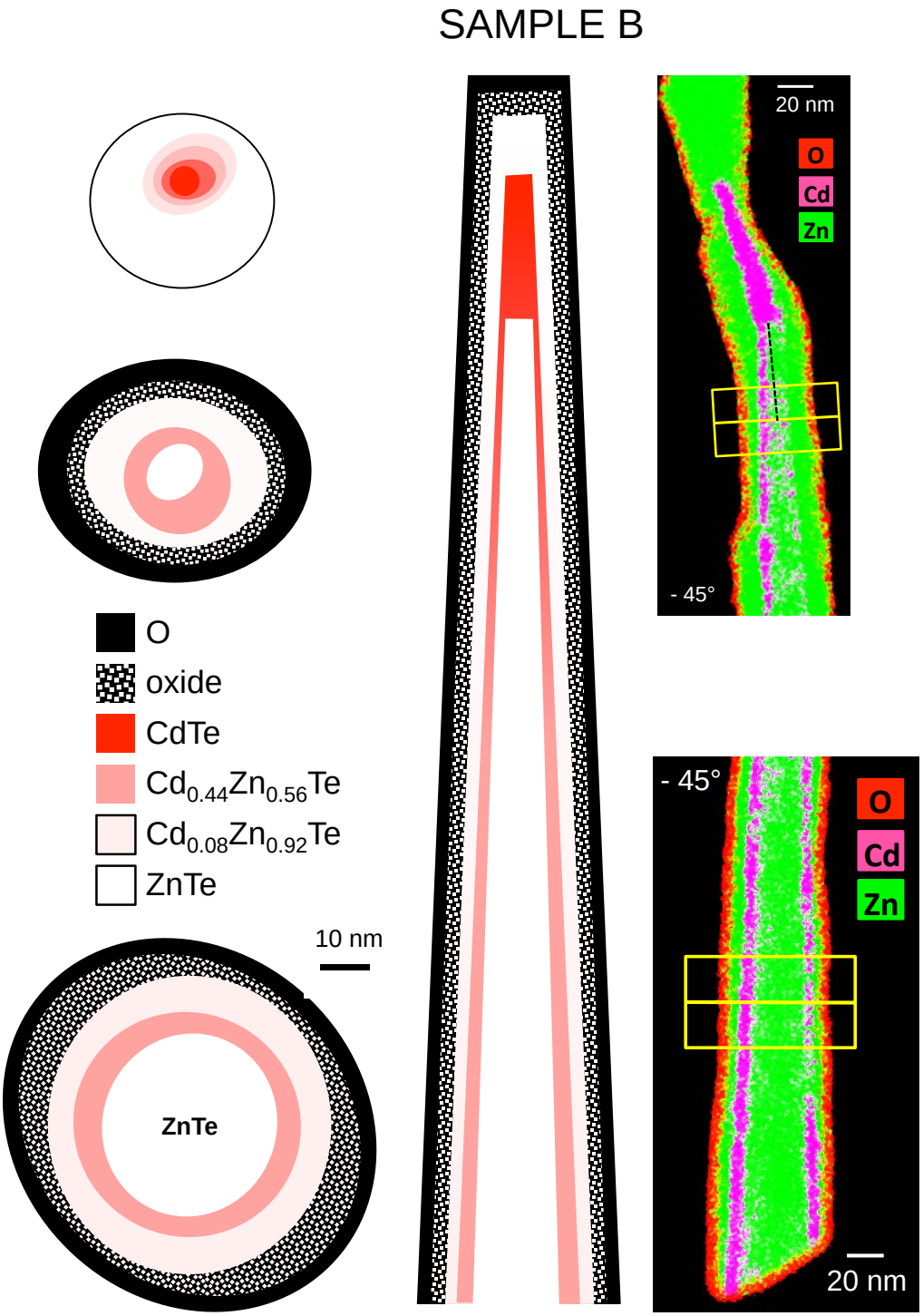

Figure 4.38 – Scheme of the structure of the NW (composition and size of each layer) from sample B obtained from the geometrical models proposed in section 4.4.

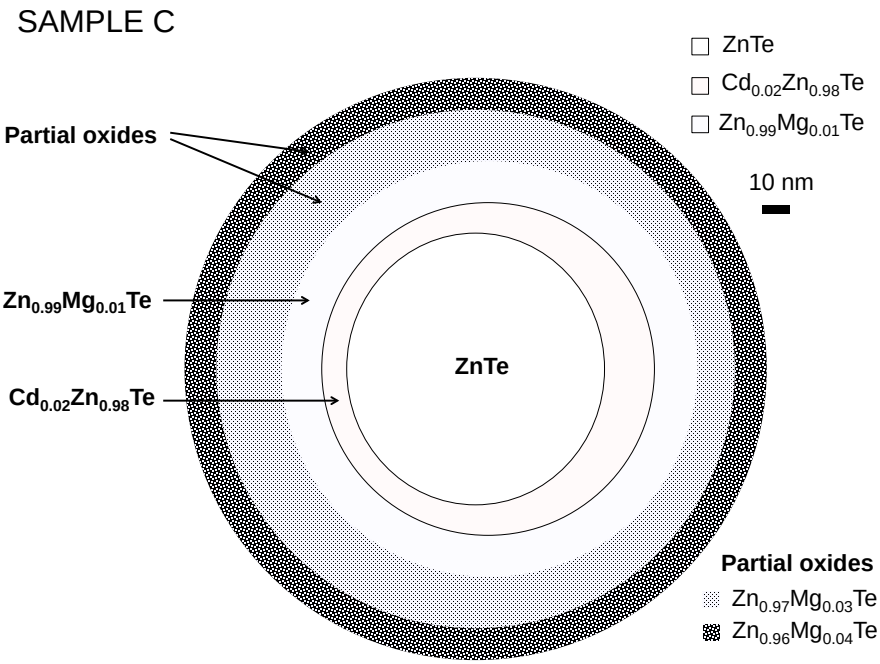

Figure 4.39 – Scheme of the structure of the NW's base (composition and size of each layer) from sample C obtained from the models proposed in section 4.4.

As discussed in chapter 3, the Cd-rich inner shell demonstrates the lateral growth observed in tapered NWs. We attribute the different Cd concentration in the two shells to the higher incident flux arriving to the NW's side walls from the Cd+Te cells (higher angle with respect to the samples normal) than from the CdTe cell (aligned with the samples normal). As we mentioned previously, the position of cells in our MBE chamber determines the flux impinging on the NWs side walls[22]. Since the NWs from sample B were grown using the Cd+Te and the NWs from sample C using the CdTe, it is coherent to observe a shell with higher Cd content at the base of the NW from samples B.

Below the QD insertion:

- We only detected a Cd-rich shell in the zone below the QD insertion for the NW from sample B. We did not observe a peak of Cd in the spectra corresponding to the line scan taken at the zone below the QD for the NW from sample C (Fig.4.25). In the model, the Cd noise level is fitted with a concentration of 0.3 at.% in all the ellipses. We conclude that either there is no lateral growth of

[22]The importance of the lateral flux on the growth of cone-shaped NW was demonstrated using a diffusion-driven growth model in section 3.7.

CdTe in this zone or that the thickness of the Cd-rich shell is below the spacial resolution limits of the set up ($\Delta x = 3$ nm).

The fact that a Cd-rich shell is observed at the base of the NW from sample C and not at the upper zone (below the QD), can be explained by i) the fact the NWs from this samples are grown with the CdTe cell (aligned along the normal to the surface) then the incident flux arriving to the NWs side walls is low, and ii) the high NW height (3-5 μm: in average 6-10 times larger for NWs from sample C than NWs from sample B). These facts imply that the main contribution to the lateral growth of CdTe is from adatoms diffusing from the 2D surface up to the NWs side walls. Certainly for this sample, the NW height is much higher than the Cd diffusion length explaining why lateral growth is only observed at the base (near the substrate).

- According to the models presented in section 4.4, the Cd-rich shell observed for sample B, is homogeneous from the base to the part below the QD insertion: shell thickness and composition are very close. This is not surprising since the NW from sample B, was grown using the Cd+Te cells (high incident flux arriving to the NW side walls) and the height of the NW is relatively low. In this case, the contribution to the lateral growth from atoms arriving directly to the side walls should be similar at the upper and lower part of the NW (for the same exposure time). Also, the contribution to the lateral growth from adatoms diffusing from the surface up to the NW walls seems to be homogeneous since the thickness of the shell is not bigger at the base: the Cd diffusion length is probably slightly lower or similar to the NW height. We conclude that, even if the total amount of CdTe sent directly to the base of the NW is higher (exposure of CdTe for a longer time), diffusion of adatoms on the sidewall is high enough to homogenize these contributions and grow an uniform shell. Note that, as it is expected, no Cd was detected above the QD insertion.

Around the pure CdTe QD insertion:

- The QD studied from samples B is modeled by a central core of pure CdTe that is surrounded by a CdZnTe zone with Cd decreasing from the interior to the exterior. In figure 4.40, the Zn (or Cd) content at the level of the QD insertion according to the geometrical model (model C) is plotted as a function of the position. This profile can be fitted with an exponential function (in red) with characteristic length of 5 nm. This exponential broadening can be explained by a diffusion of Cd (or Zn) during and/or after the growth[23]. We conclude that even if

[23] After the growth, the samples are heated up to $200-230°$C to be removed from the sample holder.

the Au catalyst are most probably solid during the growth, there is inter diffusion of atoms between the pure CdTe and ZnTe zones (during or after growth). This may be connected to a reservoir effect even if the Au catalyst is solid. In spite of the fact that the CdTe/ZnTe interface is not atomically abrupt, the spectroscopy results confirm that the steepness of the interface is high enough to confine carrier in the QD.

- We observe that the QD (from sample B) is tapered. The model proposed in this chapter is from a line scan taken at the upper section of the elongated QD (from the thinnest section of the QD). In the lower sections of the QD the Cd distribution is thicker. This is attributed to the lateral growth of CdTe at the lower part of the QD while the axial growth (through the catalyst) takes place in the upper part.

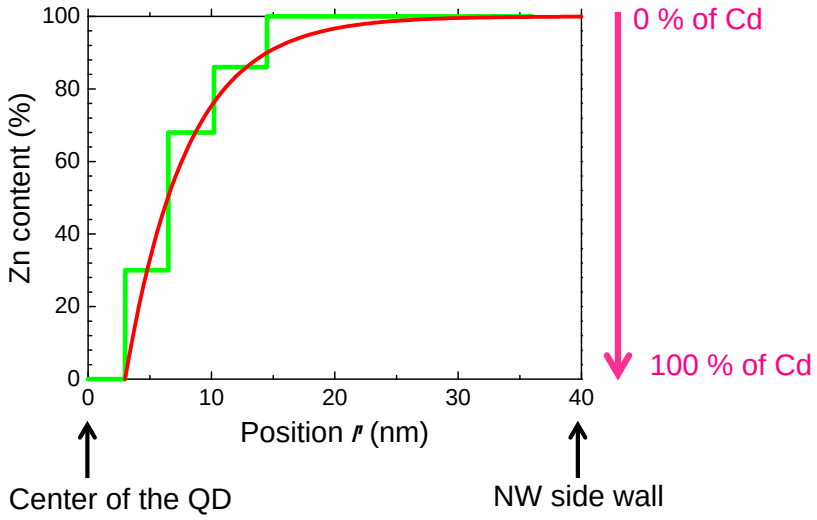

Figure 4.40 – In green: Zn concentration (Cd at the right) as a function of the position (zero is defined as the center of the QD insertion) for the QD insertion of the NW from sample B. The profile is taken from the geometrical model (model C) proposed in section 4.4. In red: a fit of the Zn profile using an exponential function with characteristic length of 5 nm.

This step may be responsible for the inter mixing of species. Further studies need to be done to verify this possibility.

ZnMgTe shell

- EDX results confirm the growth of a ZnMgTe shell around the NW from sample A and B. For sample A, quantifying the amount of Mg in the shell is very difficult because of the low statistical count (data was acquire with an SEM instead of a TEM). Additionally, there is an overlap between the K- energy line of the Mg peak and the L-line of Zn, making the quantification of Mg very delicate in samples where Zn is one of the principal elements. Nevertheless, the EDX map of Mg shows clearly that the ZnMgTe shell does not contain a homogeneous Mg content (higher Mg composition in one side than in the other or thicker shell in one side than in the other). The optimal growth conditions of this shell need to be explored in order to grow an homogeneous ZnMgTe shell.

- In spite of the non-homogenity of Mg content in the shell, the optical response from NW covered with this ZnMgTe is highly enhanced (the intensity of the main PL peak is 10.000 times higher with the shell than without). Additionally, we clearly observed the strain effect of this shell in the PL energy. This measurement suggests 5% of Mg averaged over the NW.

  The average Mg composition is a parameter good enough to study the effect of strain on the core (the local distribution of concentration is not needed [3]). A method to get this quantitative value from EDX measurements is to sum the spectra acquired for a large region and then calculate the average concentration from these summed spectra (better statistical count).

- For sample C, the Mg concentration is very different at the level of the QD (between 2.5 and 8 at.% in upper zone of the NW) than at the NW's base (0.4-1.5 at.% in lower zone of the NW). To compare this values we can calculate the equivalent thickness of MgTe: 1.8 nm in the upper zone and 1 nm at the base. There is no evident explanation to interpret this result. Note that the Mg cell is aligned in a high angle with respect to the surface normal (like the Cd and Te cells) hence there is an important contribution of Mg atoms arriving to the NW's side walls.

- Mg is detected over a large zone: 22 nm of thickness at the upper zone and 30 nm at the base. At the upper zone, the Mg concentration presents a peak and then it decreases at the exterior part of the NW. If this gradient of concentration is confirmed in new Mg profiles performed with better noise to signal ratio, it may suggest a diffusion of Mg atoms into the NW.

Overall NW shape

- The NWs studied are not straight. This is indicated by the fact that the shells are not circular and centered around the NWs axis. We detect a higher composition of Cd and Mg in one side of the NW than in the other. As mentioned previously, for inclined NW this can be explained by a shadowing effect of the NW it self (one NW side will be directly exposed to the flux and the other one will be facing the substrate). This can also be explained by the shadowing effect from a kinked section of the NW (the kink is usually observed between the QD insertion and the NW's tip, see figure 3.11).

- All NWs studied by EDX clearly show an O-rich zone on the surface of the NW. The model proposed in this chapter indicates that the native oxide formed around the ZnTe NW, is pure ZnO (Zn and O in the same proportions at the exterior shell)[24]. The thickness of this shell varies between 2.5-5.5 nm depending on the direction and on the position along the NW. Apart from the pure ZnO exterior shell, we also observed that there is a non-homogeneous penetration of O at the interior of the NW. The oxidation of the ZnMgTe shell is more complicated, it seems to be a mix of ZnO and Mg_xTe_{x-1}.

[24] ZnTe NWs with a ZnO shell were previously reported by K. Gas et al. in 2011 [104]. They demonstrated the formation of a polycrystalline ZnO shell obtained by thermal oxidation of ZnTe NWs grown by MBE.

4.6 Conclusion

To summarize, we present a list of the main results presented in this chapter. These are divided into two equally important aspects: the improvement of characterization methods and the growth of QD in NWs and core-shell NWs.

Characterization methods:

- The shape and size of two different QDs, as well as the core-multishell structure of the NWs that contain the QD has been determined in detail by analyzing the EDX measurements. The projected EDX signal of each element detected was fitted using a model where the NW is divided in a series of ellipses of different sizes and compositions. This method allowed us to determine which set of ellipses fitted better the EDX profiles (for all the detected elements and from several hypermaps taken at different tilts) and correspondingly, which model corresponds to the real structure of the QD. This method shows that the EDX is an interesting characterization technique capable of fully characterizing the QD and the NW structure.

- Cathodoluminescence measurements allowed us to observe the localized emission of the QD inserted in the NWs. The CL image was then used as a guide to search the actual position of the QD insertion by EDX.

- We performed a detailed study to fully characterize a single CdMnTe QD. We were able to correlate the structural and optical properties of **the same QD (same NW)** by coupling several characterization techniques.

- No information on the position of this QD along the electron beam direction and on the orientation of the ellipse can be obtained from an EDX measurement along a single azimuth. To exactly determine the position and shape of a QD, it is necessary to perform EDX measurements along several direction with respect to the NW axis. For a cylindrical NW (circular geometry), only two perpendicular directions are needed.

- To model the NW's shells, an elliptical approximation may be too simple. Taking the exterior shape of the NW as an ellipse induces some averaging errors. To be more precise (study defects or facets) a model based on hexagons needs to be developed.

- In spite of the complex morphology evidence on the shell, a circular section is found to be a good approximation for the quantum dot.

MBE growth of QD in NWs & core-shell NWs:

- We accomplished the growth of pure CdTe and CdMnTe elongated QD insertions in ZnTe NWs. These insertions have small diameters (6 nm and 8 nm) determined by the contact section between the NW and the Au catalyst particle and height values from 18 to 85 nm that are controlled mainly by the lateral flux. The luminescence detected from these insertions was proven to originate from well confined excitons inside the QD (autocorrelation measurements).

- The interface between the pure CdTe QD and the ZnTe NWs (sample B) is not atomically sharp (presence of a ZnCdTe shell). The exponential decrease of the Cd concentration may indicate a diffusion of Cd atoms.

- A small percentage of Mn (5 at.%) was successfully incorporated in the CdMnTe QD. A low-energy shift of the exciton-peak was observed under magnetic field due to the Giant Zeeman effect.

- A ZnMgTe shell was grown over cone-shaped ZnTe NWs by lateral growth. Even if the Mg content is not homogeneously distributed around the NW, the shell works very efficiently to passivate the surface of the NW which is proven by a 10.000 times higher intensity PL peak.

- The native oxidation of ZnTe NWs was observed and determined to be ZnO . The ZnTe NWs covered with a ZnMgTe shell are also oxidized but the nature of the oxide is different due to the presence of Mg (complex to determine).

- The high-quality of the NW crystal structure is demonstrated by an intense localized luminescence response (CL and PL) from both the QD and the NW.

General conclusions

The aim of this work was to develop a novel type of magnetic structure taking advantage of the properties offered by semiconductor nanowires. In this context we investigated the growth and fundamental properties of complex nanowire-based core-shell heterostructures: Cd(Mn)Te QDs embedded in ZnTe NWs covered by ZnMgTe shells.

Two main questions were addressed:

1. How to master the growth of those nano-structures to select desirable structural, electronic and magnetic properties?
2. How to interpret the chemical characterization, based on electron microscopy, of those complex non-homogeneous objects in order to gain quantitative local knowledge on their composition?

The first question was tackled in 3 stages: i) control of the formation of Au particles to catalyze the growth of nanowires, ii) analysis of the mechanisms and parameters governing the growth of ZnTe nanowires, and iii) study of the insertion of CdTe QDs containing Mn ions in Te-based core-shell nanowire.

i) Dewetting of Au to form catalyst particles over a ZnTe pseudo-substrate was examined. The optimal conditions to grow a low roughness ZnTe(111)B layer over a GaAs(111)B substrates were established. The principal results found are:

- A $3\sqrt{3} \times 3\sqrt{3}$ R30° surface reconstruction is formed over the ZnTe(111)B layer using only 7% of a ML of Au. We propose a model for its structure based on similar Au-induced surface reconstruction found over GaAs(111)B surfaces.
- The Au particles formed have a volume corresponding to 40% of the volume of a complete sphere and are in a solid phase.
- The dewetting temperature controls the diameter of the catalyst.
- The amount of Au sent onto the surface only influences the density of particles, once the surface reconstruction is completed and the particle size is fixed.

Finally, ZnTe surfaces covered with an ultra-low density of Au particles ($<$ 10 particles/μm^2) of homogenous diameter in the 10-20 nm range were prepared to initialize the growth of nanowires.

ii) ZnTe nanowires were grown by molecular beam epitaxy at low temperature (350°C). The coexistence of nanowires with the zinc-blende structure and nanowires with the wurtzite structure, homogeneously distributed on the whole wafer, is observed under stoichiometric flux ratio conditions. All structures have the same Te-terminated polarity as the substrate.

Nanowires with the **wurtzite structure** assume a **cylinder shape**, probably resulting from a diffusion length along the nanowire larger than the nanowire length. The formation of a pyramid around the base of each nanowire is favored by the presence of a lateral flux on the nanowire sidewalls. They show a narrow height distribution which is probably limited by nucleation mechanisms at the nanowire-catalyst interface.

Nanowires with the **zinc-blende structure** assume a **cone shape**, due to a lower diffusion length on the sidewalls, which gives rise to lateral growth, reduces the axial growth rate and favors the persistence of a crater at the base of each nanowire. The morphology of cone-shaped nanowires was explained considering a purely diffusion-driven growth model, where the diffusion lengths at the substrate and at the nanowire facets are estimated to 60 nm and 180 nm respectively.

The growth was also explored under Te-rich flux ratio conditions: cylinder-shaped nanowires are suppressed at low temperature (350°C), but enhanced at higher temperature ($375 - 400$°C). In contrast, under Zn-rich flux ratio conditions the growth of nanowires is totally inhibited.

iii) Pure (Cd,Mn)Te QD elongated insertions in cone-shaped ZnTe nanowires were successfully grown. The QD diameter is determined by the contact section between the nanowire and the Au catalyst particle (6-8 nm of diameter). The height of the insertion is controlled by the flux rate and by the angle of incidence of the lateral flux. The interface between the CdTe QD and the ZnTe nanowires is not atomically sharp: it is characterized by an exponential decrease of the Cd concentration. Successful incorporation of $\sim$ 10% of Mn in the CdTe sublattice, corresponding to the Mn/Cd flux ratio, was achieved thanks to the low growth temperature.

Finally, the growth of a ZnMgTe shell over cone-shaped ZnTe nanowires demonstrated efficient passivation of the surface paving the way for future control of strain.

The second question was undertook by developing a method to interpret the measurements performed using Energy-Dispersive X-ray spectroscopy (EDX) on single nanowire heterostructures. Two nanowires were analyzed in detail: a ZnTe nanowire with a CdTe insertion and a ZnTe nanowire with a CdMnTe insertion covered by a ZnMgTe shell. A geometrical model was proposed to fit the EDX measurements. This model allowed us to retrieve the shape, the size and the local composition of the QD insertions and of the multiple layers of the heterostructures. To our knowledge, it is the first time that an **EDX study assesses the quantitative local chemical composition of complex core-multishell semiconductors nanowires**. This method can be extended to all nanowires heterostructures.

This quantitative EDX study was coupled to other complementary characterization measurements **on the same nanowire**, such as cathodo- and photo-luminescence and magneto-optical spectroscopy. The correlation of those measurements will be presented in the PhD thesis of Alberto Artioli.

Prospects

The origin of cylinder-shaped nanowires with the wurtzite structure and cone-shaped nanowires with the zinc-blende structure remains unexplained. Several approaches can be taken to study this phenomena. On one hand, complementary measurements to determine the crystal structure of nanowires grown at other growth conditions or, the influence of different domains on the 2D surface (for example using in situ scanning tunneling microscope) may provide useful information. On the other hand, the nucleation mechanism on the Au catalyst probably plays an essential role on the growth of those nanowires and deserves to be explored in detail. In particular, the orientation of the Au catalyst particles relatively to the ZnTe(111)B surface may influence the nucleation process. To elucidate this point, diffraction measurements are planned at the European Synchrotron Radiation Facility (ESRF).

The investigation of the growth and properties of other nanowire-based structures can be interesting to explore. For instance, the study of the strain effects of QD with different morphologies embedded in core-shell nanowires and of the incorporation of different concentrations of Mn in CdTe QD, may allow to gain knowledge on the formation of the magnetic polaron. Additionally, a control of the transport properties of telluride-based nanowires is a key point to develop spintronic devices.

In summary, II-VI magnetic nanowire-based heterostructures have been developed, as well as a powerful characterization method to measure their chemical composition. This study opens many possibilities for future research on the magnetic properties of semiconductor heterostructures.

Appendix

Optical properties of single ZnTe nanowires grown at low temperature

A. Artioli,[1,2] P. Rueda-Fonseca,[1,2,3,a)] P. Stepanov,[1,2] E. Bellet-Amalric,[3] M. Den Hertog,[1,2] C. Bougerol,[1,2] Y. Genuist,[1,2] F. Donatini,[1,2] R. André,[1,2] G. Nogues,[1,2] K. Kheng,[3] S. Tatarenko,[1,2] D. Ferrand,[1,2] and J. Cibert[1,2]
[1]*Inst NEEL, Universiy of Grenoble Alpes, F-38042 Grenoble, France*
[2]*Inst NEEL, CNRS, F-38042 Grenoble, France*
[3]*INAC, CEA and Université de Grenoble, 17 rue des Martyrs, 38054 Grenoble, France*

(Received 17 June 2013; accepted 25 October 2013; published online 26 November 2013)

Optically active gold-catalyzed ZnTe nanowires have been grown by molecular beam epitaxy, on a ZnTe(111) buffer layer, at low temperature (350 °C) under Te rich conditions, and at ultra-low density (from 1 to 5 nanowires per μm^2). The crystalline structure is zinc blende as identified by transmission electron microscopy. All nanowires are tapered and the majority of them are ⟨111⟩ oriented. Low temperature micro-photoluminescence and cathodoluminescence experiments have been performed on single nanowires. We observe a narrow emission line with a blue-shift of 2 or 3 meV with respect to the exciton energy in bulk ZnTe. This shift is attributed to the strain induced by a 5 nm-thick oxide layer covering the nanowires, and this assumption is supported by a quantitative estimation of the strain in the nanowires. © *2013 AIP Publishing LLC*.
[http://dx.doi.org/10.1063/1.4832055]

There is currently a wide-spread interest for semiconductor nanowires (NWs), driven by their potential to constitute suitable building blocks for future nanoelectronic and nanophotonic devices.[1] During the past decade, selenide and telluride II-VI NWs have been extensively investigated for various applications such as nano-pillar solar cells,[2] photodetectors,[3] or single photon sources.[4] Among II-VI's, ZnTe based NWs are particularly promising as offering a large range of potentialities. They can be grown by molecular beam epitaxy (MBE) using gold particles as catalyst. They can be efficiently doped electrically.[5] They can also be doped with magnetic impurities,[6,7] while the large difference between the temperatures suitable for the growth of GaAs NWs and for the incorporation of Mn as substitutional impurities makes the growth of (Ga,Mn)As NWs challenging.[8] As (Zn,Mn)Te can be doped strongly p-type so that ferromagnetism appears and transport studies are feasible in 2D,[9] ZnTe-based NWs are attractive for a basic study of spintronics mechanisms in 1D. In addition, CdTe quantum dots can be incorporated and used as a single photon source[10] or as a very sensitive optical probe of the spin properties.[11] Amongst the many reasons to grow these NWs at low temperature, we expect CdTe quantum dots and Mn impurities to be more easily incorporated.

A good control and the optimization of the growth conditions are prerequisites to improve the electronic and optical properties of the NWs. We present the MBE growth and the structural analysis of ultra-low density ZnTe NWs, and we show that their high crystalline quality allows us to observe micro-photoluminescence (μPL) and cathodoluminescence (CL) emissions from single NWs.

ZnTe NWs were grown by MBE, using gold particles as a catalyst. A fraction of a monolayer of gold was deposited on a 500 nm-thick ZnTe(111) buffer layer previously grown on a GaAs(111)B substrate. Gold droplets were formed at 350 °C, and the NWs were grown at the same temperature. As we observed that Te-rich conditions result in a larger diffusion length on the (111) ZnTe surface,[12] the present NWs were grown with a Zn:Te flux ratio 1:2.3 for 30 or 60 min. More details are given in Ref. 12.

Typical ZnTe NWs have been imaged by scanning electron microscopy (SEM), see Fig. 1. This sample presents an ultra-low-density of NWs, down to 2 NWs per μm^2. These NWs have been grown under Te-rich conditions; they are tapered, with a thick base (50–70 nm) and a thin tip (15 nm roughly equal to the gold particle diameter). This cone shape is due to lateral growth induced by the low growth temperature.[12] The NW height distribution is large, from 300 nm to 1.5 μm for a 30 min growth time.

The majority (about two thirds) of the NWs are oriented ⟨111⟩, and most of the remaining NWs oriented ⟨112⟩. Transmission Electron Microscopy (TEM) was performed on a Philips CM300 microscope equipped with a CCD camera and operated at 300 kV. Images reveal a zinc-blende crystal structure, see Fig. 2. Some NWs do not present any defect, but many of them show twins, as frequently observed

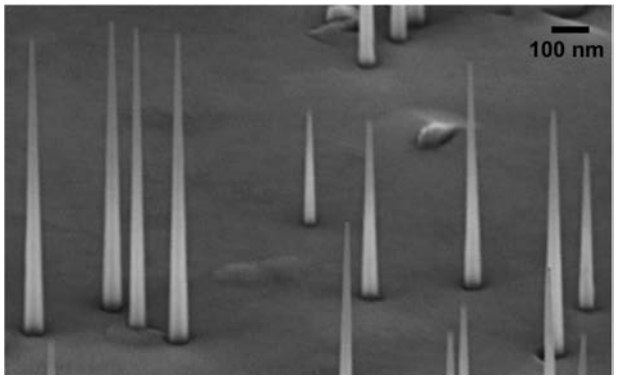

FIG. 1. SEM image of ZnTe NWs grown at 350 °C for 30 min under Te rich conditions.

[a)]Electronic mail: pamela.rueda@grenoble.cnrs.fr

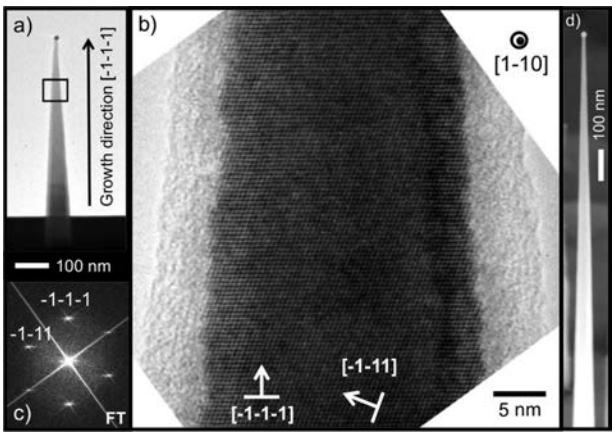

FIG. 2. (a) Low resolution TEM image of a ZnTe NW grown for 30 min. (b) High resolution TEM image, and (c) Fourier transform. (d) A ZnTe NW grown for 60 min, at the same scale than in (a).

in ⟨111⟩ zinc-blende NWs. We systematically observe an amorphous layer (5 nm thick) all around the NW, which we attribute to oxidation after growth (see Fig. 2(b)). ZnTe(111) surfaces tend to be rapidly oxidized either by forming TeO_2 or/and ZnO.[13] In the case of ZnTe NWs, the formation of a partially crystallized ZnO shell has been reported,[14,15] although the presence of Te-oxide in the outermost part was also suggested by electron energy loss spectroscopy analysis. In our samples, energy dispersive x-ray analysis (EDX) also detects the presence of Zn oxide and of some Te oxide.[12]

The cone shape of these NWs indicates that, under these growth conditions (low temperature and Te excess), the diffusion length of adatoms on the facets of the NW is not large.[12] This could limit the range of NW length which can be achieved. Nevertheless, NWs grown for a longer time (60 min) exhibit a larger length, as shown in Fig. 2(d). For the same size of the gold droplets, the average diameter at the base of the NWs was increased to 80–100 nm, and the length distribution to 0.8 μm.

The optical properties of single NWs have been characterized by low temperature μPL and CL. ZnTe NWs were first deposited on a patterned silicon substrate by rubbing as-grown samples on the silicon surface. Isolated NWs were identified and precisely located on the substrate using a high-resolution SEM, see Fig. 3(a). Then low temperature (6 K) spectra of these NWS were recorded using a cold-finger cryostat and a confocal μPL set-up. The NWs were excited by 100 μW of a 488 nm cw laser beam focused to 4 μm^2 on the selected single NW using a microscope objective and a piezoelectric scanner. The light emitted by the NW was collected by the microscope objective and sent to a 0.46 m Jobin-Yvon spectrometer equipped with a CCD camera.

CL images of the same NWs deposited on the silicon substrate were recorded using an FEI Quanta 200 SEM equipped with a CL accessory and a low temperature Gatan stage able to cool down the sample to 6 K.[16] The single NW was excited by an electron beam of 30 keV and a current of typically 250 pA. In comparison with high resolution field-effect SEM images, the spatial resolution of the CL images is limited by the low spatial resolution of the thermionic SEM. The CL light was collected by a parabolic mirror and sent to an avalanche photodiode synchronized with the electron beam scan.

As shown in Fig. 3(b), μPL spectra are dominated by a single emission peak close to the ZnTe exciton band edge. The spectrum has been fitted using two Gaussian lines

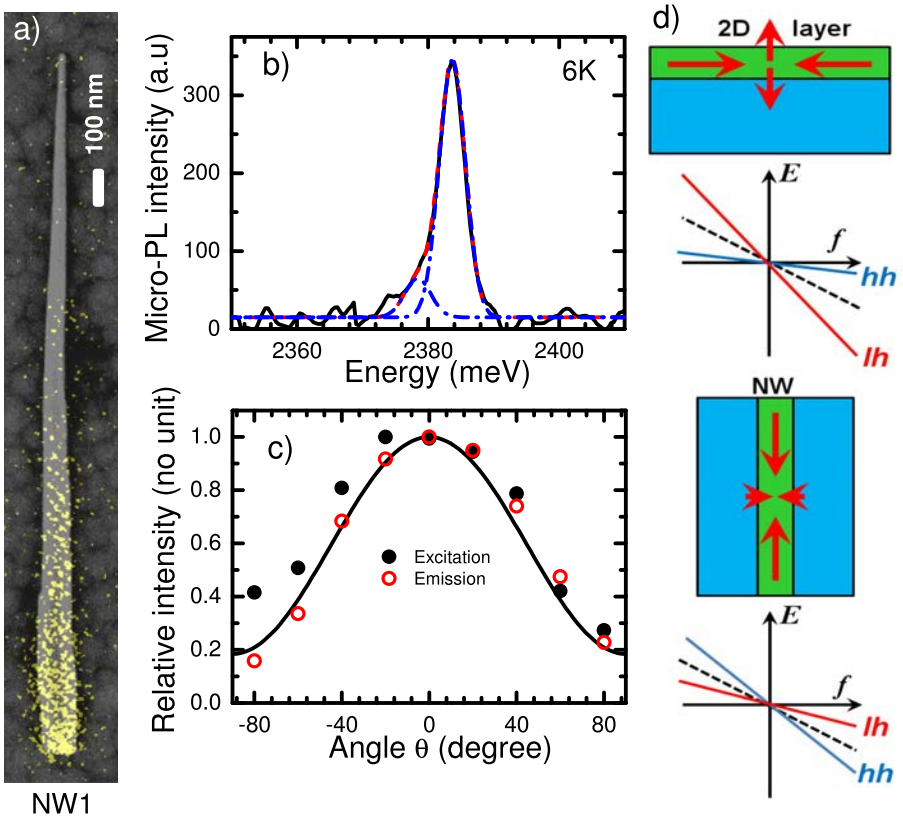

FIG. 3. (a) Superposition of the high resolution SEM image and the CL image (yellow pixels) of a ZnTe NW deposited on a patterned silicon substrate. (b) μPL spectra of the NW shown in (a), recorded at 6 K using a 488 nm laser excitation at 25 $\mu W/\mu m^2$. The dashed line is a Gaussian fit with a main peak at 2383.7 meV and a satellite line at 2378.4 meV. (c) Dependence of the PL intensity on the angle θ, shown in (a), between the NW axis and the direction of the linear polarization of the laser excitation (closed circles) or the emitted light (open circles). The solid line is the dependence expected from dielectric screening. (d) Strain imposed by the substrate on an epitaxial layer (top) and by the shell on the NW core (bottom), schematically depicted by the arrows, and their effect on the heavy hole (hh) and light hole (lh) recombination energy (and the average, dashed line) as a function of lattice mismatch.

having a full width at half maximum equal to 4 meV. The main peak is at 2383.7 meV, very close to the bulk exciton at 2381 meV:[20,21] we will discuss it below as originating from a free or slightly localized exciton. The small satellite peak observed 5 meV below the main peak is attributed to bound excitons.[21]

These results apparently contrast with previous studies performed with ZnTe/(Zn,Mg)Te core-shell NWs,[7] where a band edge emission is observed at 2.31 meV. A line at lower energy might be ascribed to trapped excitons or complexes, but the position of the line in the present study, slightly above the exciton in bulk ZnTe, cannot be ascribed to the influence of lateral confinement, which remains negligible for the present range of NW diameters. Indeed such a difference in the exciton energy is expected from the high sensitivity of the band edge emission to the strain induced by the presence of a shell around the NW.

According to Ref. 22, the stress induced in the core by a lattice mismatched shell covering an infinitely long cylindrical NW is uniform, equal to $\sigma_{\parallel} = 2 \times \sigma_{\perp} = \frac{18\mu K}{3K+4\mu}(1-\frac{D_c^2}{D_s^2})f$. Here, $\sigma_{\parallel}$ is the component of the core stress parallel to the NW, and $\sigma_{\perp}$ the perpendicular component; K is the bulk modulus and μ is the shear modulus of the core and the shell materials, assumed to have the same isotropic elastic properties; f is the lattice mismatch between the core and the shell ($f > 0$ if the shell has a larger lattice parameter); D_c is the core diameter and D_s the external diameter of the core-shell structure. For semiconductor NWs, a more complete calculation,[23] which is beyond the scope of this paper, shows that the previous expressions can be used for $\langle 111 \rangle$ oriented semiconductor NWs using the bulk modulus $K = (c_{11} + 2c_{12})/3$ and a shear modulus $\bar{\mu} = \frac{1}{4}\frac{c_{11}-c_{12}}{2} + \frac{3}{4}c_{44}$, where c_{11}, c_{12}, and c_{44} are the stiffness coefficients of a cubic semiconductor. This leads to an hydrostatic shift of the band edge emission Δ_{hyd} and a heavy hole-light hole splitting Δ_{HL} proportional to the lattice mismatch f, reduced by the geometrical factor $(1-\frac{D_c^2}{D_s^2})$, i.e., the ratio of the shell to the total cross section areas: $\Delta_{hyd} = -a\frac{12\bar{\mu}}{3K+4\bar{\mu}}(1-\frac{D_c^2}{D_s^2})f$ and $\Delta_{HL} = -\frac{d}{\sqrt{3}}\frac{9K}{3K+4\bar{\mu}}(1-\frac{D_c^2}{D_s^2})f$.

For the deformation potentials in ZnTe, we take the values[20] $a = 5.3$ eV and $d/\sqrt{3} = 2.5$ eV, and for the stiffness coefficients,[24] $c_{11} = 73.7$ GPa, $c_{12} = 42.3$ GPa, and $c_{44} = 32.1$ GPa. Then the excitonic emission of a $\langle 111 \rangle$ oriented cubic ZnTe NW is (in meV, with f in %) $E_{NW} = 2381 - 88(1-\frac{D_c^2}{D_s^2})f$ for the heavy hole and $E_{NW} = 2381 - 44(1-\frac{D_c^2}{D_s^2})f$ for the light hole. The heavy hole is the ground state if $f > 0$, i.e., as noticed in Ref. 7, if the core is under tensile strain.

For the NWs studied in Ref. 7, with $D_c = 70$ nm, $D_s = 130$ nm, and $f = 1.04\%$ corresponding to the lattice mismatch between a ZnTe core and a $Zn_{0.8}Mg_{0.2}Te$ shell,[25] we obtain 2.31 eV for the heavy-hole exciton, in agreement with the observed PL line. One can note that in this core-shell geometry, the position of the heavy-hole emission is more sensitive to the strain than in an epitaxial layer under compressive biaxial strain: the shifts of the heavy-hole state due to the hydrostatic and the shear strain add, while they partially compensate in the epitaxial layer. For the NWs studied in this work, we expect a compressive strain induced by the oxide layer around the NW. For instance, the Zn-Zn distance is 20% smaller in ZnO than in ZnTe. The shell thickness is small, 5 nm, resulting in a small geometrical factor, less than 0.2. Moreover, the shell is complex, amorphous, and probably strongly relaxed. The band edge emission observed at 2383.7 meV can be interpreted as the influence of a small residual compressive strain $f = -0.4\%$ on the light hole exciton. Hence, even if the nature of the lines observed in PL here and in Ref. 7 cannot be assessed without a complementary study such as PL excitation or photoconductivity, their position well agrees with the effect expected from the strain induced by the shells.

In Fig. 3(c), we plot the variation of the intensity of the band-edge emission peak when rotating the linear polarization of the laser excitation (solid symbols) or of the detection (open symbols) with respect to the NW axis (determined by SEM, using substrate marks). The maximum of the emission intensity is reached when the polarization is parallel to the NW axis (zero angle). Polarization rates of about 70% are observed for emission and detection, in agreement with the value reported with III-V standing NWs.[26] These effects result from the dielectric screening induced by the characteristic aspect ratio of the NWs.[27]

For small objects such as the present NWs, the CL excitation efficiency is more than three orders of magnitude lower than the μPL one. The ratio between the electron-hole excitation density in CL experiments and in μPL is given by $\frac{P_e/3}{P_{ph}} \times \frac{\eta_e}{\eta_{ph}}$. Here, $P_e \simeq 2$ $\mu W/\mu m^2$ is the mean value of the electrical power density of the CL electron beam when recording a typical image from which it is generally considered that about one third gives rise to luminescence.[17] $P_{ph} \simeq 25$ $\mu W/\mu m^2$ is the laser power density used in the μPL experiment. The excitation in μPL is non-resonant, 160 meV above the ZnTe gap, so that we consider that a good order of magnitude of the absorption by an object of thickness D (the NW diameter) is given by $\eta_{ph} = \alpha_{ph} D$, where $\alpha_{ph} \approx 4 \times 10^4$ cm^{-1} is the value for bulk ZnTe.[18] The effect of electrons can be calculated using a Monte-Carlo simulation software (CASINO[19]). An incident electron has a very small probability to be scattered inelastically and create an electron-hole pair in the NW; most of its energy is deposited in the substrate where it is scattered many times and propagates randomly. As a result, the creation of electron-hole pairs in the NW is also proportional to D, and much smaller, with an $\alpha_e \approx 4 \times 10^2$ cm^{-1}. This low excitation density prevents any spectral analysis of the CL images

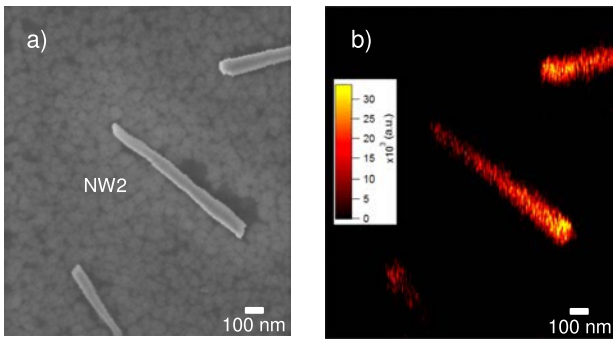

FIG. 4. (a) High resolution SEM image of 3 broken ZnTe NWs deposited on a silicon substrate. (b) CL image of the NWs shown in (a) recorded at 6 K.

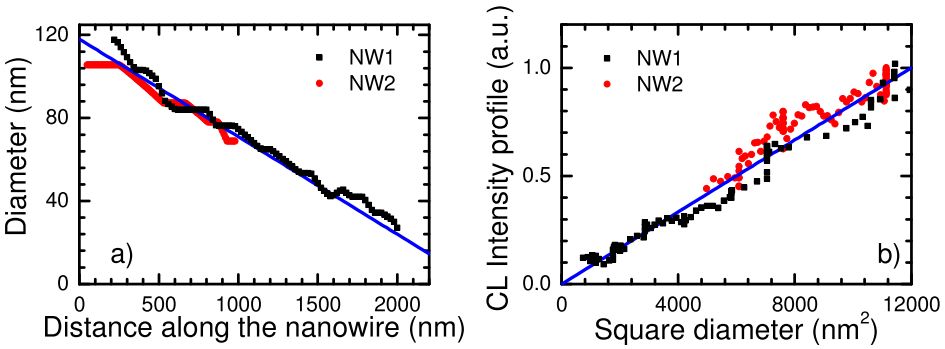

FIG. 5. (a) NW diameter as a function of the position along the NW axis for the two NWs shown in Figs. 3 and 4. (b) CL intensity (integrated over a 12 nm × 120 nm window) as a function of the square of the NW diameter.

for the small NWs studied in this work. Note finally that the CL signal integrated over the NW width corresponds to an energy deposited in the NW proportional to D^2.

Low temperature, polychromatic CL images were recorded in order to assess the homogeneity of the optical properties. CL emission was systematically observed from the NWs, as shown in Fig. 4(b) for the three isolated, broken NWs of Fig. 4(a). For thin cone-shaped NWs like the one labelled NW_1 in Fig. 3(a), and NW_2 in Fig. 4, the CL intensity decreases from the base to the tip. The local diameter D of NW_1 and NW_2, determined from the high resolution SEM images, is shown in Fig. 5(a) as a function of the position along the NW. Both NWs display a similar cone shape with the same angle value. Fig. 5(b) shows that the CL intensity integrated across the NW diameter at different positions along its axis is proportional to the square of the diameter. This suggests that the radiative efficiency remains constant along the NW, with a CL intensity determined by the excitation density which is proportional to D^2.

To conclude, ultra-low density ZnTe NWs have been grown by MBE at low temperature. These NWs feature a high crystalline quality that is reflected in their optical response. CL of single ZnTe NWs deposited on Si substrates was obtained indicating an homogeneous radiative efficiency along the NWs. Near band edge PL emission was observed from single NWs. A small blue shift (2–3 meV) of the PL energy is attributed to the strain induced by the amorphous oxide layer surrounding the NWs. This assumption is supported by a quantitative calculation of the excitonic shifts induced by strain in core-shell NWs.

Most of this work has been done within the CEA-CNRS joint team "Nanophysique & Semiconducteurs." We acknowledge the help of the technical teams of Institut Néel, *Nanofab* (clean room) and *Optical Engineering* (SEM, S. Pairis), and of J.-P. Poizat. This work was supported by the French National Agency (Magwires, ANR-11-BS10-013).

[1]X. F. Duan, Y. Huang, Y. Cui, J. F. Wang, and C. M. Lieber, Nature **409**, 66 (2001).
[2]Z. Fan, D. J. Ruebusch, A. A. Rathore, R. Kapadia, O. Ergen, P. W. Leu, and A. Javey, Nano Res. **2**, 829 (2009).
[3]Q. F. Meng, C. B. Jiang, and S. X. Mao, Appl. Phys. Lett. **94**, 043111 (2009).
[4]S. Bounouar, M. Elouneg-Jamroz, M. den Hertog, C. Morchutt, E. Bellet-Amalric, R. Andre, C. Bougerol, Y. Genuist, J. -Ph. Poizat, S. Tatarenko, and K. Kheng, Nano Lett. **12**, 2977 (2012).
[5]Z. Liu, G. Chen, B. Liang, G. Yu, H. Huang, D. Chen, and G. Shen, Opt. Express **21**, 7799 (2013).
[6]P. V. Radovanovic, C. J. Barrelet, S. Gradecak, F. Qian, and C. M. Lieber, Nano Lett. **5**, 1407 (2005).
[7]P. Wojnar, E. Janik, L. T. Baczewski, S. Kret, E. Dynowska, T. Wojciechowski, J. Suffczynski, J. Papierska, P. Kossacki, G. Karczewski, J. Kossut, and T. Wojtowicz, Nano Lett. **12**, 3404–3409 (2012).
[8]A. Bouravleuv, G. Cirlin, V. Sapega, P. Werner, and A. Savin, J. Appl. Phys. **113**, 144303 (2013).
[9]D. Ferrand, J. Cibert, A. Wasiela, C. Bourgognon, S. Tatarenko, G. Fishman, T. Andrearczyk, J. Jaroszynski, S. Kolesnik, T. Dietl, B. Barbara, and D. Dufeu, Phys. Rev. B **63**, 85201 (2001).
[10]P. Wojnar, E. Janik, L. T. Baczewski, S. Kret, G. Karczewski, T. Wojtowicz, M. Goryca, T. Kazimierczuk, and P. Kossacki, Appl. Phys. Lett. **99**, 113109 (2011).
[11]L. Besombes, Y. Leger, L. Maingault, D. Ferrand, H. Mariette, and J. Cibert, Phys. Rev. Lett. **93**, 207403 (2004).
[12]P. Rueda-Fonseca, E. Bellet-Amalric, P. Stepanov, Y. Genuist, M. Den Hertog, D. Ferrand, K. Kheng, R. André, J. Cibert, and S. Tatarenko, EuroMBE Workshop, Levi, Finland, 2013.
[13]A. Ebina, K. Asano, and T. Takahashi, Phys. Rev. B **18**, 4341 (1978).
[14]H. Kirmse, W. Neumann, S. Kret, P. Dluzewski, E. Janik, G. Karczewski, and T. Wojtowicz, Phys. Status Solidi C **5**, 3780 (2008).
[15]E. Janik, P. Dluzewski, S. Kret, A. Presz, H. Kirmse, W. Neumann, W. Zaleszczyk, L. T. Baczewski, A. Petroutchik, E. Dynowska, J. Sadowski, W. Caliebe, G. Karczewski, and T. Wojtowicz, Nanotechnology **18**, 475606 (2007).
[16]F. Donatini and L. S. Dang, Nanotechnology **21**, 375303 (2010).
[17]C. A. Klein, J. Appl. Phys. **39**, 2029 (1968).
[18]B. Langen, H. Leiderer, W. Limmer, W. Gebhardt, M. Ruff, and U. Roessler, J. Cryst. Growth **101**, 718 (1990).
[19]D. Drouin, University of Sherbrooke, Canada.
[20]L. S. Dang, J. Cibert, Y. Gobil, K. Saminadayar, and S. Tatarenko, Appl. Phys. Lett. **55**, 235 (1989).
[21]J. Camacho, A. Cantarero, I. Hernndez-Caldern, and L. Gonzlez, J. Appl. Phys. **92**, 6014 (2002).
[22]K. E. Aifantis, A. L. Kolesnikova, and E. Romanov, Philod. Mag. **87**, 4731 (2007).
[23]D. Ferrand and J. Cibert, "Transversely isotropic approximation of strain in core-shell semiconductor nanowires" (unpublished).
[24]D. Berlincourt, H. Jaffe, and L. R. Shiozawa, Phys. Rev. **129**, 1009 (1963).
[25]J. M. Hartmann, J. Cibert, F. Kany, H. Mariette, M. Charleux, P. Alleyson, R. Langer, and G. Feuillet, J. Appl. Phys. **80**, 6257 (1996).
[26]M. H. M. van Weert, N. Akopian, F. Kelkensberg, U. Perinetti, M. P. van Kouwen, J. Gomez Rivas, M. T. Borgstrom, R. E. Algra, M. A. Verheijen, E. P. A. M. Bakkers, L. P. Kouwenhoven, and V. Zwiller, Small **5**, 2134 (2009).
[27]J. Wang, M. S. Gudiksen, X. Duan, Y. Cui, and C. M. Lieber, Science **293**, 1455 (2001).

BIBLIOGRAPHY

[1] Franchi, S. In *Molecular beam epitaxy: from research to mass production*, M. Henini Eds. Elselvier **2012**.

[2] Glas, F.; *Phys. Rev. B* **2006**, *74*, 121302.

[3] Ferrand, D.; Cibert, J. *Eur. Phys. J. Appl. Phys.* **2014**, *67*, 30403.

[4] Wojnar, P.; Janik, E.; Baczewski, L. T.; Kret, S.; Dynowska, E.; Wojciechowski, T.; Suffczynski, J.; Papierska, J.; Kossacki, P.; Karczewski, G.; Kossut, J.; Wojtowicz, T. *Nano Lett.* **2012**, *12*, 3404-3409.

[5] Vegard, L. Z.; *Phys* **1921**, *5*, 17.

[6] Stepanov, P. Magneto-optical spectroscopy of semiconductor magnetic quantum dots. Ph.D. Thesis, Universite de Grenoble, 2013.

[7] Jungwirth, T.; Horodyska, P.; Tesarova, N.; Nemec, P.; Subrt, J.; Maly, P.; Kuzel, P.; Kadlec, J.; Masek, I.; Nemec, I.; Orlita, M.; Navak, V.; Olejnik, K.; soban, Z.; Vasek, P.; Svoboda, P.; Sinova, J.; *Phys. Rev. Lett.* **2010**, *105*, 227201.

[8] Ferrand, D.; Cibert, J.; Wasiela, A.; Bourgognon, C.; Tatarenko, S.; Fishman, G.; Andrearczyk, T.; Jaroszynski, J.; Kolesnik, S.; Dietl, T.; Barbara, B. Dufeu, D.; *Phys. Rev. B* **2001**, *63*, 085201.

[9] Maksimov, A. A.; Bacher, G.; McDonald, A.; Kulakovskii, V. D.; Forchel, A.; Becker, C. R.; Landwehr, G.; Molekamp, L. W.; *Phys. Rev. B* **2000**, *62*, 7767.

[10] Hestroffer, K.; Croissance et caractérisation de nanofils de GaN et d'hétérostructures filaires de GaN/AlN. Ph.D. Thesis, Université de Grenoble, **2012**.

[11] den Hertog, M. Characterization of silicon nanowires by transmission electron microscopy. Ph.D. Thesis, Universite Joseph Fourier, Grenoble, 2009. http://tel.archives-ouvertes.fr/tel-00493934.

[12] den Hertog, M.; Schmid, H.; Cooper, D.; Rouviere, J.; Bjork, M.; Riel, H.; Rivallin, P.; Karg, S.; and Riess, W. *Nano Lett.* **2009**, *11*, 3837.

[13] Villain, J.; Pinpinelli, A. D. *Physics of crystal growth* **1998**, *Cambridge University Press.*

[14] Venables, J. A.; Spiller, G. D. T.; Hanbucken, M. *Rep. Prog. Phys.* **1984**, *47*, 399.

[15] Qiming, L.; Wang, G. T. *Appl. Phys. Lett.* **2008**, *93*, 043119.

[16] Hilner, E.; Mikkelsen, A.; Eriksson, J.; Andersen, J. N.; Lundgren, E. *Appl. Phys. Lett.* **2006**, *89*, 251912.

[17] Silly, F.; Castell, M. R. *Phys. Rev. Lett.* **2006**, *96*, 086104.

[18] Plass, R.; Marks, L. D. *Surface Science* **1997**, *380*, 497.

[19] Sui, M.; Li, M.; Kim, E.; Lee, J. *J. Appl. Cryst.* **2014**, *47*, 505.

[20] Daudin, R.; Nogaret, T.; Schulli, T. U.; Jakse, N.; Pasturel, A.; Renaud, G. *Phys. Rev. B* **2012**, *86*, 094103.

[21] Plante, M. C.; Garrett, J.; Ghosh, S. C.; Kruse, P.; Schriemer, H.; Hall, T.; LaPierre, R. R. *Appl. Surf. Sci.* **2006**, *253*, 2348.

[22] Seifert, C.; Hild, R.; Horn-von Hoegen, M.; Zhachuk, R. A.; Olshanetsky, B.Z. *Surface Science* **2001**, *488*, 233.

[23] Chan, S. K.; Lok, S. K.; Wang, G.; Cai, Y.; Wang, N.; Sou, I. K. *Appl. Phys. Lett.* **2008**, *92*, 183102.

[24] Bellet-Amalric, E.; Elouneg-Jamroz, M.; Rueda-Fonseca, P.; Bounouar, S.; Den Hertog, M.; Bougerol, C.; André, R.; Genuist, Y.; Poizat, J. P.; Kheng, K.; Cibert, J.; Tatarenko, S. *J. Crys. Growth* **2013**, *378*, 233.

[25] Elouneg-Jamroz, M. *Croissance Catalysée de Nanofils de ZnSe avec Boîtes Quantiques de CdSe.* PhD thesis **2013**, Université de Grenoble.

[26] Janik, E.; Dluzewski, P.; Kret, S.; Presz, A.; Kirmse, H.; Neumann, W.; Zaleszczyk, W.; Baczewski, L.T.; Petroutchik, A.; Dynowska, E.; Sadowski, J.; Caliebe, W.; Karczewski, G.; Karczewski, G. *Nanotechnology* **2007**, *18*, 475606.

[27] Yang, K.; Schowalter, L. J.; *Appl. Phys. Lett.* **1952**, *60*, 1852.

[28] Arnoult, A.; Cibert, J. *Appl. Phys. Lett.* **1995**, *66*, 2397.

[29] Etgens, V. H.; Sauvage-Simkin, M.; Pinchaux, R.; Massies, J.; Jedrecy, N.; Waldhauer, A.; Tatarenko, S; Jouneau, P. H. *Phys. Rev. B* **1993**, *47*, 10607.

[30] Jouneau, P. H,; Etude de microscopie electronique haute resolution d'heterostructures de semiconducteurs II-VI epitaxiees par jet moleculaires. Ph. D Thesis, Institut National Polytechnique de Grenoble, Grenoble, 1993.

[31] Cibert, J.; Gobil, Y.; Saminadayar, K.; Tatarenko, S.; Chami, A.C.; Feuillet, G.; Le Si Dang, L. S.; Ligeon, E. *Appl. Phys. Lett.* **1989**, *54*, 828.

[32] Ligeon, E.; Chami, A.; Danielou, R; Feuillet, G.; Fontenille, J.; Saminadayar, K.; Ponchet, A; Cibert, J.; Gobil, Y.; Tatarenko, S. *J. Appl. Phys.* **1990**, *67*, 2428.

[33] Duszak, R.; Tatarenko, S.; Cibert, J.; Mqgnea, N.; Mariette, H. Saminadayar, K. *Surface Science* **1991**, *251*, 511.

[34] Egan, C. K.; Jiang, Q. Z.; Brinkman, A. W. *J. Vac. Sci. Technol. A* **2011**, *29*, 1.

[35] Lensch-Falk, J. L.; Hemesath, E. R.; Perea, D. E.; Lauhon,L. J. *J. Mater. Chem.*, **2009**, *19*, 849-857.

[36] Okamoto, H.; Massalski, T. B.; *Binary Alloy Phase Diagrams*, **1984**, 322-338.

[37] Buffat, Ph.; Borel, J.P. *Phys. Rev. A*, **1976**, *13*, 2287.

[38] Alcock, C.B.; Itkin, V.P.; Horrigan, M.K. *Canadian Metallurgical Quarterly*, **1984**, *23*, 309.

[39] Lide,D. R. *CRC Handbook of Chemistry and Physics*, *Properties of the Elements and Inorganic Compounds, Vapor Pressure of the Metallic Elements* **2003**, *4*.

[40] Duszak, R.; Tatarenko, S.; Saminadayar, K.; Deshayes, C.; *J. Vac. Sci. Technol. A* **1991**, *9*, 6.

[41] Magnea, N.; Pautrat, J. L.; Saminadayar, K., Pajot, B.; Marin, P.; Bontemps, A. *Rev. Phys. Appl.* **1980**, *15*, 701.

[42] Trexler,J. T.; Fijol, J. J.; Calhoun, L. C.; Park, R. M.; Holloway, P. H. *J. Electron. Mater.* **1996**, *25*, 1474.

[43] Akkad, F. E. *Appl. Phys. Lett.* **2013**, *103*, 232101.

[44] Huo, H. B.; Dai, L.; Liu, C.; You, L. P.; Yang, W. Q.; Ma, R. M.; Ran, G. Z.; Qin, G. G. *Nanotechnology* **2006**, *17*, 5912.

[45] Lin, Y.; Chen, W.; Lu, J. Y.; Chang Y. H.; Liang, C. Chen, Y.F. and Lu, J. Y. *Nanoscale Research Lett.* **2012**, *7*, 401.

[46] Kahen, K. B.; Goldthorpe, I. R.; Holland, M. *Nanotechnology* **2013**, *24*, 455603.

[47] Chao, H. Y.; Cheng, J. H.; Lu, J. Y.; Chang, Y. H.; Cheng, C. L.; Chen, Y. F. *Superlattices and Microstructures* **2010**, *47*, 160.

[48] Li, L.; Yang, Y.; Huang, X.; Li, G. and Zhang, L. *J. Phys. Chem. B* **2005**, *109*, 12394.

[49] Petchsang, N.; Shapoval, L.; Vietmeyer, F.; Yu, Y.; Hodak, J. H.; Tang, I. M.; Koselg, T. H.; Kuno, M. *Nanoscale* **2011**, *3*, 3145-3151.

[50] Janik, E.; Sadowski, J.; Dluzewski, P.; Kret, S.; Baczewski, L.T.; Petroutchik, A.; Lusakowska, E.; Wrobel, J.; Zaleszczyk, W.; Karczewski, G.; Wojtowicz, T.; Presz, A. *Appl. Phys. Lett.* **2006**, *89*, 133114.

[51] Hertog, M. den; Elouneg-Jamroz, M.; Bellet-Amalric, E.; Bounouar, S.; Bougerol, C.; André, R.; Genuist, Y.; Poizat, J.-P.; Kheng, K.; Tatarenko, S.; *Nano Lett.* **2012**, *12*, 2977-2981.

[52] Cai, Y.; Wong, T. L.; Chan,S. K.; Sou,I. K.; Su, D. S.; Wang, N. *Appl. Phys. Lett.* **2008**, *93*, 233107.

[53] Chan, Y. F.; Duan, X. F.; Chan,S. K.; Sou,I. K.; Zhang, X. X.; Wang, N. *Appl. Phys. Lett.* **2003**, *83*, 2665.

[54] Cai, Y.; Chan,S. K.; Sou,I. K.; Chan, Y. F.; Su, D. S.; Wang, N. *Adv. Mater.* **2006**, *18*, 109.

[55] Cai, Y.; Chan,S. K.; Sou,I. K.; Chan, Y. F.; Su, D. S.; Wang, N. *Small* **2007**, *1*, 111-115.

[56] Colli, A.; Hofmann, S.; Ferrari, A. C.; Ducati, C.; Martelli, F.; Rubini, S.; Cabrini, S.; Franciosi, A.; Robertson, J. *Appl. Phys. Lett.* **2005**, *86*,153103.

[57] Aichele, T.; Tribu, A.; Bougerol, C,; Kheng, K.; Andre, R.; Tatarenko, S.; *Appl. Phys. Lett.* **2008**, *93*, 143106.

[58] Dick, K. A. *Progress in Crystal Growth and Characterization of Materials* **2008**, *54*, 138-173.

[59] Johansson, J.; Dick, A. *CrystEngComm* **2011**, *13*, 7175.

[60] Dubrovskii, V. G.; Cirlin, G. E.; Ustinov, V. M. *Semiconductors* **2009**, *12*, 1539.

[61] Joyce, H. J.; Gao, Q.; Hoe Tan, H.; Jagadish, C.; Kim, Y.; Zou, J.; Smith, L. M.; Jackson, H. E.; Yarrison-Rice, J. M.; Parkinson, P.; Johnston, M. B. *Progress in Crystal Growth and Characterization of Materials* **2011**, *35*, 23-75.

[62] Wojnar, P.; Zielinski, M.; Janik, E.; Zaleszczyk, W.; Wojtowicz, T.; Wojnar, R.; Szymura, M.; Klopotowski, L.; Baczewski, L. T.; Pietruchik, A.; Wiater, M.; Kret, S.; Karczewski, G.; Wojciechowski, T.; Kossut, J. *Appl. Phys. Lett.* **2014**, *104*, 163111.

[63] Kodambaka, S.; Tersoff, J.; Reuter, M. C.; Ross, F. M. *Science* **2007**, *316*, 729.

[64] Ross, F. M. *Rep. Prog. Phys.* **2010**, *73*, 114501.

[65] Wojnar, P.; Janik, E.; Baczewski, L. T.; Kret, S.; Karczewski, G.; Wojtowicz, T.; Goryca, M.; Kazimierczuk, T.; Kossacki, P. *Appl. Phys. Lett.* **2011**, *99*,113109.

[66] Wagner, R. S. Proceedings of the International Conference on Crystal Growth, **1966**, *347*.

[67] Lungstein, A.; Steinmair, M.; Hyun, Y. J.; Hauer, G.; Pongratz, P.; Bertagnolli, E. *Nano Lett.* **2008**, *8*, 8.

[68] Tian, B.; Xie,P.; Kempa, T. J.; Bell, D. C.; Lieber, C. M. *Nature Nanotechnology* **2009**, *4*, 824.

[69] de la Mata, M.; Magen, C.; Gazquez, J.; Utama, M. I. B.; Heisse, M.; Lopatin, S.; Furtmayr, F.; Fernandez-Rojas, C. J.; Peng, B.; Morante, J. R.; Rurali, R.; Eickhoff, M.; Fontacuberta i Morral, A.; Xiong, Q.; Arbiol, J. *Nano Lett.* **2012**, *12*, 2579.

[70] Perillat-Merceroz, G.; Thierry, R.; Jouneau, P.-H.; Ferret, P.; Feuillet, G. *Nanotechnology* **2012**, *23*, 155702.

[71] Shtrikman, H.; Popovitz-Biro, R.; Kretinin, A.; Houben, L.; Heiblum, M.; Bukala, M.; Galicka, M.; Buczko, R.; Kacman, P. *Nano Lett.* **2009**, *9*, 4.

[72] Carroff, P.; Dick, K. A.; Johansson, J.; Messing, M. E.; Deppert, K.; Samuelson, L. *Nature Nanotechnology* **2009**, *4*, 50.

[73] Joyce, H. J.; Wong-Leung, J.; Gao, Q.; Hoe Tan, H.; Jagadish, C. *Nano Lett.* **2010**, *10*, 908.

[74] Glas, F.; Harmand, J. C.; Patriarche, G.; *Phys. Rev. Lett.* **2007**, *99*, 46101.

[75] Rieger, T.; Schäpers, T.; Grützmacher, D.; Lepsa, M. I. *Cryst. Growth Des.* **2014**, *14*, 1167.

[76] Priante, G.; Harmand, J. C.; Patriarche, G.; Glas, F. *Phys. Rev. B* **2014**, *89*, 241301.

[77] Krogstrup, P.; Jorgensen, H. I.: Johnson, E.; Madsen, M. H.; Sorensen, C. B.; Fontcuberta i Morral, A.; Aagesen, M.; Nygard, J.; Glas, F. *J. Phys. D: Appl. Phys.* **2013**, *46*, 313001.

[78] Dubrovskii, V. G.; Sibirev, N. V.; Suris, R. A.; Cirlin, G. E.; Ustinov, V. M.; Tchernysheva, M.; Harmand, J. C.; *Semiconductors* **2006**, *9*, 1075.

[79] Dubrovskii, V. G.; Sibirev, N. V.; Cirlin, G. E.; Soshnikov, I. P.; Chen, W. H.; Larde, R.; Cadel, E.; Pareige, P.; Xu, T.; Grandidier, B.; Nys, J.-P.; Stievenard, D.; Moewe, M.; Chuang, L.C.; Chang-Hasnain, C. *Phys. Rev. B* **2009**, *79*, 205316.

[80] Dubrovskii, V. G.; Bolshakov, A. D.; Williams, B.L.; Durose, K. *Nanotechnology* **2012**, *23*, 485607.

[81] Glas, F. *J. Appl. Phys.* **2010**, *108*, 073506.

[82] Lauhon, L. J.; Gudiksen, M. S.; Wang, D.; Lieber, C. M. *Nature* **2002**, *420*, 57.

[83] Wen,Y.; Reuter, M. C.; Bruley, J.; Tersoff, J.; Kodambaka, S.; Stach, A.; Ross, F. M. *Science* **2009**, *326*, 1247.

[84] Zakharov, N.D.; Werner, P.; Gerth, G.; Schubert, L.; Sokolov, L.; Gosele, U. *Journal of Crystal Growth* **2006**, *290*, 6.

[85] Heiss, M.; Fontana, Y.; Gustafsson, A.; Wust, G.; Magen, C.; O'Regan, D.D.; Luo, J. W.; Ketterer, B.; Conesa-Boj, S.; Kuhlmann, A. V.; Houel, J.; Russo-Averchi, E.; Morante, J. R.; Cantoni, M.; Marzari, N.; Arbiol, J.; Zunger, A.; Warburton, R. J.; Fontcuberta i Morral, A. *Nature Materials* **2013**, *12*, 439.

[86] Uccelli, E.; Arbiol, J. Morante, J. M.; Fontcuberta i Morral, A. *ACS Nano* **2010**, *10*, 5985.

[87] Tchernychev, M.; Cirlin, G. E.; Patriarche, G.; Travers, L.; Zwiller, V.; Perinetti, U.; Harmand, J. C. *Nano lett.* **2007**, *7*, 1500.

[88] Harmand, J. C.; Jabeen, F.; Liu, L.; Patriarche, G.; Gauthron, K.; Senellart, P.; Elvira, D.; Berveratos, A. *Journal of Crystal Growth* **2013**, *378*,519.

[89] Qian, F.; Li, y.; Gradecak, S.; Wang, D.; Barrelet, C. J.; Lieber, C. M. *Nano Lett.* **2004**, *4*, 1975.

[90] Tomioka, K.; Motohisa, J.; Hara, S.; Hiruma, K.; Fukui, T.; *Nano lett.* **2010**, *10*, 1639.

[91] Bjork, M.T.; Ohlsson, B. J.; Sass, T. Persson, A. I.; Thelander, C.; Magnusson, M. H.; Deppert, k.; Wallenberg, L. R.; Samuelson, L. *Appl. Phys. Lett.* **2002**, *80*, 1058.

[92] Hertog, M. den; Elouneg-Jamroz, M.; Bellet-Amalric, E.; Bounouar, S.; Bougerol, C.; André, R.; Genuist, Y.; Poizat, J.-P.; Kheng, K.; Tatarenko, S.; *J. Appl. Phys.* **2011**, *110*, 034318.

[93] Hsiao, C. H.; chang, S. J.; Hung, S. C.; Cheng, Y. C.; Huang, B. R.; Wang, S. B.; Lam, B. W.; Chih, S. H. *Journal of Crystal Growth* **2010**, *312*, 1670.

[94] Hocevar, M.; Immink, G.; Verheijen, M.; Akopian, N.; Zwiller, V.; Kouwenhoven, L.; Bakker, E. *Nature Communications* **2012**, *3*, 1266.

[95] Conesa-Boj, S.; Dunand, S.; Russo-Averchi, E.; Heiss, M.; Ruffer, D.; Wyrsch, N.; Fontcuberta i Morral, A. *Nanoscale* **2013**, *5*, 9633.

[96] Bounouar, S.; Elouneg-Jamroz, M.; Hertog, M. den, Morchutt, C.; Bellet-Amalric, E.; André, R.; Bougerol, C.; Genuist, Y.; Poizat, J.-P.; Tatarenko, S.; Kheng, K. *Nano Lett.* **2012**, *12*, 2977-2981.

[97] Tambe, M. J.; Allard, L. F.; Gradecak, S.; *Journal of Physics: Conference Series* **2010**, *209*, 012033.

[98] Ma, C.; Moore, D.; Ding, Y.; Li, J.; Wang, Z. L. *Int. J. Nanotechnology* **2004**, *4*, 431.

[99] Wang, Y. Q.; Philipose, U.; Ruda, H.; Kavanagh, K. L. *J. Mater Sci: Mater Electron* **2006**, *17*, 1065.

[100] Watanabe, M; Williams, D. B. *Journal of Microscopy* **2006**, *221*, 89.

[101] Robin, E.; Lopez-Haro, M. *to be published.*

[102] Artioli, A.; Rueda-Fonseca, P.; Stepanov, P.; Bellet-Amalric, E.; Hertog, M.D.; Bougerol, C.; Genuist, Y.; Donatini, F.; André, R.; Nogues, G.; Kheng, K.; Tatarenko, S.; Ferrand, D.; Cibert, J. *Appl. Phys. Lett.* **2013**, *103*, 222106.

[103] Hanbury-Brown, R.; Twiss, R. *Nature* **1956**, *177*, 1956.

[104] Gas, K . et al. *Acta Physica Polonica A* **2011**, *119*, 612.